JOURNAL OF GEOPHYSICAL RESEARCH

The continuation of

RRESTRIAL MAGNETISM AND ATMOSPHERIC ELECTRICITY
(1896-1948)

An International Quarterly

OLUME 63 March, 1958 NUMBER 1

CONTENTS

(Contents concluded on outside back cover)

Published at

THE WILLIAM BYRD PRESS, INC.

P. O. BOX 2-W, SHERWOOD AVE. AND DURHAM ST.

RICHMOND 5, VIRGINIA

Address all correspondence to

JOURNAL OF GEOPHYSICAL RESEARCH

5241 BROAD BRANCH ROAD, NORTHWEST

WASHINGTON 15, D.C., U.S.A.

SIX DOLLARS A YEAR

SINGLE NUMBERS, TWO DOLLARS

JOURNAL OF GEOPHYSICAL RESEARCH

The continuation of

Terrestrial Magnetism and Atmospheric Electricity

(1896-1948)

An International Quarterly

Founded 1896 by L. A. BAUER *Continued 1928-1948 by* J. A. FLEMING

Fields of Interest

Terrestrial Magnetism
Atmospheric Electricity
The Ionosphere
Solar and Terrestrial Relationships
Aurora, Night Sky, and Zodiacal Light
The Ozone Layer
Meteorology of Highest Atmospheric Levels
The Constitution and Physical States of the Upper Atmosphere
Special Investigations of the Earth's Crust and Interior, including experimental seismic waves, physics of the deep ocean and ocean bottom, physics in geology
And similar topics

This Journal serves the interests of investigators concerned with terrestrial magnetism and electricity, the upper atmosphere, the earth's crust and interior by presenting papers of new analysis and interpretation or new experimental or observational approach, and contributions to international collaboration. It is not in a position to print, primarily for archive purposes, extensive tables of data from observatories or surveys, the significance of which has not been analyzed.

Forward *manuscripts* to one of the Associate Editors, or to the editorial office of the Journal at 5241 Broad Branch Road, Northwest, Washington 15, D.C., U.S.A. It is preferred that manuscripts be submitted in English, but communications in French, German, Italian, or Spanish are also acceptable. A brief abstract, preferably in English, must accompany each manuscript. A *publication charge* of $8 per page will be billed by the Editor to the institution which sponsors the work of any author; private individuals are not assessed page charges. Manuscripts from outside the United States are invited, and should not be withheld or delayed because of currency restrictions or other special difficulties relating to page charges. Costs of publication are roughly twice the total income from page charges and subscriptions, and are met by subsidies from the Carnegie Institution of Washington and international and private sources.

Back issues and *reprints* are handled by the Editorial Office, 5241 Broad Branch Road, N.W., Washington 15, D.C., U.S.A.

Subscriptions are handled by the Editorial Office, 5241 Broad Branch Road, N.W., Washington 15, D.C., U.S.A.

Second-class mail privileges authorized at Richmond, Virginia

Journal of

GEOPHYSICAL RESEARCH

The continuation of

Terrestrial Magnetism and Atmospheric Electricity

VOLUME 63 MARCH, 1958 No. 1

COSMIC-RAY TRAPPING IN INTERPLANETARY SPACE

BY ARTHUR BEISER

New York University, University Heights, New York 53, New York

(Received May 4, 1957)

ABSTRACT

The existence of long-term variations in cosmic-ray intensity negatively correlated with sunspot activity, a discovery due to Forbush, has been explained by Davis in terms of a cavity in the galactic magnetic field centered about the sun. In the present paper, it is shown that a "diamagnetic" interplanetary region, rather than a "superconducting" one, can account for the cut-off in the primary cosmic-ray rigidity spectrum, as well as for the 11-year variations. The suggested diamagnetic region is an oblate spheroid in shape, with semiaxes of roughly 5×10^{15} cm and 5×10^{14} cm, and its effective permeability of 10^{-4} implies a mean interplanetary field of about 10^{-9} gauss. The 11-year variations and the rigidity cut-off are analyzed in detail on the basis of this model.

INTRODUCTION

Recently, several proposals have been made to account for the apparently anomalous (in the sense of not being characteristic of galactic space generally) propagation of cosmic rays in the vicinity of the solar system. One, by Davis [see 1 of "References" at end of paper], suggests that ion streams emitted by the sun push back the lines of force of the galactic magnetic field, creating a field-free cavity around the sun. Such a cavity can trap cosmic rays in an extensive energy interval for long periods of time. Fluctuations in the rate of solar corpuscular emission cause changes in the cavity volume, providing a plausible explanation for the long-term cosmic-ray variation observed by Forbush [2] to occur out of

phase with the sunspot cycle. This scheme, however, does not deal satisfactorily with the serious problem of the cut-off at the low end of the primary cosmic-ray magnetic rigidity spectrum, a deficiency that has led to the consideration of alternate magnetic models [3] of the interplanetary region. In this paper, it will be shown that a modification of the cavity hypothesis seems able to account for the cut-off while preserving the other virtues of the idea.*

DIAMAGNETIC SPHEROID MODEL

Ion streams from the sun are able to transport the galactic field H ($\sim 10^{-5}$ gauss) outward until the magnetic pressure $H^2/8\pi$ begins to exceed the material pressure, which for radial streams decreases as r^{-2}. The ions then proceed along the lines of force. If the electrical conductivity of interplanetary space were infinite, streams reasonably uniform in time and space could sweep the neighborhood of the sun completely free of magnetic field out to where the pressure balance occurs. This situation is assumed by Davis. Actually, however, the conductivity does not become infinite and the solar emissions are quite irregular; a more realistic statement might be that the region is diamagnetic, leaving the possibility open for the existence of a small remnant field. We suppose now that this is the case, and that a relative permeability $\mu > 0$ is present owing to the inefficiency of the expulsion process for the galactic field. As we will see, μ need not exceed an average value of about 2×10^{-5} to produce a magnetic cosmic-ray cut-off of the kind that is observed. Essentially, the cavity is here being replaced by a diamagnetic spheroid (or DS).

Estimates of the flux of solar corpuscular radiation may be obtained from considerations of their geomagnetic effects [4], of the deflections they cause in comet tails [5], and of their optical and rf absorption [6]. The solar events that apparently give rise to much of the radiation occur most frequently near the solar equator; we will adopt the figure 300 cm^{-3} for the density at the earth of slow protons originating in the equatorial region of the sun. (Only the square root of this density will be needed, so the uncertainty in this quantity does not introduce undue error.)

Corpuscular radiation from the polar regions of the sun is less than that from lower latitudes, but the observational data do not yield a quantitative statement of the difference. A guess might be that the flux from the equator exceeds that from the poles by a factor of 100. This follows from the assumption that, since flares, sunspots, and other such phenomena are absent from the higher latitudes, electromagnetic acceleration processes associated with them are likewise absent, leaving thermal evaporation [7] as the dominant contributor. Normally, the density of the corona is ten times greater at the equator than at the poles, and a ratio of approximately the same size should prevail for the evaporation rates. In addition, the energetic auroral and cosmic-ray streams emitted near the equator,

*S. Chandrasekhar has kindly drawn my attention to the possibility that instabilities of various kinds may disrupt the cavity wall, thereby providing trajectories that would permit the escape of trapped particles. The discussion that follows may accordingly have to be modified, perhaps drastically, but it seems premature to regard its agreement with the available data as being entirely fortuitous.

although not in themselves adding significantly to the flux from there, are very likely accompanied by slower streams from the same sources and, furthermore, provide a "wind" that propels additional coronal material outward. An estimate of the enhancement from these effects is another factor of ten; thus, the net ratio is 100, and at a distance corresponding to the earth's mean orbital radius the polar flux is ~ 3 protons cm^{-3}.

The distance R at which equilibrium between the solar proton streams and the galactic magnetic field takes place can be obtained from the equation of this equilibrium

$$n_{earth} r_{earth}^2 m_p v^2 R^{-2} = H^2/8\pi \quad \ldots\ldots\ldots\ldots\ldots\ldots (1)$$

where n_{earth} is the number density of the protons at the distance $r_{earth} = 1.5 \times 10^{13}$ cm from the sun, m_p the proton mass, and v the mean proton velocity, believed to be about 6×10^7 cm sec^{-1}. The proper value of H to use is not its unperturbed value $H_0 \sim 10^{-5}$ gauss, but instead its increased magnitude at R. If the cavity were spherical and field-free, the field just outside it would be $3H_0/2$ at its equator. In the present case, the region is a diamagnetic oblate spheroid and H at its surface must be greater than this; let us suppose $2H_0$. In the equatorial plane, therefore, $R_a \approx 5 \times 10^{15}$ cm, and in the polar regions $R_b \approx 5 \times 10^{14}$ cm. Too much credence should not be placed in these figures, but they provide a not unreasonable starting point.

The magnitude and direction of the magnetic field H_i inside a spheroid of the above kind, characterized by a relative permeability μ and located in a uniform external field H_0 , may be calculated from the general solution for the corresponding electric case [8], yielding

$$H_{ix} = \frac{\mu H_0 \cos\theta}{1 + \frac{1}{2}R_a^2 R_b(\mu - 1)A_1}$$

$$H_{iy} = \frac{\mu H_0 \sin\theta}{1 + \frac{1}{2}R_a^2 R_b(\mu - 1)A_2}$$

for the x and y components of H_i , where R_b is directed along the y axis. The angle θ is taken between H_0 and R_a , and A_1 and A_2 are, in general, elliptic integrals, which for the present degenerate ellipsoid yield the result

$$A_1 = \frac{1}{R_a^2 - R_b^2}\left[-\frac{R_b}{R_a^2} + \frac{1}{(R_a^2 - R_b^2)^{1/2}} \tan^{-1} \frac{(R_a^2 - R_b^2)^{1/2}}{R_b}\right]$$

and

$$A_2 = \frac{2}{R_a^2 - R_b^2}\left[\frac{1}{R_b} - \frac{1}{(R_a^2 - R_b^2)} \tan^{-1} \frac{(R_a^2 - R_b^2)^{1/2}}{R_b}\right].$$

Using $R_a = 5 \times 10^{15}$ cm and $R_b = 5 \times 10^{14}$ cm,

$$H_{ix} = \frac{\mu H_0 \cos\theta}{1 + 0.093(\mu - 1)}$$

$$H_{iy} = \frac{\mu H_0 \sin\theta}{1 + 0.820(\mu - 1)}$$

which for small permeability become

$$H_{ix} = 1.10\mu H_0 \cos\theta$$

$$H_{iy} = 5.56\mu H_0 \sin\theta$$

The angle θ' between H_i and the equatorial plane is

$$\theta' = \tan^{-1} H_{iy}/H_{ix}$$

$$= \tan^{-1} 5.05 \tan\theta$$

Since θ is believed [9] to be about 60°, θ' is 83°. The net result is that the magnetic field within the spheroid is uniform, with a magnitude

$$\left.\begin{aligned} H_i &= 4.85\mu H_0 \\ &= \mu' H_0 \end{aligned}\right\} \quad \ldots\ldots\ldots\ldots\ldots\ldots\ldots\ldots (2)$$

and is bent toward the minor axis relative to the external field. Figure 1 is a sketch of this situation.

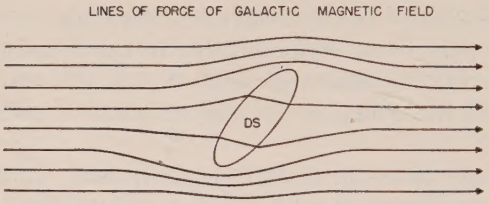

FIG. 1—Distortion of the galactic magnetic field in the vicinity of the sun

EFFECT ON PRIMARY COSMIC RADIATION

The primary cosmic radiation is usually understood to mean the high-energy corpuscular radiation, largely protons, but with some alpha particles and heavier nuclei present, of non-solar origin, that is incident on the top of the earth's atmosphere. The experimental integral momentum spectrum $J(> p)$ of each primary component for $p > \sim 5$ Bev/c is well represented by an equation of the form

$$J(> p) = A_z p^{-n_z} \quad \ldots\ldots\ldots\ldots\ldots\ldots\ldots\ldots (3)$$

where A_z and n_z are constants whose values are different for each component. (Another common representation for this spectrum is in terms of the energy per nucleon E, namely, $J(> E) = A_z(1 + E)^{n_z}$. However, since $(1 + E) = (1 + p^2)^{1/2}$, both forms are identical for $p^2 \gg 1$.) At low momenta, Eq. (3) predicts far more primaries than are found; in fact, below a certain momentum, whose value apparently varies somewhat, no further primaries at all are present. Spectra of the above power-law type have been shown to result from acceleration processes in the galaxy of the sort generally accepted, and it must, therefore, be concluded that the departures from these spectra are of local origin and are not characteristic of the rest of the galaxy. The cut-off occurs at different momentum figures for the various components, but for each one the magnetic rigidity Hr, equal to $10^7 Mp/3Z$ gauss-cm, where M is the mass number of the particle, Z its atomic number, and p its momentum in Bev/c, of the cut-off is the same. Hence, the anomaly has a magnetic origin. However, neither the solar dipole field (if any),

nor the effect of the opening out of the geomagnetic shadow cone at high altitudes, is quantitatively adequate to account for it.

The presence of the DS seems to provide a natural explanation for the cut-off. Its effects are best described in terms of the quantity

$$\frac{\sin^2 \alpha}{H} = K \quad \ldots\ldots\ldots\ldots\ldots\ldots\ldots\ldots\ldots\ldots (4)$$

where α is the angle between the velocity vector of an ion moving in a magnetic field of magnitude H and the direction of **H**. K is a constant of the motion, provided that H does not vary too rapidly. Cosmic-ray ions spiraling around the lines of force of the galactic magnetic field H_0 that approach the solar system as described by the DS model may be divided into three classes:

I. Primaries whose helix radii in the galactic field exceed the major axis R_a of the DS, that is, when

$$p(K/H_0)^{1/2} > 3R_a \times 10^{-7} \quad \ldots\ldots\ldots\ldots\ldots\ldots\ldots\ldots (5)$$

II. Primaries whose helix radii are less than R_a in the galaxtic field but which exceed R_a in the smaller field H_i within the DS, that is, when

$$p(K/H_0)^{1/2} < 3R_a \times 10^{-7} < p(K/H_i)^{1/2} \quad \ldots\ldots\ldots\ldots\ldots\ldots\ldots\ldots (6)$$

III. Particles whose helix radii are less than R_a, both in the galactic field H_0 and in the DS field H_i, that is, when

$$p(K/H_i)^{1/2} < 3R_a \times 10^{-7} \quad \ldots\ldots\ldots\ldots\ldots\ldots\ldots\ldots (7)$$

Eqs. (5) to (7) can be extended to primaries other than protons by making use of the definition of magnetic rigidity.

Class I particles can move more or less freely through the DS, although their trajectories may suffer some distortion in its vicinity (Fig. 2). By Liouville's theorem in its usual modification for the motion of charged particles in magnetic fields [10], Class I particles have the same density inside as outside the DS.

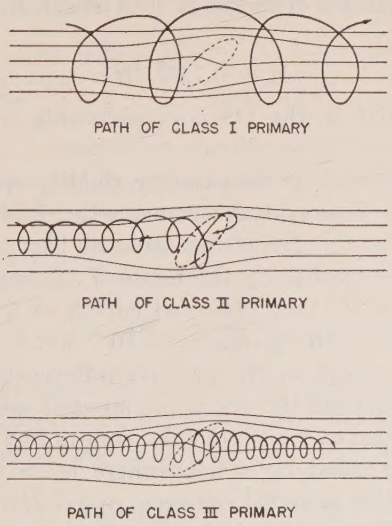

FIG. 2—Trajectories of Class I, II, and III primary cosmic-ray particles near the DS (dotted ellipse)

Class II particles can enter the DS only along a limited number of paths (to be described later). Once inside, the tubes of force enclosed by their trajectories diverge to the DS boundary and the particles are reflected there by the higher field with a probability to be evaluated subsequently. The exit of the particles at the end of the DS opposite to the one of entry is possible only along paths corresponding to those along which oppositely-charged particles of the same momentum are able to enter. Hence, Class II primaries that get inside are trapped and cannot immediately escape. Their probability for escape equals their probability for entry, so that at equilibrium the inside and outside densities of Class II particles are the same. (Actually, oscillations about equilibrium occur, causing changes in the Class II density inside, but these amount to only a few per cent and will be ignored here, pending the detailed treatment later.) Class II primaries within the DS lose all traces of their original directions of motion after the repeated reflections at the DS walls.

Class III primaries can enter the DS only along tubes of force whose radii do not exceed R_a even inside the DS. Since $H_i < H_0$, such tubes of force are centered along or very close to the axis of revolution of the DS (Fig. 2). No reflection of the kind predicted by Eq. (4) takes place, since the particles that are able to enter can subsequently emerge back into the galactic field at the other end of the DS without ceasing to encircle the tubes of force whose surfaces they entered on. Only a small fraction of the Class III particles whose helices intersect a cylinder of radius R_a , coaxial with the DS, can enter, and these are not trapped. The density of these inside the DS may be determined by considering the radius R' of the largest tube of force in the galactic field wholly included within the DS, which is given by

$$R' = R_a(H_i/H_0)^{1/2} \quad \ldots\ldots\ldots\ldots\ldots\ldots\ldots\ldots\ldots\ldots (8)$$

The fractional reduction Y in the density of Class III primaries within the DS equals the volume of a cylinder of radius R' and length R_b divided by the volume of the DS, so that

$$Y = 0.75H_i/H_0 \quad \ldots\ldots\ldots\ldots\ldots\ldots\ldots\ldots\ldots\ldots\ldots (9)$$

Thus, the Class III density in the DS is considerably smaller than the outside density.

The meaning of the cut-off in the primary rigidity spectrum on the basis of this picture is clear: it is that transverse magnetic rigidity separating Class II particles, whose density in the DS is the same as that outside, from Class III particles, whose density is smaller by the factor Y. If the radius of curvature of the limiting trajectories is R_a , the observed cut-off at 5×10^6 gauss-cm yields $H_i = 10^{-9}$ gauss. Since $H_0 = 10^{-5}$ gauss, $\mu' = 10^{-4}$ and $Y = 7.5 \times 10^{-5}$.

The effect of the DS model on the primary differential momentum spectrum will now be computed, and from the result the integral spectrum will be obtained.

The solid angle subtended by a right circular cone of half-angle θ is $2\pi(1 - \cos\theta)$ steradians, and that subtended by a hemisphere is 2π steradians. If the helix angles θ (that is, the angles included between p and H_i) of the primary cosmic rays in the galactic field are isotropically distributed, the probability that the helix angle of any particle be less than or equal to θ is therefore $(1 - \cos\theta)$.

Now, let p_c be the momentum of a proton (the formulation may be extended to heavier particles by substituting Mp/Z for p) perpendicular to H_i such that

$$10^7 p_c/3H_i = R_a \quad \ldots\ldots(10)$$

Thus p_c is the maximum transverse momentum a Class III proton may have, and all protons for which

$$p \sin \theta \leq p_c \quad \ldots\ldots(11)$$

fall into Class III. The probability W_{III} that a proton of momentum p falls into Class III is just the probability that its helix angle in the DS equals or is less than the value of θ specified by Eq. (11), namely,

$$\left.\begin{aligned} W_{III} &= 1 - \cos\theta \\ &= 1 - (1 - p_c^2/p^2)^{1/2} \end{aligned}\right\} \quad \ldots\ldots(12)$$

The corresponding probability $W_{I,II}$ that the proton falls into Class II and is trapped or into Class I and is not affected by the DS (in both cases the DS density and the galactic density are the same) is

$$W_{I,II} = (1 - p_c^2/p^2)^{1/2} \quad \ldots\ldots(13)$$

If $j_0(p)\mathrm{d}p$ is the density of primary protons in the galactic field having moments between p and $p + \mathrm{d}p$, their density in the DS is, for Class I and II, j_0 multiplied by $W_{I,II}$, while for Class III it is j_0 multiplied by both W_{III} and Y, the density reduction factor. The differential momentum spectrum $j_i(p)\mathrm{d}p$ of primary protons within the DS, which is what is observed at the earth, is thus given by

$$\left.\begin{aligned} j_i(p)\,\mathrm{d}p &= j_0\{(1 - p_c^2/p^2)^{1/2} + Y[1 - (1 - p_c^2/p^2)^{1/2}]\}\,\mathrm{d}p, \qquad p \geq p_c \\ &= j_0(p)\,Y\,\mathrm{d}p, \qquad p_{\min} \leq p \leq p_c \\ &= 0, \qquad p < p_{\min} \end{aligned}\right\} \quad \ldots\ldots(14)$$

The value of quantity $p_{\min}$ depends on the nature of the acceleration process and on the distribution of sources. Particles known to originate in the sun, such as those responsible for aurorae, are not considered part of the cosmic radiation.

The observed differential momentum spectrum corresponding to j_i at high momenta may be obtained by differentiating Eq. (3). Dropping the subscript i,

$$j_i(p)\,\mathrm{d}p = nAp^{-(n+1)}\,\mathrm{d}p \quad \ldots\ldots(15)$$

Assuming that the departure from this inverse power-law spectrum near p_c is a local phenomenon arising from the DS magnetic field, an hypothesis supported by current theories of cosmic-ray origin, Eq. (15) may be rewritten

$$j_0(p)\,\mathrm{d}p = nAp^{-(n+1)}\,\mathrm{d}p$$

Substituting this equation into Eq. (14) yields

$$\left.\begin{aligned} j_i(p)\,dp &= nAp^{-(n+1)}\{(1 - p_c^2/p^2)^{1/2} \\ &\qquad + Y[1 - (1 - p_c^2/p^2)^{1/2}]\}\,dp, \qquad p \geq p_c \\ &= YnAp^{-(n+1)}\,dp, \qquad p_{\min} \leq p \leq p_c \\ &= 0, \qquad p < p_{\min} \end{aligned}\right\} \quad \ldots\ldots(16)$$

This expression contains no arbitrary constants, and is plotted for primary protons in Figure 3 for $p_c = 1.6$ [11], $n = 1.1$ [11], and $Y = 7.5 \times 10^{-5}$.

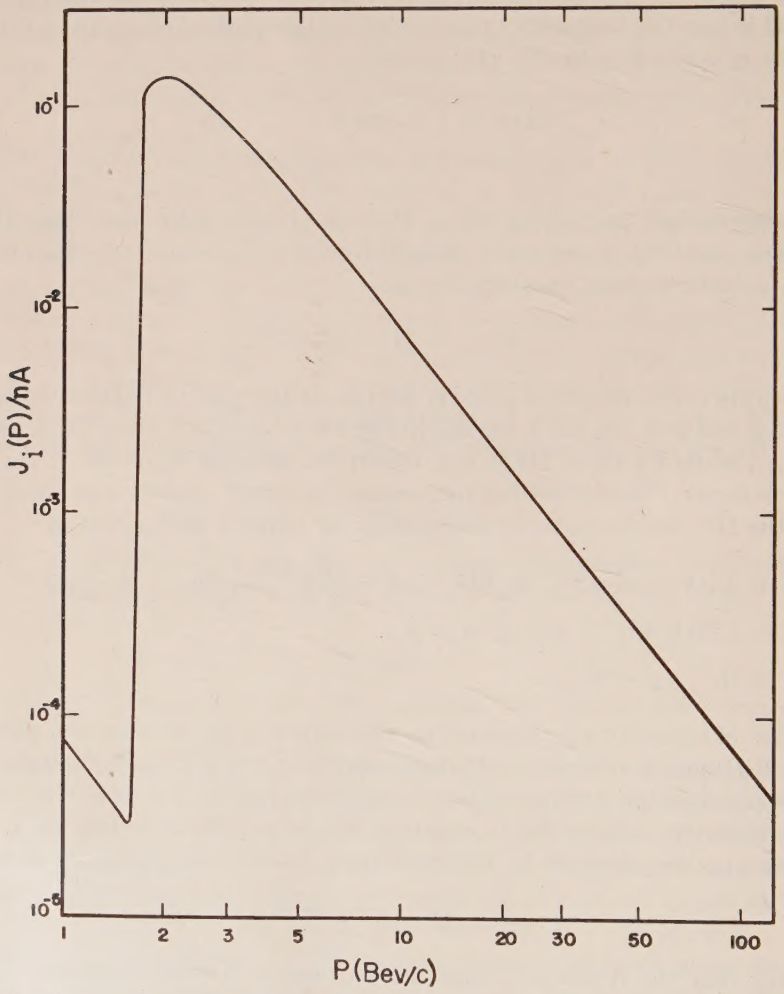

FIG. 3—The primary differential cosmic-ray momentum spectrum after its modification in the interplanetary region

The quantity $J(< p)$ is the density of primary cosmic rays with momenta exceeding p, and it is the spectrum that is usually measured experimentally. To find $J(> p)$, it is necessary to integrate Eq. (16) from p to infinity, which gives

$$
\left.
\begin{aligned}
J(>p) &= \int_p^\infty j_i(p)\,dp \\
&= A\left\{\left[p^{-n} - \frac{np_c^2p^{-(n+2)}}{2(n+2)} - \frac{np_c^4p^{-(n+4)}}{8(n+4)} - \frac{np_c^6p^{-(n+6)}}{16(n+6)} - \cdots\right]\right. \\
&\qquad \left. + Y\left[\frac{np_c^2p^{-(n+2)}}{2(n+2)} + \frac{np_c^4p^{-(n+4)}}{8(n+4)} + \frac{np_c^6p^{-(n+6)}}{16(n+6)} + \cdots\right]\right\} \qquad p > p_c \\
&= J(>p_c) + AY_p^{-n}, \qquad p_{\min} \le p \le p_c \\
&= J(>p_{\min}) \qquad p < p_{\min}
\end{aligned}
\right\} \quad \ldots . (17)
$$

The results of recent primary intensity measurements [12] on the proton, alpha particle, and heavy nucleus components are plotted, respectively, in Figures 4, 5, and 6, together with curves calculated from Eq. (17), using the constants listed below:

Component	A		n
Protons	0.50	$(\text{cm}^2\text{-sec-ster})^{-1}$	1.1
Alpha particles	0.031	"	1.4
Heavy nuclei	0.0042	"	1.4

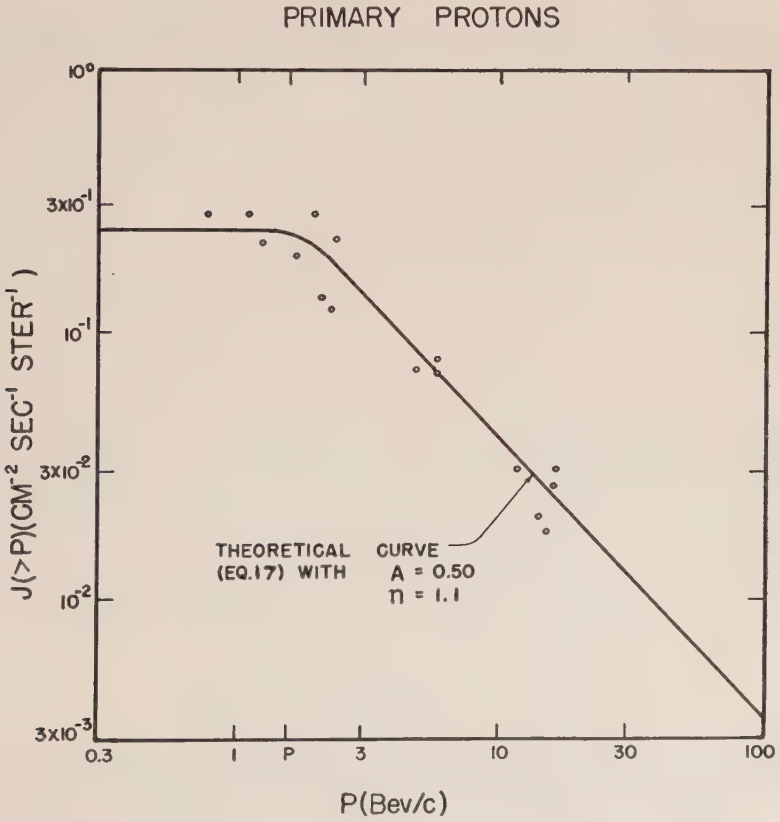

FIG. 4—The integral momentum spectrum of primary protons

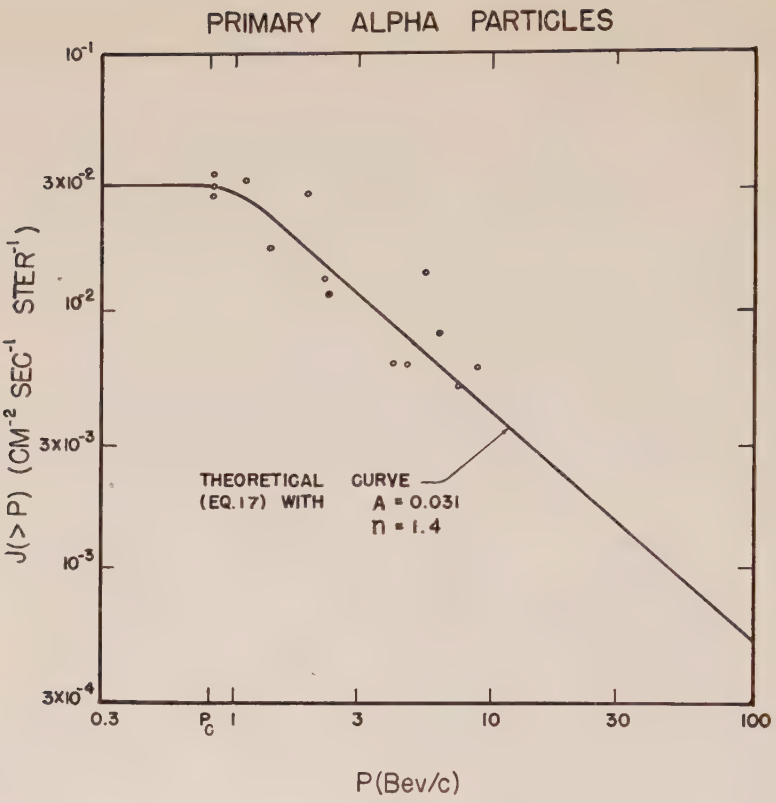

FIG. 5—The integral momentum spectrum of primary alpha particles

There seems to be substantial agreement between the integral spectrum predicted by Eq. (17) and the experimental results.

LIFETIME OF CLASS II PARTICLES

The escape probability for Class II particles from the DS is of interest, since from it can be obtained the corresponding average lifetime of these particles within the DS. Positive and negative particles have identical probabilities for entry, and, as the possible trajectories of escaping positive particles are the same as those of negative particles entering, the equilibrium density in the DS, under constant conditions, equals the outside density. The rate of entry of positive Class II particles will now be calculated.

The number of particles having momenta between p and $p + \mathrm{d}p$ in the galactic field is $j_0(p)\mathrm{d}p$, and for a helix angle θ a particle of momentum p in this field moves on the surface of a cylinder of radius

$$r = \frac{10^7 p \sin \theta}{3H_0}$$

Class II particles are those whose helical paths surround at least one line of force split by the DS and which diverges around it (Fig. 2). Hence, if R' is the radius

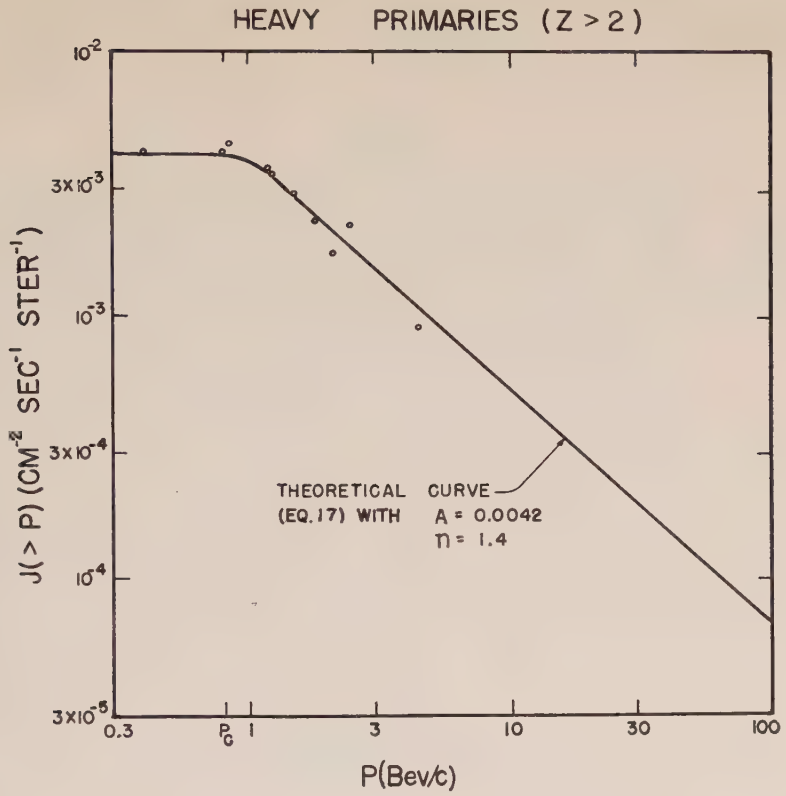

FIG. 6—The integral momentum spectrum of primary heavy nuclei ($Z > 2$)

of the largest tube of force in the galactic field wholly included within the DS field, all particles of momentum p whose guiding cylinders overlap a cylinder of radius $R' + r$ coaxial with the DS fall into either Class II or Class III. The volume of a cylinder of unit length and radius $R' + r$ is

$$\pi\left(R' + \frac{10^7 p \sin\theta}{3H_0}\right)^2$$

If the angles θ are isotropically distributed, the probability that a particle has a helix angle between θ and $\theta + d\theta$ is

$$\frac{2\pi \sin\theta\, d\theta}{4\pi} = \frac{\sin\theta\, d\theta}{2}$$

Hence, there are

$$\left(R' + \frac{10^7 p \sin\theta}{3H_0}\right)^2 \frac{j_0(p)\, dp \sin\theta\, d\theta}{2}$$

particles of both Class II and Class III per unit distance along lines of force encircled by the trajectories of these particles in the above momentum and angular

limits. All particles for which $p < p_c$ fall into Class III, and the probability W_{II} that those for which $p > p_c$ fall into Class II is

$$\left.\begin{aligned} W_{II} &= (1 - p_c^2/p^2)^{1/2}, \qquad p_m \geq p \geq p_c \\ &= 1 - (1 - p_m^2/p^2)^{1/2}, \qquad p > p_m \end{aligned}\right\} \quad \ldots\ldots\ldots\ldots\ldots\ldots (18)$$

where p_m is the maximum transverse momentum a Class II particle can have. Since $p_m \approx 1{,}500$ and the spectral intensity drops off steeply with increasing momentum, retaining only the first of Eqs. (18) will introduce negligible error. The linear density of Class II particles incident on the DS is, therefore,

$$j_0(p)\pi\left(R' + \frac{10^7 p \sin\theta}{3H_0}\right)^2 \frac{\sin\theta\, d\theta}{2}\left(1 - \frac{p_c^2}{p^2}\right)^{1/2} dp$$

The forward velocity of these particles is

$$v \cos\theta = \frac{p_c \cos\theta}{(1 + p^2)^{1/2}}$$

and the net rate at which Class II particles enter the DS (including a factor of 2 to take into account the two possible directions of entry) is

$$j_0(p)\left[\frac{p^2 - p_c^2}{p^2 + 1}\right]^{1/2} dp\pi c \int_0^{\pi/2}\left(R' + \frac{10^7 p \sin\theta}{3H_0}\right)^2 \sin\theta \cos\theta\, d\theta$$

$$= j_0(p)\left[\frac{p^2 - p_c^2}{p^2 + 1}\right]^{1/2} \pi c\left[\frac{R'^2}{2} + \frac{2 \times 10^7 R' p}{9H_0} + \frac{10^{14} p^2}{36H_0^2}\right] dp \quad \text{particles sec}^{-1}$$

At equilibrium, the number of particles *within* the DS having momenta between p and $p + dp$ is, for Class II particles,

$$\frac{4}{3}\pi R_a^2 R_b j_i(p)\, dp = \frac{4}{3}\pi R_a^2 R_b j_0(p)(1 - p_c^2/p^2)^{1/2}\, dp$$

Hence, the probability for entry of a particle of momentum p becomes

$$\frac{1}{\tau} = \frac{3c}{4R_a^2 R_b}\left[\frac{p^2}{p^2 + 1}\right]^{1/2}\left[\frac{R'^2}{2} + \frac{2.2 \times 10^6 R' p}{H_0^2} + \frac{2.8 \times 10^{12} p^2}{H_0^2}\right] \text{sec}^{-1} \quad \ldots\ldots (19)$$

The value of R' may be obtained from Eq. (8) and is 5×10^{13} cm. For $p_c = 1.6$, $H_0 = 10^{-5}$ gauss, $R_a = 5 \times 10^{15}$ cm, and $R_b = 5 \times 10^{14}$ cm, the mean lifetime τ is plotted *versus* momentum in Figure 7. The significance of this curve will be discussed below.

It is also necessary to determine the probability that a particle will be able to penetrate the DS walls rather than be reflected and remain trapped. A simple calculation shows that this probability is H_i/H_0 , which is 10^{-4} here. Choosing the "average" DS diameter to be $2(R_a^2 R_b)^{1/3} = 5 \times 10^{15}$ cm, the time required for a primary Class II particle of velocity close to the velocity of light to make 10^4 traversals of the DS is 1.7×10^7 sec, or about 60 years. This probability exceeds τ for all $p > p_c$.

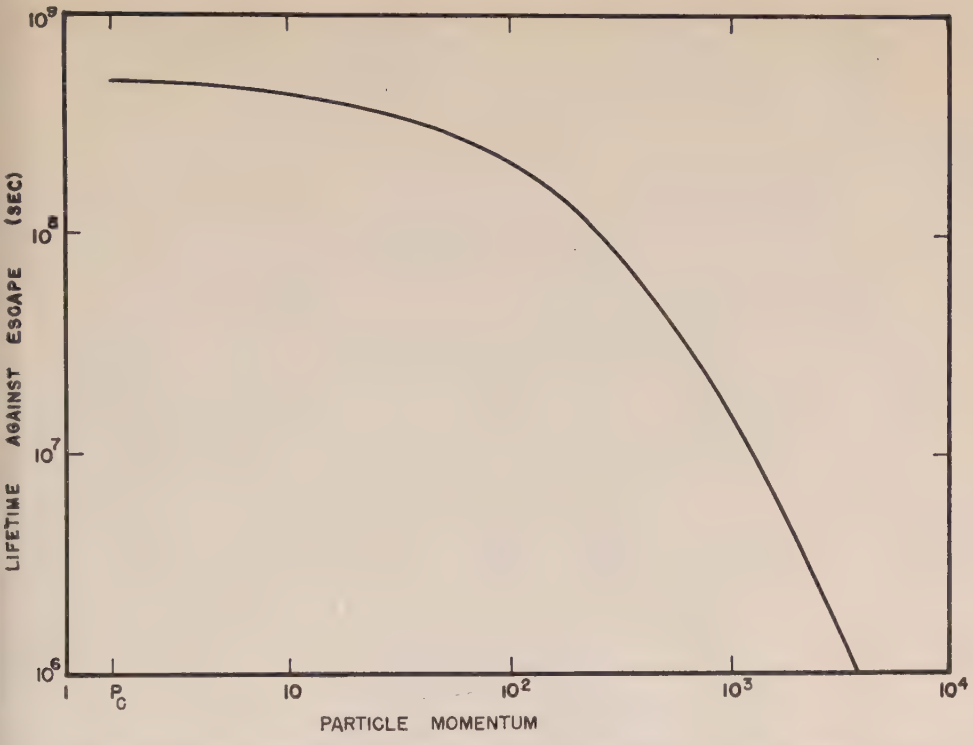

FIG. 7—Mean lifetime against escape from the DS for cosmic-ray primaries as a function of their momentum in Bev/c

DENSITY FLUCTUATIONS OF CLASS II PRIMARIES

Regular long-term variations in cosmic-ray intensity as measured by low-altitude ionization chambers have been observed by Forbush [2] to have a period equal to the duration of the sunspot cycle. These observations, shown in Figure 8, show a fluctuation of about four per cent that is negatively correlated with sunspot numbers, and which is of about the same magnitude at the various stations: Godhavn, Greenland, $\lambda = 79.9°$N; Cheltenham, Maryland, $\lambda = 50.1°$N; Huancayo, Peru, $\lambda = 0.6°$S; and Christchurch, New Zealand, $\lambda = 48.6°$S. The variation is similar for annual means, means of magnetically quiet days, and means of magnetically disturbed days, ruling out the possibility that the changes originate in cosmic-ray "storms" accompanying some magnetic storms. These long-term variations, being out of phase with the observed cycle of solar activity and occurring in the high-energy (15 Bev and greater) component of the primary cosmic radiation, cannot be accounted for by any conventional theories of cosmic-ray origin. However, as Davis [1] has pointed out, changes in the dimensions of a volume that can trap cosmic rays in the vicinity of the solar system are able to account, at least qualitatively, for the observed cosmic-ray changes. A detailed calculation of this hypothesis in terms of the DS model will now be given.

Consider the density of Class II primary cosmic-ray protons in the DS having energies between E and $E + dE$. Denoting this density by n,

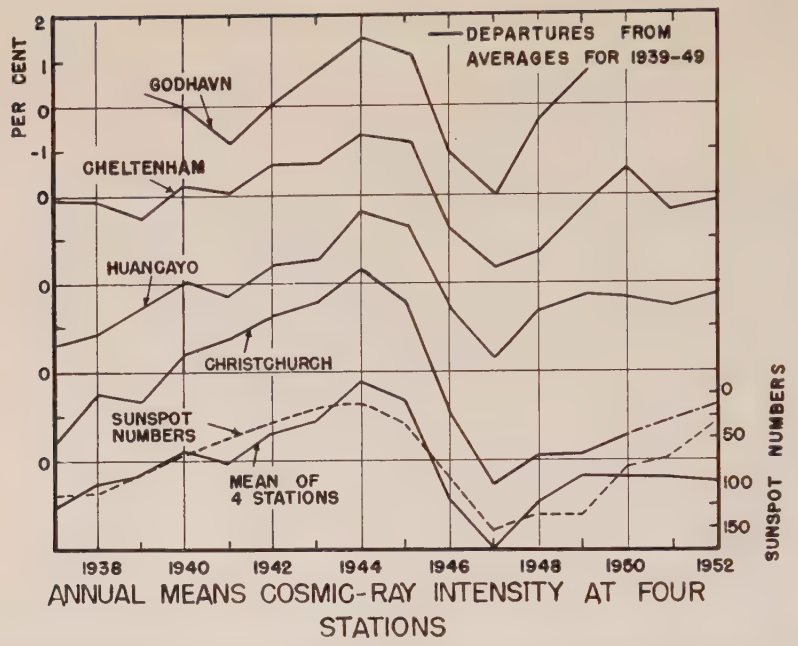

FIG. 8—Long-term variations in the annual means of cosmic-ray intensity at Godhavn, Cheltenham, Huancayo, and Christchurch. Sunspot numbers for the same period are shown as the dashed line. (From Forbush [2])

$$\frac{dn}{dt} = \left(\frac{\partial n}{\partial V}\right)\frac{dV}{dt} + \left(\frac{\partial n}{\partial E}\right)\frac{dE}{dt} + \frac{\partial n}{\partial t} \qquad (20)$$

where V is the volume of the DS. If the total number of primaries of energy between E and $E + dE$ present in the DS is N when the volume is V, $n = N/V$ and

$$\frac{\partial n}{\partial V} = -\frac{n}{V}$$

For $E > 10$

$$n \approx CE^{-k}$$

according to Eq. (15), where $k \approx n + 1$. [The "n" here refers to the exponent in Eq. (15).] Hence,

$$\frac{\partial n}{\partial E} = -\frac{kn}{E}$$

Also, dE is the work done *on* each proton by the moving walls of the DS if it is contracting, or the work done *by* each proton if the DS is expanding, and is simply the pressure on the walls times the volume change divided by the total number of protons N in the energy interval:

$$dE = \frac{nE\,dV}{3N} = \frac{E\,dV}{3V}$$

The last term of Eq. (20) is the difference between the number of primaries entering the DS with energies between E and $E + dE$ per unit time and the number leaving, namely,

$$\frac{\partial n}{\partial t} = \frac{n_0 - n}{\tau}$$

where $1/\tau$ is the probability for entry or departure from the DS [Eq. (19)] and n_0 the density of such protons outside. Eq. (20), therefore, reads

$$\frac{dn}{dt} = -\left[1 + \frac{k}{3}\right]\frac{n}{V}\frac{dV}{dt} + \frac{n_0 - n}{\tau} \quad \ldots\ldots\ldots\ldots\ldots\ldots (21)$$

It is now supposed that V varies because of fluctuations in the total corpuscular emission of the sun. If the variation in V with time is sinusoidal, a reasonable approximation in view of the Wolf-number *vs* time curves for the past 200 years, with a maximum amplitude V_1 and a period T,

$$V = V_0 + V_1 \cos 2\pi t/T$$

If V_1 is small compared with V_0, no great error ensues from letting

$$\frac{1}{V}\frac{dV}{dt} = -\frac{V_1}{V_0}\frac{2\pi}{T}\sin 2\pi t/T$$

so that Eq. (21) now becomes

$$\frac{dn}{dt} = \left[1 + \frac{k}{3}\right]n\frac{V_1}{V_0}\frac{2\pi}{T}\sin 2\pi t/T + \frac{n_0 - n}{\tau} \quad \ldots\ldots\ldots\ldots\ldots\ldots (22)$$

Eq. (22) has the solution

$$n = n_0\left[1 - \left(1 + \frac{k}{3}\right)\frac{V_1}{V_0}\cos\phi\,\cos\left(2\pi\frac{t}{T} + \phi\right)\right] \quad \ldots\ldots\ldots\ldots\ldots\ldots (23)$$

where the angle ϕ is defined by

$$\phi = \tan^{-1} T/2\pi\tau \quad \ldots\ldots\ldots\ldots\ldots\ldots\ldots\ldots\ldots\ldots (24)$$

When the mean lifetime τ of the Class II particles trapped in the DS is much greater than T, which equals 11 years, ϕ approaches 0 and $\cos\phi$ approaches unity. In that event, the relative amplitude of the variations in n is related to those in V by

$$\frac{\Delta n}{n} = -\left(1 + \frac{k}{3}\right)\frac{\Delta V}{V}$$

A variation in n of 4 per cent [2] implies, since k is about 2.1, that V varies by 2.4 per cent. From the dependence of the DS volume on Q, the solar corpuscular flux,

$$\frac{\Delta V}{V} = \frac{3}{2}\frac{\Delta Q}{Q}$$

so the 4 per cent cosmic-ray fluctuations can be accounted for by a 1.6 per cent fluctuation in the total corpuscular output of the sun over a sunspot cycle.

From Figure 7, one notes that $\tau \sim T$ for low p, the most populous part of the spectrum. From Eq. (23), this evidently suggests a phase difference between n and V (other than the phase difference of 180°), with the minimum in n occurring earlier than the maximum in V. In this energy region,

$$\frac{\Delta n}{n} = -\left(1 + \frac{k}{3}\right) \cos \phi \, \frac{\Delta V}{V}$$

If the average energy of the primaries causing the long-term variation is 15 Bev, which follows from the small difference in $\Delta n/n$ measured at Godhavn and at Huancayo, $\tau = 15$ years and ϕ is about 6°. The resulting phase change is equivalent to only 2.3 months, too small to be perceptible at the present stage of our knowledge.

VARIATIONS IN THE CUT-OFF

Recently, it has been observed [13] that the "knee" of the high-altitude latitude effect is shifting to higher geomagnetic latitudes, that is, that p_c is apparently decreasing. In 1951, the cut-off was observed to lie near 800 Mev, while in 1954 it had decreased to 150 Mev, and at present is even lower. (It is important to note that such a change cannot effect the sea-level and low-altitude cosmic-ray intensity, since primaries of these low energies are not able to propagate through the entire atmosphere.) For protons, the dominant constituent of the primary radiation, the cut-off momentum is related to the DS field H_i and the DS major axis R_a by

$$p_c = 3 \times 10^{-7} H_i R_a$$

Changes in R_a can be neglected, since they amount to only one per cent or so, and the cut-off shift must, therefore, arise from a change in H_i . That H_i varies is to be expected, as it is a function of the conductivity of the interplanetary medium and of the regularity of the solar ion streams. In the event that H_i decreases, the low-momentum primaries formerly constituting the upper end of the Class I spectrum are now trapped, and the influx of such particles exceeds the efflux until equilibrium. Hence, a fairly prompt change in their density should follow a decrease in H_i . If H_i increases, low-momentum Class II particles no longer are scattered by the DS walls and tend to leave the DS. Again, it seems likely that the changes in the density of such particles follow changes in H_i with only a small phase lag.

ACKNOWLEDGMENTS

I should like to thank Profs. S. A. Korff and L. Biermann for helpful conversations. This investigation was supported by the joint program of the Office of Naval Research and the Atomic Energy Commission.

References

[1] L. Davis, Phys. Rev., **100**, 1440 (1955).
[2] S. E. Forbush, J. Geophys. Res., **59**, 525 (1954).
[3] For example, E. N. Parker, Phys. Rev., **103**, 1518 (1956).
[4] S. Chapman and J. Bartels, Geomagnetism, Clarendon Press, Oxford (1940) and references therein; V. C. A. Ferraro, J. Geophys. Res., **57**, 15 (1952).

[5] L. Biermann, Zs. Astroph., **29**, 274 (1951); K. O. Kiepenheuer, The Sun (edited by G. P. Kuiper), Chicago University Press, Chicago (1953); Chap. 6.
[6] A. Unsöld and S. Chapman, Observatory, **69**, 219 (1949).
[7] H. C. van de Hulst, The Sun (edited by G. P. Kuiper), Chicago University Press, Chicago (1953); Chap. 5.
[8] J. A. Stratton, Electromagnetic Theory, McGraw-Hill Book Co., Inc., New York (1941); p. 212.
[9] L. Davis, Phys. Rev., **96**, 743 (1954).
[10] For example, L. Jánossy, Cosmic Rays, Clarendon Press, Oxford (1948); p. 267.
[11] R. A. Ellis, M. B. Gottlieb, and J. A. Van Allen, Phys. Rev., **95**, 147 (1954).
[12] H. L. Bradt and B. Peters, Phys. Rev., **77**, 54 (1950); M. Pomerantz, Phys. Rev., **77**, 830 (1950); J. A. Van Allen and S. F. Singer, Phys. Rev., **78**, 819 (1950); E. P. Ney and D. M. Thon, Phys. Rev., **81**, 1069 (1951); M. A. Clark, Phys. Rev., **87**, 87 (1952); T. H. Stix, Phys. Rev., **91**, 431 (1953) and Phys. Rev., **95**, 782 (1954); S. N. Vernov and A. N. Charakhchyan, Doklady Akad. Nauk SSSR, **91**, 487 (1953); C. J. Waddington, Phil. Mag., **45**, 1312 (1954); B. Peters, Proc. Indian Acad. Sci., **40**, 231 (1954); M. Pomerantz, J. Frank. Inst., **258**, 443 (1954); G. W. McClure, Phys. Rev., **96**, 1391 (1954); M. F. Kaplon, J. H. Noon, and C. Racette, Phys. Rev., **96**, 1408 (1954); J. Linsley, Phys. Rev., **97**, 1292 (1955); N. Horwitz, Phys. Rev., **98**, 165 (1955); W. R. Webber and F. B. McDonald, Phys. Rev., **100**, 1460 (1955); J. Linsley, Phys. Rev., **101**, 826 (1956); L. R. Davis, H. M. Caulk, and C. Y. Johnson, Phys. Rev., **101**, 800 (1956); F. B. McDonald, Phys. Rev., **104**, 1723 (1956).
[13] For example, H. V. Neher and E. A. Stern, Phys. Rev., **98**, 845 (1955).

STUDY OF SODIUM VAPOR EJECTED INTO THE UPPER ATMOSPHERE

BY J. F. BEDINGER, E. R. MANRING, AND S. N. GHOSH

Geophysics Research Directorate,
Air Force Cambridge Research Center,
Air Research and Development Command,
L. G. Hanscom Field, Bedford, Massachusetts

(Received August 15, 1957)

ABSTRACT

Two Aerobee rockets were employed to eject relatively large amounts of sodium vapor into the earth's atmosphere. One of the flights occurred during evening twilight and sodium was placed in the sunlit atmosphere from 75 to 110 km. Sodium D-line emission (λ 5890 A) was observed in the ejected trail above 90 km, and 5890 A is discussed in terms of resonance scattering of solar radiation. Below 90 km, D-line radiation was not apparent, and the trail was white in appearance. This requires the formation of aerosols and indicates that sodium is unlikely to remain in the atomic state below 90 km.

The second flight occurred at night. Strong D-line emission and a persistent trail were observed at about 65 km, 100 km, and 140 km. This emission is discussed in terms of chemical processes which have been proposed to explain the sodium airglow. These processes cannot produce the observed brightness of the trail at the high altitudes. Excited atomic nitrogen (N^2D) is proposed as a possible source of the energy. The observed presence of large amounts of energy stored in the earth's atmosphere above 100 km requires revision of some of the proposals regarding the sodium airglow and its origin.

OBSERVATIONS

The third and fourth rockets in the series to study the effects of ejecting sodium vapor into the earth's upper atmosphere have been launched from Holloman Air Development Center, New Mexico. During evening twilight on 11 April 1956, sodium was ejected over an altitude range from 75 to 100 km. Observations of the sodium trail with ground-based equipment were made from the Upper Air Research Observatory, at Sacramento Peak, New Mexico. The rapid scanning photometer used for night sky studies [see 1 of "References" at end of paper] continually recorded intensity and position of the trail. Two grating spectrographs, one sensitive in the visible and the other with quartz optics with sensitivity in the near-ultraviolet, recorded the emission from the trail during the twilight period. A 17.54-Mc radar tracked the cloud during twilight to study ionization.

The vertical sounding ionospheric station at nearby White Sands Proving Ground also continuously recorded ionospheric properties over a wide frequency band. Every 60 seconds, simultaneous photographs of the trail were taken from three widely separated stations with Speed-Graphic cameras which were equipped with f-2.8 lenses.

The rocket-borne instrumentation was similar to that of the first two flights [2]. Two sodium vaporizers, which were to have been ignited sequentially, 30

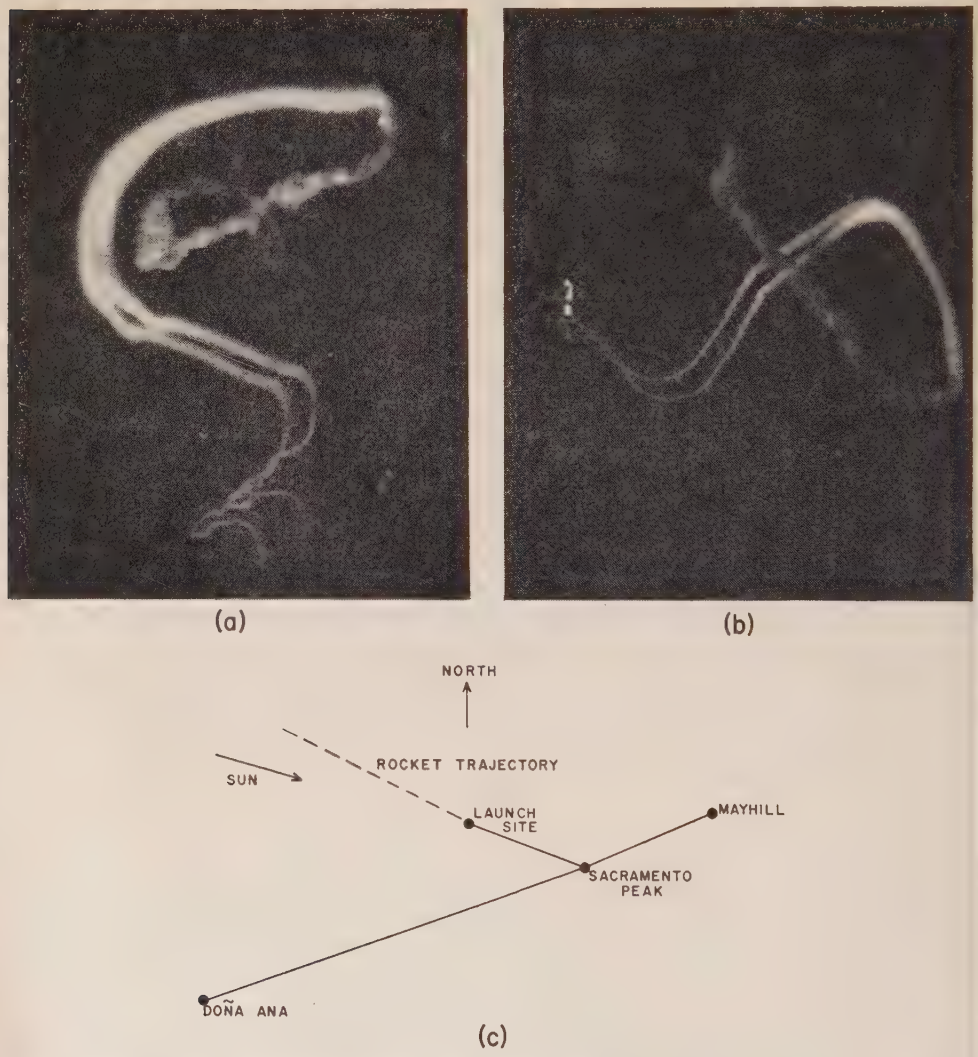

Fig. 1--Fig. 1(*a*) and (*b*) are simultaneous photographs of the sunlit sodium trail from two different sites, Doña Ana and Mayhill, respectively. Fig. 1(*c*) shows the relative position of these sites, the launch site, and the direction of incident solar rays. (The distance from the launch site to Sacramento Peak is 20 miles.) Note the difference in visual appearance of the trail due to self-absorption. The small white dots are star images which enabled accurate height determination of the trail.

seconds apart, were carried in the rocket. Due to some unexplained malfunction of the firing sequences, both the vaporizers were apparently ignited at about the same time and an explosion occurred in the instrumentation section. As a result of the explosion, the beacon triangulation system failed to give information on the rocket trajectory and at least one of the vaporizers was separated from the instrument rack. This latter fact is evidenced by the formation of two distinct and separate trails of illuminated sodium (Fig. 1). Sodium vapor was ejected from 75 to 100 km, producing λ 5890 emission, which was clearly visible for 10 minutes during twilight. As in the previous flights, the lower trail was white and that above about 100 km, yellow. However, the white portion above about 90 km later became faintly yellow before the earth's shadow caused it to disappear. As in previous flights, the sodium trail decreased greatly in brightness prior to being shaded by the earth's shadow, and then completely disappeared to visual observers as the shadow reached the region. Perhaps the most interesting observations from this flight were made by the photometer, which recorded emission from the cloud after the region was enclosed by the earth's optical shadow. Intensities 15 times the normal night sky emission were recorded until 1935 MST, and values two or three times normal night sky were recorded as late as 2000 MST. This later time is after the end of astronomical twilight.

On 1 November 1956, sodium vapor was ejected into the earth's atmosphere at night. The firing occurred at 1042 p.m. (MST). Two kilograms of sodium were ejected from 60 km to 140 km along the trajectory of an Aerobee rocket. At three different altitudes, a yellow glow and persistent trail were observed visually. The night sky photometer at Sacramento Peak continually recorded the intensity of the emission at all altitudes and determined that it was primarily sodium D at 5890 A. Super-Schmidt cameras, ordinarily used by Harvard University for meteor studies, recorded the emission over the 80- to 120-km region from two separate stations, Figure 2. The photographic method was similar to that used in meteor studies [3], and it allows accurate determination of altitude and relative intensity.

A dim glow was visible at 60 km and a trail of short persistence was photographed. The brightness of the glow and the trail decreased with altitude, until at about 90 km neither was visible, although the glow was photographed. At about this point, the glow again brightened, and at 100 km a very bright glow and persistent trail were observed. The trail persisted for about 30 seconds, with intensity decreasing approximately exponentially with altitude. Between 120 km and 135 km, no emission was observed visually, but a dim glow was photographed. At about 140 km, the glow was again very bright and persistent. Since this altitude was at the peak of the rocket trajectory, variations of brightness with altitude above this region were not obtained.*

*At $22^h42^m54.8^s$ on 19 August 1957, another night flight occurred which gave an exact repetition of the results described in this paper, except that the glow at 140 km extended practically constant to the peak of the rocket trajectory at 180 km. Also the fact that the glow at all altitudes was undiminished during the usual seasonal minimum of the nightglow emission indicates that the seasonal effect is due to an actual variation in the amount of atmospheric sodium.

RESULTS AND DISCUSSION

Resonance Effect

With regard to the twilight effects, the number of photons emitted per illuminated atom by resonance radiation is given by

$$N = \frac{g_1}{tg_2} \times e^{-E/kT} D$$

where t = radiative lifetime, g_1 , g_2 = statistical weights of the upper and lower states, T = temperature of the sun, and D = dilution factor ($= 5.4 \times 10^{-6}$). Thus, if the sun's temperature is assumed to be 6000°K, and a Fraunhofer central intensity of about 0.05 is used [4], then D-line resonance from solar rays would give $N = 0.85\ \text{sec}^{-1}$.

The trail diameter by photography was about 1 km, which yields an average density of 10^9 atoms/cm^3* inside the trail. For such densities, practically all photons will undergo at least one resonance transition within five meters [5]. The trail has maximum brightness when viewed from the same direction as the incident solar photons and minimum brightness when viewed from the opposite direction. The maximum from any direction can be no more than one-half of the total emission, or about 5×10^{11} photons/cm^2·sec [6].

The photometric measurements show that the intensity of the emission decreases slowly as attenuation of the incident solar energy by the earth's atmosphere increases. The intensity drops suddenly to about the night-time value as the earth's shadow reaches the region.

Spectrographic Observation

The visible spectrograph recorded emission only from λ 5890. Any other emission in the visible spectra was less intense than 10^9 photons/cm^2·sec. Particular notice should be taken of the fact that no trace of the Na_2 molecular spectrum ($^1\Sigma^+_g$ - $^1\Sigma^+_u$, 6800 band) was observed. This indicates that the vaporizer ejected little molecular sodium or that it was dissociated by solar rays.

An attempt was made to observe the second doublet of the principal series of sodium (λ 3302) by an ultraviolet spectrograph. Computation with the best available data indicated the ratio of the intensities of λ 5890/λ 3302 to be about 10^2 to 10^3 when sodium vapor is illuminated by unfiltered sunlight. Due to the great enhancement of λ 5890 radiation, it was felt that λ 3302 emission should be detectable if the phenomena is due to optical resonance. Exposures sufficient to record a line of this intensity did not detect the λ 3302 radiation. However, a five-minute delay in firing, due to difficulties in launching the rocket, greatly increased the attenuation of the solar rays in the λ 3300 region due to the earth's ozone shadow. Thus, it is not disturbing that the emission was not detected. An attempt to determine this ratio will be made in future experiments under more optimum conditions.

*In the 12 October flight, 2 kg of sodium, which contained 5.2×10^{25} atoms, were dispersed into a trail 1 km in diameter and 50 km long. Thus, it follows that

Density of Na atoms = $(5.2 \times 10^{25})/(4 \times 10^{16}) = 10^9$ atoms/cm^3

Ionization

From the amount of sodium in the cloud and intensity of the illuminative sunlight, the amount of ionization may be estimated.

The rate of production of Na^+ ions during the daytime is 10^{-5} per Na atom per sec [7] and the density of Na atoms in the cloud is $10^9/cm^3$; it follows that the rate of production of Na^+ ions is equal to $10^{-5} \times 10^9 = 10^4$ ions per cm^3.

Assuming that the cross-section for recombination of Na^+ ions and electrons is 1.6×10^{-19} cm^2, or that the coefficient of recombination is equal to 1.7×10^{-12} cm^3/sec, it follows that at equilibrium the density of electrons is given by

$$n^2 = 10^4/(1.7 \times 10^{-12})$$

$$n = 7.6 \times 10^7 \text{ per cm}^3$$

The critical frequency of radio waves for such an ionized cloud is about 80 Mc.

Neither the vertical sounding ionospheric station, which has a variable frequency range, nor the 17.54-Mc radar detected any ionization due to the cloud. Again, this is not surprising, since the long path through the atmosphere attenuates the 2400 A solar radiation necessary for ionization of Na atoms even more than the λ 3302 radiation. Ionization measurements will also be made in future experiments under more optimum conditions.

Night-Time Observations

Emission from sodium vapor in the earth's atmosphere at night was measured and these measurements are recorded in Figure 2. It is considered realistic to

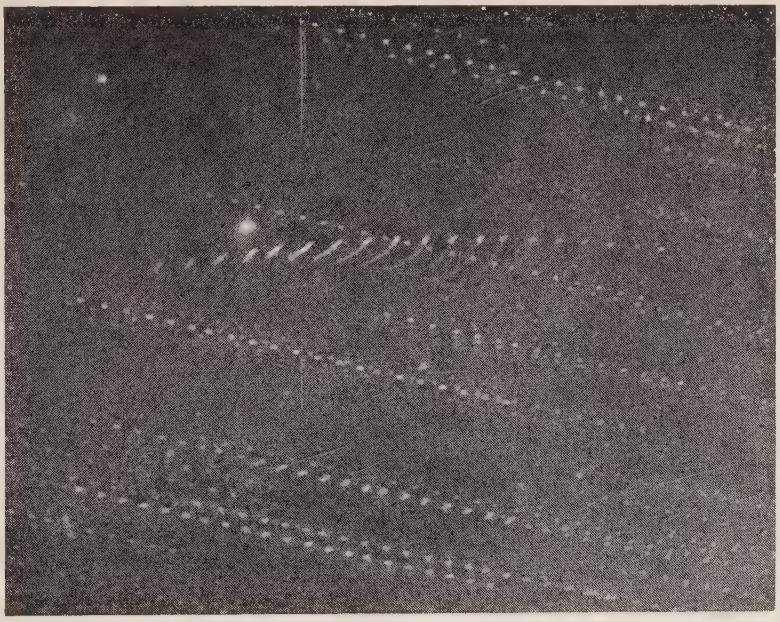

FIG. 2—The persistent trail at 100 km as taken with successive 2-sec exposures with the Schmidt camera. After each exposure, the camera was automatically shifted in declination so that the images would not coincide. The numerous dots are star images.

assume that the emission may be explained by the same processes which produce the normal night airglow radiation from atomic sodium. The most widely accepted processes are described as follows. Free sodium atoms may be removed from the atmosphere by the following reactions:

$$Na + O + M \rightarrow NaO + M \cdots \quad (1)$$

$$Na + O_3 \rightarrow NaO + O_2 \cdots \quad (2)$$

$$Na + O_2 + M \rightarrow NaO_2 + M \cdots \quad (3)$$

(reactions involving N and N_2 are usually considered less probable). Assuming that the coefficient of the reactions are, respectively, equal to 10^{-32} cm^6/sec [8], 1.5×10^{-11} cm^3/sec [9], and 5×10^{-30} cm^6/sec [10], and that the densities of O_3, O_2, and O are as given in Table 1, then predicted products are listed in Table 2.

TABLE 1

No. density of (cm^{-3})	50 km	60 km	70 km	80 km	90 km	100 km	110 km
O_3	1.2×10^{10}	1.6×10^{9}	5×10^{8}	10^{7}	3.2×10^{6}	1.2×10^{5}	1.2×10^{4}
O_2	4×10^{15}	1.2×10^{15}	5×10^{14}	10^{14}	1.2×10^{13}	6.3×10^{11}	10^{10}
O	1.2×10^{10}	2×10^{10}	5×10^{10}	6.3×10^{10}	1.6×10^{11}	6.3×10^{12}	2×10^{12}
H	...	...	...	5×10^{9}	3.8×10^{9}	6.8×10^{8}	1.5×10^{8}

TABLE 2

Rate of formation of ($cm^{-3}sec^{-1}$)	50 km	60 km	70 km	80 km	90 km	100 km	110 km
NaO-Reaction (1)	6×10^{2}	3×10^{2}	3.1×10^{2}	7.8×10	2.4×10	5×10^{2}	5×10
NaO-Reaction (2)	2.3×10^{8}	3×10^{7}	9.5×10^{6}	1.9×10^{5}	6.2×10^{4}	2.3×10^{3}	2.3×10^{2}
NaO_2-Reaction (3)	1×10^{11}	9×10^{9}	1.5×10^{9}	6×10^{7}	9×10^{5}	2.5×10^{4}	1.3×10^{2}

It is apparent from Table 2 that up to 100 km reaction (3) is most effective in the removal of free sodium atoms, that all sodium atoms will be converted to NaO_2 within one second up to 70 km, and within 10 seconds at 80 km.

NaO_2 molecules thus formed can produce $Na(^2P)$ atoms by the following reactions:

$$NaO_2 + O \rightarrow NaO + O_2 \cdots \quad (4)$$

$$NaO + O \rightarrow Na(^2P) + O_2 \cdots \quad (5)$$

$$NaO_2 + H \rightarrow NaH + O_2 \cdots \quad (6)$$

$$NaH + O \rightarrow Na(^2P) + OH \cdots \quad (7)$$

The coefficients of these reactions are not known. A rough estimate of their values can be obtained from the following considerations.

Assuming the Na-airglow at night originates from a mean height of 70 km, it follows from the rapid rate of the formation of NaO_2 that most Na will be present in the atmosphere at night as NaO_2 . (In twilight, the formation of this compound is prevented by the dissociative action of the solar rays.) Now, assuming an equilibrium rate of production of NaO_2 and NaO, we have from reactions (3), (4), and (5)

$$\alpha n_1 n_2 n_3 = \beta n_4 n_5$$

and

$$\beta n_4 n_5 = \beta' n_6 n_5$$

where n_1 through n_6 are the densities of Na, O_2 , M, NaO_2 , O, and NaO, respectively; β and β' are the coefficients of reactions (4) and (5).

From the measured intensity of night airglow, the rate of production of Na(^{2}P) is about 20 per cm^3 per sec and the concentration of Na is about 10^3/cm^3. Thus,

$$20 = \beta \times 10^3 \times 5 \times 10^{10}$$

or

$$\beta = 20/(5 \times 10^{13}) = 4 \times 10^{-13} \text{ cm}^3/\text{sec}$$

again,

$$20 = \beta' n_6 n_5$$

or

$$\beta' n_6 = 20/(5 \times 10^{10}) = 4 \times 10^{-10}/\text{sec}$$

Since the maximum value of $n_6 = 10^3/\text{cm}^3$, we have

$$\beta'_{\text{min}} = 4 \times 10^{-13} \text{ cm}^3/\text{sec}$$

If the actual coefficient is assumed to be 10 times the minimum value, we have that $\beta' = 4 \times 10^{-12}$ cm^3/sec.

Using these coefficients, Table 3 gives the rate of formation of Na (^{2}P) at different altitudes. It thus follows from the Table that if a sodium cloud having 10^9 Na-atoms per cm^3 is artificially produced at night between altitudes 50 to 110 km, the chemi-luminescence will decrease rapidly above 90 km. The use of reactions (6) and (7) at 100 km would produce even less emission due to the much lower concentration of hydrogen, unless the reaction rates are unrealistically fast.

In Figure 3, the computed values are compared with those actually observed. Curve *A* is computed from reactions (3), (4), and (5), as tabulated in Table 3. Curve *B* is the lowest altitude at which sodium D radiation was observed from an ejected sodium trail at twilight. Below this altitude, rapid formation of stable compounds is highly probable. Curve *C* is the observed emission from the trail ejected at night.

The computed Curve *A* can explain only that part of Curve *C* which is below

Table 3

Rate of formation of ($cm^{-3}sec^{-1}$)	50 km	60 km	70 km	80 km	90 km	100 km	110 km
NaO_2 - Reaction (3)	10^9	10^9	10^9	6×10^7	9×10^5	2.5×10^4	1.3×10^2
NaO - Reaction (4)	4.8×10^6	8×10^6	2×10^7	1.5×10^6	5.8×10^4	2.5×10^4	1.04×10^2
Na(^{2}P) - Reaction (5)	2.3×10^5	6.4×10^5	4×10^6	3.8×10^5	3.7×10^4	2.5×10^4	1.04×10^2
Surface brightness in photons/$cm^2\cdot$sec for a trail 0.1 km in diameter	2.3×10^9	6.4×10^9	4×10^{10}	3.8×10^9	3.7×10^8	2.5×10^8	1.04×10^6

about 90 km. This lower part was of low intensity and very short persistence. The combination of Curves *A* and *B* produces a maximum at about 85 km, whereas Curve *C* has a minimum. The rapid increase in emission at about 90 km and the

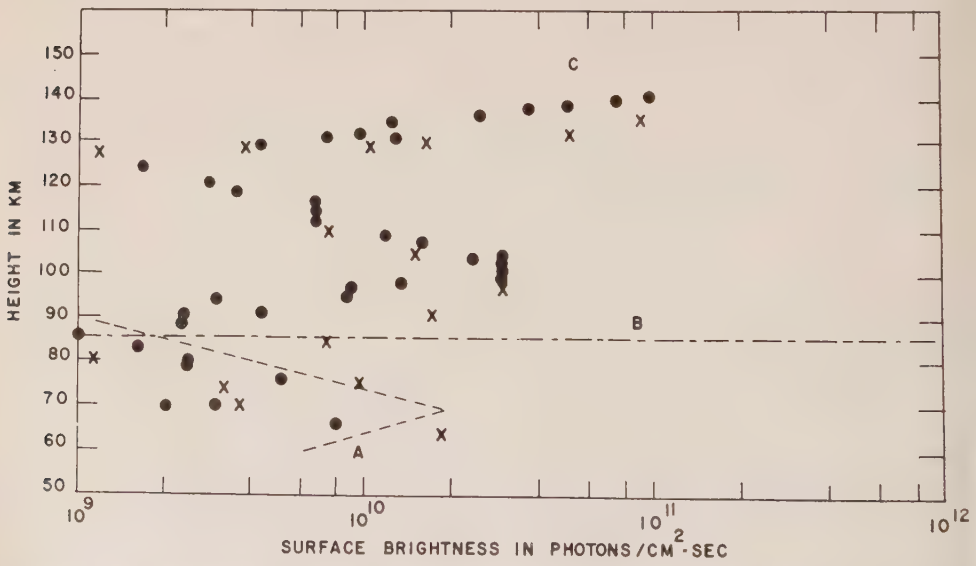

Fig. 3—The broken curve, *A*, is the computed value of trail brightness from Table 3. The dashed line, *B*, at 85 km is the lowest altitude from which sodium emission was observed in the twilight rocket flights. Curve, *C*, is the observed emission from the night flight as obtained by photography and photometry. The dots (·) represent relative values of trail brightness reduced by the authors from photographs taken with the Schmidt cameras. The crosses (x) were reduced completely independently by the Harvard Meteor Group from different photographs. All absolute values were established from photometric measurements at 140 km.

sharp maximum at 100 km can be explained by A only if the concentration of O_2 and O or the reaction rates are in error by more than two orders of magnitude. The similarity between the emission curve from 100 to 120 km and the distribution of atomic oxygen suggests a close connection between the two. Any reaction producing the observed luminescence must be fast, probably of the two-body type. It is difficult to suggest a process involving a metastable state of atomic oxygen, since the number of atoms in the ^1D and ^1S states is known from night airglow measurements and is much too small.

The part of Curve C which is above 135 km can certainly not be described by the processes which predict Curve A. The intensity of the emission and the atmospheric density at 140 km indicate that a single-stage chemi-luminescent process

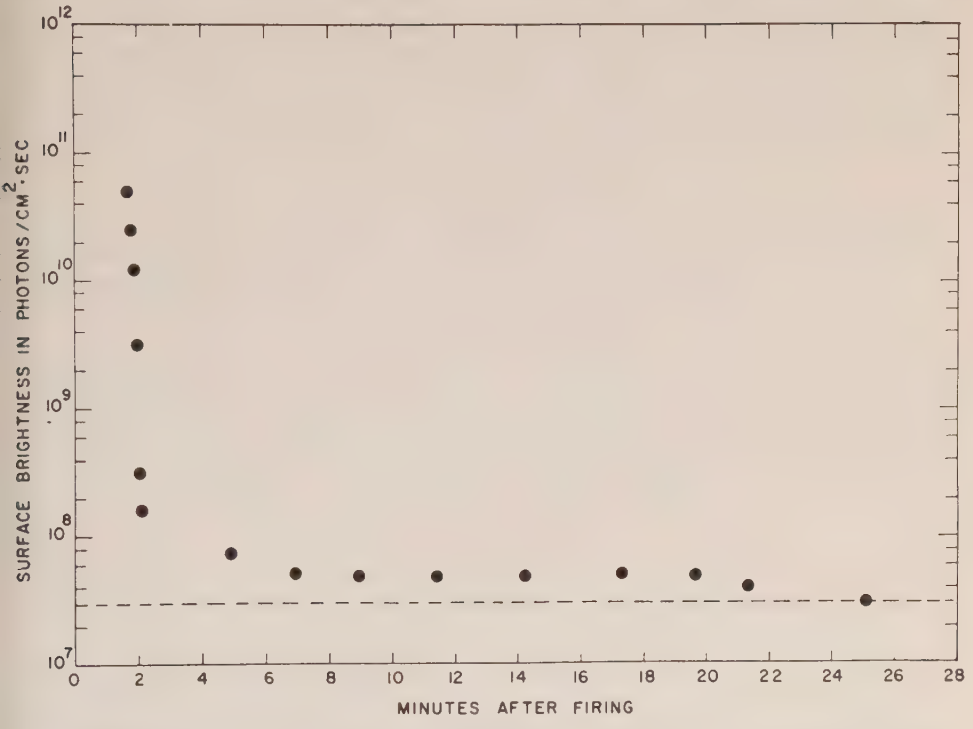

FIG. 4—The persistence of the trail at 100 km as determined from Fig. 2 and photometric measurements

of the two-body type is required. The photographed* trail diameter at this height was 100 meters, and the surface brightness of the trail was 10^{10} photons/cm^2/sec. Thus, the photon emission was 10^6 photons/cm^3/sec, and the number density of the ejected sodium 10^{10} atoms/cm^3. A two-body process is thought to proceed as follows:

*A faint glow, about 1 km across, was observed visually with a bright spot presumably at the vaporizer orifice which was of the order of 10 meters in diameter. The value of 10^{11} photons/cm^2.sec determined with the night sky photometer was deduced from the photometer deflection, and the above spot diameter as observed visually. The scale used in Figure 3 is for maximum brightness or that near the orifice.

$$\alpha\, n(x)10^{10} = 10^{6}\ \text{photons/cm}^3\cdot\text{sec}$$

or

$$\alpha\, n(x) = 10^{-4}/\text{sec} \quad \ldots\ldots\ldots\ldots\ldots\ldots\ldots\ldots\ldots\ldots (8)$$

where α is the rate coefficient of the reaction and $n(x)$ is the number density of the second reacting body. If the second body is excited and the process is of the energy transfer type, α may be of the order of 10^{-9} cm^3/sec. However, the necessary concentration of $n(x)$ requires that its excitation be to a metastable level or the resulting direct emission would be readily observable.

Atomic nitrogen in the (^{2}D) state with radiative half-life of 26 hours has been observed in aurora and it may exist in the atmosphere [11, 12, 13] in the required densities. The energy of this state is 2.37 electron volts, which is sufficient to excite the 2.11-volt sodium line. The distribution of atomic nitrogen, the effective lifetime of the metastable state, and the rate of formation of excited atomic nitrogen are not known. However, a process similar to the following may be acting.

$$\text{N } (^2\text{D}) + \text{Na } (^1\text{S}) \rightarrow \text{N } (^4\text{S}) + \text{Na } (^2\text{P})$$

This reaction does not obey the spin conservation rule, and its rate, as a consequence, is expected to be considerably smaller than 10^{-9} cm^3/sec, which is reasonable for allowed processes. Dufay [12] reports that at twilight the density of N (^{1}D) may be as high as 10^7 atoms/cm^3, with an effective rate of decay of an hour or so. If a value of 10^6 excited atoms/cm^3 is assumed at night, and a reaction rate for transfer of its energy to the sodium atom 10^{-10} cm^3/sec, the observed intensity of 5890 A from the artificial sodium cloud is accounted for and the emission of 5200 A radiation at night would not be detected because of the 26-hour radiative half-life. The luminescence at 140 km decayed with a half-life of about 1 sec, determined from the photographic records. This value is consistent with the sodium concentration of 10^{10} atoms/cm^3 and a reaction rate of 10^{-10} cm^3/sec. It is difficult to determine a rate for the transfer of excitation, but the value above is considered reasonable in view of the nearness of resonance for the two atomic levels considered.

It has not been possible to account for the observed intensity at 140 km by other processes, although many have been attempted. The intensity and time of decay are not consistent with what might be expected from such things as electron collisions, cosmic rays, or meteoric particles. The sparsity of the medium imposes severe limitations on possible reactions of the ordinary photochemical type.

Two methods of production of N (^{2}D) have been suggested, (1) [14] a dissociative recombination process such as

$$N_2^+ + e \rightarrow \text{N } (^2\text{D}) + \text{N } (^2\text{P})$$

and (2) [15] predissociation by solar energy,

$$N_2\ (X\ ^1\Sigma_g^+) + h\nu \rightarrow N_2\ (a\ ^1\Pi_g)$$

$$N_2\ (a\ ^1\Pi_g) \rightarrow N(^2D) + N(^2P)$$

Other processes involving excited nitrogen should also be considered. Preliminary laboratory experiments indicate that sodium vapor in the presence of active nitrogen produces a very intense emission.

CONCLUSIONS

The observed emission positively establishes the presence and availability of the energy necessary to excite the Na-D lines at high altitudes in the atmosphere during the night. Observed intensities are such that rapid two-body processes appear probable. At 100 km, the maximum of the emission is coincidental and similar in distribution to the maximum concentration of atomic oxygen. At 140 km, excited nitrogen is a possible source.

The observations of emission from high altitudes allow a reevaluation of the proposed sources of atmospheric sodium. Since efficient processes for excitation are known to occur above 90 km, the source may be meteors or meteoritic particles. Such a proposal may also explain the much neglected but positively observed seasonal effects in the sodium airglow by attributing them to the variation in sodium concentration produced from extra-terrestrial sources.

Lastly, heights of the normal sodium airglow are functions of the naturally occurring sodium distribution, as well as a reaction efficiency as measured and shown in Curve *C*. The low efficiency of the reaction at 85 km indicates that the heights of this portion of the night airglow may be above 90 km.

ACKNOWLEDGMENTS

The authors wish to express their sincere appreciation to Miss Helen Pettit for her tireless assistance in the data reduction and preparation of the manuscript, to the Harvard Meteor Group, especially R. E. McCrosky and G. Schwartz, for using the Schmidt cameras to record the emission, and to A. Delgarno for his critical reading of the manuscript.

References

[1] R. B. Dunn and E. R. Manring, J. Optical Soc. Amer., **46**, 572 (1956).
[2] H. D. Edwards, J. F. Bedinger, E. R. Manring, and C. D. Cooper, The Airglow and the Aurorae, Pergamon Press, Ltd., London (1955); p. 122.
[3] Smithsonian Contrib. Astroph., **1**, 183 (1957).
[4] C. D. Shane, Lick Obs. Bull., **19**, 119 (1941).
[5] T. M. Donahue and A. Foderaro, J. Geophys. Res., **60**, 75 (1955).
[6] M. Minnaert, The Sun, University of Chicago Press, Chicago (1953); p. 92.
[7] D. R. Bates and M. J. Seaton, Proc. Phys. Soc., B, **63**, 129 (1950).
[8] D. M. Hunten, J. Atmos. Terr. Phys., **5**, 144 (1954).
[9] D. M. Hunten, J. Atmos. Terr. Phys., **5**, 144 (1954).
[10] C. E. H. Bawn and A. G. Evans, Trans. Faraday Soc., **33**, 1571, 1580 (1937).
[11] G. Courtes, Paris, C.-R. Acad. sci., **231**, 62 (1950).
[12] M. Dufay, L'étude optique de l'atmosphère terrestre, Mém. Soc. roy. sci., Liége, 4th Ser. **12**, 141 (1952).
[13] M. Nicolet and R. Pastiels, L'étude optique de l'atmosphère terrestre, Mém. Soc. roy. sci., Liége, 4th Ser., **12**, 147 (1952).
[14] D. R. Bates, The Earth as a Planet (G. P. Kuiper, Ed.), University of Chicago Press, Chicago (1954); p. 588.
[15] G. Herzberg and L. Herzberg, Nature, **161**, 283 (1948).

AN ATTEMPT TO MEASURE ATOMIC NITROGEN BY ROCKET RELEASE OF ETHYLENE AT 105 AND 143 KM

BY MURRAY ZELIKOFF, FREDERICK F. MARMO, JEROME PRESSMAN, EDWARD R. MANRING, LEONARD M. ASCHENBRAND, AND ADOLPH S. JURSA

Geophysics Research Directorate,
Air Force Cambridge Research Center,
Air Research and Development Command,
L. G. Hanscom Field, Bedford, Massachusetts

(Received October 18, 1957)

ABSTRACT

Ethylene gas was released from a rocket at 105 and 143 km in an attempt to detect atomic nitrogen in the upper atmosphere. The artificial chemi-luminescence produced by the gas clouds was observed from the ground and recorded on Super-Schmidt meteor cameras, using red-sensitive and blue-sensitive photographic plates. The color and intensity of each image can be related to the predominant chemical reaction producing the luminescence. The observations indicate that the lower cloud was caused by the reaction of ethylene and atomic nitrogen, and the upper cloud was caused by the reaction of ethylene with atomic oxygen.

I. INTRODUCTION

The detection of light emission from atomic nitrogen in the high atmosphere has been reported in auroral observations by Bernard [see 1 of "References" at end of paper], by Dufay and Tcheng [3], and by Götz [6]. On the other hand, reports of atomic nitrogen lines in the night sky [2, 4, 12] are conflicting, so that up to now the presence of atomic nitrogen in other than auroral regions remains a matter of conjecture. This paper will describe a recent attempt to establish the presence of atomic nitrogen in the upper atmosphere by the release of ethylene gas from an Aerobee rocket at 105 km and 143 km. Nine pounds of gas were released at each altitude from high pressure, spherical containers.* Ethylene was chosen, since it is known to react with atomic nitrogen [13] with the production of chemi-luminescent CN bands. Spectrophotometric observations were taken on the ground in an attempt to identify these bands. The intensities of the artificially produced luminescent clouds were too weak for satisfactory spectra to be obtained, but some crude photometry [11] was done, using Super-Schmidt meteor cameras equipped with X-ray (blue sensitive) and Tri-X (red sensitive) film.

*Each cloud produced luminescence visible on the ground to the naked eye.

II. DATA AND INTERPRETATION

A brief summary of the data obtained by McCrosky for the ethylene clouds is presented in Table 1. Reference to the Table shows that the lower cloud (at 105 km) produced no image on the blue-sensitive plate, even though exposure was three times as long as that on the red-sensitive plate (which recorded several

TABLE 1—*Photometric data*

Cloud altitude	Film	Exposure time	Relative intensity
km		*sec*	*arbitrary units*
105	X-ray	105	0
105	Tri-X	*a* 34	4.34
105	Tri-X	*a* 12	0.53
105	Tri-X	*a* 10	0.03 (very faint)
143	X-ray	*b* 12	1.92
143	X-ray	*b* 6	0
143	Tri-X	*c* 2	0
143	Tri-X	*c* 10	0.81
143	Tri-X	*c* 11	2.06
143	Tri-X	*c* 10	0

Note: Exposures marked *a*, *b*, and *c* are consecutive exposures on the same cloud. Intensities are in relative units of total energy integrated in space and time.

reasonably good images). The upper cloud (at 143 km) produced images on both the red- and blue-sensitive plates. Since the intensities on both X-ray and Tri-X plates are comparable, and since the Tri-X (red) plate is also sensitive to blue light, it is probable that essentially none of this luminosity occurred in the red. Elias and Schiff [5] have made a study of the chemi-luminescent characteristics of the ethylene - atomic N and ethylene - atomic O reactions. Inspection of their spectra [11] shows that the reactions are well separated in color, the N - C_2H_4 system producing at least 90 per cent of its light in the red and the O - C_2H_4 system producing at least 80 per cent of its light in the blue. The pressures used by Schiff [5] were 2.5 mm Hg for N_2 (about one per cent atomic N) and 1.9×10^{-3} to 3.5×10^{-2} mm Hg for C_2H_4 . Similar pressures were used for O - C_2H_4 for O_2 and C_2H_4 , respectively, although, in the case of oxygen, atomic O was about 10 per cent of O_2 .

At this point, some conclusions can be drawn by examining the data, first assuming the atmospheric chemi-luminescence to have been caused by O - C_2H_4 and then by N - C_2H_4 . We have stated that the O - C_2H_4 system produces most of its light in the blue. It is possible to suppose that the luminescent intensity can shift to longer wavelengths as the reactant pressures vary, although quantitative data are lacking on phenomena of this sort. However, to explain the observed atmospheric processes, one must postulate that at total O - C_2H_4 pressures in the

10^{-1} mm range, the luminescence is blue; at total pressures in the 10^{-3} mm range (at 105 km), the luminescence is red, and at total pressures in the 10^{-5} range (at 143 km), the luminescence is again blue. This postulate seems artificial and unreasonable, particularly since at all pressures the ethylene to atomic oxygen ratios are approximately the same. We are, therefore, led to conclude that the laboratory and upper atmospheric luminosity observations do not correspond with what might be expected of the O - C_2H_4 system. Also, it is worth while to note here that other atomic and molecular species, both in normal and in excited states, were not present in significant amounts in the laboratory, nor in the atmosphere at the altitudes in question. Indeed, the maximum impurity concentration in all cases is less than 10^{-4} and probably close to 10^{-6} of the total.

Let us now attempt to explain the observation on the basis of N - C_2H_4 . The presence of only red light in the lower cloud is favorable evidence. The blue color of the upper cloud is puzzling, but not necessarily unexplainable. Schiff's laboratory spectra are for somewhat higher pressures than those at 105 km. At 143 km, the total pressure is about 10^{-2} times that at 105 km [10]. It is possible that the light intensity shifts to shorter wavelengths with pressure decrease. Since the ethylene to atomic nitrogen ratio does not change appreciably with decrease in total pressure, the color shift seems unlikely, but cannot be ruled out. In any case, the entire N - C_2H_4 picture seems more credible, since the observations require only the postulate that the color shift is in one direction with pressure decrease. In the case of O - C_2H_4 , this color shift must reverse itself as the pressure continues to drop.

The question of this color shift with pressure is worth considering in some detail. In order to explain it, one may suggest that the reaction in question leads to two (or more) excited species which can emit different wavelength radiation. If one of these species is long-lived (metastable), collisional deactivation can occur at high pressures with the resultant suppression of the wavelength of light it would normally emit. As pressure decreases, this color would appear and possibly exceed the other in intensity many fold. Such an event seems possible in the laboratory where reactant pressures are quite high, but in the atmosphere at and above 105 km, the collision frequency is so low that for a metastable atom to be deactivated by collision would require it to have a lifetime in excess of 10^{-3} second (assuming a deactivating efficiency of unity). In the case of CN, both the red ($^2\Pi \rightarrow {}^2\Sigma$) and the blue bands ($^2\Sigma \rightarrow {}^2\Sigma$) are the result of allowed transitions; hence, the excited state lifetimes must be short. In the case of the O - C_2H_4 system, the reversal of the color shift is required, as described above. We, therefore, prefer to discard the collisional-deactivation hypothesis and to attempt an explanation of the differently colored clouds on another basis.

We have now reached the point where we can consider the upper and lower clouds as having been produced by the reaction of ethylene with different atomic species. We shall depend on the red color of the lower cloud to postulate its cause as the N - C_2H_4 reaction. If the O - C_2H_4 reaction occurs here also, although not producing enough light to be detected, and if its rate increases more rapidly than does that for N - C_2H_4 as the altitude increases, we have a plausible explanation for the color difference between the two clouds. Since the temperature at 105 km

is about 200°K and that at 143 km is ~ 400°K, if the energy of activation for O - C_2H_4 is significantly greater than for N - C_2H_4, the rate of luminescence produced by O - C_2H_4 might be less than that for N - C_2H_4 at 105 km and surpass it at 143 km. Greenblatt and Winkler [7] have given a value of 3 kcal for the energy of activation of N - C_2H_4. The value for O - C_2H_4 has not been measured, but is ~ 4 kcal for O - C_2H_2 and ~ 7 kcal for O - C_2H_6 [8]. A reasonable value for O - C_2H_4 is, therefore, probably between 4 and 7 kcal. Schiff [5] has given the room-temperature rate constant for N - C_2H_4 as ~ 10^{-13} cc molecule^{-1} sec^{-1}, and that for O - C_2H_4 as ~ 2×10^{-14} cc molecule^{-1} sec^{-1}. Table 2 lists the approximate rate constants as they vary with temperature, assuming ~ 3 kcal as the energy of activation for N - C_2H_4 and ~ 6 kcal as that for O - C_2H_4.

TABLE 2—*Variation of rate constants with temperature*

Temperature		Rate constant for N - C_2H_4	Rate constant for O - C_2H_4
°K			
200	(105 km)	10^{-14}	10^{-16}
300	(Schiff)	10^{-13}	2×10^{-14}
400	(143 km)	3×10^{-13}	3×10^{-13}

In order to use these rate constants for calculation of reaction rates in the upper atmosphere, certain assumptions must be made. First, one must assume that as the ethylene leaves the container, it spreads out into a roughly spherical volume and mixes instantaneously with the atmosphere, stopping its expansion (temporarily) when its pressure reaches that of the surroundings. Estimation of the temperature at which the reaction actually occurs is difficult, since the gas should cool as it is released but the surrounding air may be heated as a result of shock-wave propagation. Since the ethylene was released through an opening of about 1 cm^2 and since there was a right-angle bend in the tubing along its release path, it was probably slowed to a point where the shock heating effect was small. Probably the best estimate that can be made for the reaction temperature is roughly that of the surroundings, especially since the molecules undergo many collisions before reacting.

The ambient number densities of particles at 105 and 143 km are 10^{13}/cc and 10^{11}/cc, respectively [10], and these values are assumed for ethylene. Values [9] for O-atom concentration are 10^{12}/cc at 105 km and 10^{10}/cc at 143 km. The concentrations of atomic N are much more uncertain, being estimated as ~ 10^{10}/cc at 105 km and ~ $10^8 - 10^9$/cc at 143 km. Insertion of these data in reaction-rate expressions gives the number of reactions/cc/sec (initially) for each process at the two altitudes. These results are tabulated in Table 3.

McCrosky [11] has made some crude estimates of the total number of photons of visible light from each cloud. For the lower cloud, this number is 5×10^{24} photons integrated over the whole volume and duration. Since there are about 10^{13} ethylene molecules, the cloud volume is ~ 5×10^{12} cc. Therefore, the flux (integrated in time) was about 10^{10} photons/cc. Reference to Table 1 shows that

TABLE 3—*Initial reaction rates at* 105 *and* 143 *km*

Reaction	Rate at 105 km	Rate at 143 km
$N - C_2H_4$	10^9	3×10^6
$O - C_2H_4$	10^9	3×10^8

ts time duration was somewhat greater than 50 seconds, and hence an average ate of photon emission was $\sim 2 \times 10^8$ photons/cc/sec. The initial intensity was lmost certainly much greater than the average, and a reasonable initial value is $\sim 5 \times 10^8$/cc/sec, or possibly 10^9/cc/sec. For the upper cloud, the total flux integrated in time and volume) is about the same as that for the lower cloud; owever, its volume was about 100 times larger and its time duration slightly ower. This corresponds to a photon emission of $\sim 10^8$/cc (integrated in time), r an average emission rate of 3×10^6/cc/sec. Once again, the initial rate is probably everal times faster than the average, and we may assume a value of $\sim$ $\times 10^6$/cc/sec, or possibly 10^7/cc/sec. If the lower cloud was produced by $N - C_2H_4$, the initial photon emission rate corresponds approximately to the alculated reaction rate (see Table 3). Since the $O - C_2H_4$ reaction probably pro- luces only blue light in the upper atmosphere, its photon emission rate at 105 km hould be smaller than its actual reaction rate; that is, the number of photons per eaction (luminescent efficiency) is less than unity (at least in the visible portion f the spectrum). Indeed, Schiff [5] has found that for a given total pressure, the $N - C_2H_4$ reaction produces more visible light than does the $O - C_2H_4$ reaction. In act, the $O - C_2H_4$ system produces considerable heating of the reaction vessel, vhile the $N - C_2H_4$ system does not. Perhaps a large portion of the energy goes into he infrared or into heat. Since our film detection was insensitive to infrared, we an only report the visible intensity. If the visible luminous efficiency for $O - C_2H_4$ s 10^{-1} or less, the number of blue photons emitted by the lower cloud would be bout 10 per cent of the number of red photons (from $N - C_2H_4$) and probably ot detectable.

Looking now at the upper cloud and keeping in mind that at the pressures n the high atmosphere the luminous efficiency is probably pressure independent, ve find from Table 3 that for $O - C_2H_4$ the reaction rate at 143 km multiplied by ts luminous efficiency corresponds approximately to the observed initial intensity. For $N - C_2H_4$, the light intensity (photons/cc/sec) is greater than the calculated eaction rate. The two reactions occurring together would appear to produce bout 10 times as many blue photons (from $O - C_2H_4$) as red photons (from $N - C_2H_4$), and hence the red would probably not be detectable. We thus see that by some admittedly speculative reasoning, it is possible to explain the luminescence rom the lower cloud as having been due chiefly to $N - C_2H_4$ and that from the pper cloud to $O - C_2H_4$.

There is one further bit of evidence which can be cited to support our argument. Schiff [5] has shown that both reactions under consideration are second order, irst with respect to ethylene and first with respect to O or N. The second-order ate equation is

$$k = \frac{2.3}{t(a-b)} \log \frac{b(a-x)}{a(b-x)} \quad (1)$$

where k = rate constant, t = time in seconds, a and b are initial reactant concentrations, and x represents the amount of initial reactant disappearing after time t. Reference to Table 1 showed that for the lower cloud about 90 per cent of the light appears in the first 34 seconds, and for the upper cloud this time is about 20 seconds. It is further reasonable to assume that 90 per cent of the reaction has taken place after 90 per cent of the light has decayed. Since C_2H_4 is always present in excess, the reactions should stop when about 90 per cent of the atomic species has been exhausted. Therefore, let $a = [C_2H_4] = 10^{13}$/cc (at 105 km) and $b = [N] = 10^{10}$/cc. $x = 0.9b$. Equation (1) then reduces to

$$k = \frac{2.3}{t(a-b)} \quad (2)$$

Hence, at 105 km, with $t_{0.9.} = \sim 34$, $k \approx 7 \times 10^{-15}$, or within a small factor the value given for N - C_2H_4 at 105 km (see Table 2). Similar reasoning for the upper cloud leads to a value of $\sim 10^{-12}$, or again within a small factor the value given for O - C_2H_4 at 143 km.

There is an alternative way to look at these luminescent clouds which considers a somewhat different picture of their initial expansion. In the preceding discussion, we have assumed that the ethylene, after leaving the rocket-borne container, expands to the pressure of the surroundings and remains at that pressure, at least temporarily. To make this assumption more valid, all calculations have dealt with initial rates. Examination of the meteor camera photographs indicates that the clouds expanded very rapidly, even "over-expanded" to volumes in excess of those which they would assume if the ethylene had reached only ambient pressure; that is, the ethylene number density could initially have been somewhat lower than 10^{13}/cc at 105 km and 10^{11}/cc at 143 km. Use of these lower values, for example, $C_2H_4 = 10^{12}$ at 105 km and 10^{10} at 143 km, leads to correspondingly lower values of the initial rates given in Table 3, but also gives correspondingly lower values for the initial photon emission rates. In other words, the reaction rates and photon emission rates per cc may be smaller, but the cloud size is larger and the total light flux stays constant. The reasoning used to reconcile the different colors of the clouds, therefore, remains unchanged. Calculation of rate constants based on time for 90 per cent of reaction completion leads to values which differ somewhat from those calculated in a similar manner above. These differences are still only about a factor of ten and can be reconciled by reasonable assumptions about the probable accuracy of some of the rate constants and energies of activation for the reactions under consideration. It should be borne in mind that the cloud sizes given by the photographs are upper limits, since the images represent time exposures and would not show cloud growth with time. In fact, a time average concentration of ethylene in the two clouds would fall between the extreme values, in which case the rate constants calculated from the times of decay would agree better with those calculated using the energies of activation.

III. CONCLUSIONS

Ethylene gas released into the atmosphere at 105 and 143 km reacted with the atomic species present there, producing visible luminescence at 105 km chiefly from the N - C_2H_4 reaction, and at 143 km chiefly from O - C_2H_4 . Calculations show with "order of magnitude" accuracy that these phenomena can be explained on a plausible basis.

References

[1] R. Bernard, Phys. Rev., **55**, 511 (1939).
[2] G. Courtès, Paris, C.-R. Acad. sci., **231**, 62 (1950).
[3] J. Dufay and M. L. Tcheng, Cahiers de Physique, No. 8, 51 (1942).
[4] M. Dufay, Paris, C.-R. Acad. sci., **233**, 419 (1951).
[5] L. Elias and H. I. Schiff, J. Chem. Phys., to be published.
[6] F. W. P. Götz, Experimentia, **3**, 185 (1947).
[7] J. H. Greenblatt and C. A. Winkler, Can. J. Res., **36**, 732 (1949).
[8] P. Harteck and U. Kopsch, Zs. Elektrochem., **36**, 714 (1930).
[9] L. E. Miller, J. Geophys. Res., **61**, 351 (1957).
[10] R. A. Minzner and W. S. Ripley, The ARDC Model Atmosphere, Geophysics Research Directorate Survey No. 86.
[11] R. E. McCrosky, J. Chem. Phys., to be published.
[12] M. Nicolet and R. Pastiels, Mém. Soc. roy. sci., Liége, 4th Ser., **12**, 47 (1952).
[13] J. Versteeg and C. A. Winkler, Can. J. Chem., **31**, 1 (1953).

THE 5577 A EMISSION OF [OI] IN THE NIGHT AIRGLOW FROM SACRAMENTO PEAK, NEW MEXICO

BY E. R. MANRING AND H. B. PETTIT

Geophysics Research Directorate,
Air Force Cambridge Research Center,
Air Research and Development Command,
L. G. Hanscom Field, Bedford, Massachusetts

(Received July 29, 1957)

ABSTRACT

From a photometric study of the 5577 A airglow, made during 125 nights, extending over a two-year period, from Sacramento Peak, New Mexico, the following conclusions can be drawn: (1) The regular features form a diurnal and seasonal repetitive pattern, for which the intensity during the equinoxes is brighter than during the solstices. A diurnal and seasonal variation in the direction and amplitude of the maximum intensity is observed. This suggests a model which supposes that an intensity pattern exists on the dark side of the earth. The diurnal variation at an observing station would be due to the earth's rotation and the seasonal variation due to the change in position of the ecliptic plane with respect to the observing station. (2) The two most important sporadic features observed were arc-like structures, which appeared during six nights, and portions of auroral activity, observed during four nights. (3) From the 68 nights suitable for van Rhijn height determinations, a ratio of $I(75)/I(0) = 2.555$, corresponding to a height of 85 ± 68 km, was determined. (4) A triangulation attempt was made between Sacramento Peak and Capillo Peak, with a height between 80 and 100 km indicated.

INTRODUCTION

Systematic observations of the [OI] radiation at 5577 A were made from February 1955 to April 1957 at Sacramento Peak, New Mexico, 32°47′ north, 07^h03^m west, and at 9,260 feet altitude. The photometer [see 1 of "References" at end of paper] used possessed high spectral purity, requiring no correction for extra-terrestrial light, even during moonlit hours. A sky survey required 3^m50^s and was made each 10 minutes. Each survey consisted of an observation at the zenith and continuous recording of intensity as a function of azimuth at zenith distances of 40, 55, 70, 75, and 80 degrees. During the above period, observations were made on 180 clear nights. Of these, 125 were full nights of excellent quality sky and are the ones reported here.

The data can be divided into two classifications. Most nights, 107 of the total

125, showed highly regular features. Eighteen of the 125 nights possessed strong unusual features and have been termed disturbed nights. Even the disturbed nights possess regular features with disturbances superimposed, but have not been used in the analysis of these features.

REGULAR FEATURES

During the course of the observing, several marked regularities [2] are noted for normal or undisturbed nights. The intensity over the sky during the course of a single survey can be represented to within 10 per cent by a relation of the type

$$B(z, \alpha) = B(z)[1 + b \cos(\alpha + \delta)] \quad \ldots\ldots\ldots\ldots\ldots\ldots (1)$$

where

$B(z, \alpha)$ = measured brightness at zenith distance z and azimuth α

$B(z)$ = function of zenith distance only, $B(0)$ is zenith intensity. $B(z)$ increases with z somewhat as expected by van Rhijn considerations.

b = an amplitude determined empirically

δ = phase angle, direction of maximum brightness

Deviations from this empirical relation consist mostly of small patches of intensity which measure 20 degrees or less and are not more than 10 to 20 per cent of the background. These patches are observed to move when successive surveys, 10 minutes apart, are compared. The velocity and initial appearance of these patches appear to be random.

It was noted that the diurnal curves of intensity, the amplitude b, and the direction δ change slowly with season in a regular manner. The idea of a pattern which possesses apparent motion with respect to each observing site has been proposed by Barbier [3]. Diurnal variations can be explained by a model of this type, and an attempt is made to extend the model to also describe the seasonal changes. If the zenith intensity is spotted on a grid, with time in hours along one coordinate and time in days along the other coordinate, contour lines of equal intensity may be drawn in. It is observed that the contours do not cross each other and that comparable sets of lines or patterns centered about the equinoxes exist. Such plots, Figure 1, are a convenient method for displaying large amounts of data and suggest the patterns mentioned above.

In addition to zenith intensity displayed by plots such as Figure 1, a direction of maximum brightness δ and an amplitude b determined from Eq. (1) should be explained by any model used to describe the observed data. A model which has been used with some success supposes that an intensity pattern in 5577 A radiation exists on the dark side of the earth and is fixed with respect to the sun, the earth, and the earth's orbit. In this case, the diurnal variation at an observing station is due to rotation of the earth about its axis beneath the pattern, and seasonal variation due to the change in position of the ecliptic plane with respect to the observing station. Advantages of this model as a first attempt are:

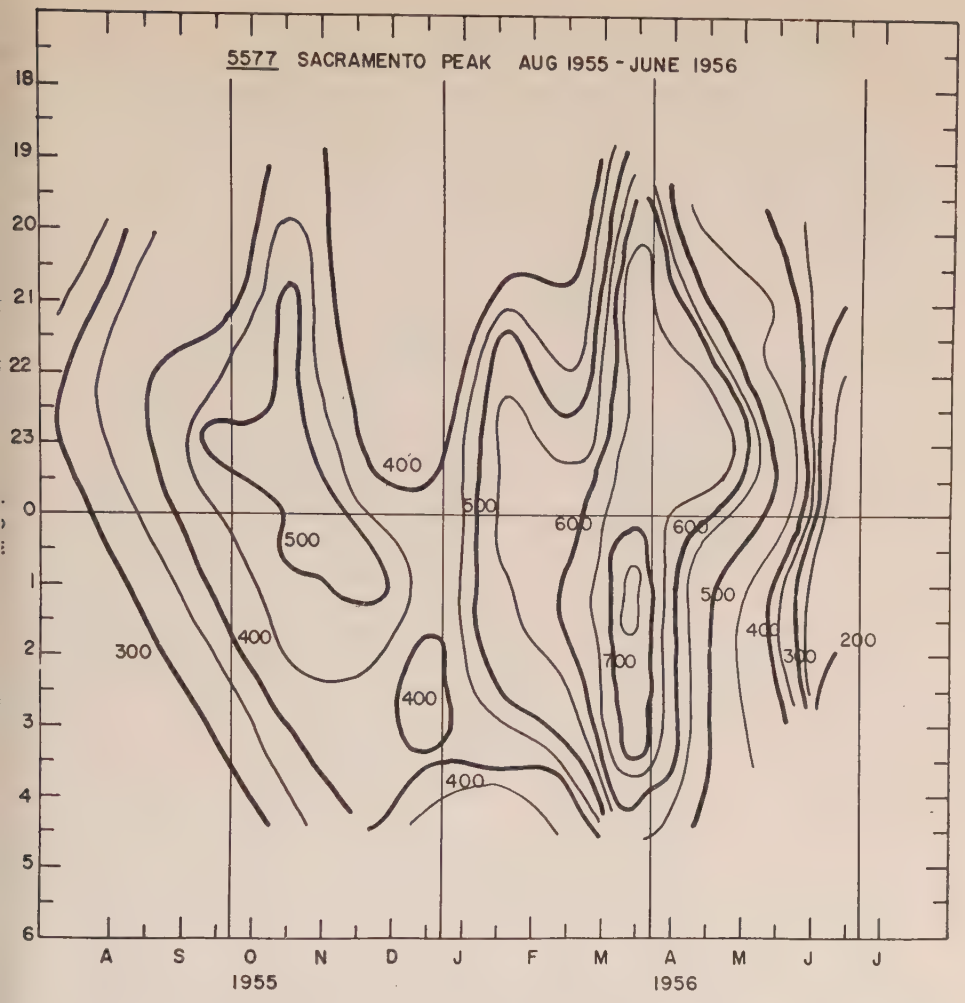

FIG. 1—Contours of equal intensity for 5577, using a grid with time in hours along the ordinate and time in days along the abscissa

1. Coordinates can be determined analytically.
2. The direction of maximum brightness δ and amplitude b can be readily interpreted in terms of the coordinates.
3. Data from various observing stations can be entered on the same plot by preparing appropriate coordinate grids for each station.

Equations for the above grid are those used for cylindrical projections and are

$$X = \sin L \cos \Delta + \cos H \sin \Delta \cos L \quad \cdots\cdots (2)$$

$$Y = \sin H \cos L \quad \cdots\cdots (3)$$

where

L = latitude of the observing station
Δ = 23.5 sin (360 m/24) degrees when m is zero at the spring equinox and takes on half-month intervals for the plots used in this paper
H = the local hour expressed in degrees with origin at midnight

Figure 2 shows a grid determined for the latitude of Sacramento Peak.

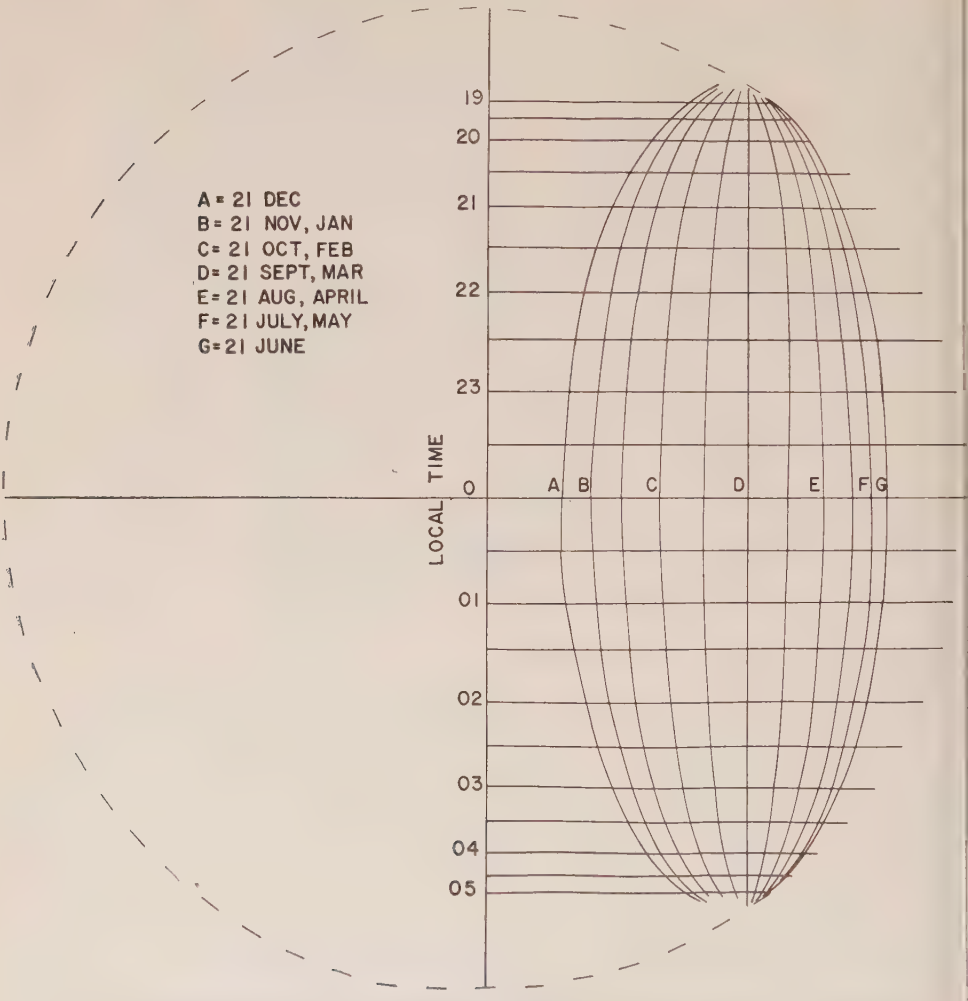

FIG. 2—Cylindrical projection of Sacramento Peak's position given by Eqs. (2) and (3)

Figure 3 gives four half-year plots, using the above coordinates. It is noted that:

1. Contour lines of equal intensity are separate and do not cross.
2. The patterns are all similar, showing that the period December 21 to June 21 has much in common with the period June 21 to December 21, although differences do exist in these two half-year periods.
3. There is a marked similarity between patterns one year apart.

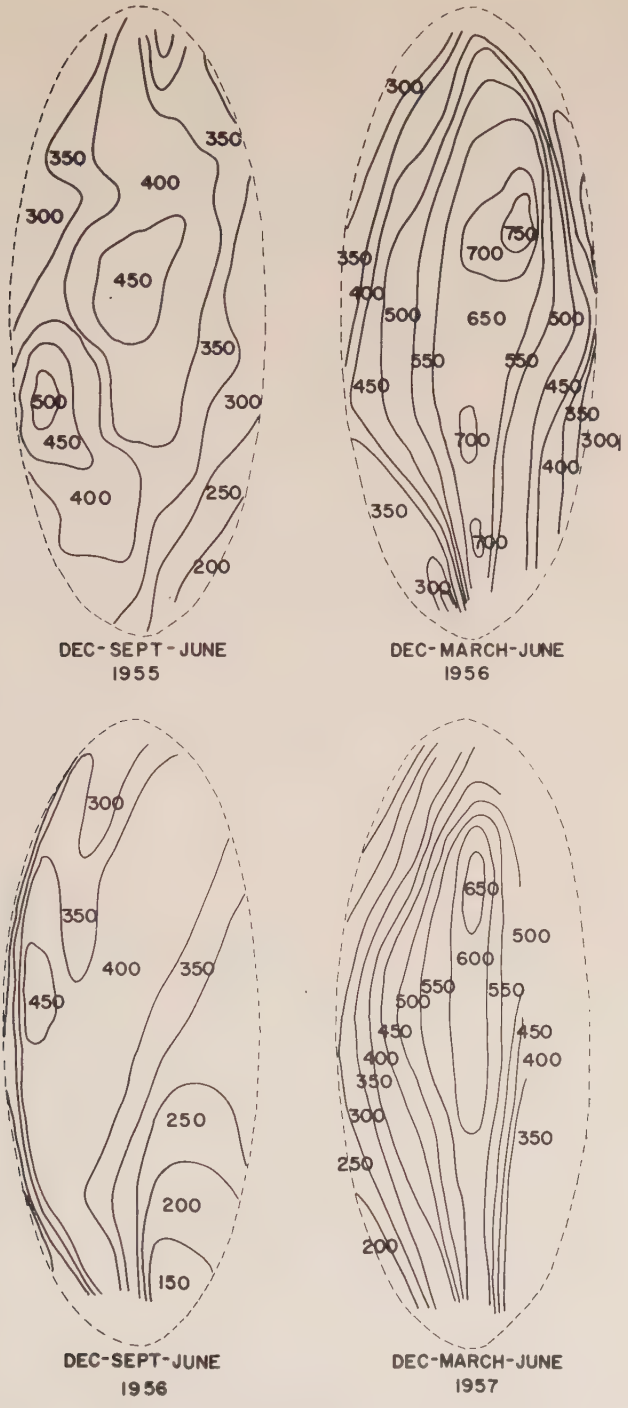

FIG. 3—Contours of equal intensity of 5577 for four half-year plots, using the coordinates of Fig. 2

If the plots of Figure 3 are interpreted in terms of the amplitude b and direction δ, west is tangent to the lines of equal m and upward, while north is normal to lines of equal m and is to the right. The space between contour lines is then a measure of the amplitude b. From Eq. (1), the amplitude b and direction δ are considered the amplitude and direction of a gradient. The gradient parameters were determined for each sky survey taken during the 107 undisturbed nights, and a vector average was obtained for each hour of operation. This is plotted in Figure 4. The patches of intensity mentioned earlier do not greatly affect the

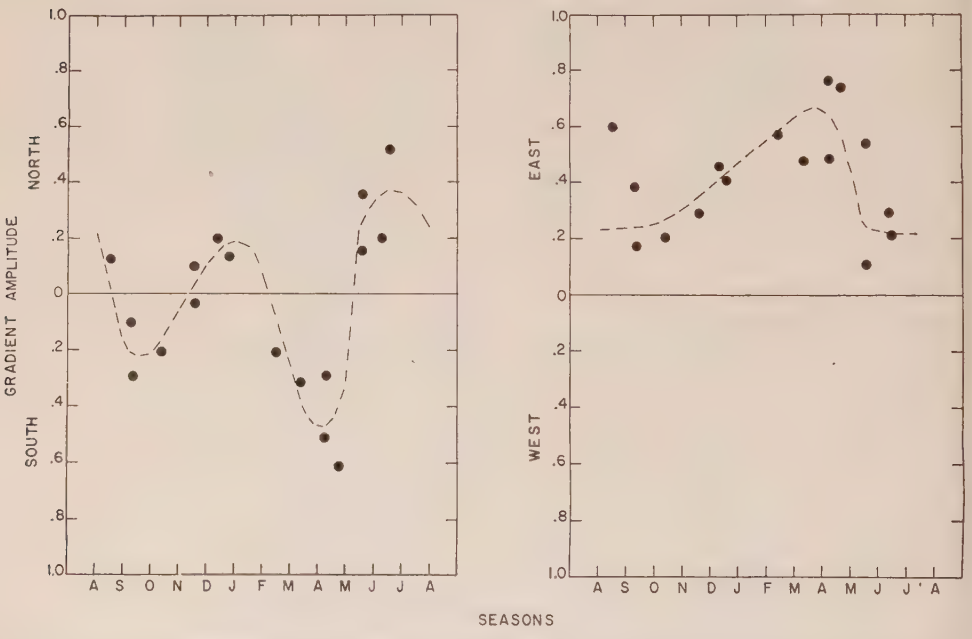

FIG. 4—Monthly averages of the north-south and east-west portion of the gradient amplitudes

average values of zenith intensity used to prepare Figure 3. They do, however, make determination of the gradient parameters difficult, since their effect, although small compared to the total intensity, is large enough to influence appreciably the values of b and δ determined for a single sky survey. Figure 5 shows the gradient amplitude and direction plotted over the contours of equal intensity. The observed gradient direction and amplitude fit predicted values about as well as can be expected. Presently available data are not sufficient to expect patchiness to average out in the determination of these parameters.

The existence of an intensity pattern which can be described, at least empirically, by a model appears very feasible. The present data are certainly not sufficient to describe the model in detail and the data presented here would fit well to within present accuracies on grids using considerably different coordinate systems. The grid proposed is a convenient one, as mentioned above, and it ties the pattern to the earth-sun position which seems reasonable for a first attempt.

FIG. 5—Fig. 3 with arrows to represent the gradient amplitude and direction averaged by hour for each month and plotted over the contours of equal intensity

SPORADIC FEATURES

The presence of small patches can be observed on practically each sky survey. Very little has been done to study or tabulate these in any regular manner. There are, however, nights of highly disturbed nature, which are considered below.

On six separate nights, arc-like structures superimposed on the regular 5577 A background have been observed. These are structures that are long thin strips, of intensity from one-half to two times the background intensity. Their characteristics can be summarized as follows:

1. They extend over the field of view in their long dimension.
2. They are 10 to 20 degrees wide.
3. Four of them first appeared in the north and two in the south, with their length running east-west.
4. They move southward or northward, perpendicular to their length.
5. The ratio of linear southward or northward velocity to their height is about two per hour.
6. There appears to be no correlation between their appearance and other geophysical disturbances such as sporadic E ionization or magnetic activity.

The same photometer is used to record 6300 A and 5890 A emission between the 5577 A surveys. On at least three nights during the period reported, the 6300 A

emission increased in the north by a factor of 50 due to auroral activity with n appreciable increase in the 5577 A emission. On 27 March 1957, auroral activit was detected in both colors, with the ratio of 6300 to 5577 enhancement equa to 4.5. In all cases, only the north intensity increased. The activity was probabl far to the north of Sacramento Peak, and the marked increase in 6300 A observe was probably due only to the upper portions of the aurora.

HEIGHT DETERMINATIONS

The method of van Rhijn with absorption and scattering as accounted for b Barbier [4] has been used to study the height of emitting regions. Average ratio of the intensity at zenith distance z to zenith intensities $I(z)/I(0)$ were plotte for the various nights, for months, and for seasons.

It was found, in general, that the experimental ratios do not indicate heigh with any degree of precision, unless the ratios are the average of many night Hourly ratios were obtained for $I(75)/I(0)$ by reading 16 points, evenly space in azimuth at 75 degrees zenith distance, as well as the zenith for each of the si surveys during an hour to determine hourly averages.

When data have been screened to eliminate all nights of questionable skie experimental difficulties which might lead to slight but accumulative errors, an nights with appreciable disturbances or high gradient amplitudes, an average fo $I(75)/I(0)$ of 2.555 is obtained. This average is obtained from 68 nights, an utilizes 488 samples, which are hourly averages. Figure 6 is a frequency distri bution curve of these data. The standard deviation is 0.232. The correspondin height is 85 $\pm$ 68 km.

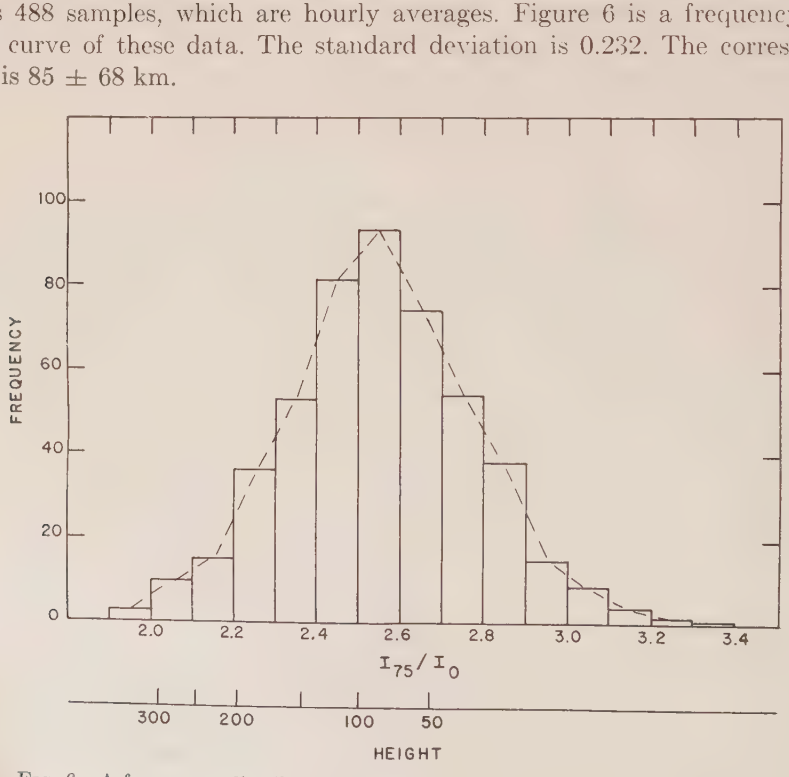

FIG. 6—A frequency distribution of $I(75)/I(0)$. Height scale is in kilometers.

It is significant that the 488 samples when grouped into days or months are not random about the average value of 2.555. Figure 7 shows the spread of monthly averages in this ratio with the standard deviation determined from the 488 hourly samples. It is noted that the monthly averages do not appear randomly about the total average.

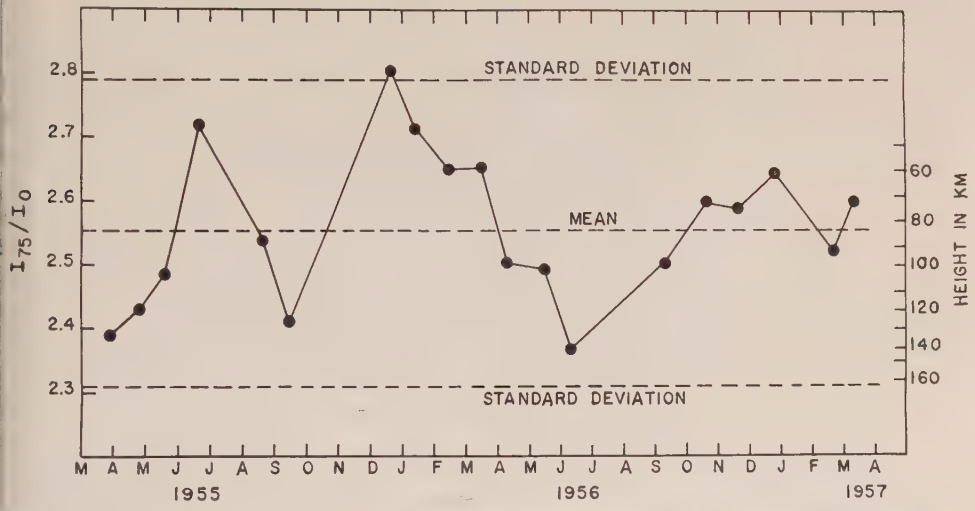

FIG. 7—The average of $I(75)/I(0)$ for each month from March 1955 through April 1957. The standard deviation is that obtained from the 488 samples.

Since the spectral purity of the instrument is high, the observed fluctuations in van Rhijn ratios must be attributed to the sky itself. Possible explanations are:

1. Variation of the height of the emitting region with season.
2. Emission from a diffuse or poorly defined region.
3. At large zenith angles, the scattered light when gradients and patches exist may be appreciably different from the amount calculated assuming a homogeneous sky intensity.

A form of triangulation has been used to study heights by an independent method [5]. Measurements simultaneous with those taken at Sacramento Peak were made at Capillo Peak (34° 42′ north, 106° 26′ west), near Albuquerque, New Mexico. Capillo Peak is 220 km and 14° 26.5′ west of north from Sacramento Peak. The fields of view of the two stations have considerable overlap.

The intensities observed from each station have been plotted on the same time scale for various "crossings" or positions where the cones of view of each photometer intersect. If a crossing occurs at a height where the emission occurs, a good correlation should be observed between the two intensity *vs* time plots. It is also possible that good correlations occur for other intersections, which merely indicates that the sky, in general, undergoes the same variation with respect to time over the two sites. Indeed, this latter condition is observed during most nights.

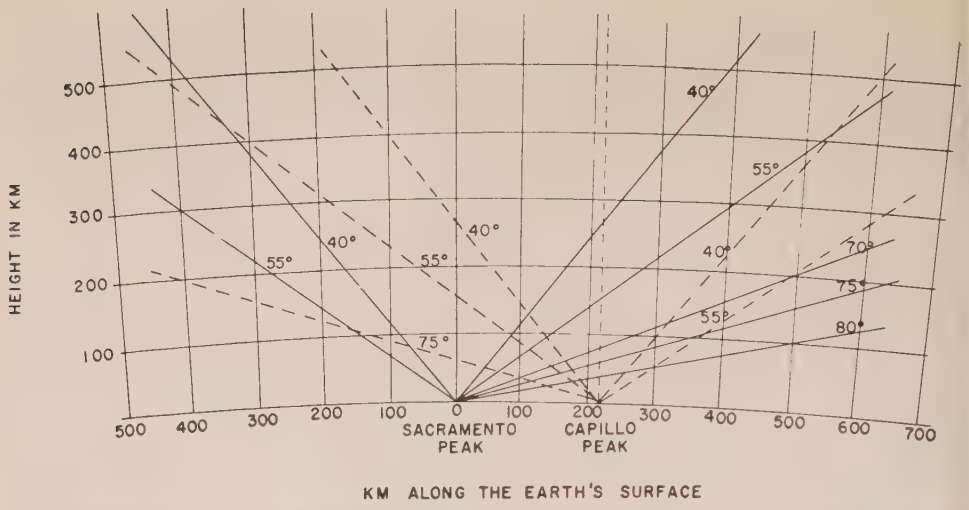

FIG. 8—A geographical representation of all the crossings considered in the perpendicular plane passing through the two stations

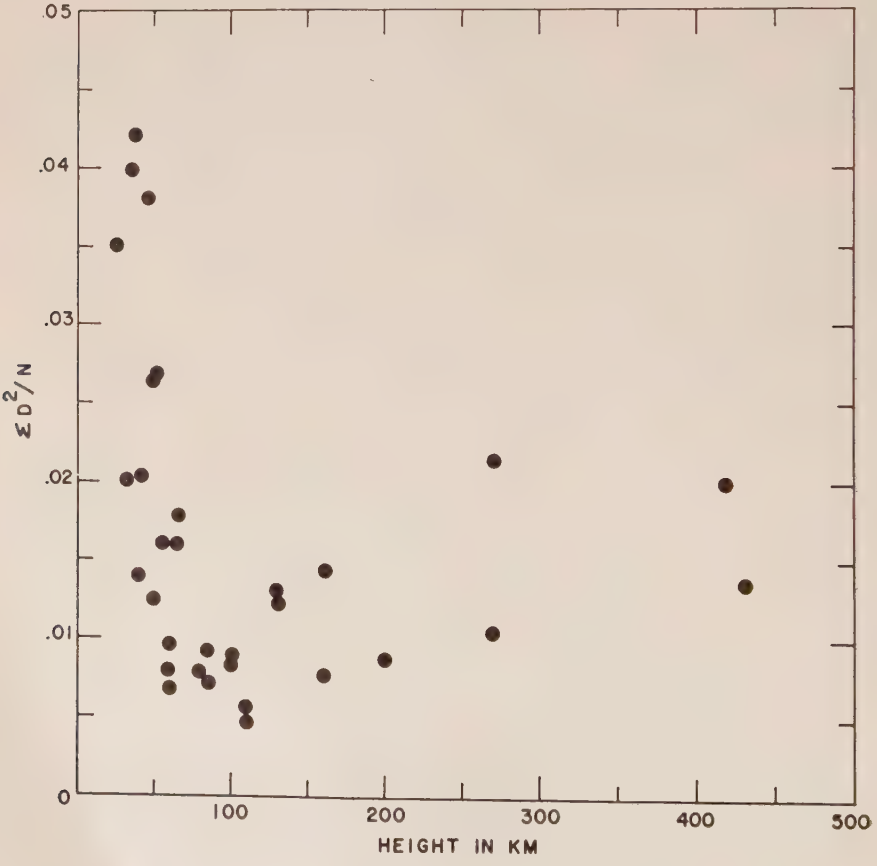

FIG. 9—The variation of $\Sigma D^2/N$ with height in kilometers

On the night of 8/9 November 1956, a set of simultaneous observations was obtained with good observing conditions and for which differing degrees of correlation existed for the various intersections. Simultaneous observations were made each 10 minutes from 2330 to 0450 hours. Figure 8 shows the crossings along a plane perpendicular to the earth through both stations that have been considered. To express the correlation quantitatively, each intensity *vs* time plot was normalized so that its average value was unity. This avoids difficulties encountered due to differences in the relative calibration of the two instruments and due to varying scattering conditions. From the normalized curves, the parameter $\Sigma D^2/N$ was determined, where D is the difference in the relative intensity at the two sites for each time observed. Figure 9 represents the change of $\Sigma D^2/N$ with the height of each intersection. It is observed that the correlation becomes good for heights between 80 and 100 km. At 80 km, $\Sigma D^2/N$ is only 0.0078.

It is important to note that most nights do not permit this type of analysis, since $\Sigma D^2/N$ plotted against height does not possess a clear-cut minimum. The existence of this minimum may be the effect of only a small portion of the total 5577 A emission. The indicated height is not necessarily the same, therefore, as that of the bulk of the emission.

ACKNOWLEDGMENTS

We wish to acknowledge the assistance of Mr. R. L. Keys for obtaining all the Sacramento Peak observations from July 1955 to the present, and to Mr. Harold E. Cronin for obtaining the Capillo Peak observations and for his help in instrumentation.

References

[1] R. Dunn and E. R. Manring, J. Optical Soc. Amer., **46**, 572 (1956).
[2] E. R. Manring and H. B. Pettit, The Threshold of Space (M. Zelikoff, Ed.), Pergamon Press, Ltd., London (1957); p. 58.
[3] D. Barbier, J. Dufay, and D. Williams, Ann. Astroph., **14**, 399 (1951).
[4] D. Barbier, Ann. Géophys., **1**, 144 (1944).
[5] P. St. Amand, H. B. Pettit, F. E. Roach, and D. R. Williams, J. Atmos. Terr. Phys., **6**, 189 (1955).

NIGHTGLOW EMISSION ALTITUDES FROM ROCKET MEASUREMENTS

By J. P. Heppner and L. H. Meredith

U. S. Naval Research Laboratory, Washington 25, D. C.

(Received September 13, 1957)

ABSTRACT

Four rocket-borne photometers measured nightglow emissions near λ 6300, λ 5893, λ 5577, and λ 5335. The emitting region of the oxygen green line, λ 5577, was entirely between 90 and 118 km, and had a very sharp lower boundary. The sodium D-lines were encountered primarily between 85 and 110 km, with a maximum intensity at 93 km. The upper boundary of D-line emission was not definite, due to tailing off of the distribution and low total intensity, but D-line emission extending into the 130- to 150-km region is indicated. The λ 6300 photometer showed two distinct features: an emitting region from 56 to 100 km, and a large signal still present at the peak of flight, 163 km. We attribute the 56- to 100-km emission to the (9-3) Meinel OH band, and conclude that the region of oxygen red line emission must lie above 163 km. On the basis of relative band intensities for the Meinel OH bands and the dissimilarity of the signal-*vs*-altitude curves for the λ 5335 and λ 6300 photometers, we conclude that practically all atmospheric emission near λ 5335 is due to an atmospheric "continuum" and not due to OH band emission. This atmospheric "continuum" has a maximum intensity between 100 and 110 km, and is at least as bright as the stellar background.

During descent of the rocket through the *E*-region, the photometers recorded a bright glow in the rocket's wake. Energy for creating the glow had to come from atmospheric gases and not the rocket. Its spectra and other features are discussed.

INTRODUCTION

Four photometers to measure the altitude distribution of the oxygen green line (λ 5577), the oxygen red lines (λλ 6300-6364), the sodium D-lines (λλ 5890-5896), and background light near λ 5335 were flown in Aerobee rocket NRL-33. The rocket was launched from White Sands Proving Ground, New Mexico, at 0052 MST on 5 July 1956. Continuous photometer readings were taken on ascent from 56 km to the peak of flight at 163 km, and on the descent to 70 km, where the rocket turned over.

Prior to these measurements, the Naval Research Laboratory had performed night airglow experiments in two rockets [see 1 and 2 of "References" at end of

paper]. On the first of these rocket flights, λ 5577 and background light near λ 5200 were measured to an altitude of 105 km. On the second, λ 5577, λλ 5890-5896, and background light near λ 5300 were measured to an altitude of 141 km. The photometers in both rockets were oriented to give a large angle between the rocket axis and the optical axes. This method has the advantage that a large signal is obtained, since the photometers look more or less horizontally through the emitting layer when the rocket axis is approximately vertical. It has the disadvantage that the rocket aspect must be known very accurately at all times.

A more direct approach was used in Aerobee NRL-33. The photometers were oriented to view 5° off the rocket's axis, such that a decreasing signal would be observed in passing vertically through a light emitting region. The van Rhijn equation shows that by the use of this technique zenith-angle corrections are negligible if the zenith angle of the rocket axis is less than about 30°. Measurements of the rocket aspect showed that the rocket behaved well for this planning. Aspect during flight was determined to ±5° by means of miniature electron-beam magnetometers [3]. This permitted positive identification of the Milky Way and bright stars. The star, Vega, was used for absolute, in-flight calibration.

The absolute total scalar magnetic field was also measured from this rocket. Results of these measurements with a proton precessional magnetometer will be given in a second paper in this JOURNAL. (Scheduled for the June issue—Ed.)

Results obtained from the airglow experiment give the altitude distributions of λ 5577 of OI, the sodium D-lines, and the (9-3) band of OH. The region of emission of the oxygen red lines was not entered, indicating that this emission occurs principally at altitudes $>$ 163 km. It is also concluded that most of the atmospheric emission near λ 5335 is not due to OH. A bright light with sharp boundaries was observed in the wake of the rocket when falling back through the *E*-region. The presence of this light and its spectral distribution raise new questions regarding energy storage in the ionosphere.

INSTRUMENTATION

Photometers—The four photometers were of the frequently used type, in which light passes successively through a color filter, interference filter, objective lens, and field lens to a 1P21 photomultiplier. Objective and field lenses, and consequently the fields of view, were identical to those used by Roach and associates [4]. Transmission curves for the various filters are shown in Figure 1. Photomultipliers were selected for high sensitivity and signal to noise ratio from a large stock of tubes. Dynode voltages were taken directly from batteries to insure constant potentials throughout flight. A Co-netic magnetic shield was placed about each photomultiplier to guard against the polarization field of the proton precessional magnetometer and changes in signal with orientation in the earth's magnetic field.

Amplifier and Gain Control Circuits—The photomultiplier outputs went to 100 per cent feedback electrometers with linear cathode follower outputs. Outputs at two sensitivity levels having the ratio 3.4 to 1 were taken from each electrometer and fed to separate telemetering channels. To provide further range, potentials on two of the nine dynodes were stepped in the sequence

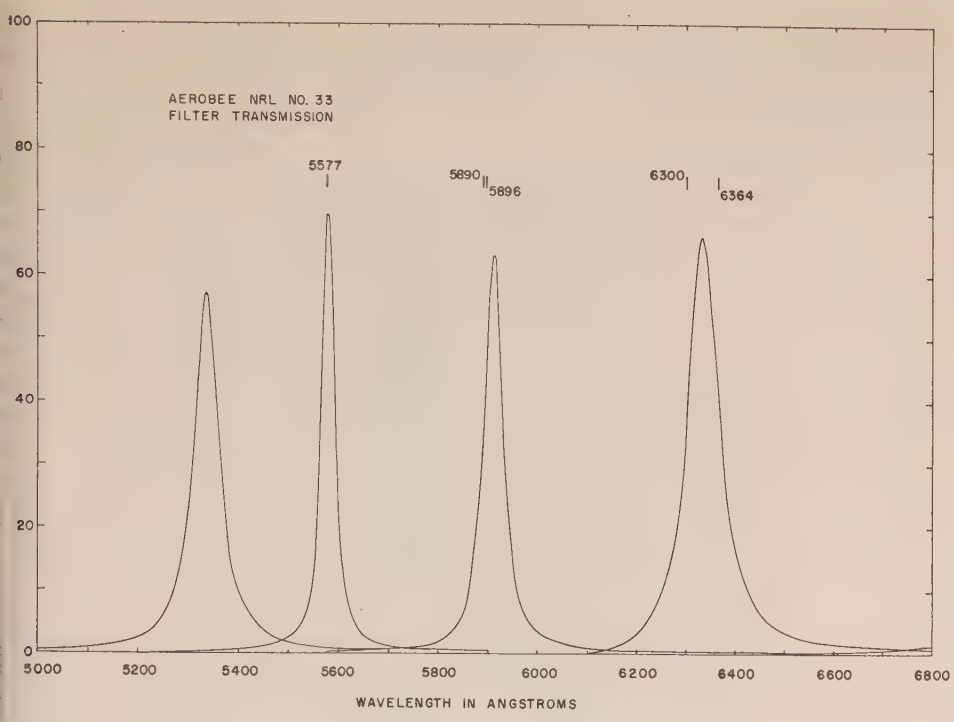

FIG. 1

0-75-90-105 volts by switching in 15-volt batteries every 0.4 second. By this means, a total range equivalent to more than 50 volts was obtained on the telemeter record. The reading accuracy was, in general, ±0.05 to 0.1 volt. The two channels with four steps per channel also give a set of simultaneous equations, which can be used to check possible zero changes when the dark current level is known. Using the preflight dark current value, no zero changes were found during flight. To measure temperature changes which could lead to dark current changes, thermistors were placed on two of the four photomultipliers. Temperature changes were negligible until re-entry into dense air, where a rise of 10°C was measured.

Rocket Installation—Nose-cone instrumentation is shown in Figure 2. The four photometers project through the bulkhead at the base of the black fiberglass cylinder containing the magnetometer coils. The photometer axes were spaced at 90° intervals and tilted 5° with respect to the rocket axis. The field of view of each photometer was 5° in diameter. Thus, as the rocket spun, each photometer swept out an annulus with an inside radius of 2.5° and outside radius of 7.5°. The fiberglass cone, shown at the left side of Figure 2, covered the magnetometer cylinder and was held down, with ejection springs compressed, by a nylon bolt at the top of the magnetometer cylinder. Small lids, fastened to the inside of the fiberglass cone, fitted over the photometer apertures. Radioactive light sources were placed on the lids to provide a constant light into each photometer. This provided an additional check for zero shifts or changes in dark current for the

first 55 seconds. No changes took place. At 55 seconds, the nylon bolt was explode and the fiberglass cone with attached photometer lids was ejected with a differ ential velocity of 15 ft/sec.

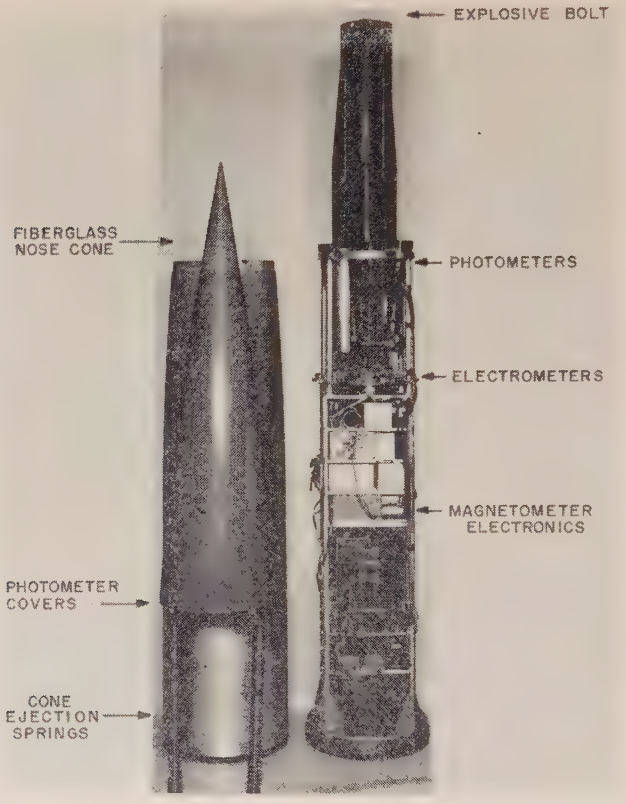

FIG. 2

ROCKET MOTION

Data reduction was straightforward, largely as a result of nearly ideal rocke behavior. The flight path had an exceptionally small horizontal component, an impact occurred within a few miles of the launch site. Between rocket burnou and re-entry into dense air, the vertical axis of the rocket completed only on precession cycle. At burnout, the axis pointed at the zenith near the star Albireo located in the Milky Way. The precession toward the northwest brought th axis out of the Milky Way to a maximum zenith angle of about 25° near the pea of flight. Completion of the precession cone, roughly centered on Vega, brought back to Albireo at about re-entry time. The roll period, 2.2 seconds, was su ficiently slow to give accurate measurements of the brightness of Vega. Combine with the slow precession, this roll rate was also rapid enough to permit practicall the same sky area to be viewed successively by the four photometers.

DATA REDUCTION

The reduction of scale values to absolute units, using star calibration, was carried out following the procedure suggested by Roach [5] for IGY surface observations. Reduction of rocket measurements is, of course, simplified and less susceptible to error than surface observations through elimination of corrections for extinction in the lower atmosphere. The equation

$$q = (4\pi/\Omega)(I_s/h\nu)(W/T)(b_v/b_s)(1/k)(1/R)$$

gives the scale conversion, q, in quanta/cm^2·column·sec·volt, or 10^{-6} Rayleighs/volt, where

Ω = photometer field in steradians

$I_s/h\nu$ = sun's energy in quanta/cm^2·sec·Angstrom at wave frequency, ν

$W = \int_0^\infty T(\lambda)d\lambda$ = equivalent filter width in Angstroms for 100 per cent transmission

T = filter transmission at the emission wavelength considered

b_v/b_s = $10^{0.4(m_s-m_v)}$ is the ratio of radiation from the star of magnitude $= m_v$ to that of the sun, magnitude $= m_s$

k = color correction applied to stars of spectral class different from that of the sun

R = scale reading in volts

For continuous rather than line radiation, the intensity per Angstrom is obtained by setting $W/T = 1$ and ν equal to the center frequency of the filter. The star Vega produced a distinct square wave deflection on a number of roll cycles. However, differences between readings and roughness in individual readings, caused primarily by faint stars near Vega and small deviations from flat response across the photometer field, probably limit the calibration accuracy to ± 10 per cent. The color correction for Vega, an AO star, was taken from reference [5]. Since Vega's spectra show no strong absorptions in the pass bands of the filters [6], the accuracy of the color correction should be good.

Scaled values from the eight sensitivity steps were first reduced to a common sensitivity and the dark current contribution removed. Roughness, due accumulatively to faint stars, variations in galactic light, and small changes in zenith angle during a roll cycle, was then partially removed by drawing smooth curves through the points of minimum signal. This process should not have introduced errors, since the roll rate was rapid compared to precession movement. For convenient presentation, the signal-*vs*-altitude curves for the four photometers were normalized to a common voltage scale, which was arbitrarily taken to be the same as the unnormalized voltage scale for λ 6300. The normalizing factors were the ratios of Rayleighs/volt·Angstrom for the λ 5335, λ 5577, and λ 5893 photometers to Rayleighs/volt·Angstrom for the λ 6300 photometer. Continuous radiation having uniform intensity over all four filter pass bands will then give equal numbers of normalized volts in each photometer. The resulting curves are given in Figure 3.

Several features of Figure 3 require explanation. First, it is obvious that the descent curve does not match the ascent curve. In the region 140 to 112 km on the

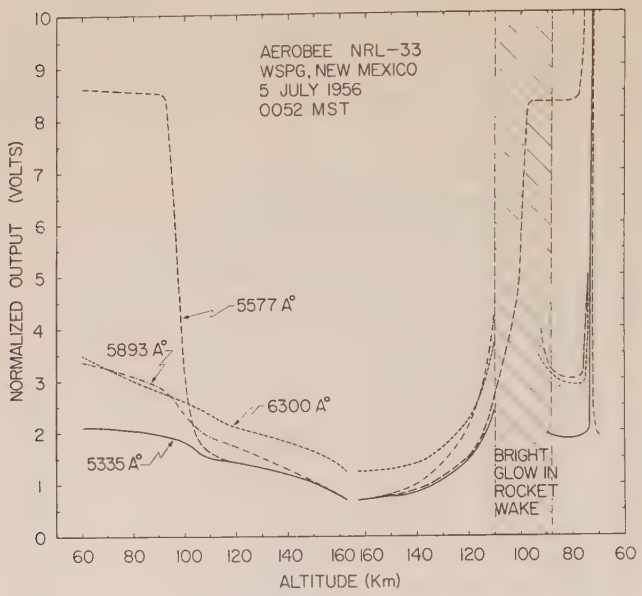

FIG. 3

descent, this is due to a gradual change in intensity, which becomes an extremely bright glow in the 112- to 88-km region. This segment of the flight is discussed in detail in a later section. Below 88 km and above the re-entry altitude, where the rocket turned over, the photometer signals return to the values observed on the ascent. Second, all four ascent curves, although showing a decrease with altitude, are slightly convex in the general region of 110 to 160 km. This is attributed to greater intensity in the Milky Way to the southwest of the star Albireo at this time of night, which is followed in turn by a cluster of faint stars in the path of the rocket's precession motion. The Milky Way and faint star contributions also cause the signal level on the ascent to be slightly higher than on descent at these altitudes.

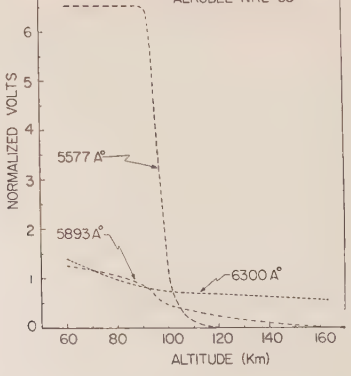

FIG. 4

Subtraction of the background light with the assumption that it is adequately given by the λ 5335 photometer gives the curves shown in Figure 4 for the ascent data. Figure 5 shows the difference between ascent and descent signal after removal of background radiation. The agreement between ascent and descent is very close in the 140- to 163-km region. From 140 to 85 km, the differences due to the bright glow, as mentioned above, are apparent. The relatively small deviation for the

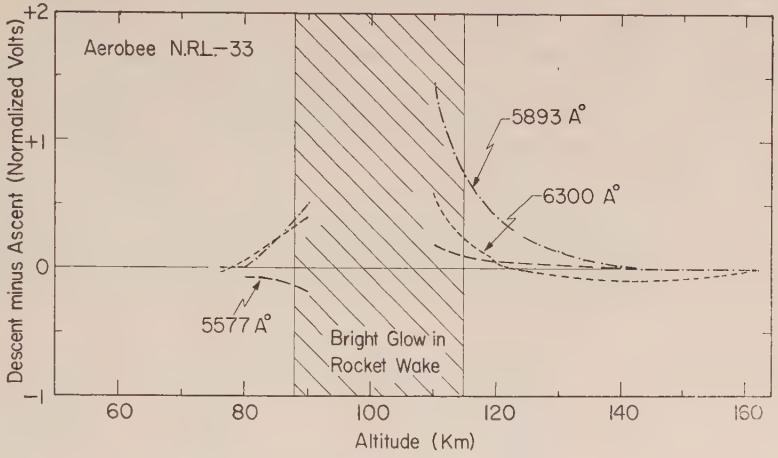

FIG. 5

λ 5577 photometer is a consequence of the spectral intensity of the glow near λ 5577 being very nearly equal to that near λ 5335, rather than a lack of the bright glow in this region.

INTERPRETATION OF REDUCED DATA

The curves of Figure 4 do not represent a specific emission until all emissions within the pass bands are taken into account. It is thus necessary to have spectrographic information on the wavelengths and probable intensities of the airglow emissions. Spectrograms indicate that the additional emissions will not contribute greatly to the λ 5577 measurements when a reasonably correct background subtraction is performed. The same is not true for λλ 5890-5896 and λλ 6300-6364, as spectrograms in these regions show fairly intense emissions, attributed to the Meinel (rotational-vibrational) OH bands.

The present results appear to verify the assumption that the light recorded by the λ 5335 photometer is a good measure of radiations other than the oxygen green line recorded by the λ 5577 photometer. This is indicated in several ways. First, subtraction of the λ 5335 light removes the slight slope of the λ 5577 curve between 56 and 90 km. Second, between 120 and 163 km, the λ 5335 and λ 5577 photometers recorded equal light intensities per unit wavelength. It is thus assumed that the Figure 4 curve for the λ 5577 photometer contains only the green line of OI. The columnar intensity of λ 5577 (OI) remaining above a given altitude is shown in absolute units in Figure 6. The magnitude of possible random errors is given by the small flag.

In Figure 4, most of the decrease with altitude for the λ 6300 photometer occurs below 100 km. This completely disagrees with theoretical expectations for the red lines of OI. The ^1D level of OI from which the red lines originate has a lifetime of about 96 seconds, and the probability of collisional de-excitation is too high to expect any appreciable red line emission between 56 and 100 km. In contrast, it is highly probable that the OH emissions occur at these altitudes [7, 8, 9]. Tabulated values [5] for the relative intensities of OI and (9-3) OH emissions passed by the λ 6300 photometer indicate that approximately equal light intensities from the two sources should be expected. The light remaining at the peak of flight was actually about 40 per cent after subtraction of background light. From these arguments, it appears that the light above 163 km was almost entirely the OI red lines and that the light traversed below 100 km was the (9-3) OH band. The slight decrease between 100 and 163 km may be a tailing off of the OH distribution, but could also be largely due to statistical errors. On this basis, curves in absolute units for the columnar intensities of the (9-3) OH band and λλ 6300-6364 of OI above a given altitude are shown in Figure 6, with the probable

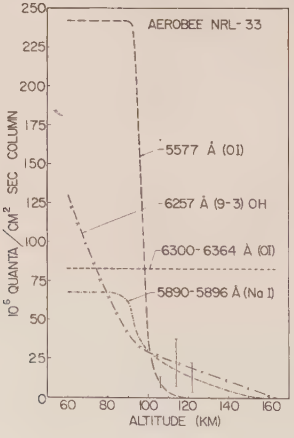

FIG. 6

range of random errors. In obtaining values for the absolute intensity of the (9-3) OH band, we have assumed a distribution of intensity *vs* wavelength from the band origin identical to that given by Chamberlain and Roesler [10] for bands farther to the red. The integrated filter transmission for the OH band was derived from this distribution.

Using the intensity-*vs*-altitude distribution of Figure 6 for the (9-3) OH band, a cross check on the assumption which led to the curve was obtained from the λ 5893 photometer, which passes the (8-2) OH band, using the relative intensities of the (8-2) and (9-3) OH bands given in reference [5]. The intensity of the (8-2) OH band derived from the (9-3) OH band was subtracted from the λ 5893 curve of Figure 4 with the assumption that the two OH bands would have identical altitude distributions. The most notable affect of this subtraction was that it made the λ 5893 curve flat from 56 to 80 km. This places the emission region for Na

D-lines above 80 km. Since this is more probable than having the Na D-lines as ow as 56 km, it gives some confirmation to the assumptions involved in the dis- ussion above. The absolute columnar intensity of the sodium D-lines above a iven altitude is shown in Figure 6.

In the discussion above, it has been assumed that light recorded by the λ 5335 hotometer was a measure of the "background" radiation in the other photo- neters, exclusive of OH band emission. Belief in the validity of this assumption or the λ 5577 photometer was expressed primarily on the basis of equal light ntensities per Angstrom in the two photometers above 120 km. There is also vidence, though not as conclusive, that it is a fair measure of the non-OH back- round in the λ 5893 and λ 6300 photometers. In the case of λ 6300, the curves see Fig. 3) for λ 5335 and λ 6300 are parallel, to the accuracy obtained, from 130 o 163 km. Thus, validity of the assumption is indicated above approximately 30 to 140 km. Below 85 km, the flattening of the λ 5577 curve, and the λ 5893 urve after subtraction of the (8-2) OH band, also indicates that the background ubtraction is valid. There is not, however, any specific evidence that the back- round subtraction is correct in the 85- to 120-km region. The evidence below and bove this region permits some confidence in the assumption that it is at least good approximation. The extent to which it is an approximation has only a small ffect on the altitude distribution of the emissions previously discussed.

In Figure 3, it is apparent that the λ 5335 photometer showed a decrease in in- ensity with altitude. The difference between the low altitude and peak values epresents the fraction due to atmospheric emission, with the exception of Milky Way contributions to the low altitude values on both ascent and descent. Since he curves of Figure 3 were taken from minimum readings, bright spots in the Milky Way were largely eliminated, especially below 90 km, where the photo- neters were viewing a section of the Milky Way containing sizable dark holes. Thus, a large percentage of the decrease must be due to atmospheric emissions. The (6-0) OH band is passed by the λ 5335 filter. However, using the tabulated ntensity ratios (reference [5]) for the (6-0) OH band relative to the (9-3) OH band ntensity deduced above and the integrated transmission through the λ 5335 ilter, the (6-0) OH band would have contributed only 0.01 normalized volt to the urve of Figure 3. The possibility that the decrease was due to OH is also ruled ut on the basis that the altitude where the maximum decrease took place, 95 to 10 km, does not agree with the altitude distribution of the (9-3) OH band. Another ossibility is that the λ 5335 readings were contaminated by the λ 5577 OI green ine. However, the filter transmission at λ 5577 was only 0.78 per cent, and this ource could only have contributed 0.05 normalized volt to the curve of Figure 3. We are thus left with the conclusion that the predominant atmospheric emission assed by the λ 5335 filter was not from OH or OI.

Exact fractions for the light due, respectively, to atmospheric and non-atmos- heric sources near λ 5335 would be valuable to future ground observations, as hese figures play an important part in surface data analyses [11]. Unfortunately, he Milky Way contributions to the readings below 90 km, although small, do ot permit us to assign definite numbers. It is, however, safe to state that a minimum of 35 per cent of the light recorded by the λ 5335 photometer below the

emitting region, excluding the Milky Way, was of atmospheric origin. A probable value from our curves would be ≥ 50 per cent. The low altitude and peak differences observed in the previous rocket flights [1, 2] also suggest that an atmospheric "continuum" contributes at least 50 per cent of the light near λ 5300. This is a considerably larger fraction than that derived by Roach and Meinel [11, 12]

BRIGHT GLOW OBSERVED DURING ROCKET DESCENT

As previously mentioned, the photometers saw a bright source on the descent when the rocket passed from 112 to 88 km. The normalized outputs of the four photometers during this time are shown in Figure 7. The lower curves give the

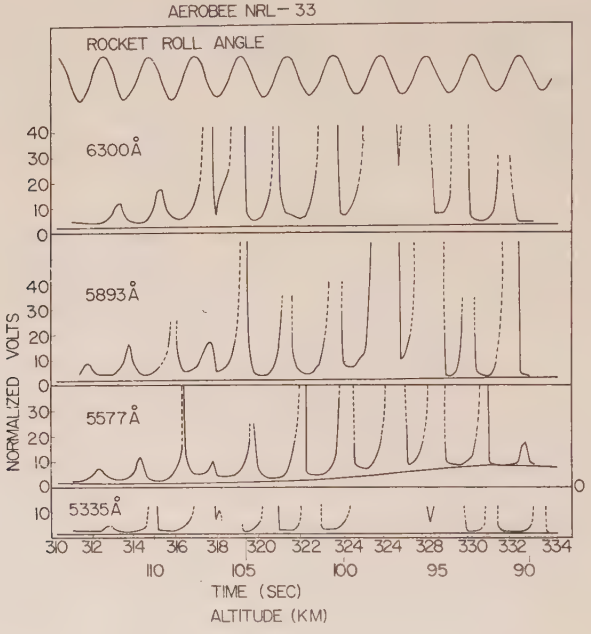

FIG. 7

ascent values for comparison. The rocket roll angle as given by one of the aspect magnetometers is also shown. At the times of minima of the roll curve, the λ 5577 photometer axis lies between the rocket axis and the magnetic zenith and in their plane. As the rocket rolled, the photometers successively saw the bright light in the order 6300-5893-5577-5335-6300 · · · . This is the expected behavior if the source is fixed in space and not in the rocket coordinates. A bright light, however, was not seen during rocket ascent, although the photometers saw the same part of the sky. The significant difference between ascent and descent was that on ascent the photometers looked ahead of the rocket, while on descent they were looking at the rocket wake. The bright glow must then be associated with the rocket wake. The rocket velocity of approximately one kilometer per second at this time could not, however, impart enough energy to excite atmospheric molecules and produce the glow. Instead, the rocket by some process must have liberated

nergy stored in the ionosphere. The process must be consistent with the observed eatures of the bright light. These are

1. *Intensity*: All photometers were saturated by the light. To do this, the light had to be at least as bright as a -3 magnitude star.
2. *Spectrum*: Since all the photometers saturate, it is difficult to accurately determine the spectrum of the bright glow. In Table 1, the relative intensities for the four photometers are given in normalized volts as measured
   (*a*) From the few unsaturated peaks near 314 seconds
   (*b*) By assuming the source had the same physical size in all photometers and determining relative voltages for a given roll duration, and
   (*c*) From the difference between intensities on ascent and the intensities between the roll peaks on descent. The lack of agreement between these methods, as evidenced in Table 1, indicates that the bright glow did not have the same spectra throughout its spatial distribution.
3. *Altitude dependence*: Peaks of intensity due to roll were not observed until 112 km on the descent. The light intensity then increased to 106 km, where it momentarily decreased. It then increased in intensity and remained bright until it faded very rapidly at 88 km. The fading was ten times more rapid than could be accounted for by the source leaving the field of view of the photometers due to rocket motion. Thus, the light source must have extinguished at 88 km.
4. *Source size*: As the distance from the rocket is unknown, the size of the source is unknown. It must, however, have been at least a few degrees wide.
5. *Source position*: From 312 to 318 seconds, the source is approximately in the plane of the rocket axis and the zenith on the opposite side of the rocket axis from the zenith. At 318 seconds, the source apparently sweeps across the photometers. From this time on, the source is approximately between the rocket axis and the zenith and in their plane. At 318 seconds, the zenith angle of the rocket axis is $\leq 5°$.

There are two types of processes by which energy might be liberated from the onosphere. The first would be due to the presence and/or motion of the rocket tself, and the second due to gas from the rocket.

In considering gas from the rocket, it should first be noted that the instrumen- ation section of the rocket was pressurized. Gas escaping from the rocket would hus have to come from excess fuel in the rocket motor. Similar rockets have been lown which measured mass composition and density at high altitudes. The results f these experiments show that at these altitudes such gas could increase the lensity in the neighborhood of the rocket by no more than one per cent. Further- nore, the gas hypothesis cannot explain the dip in intensity at about 318 seconds r the sharp changes in intensity evident in Figure 7. From the rapid termination f the light at 334 seconds, there could not have been a persistent trail behind he rocket, such as the trails observed in experiments where material is ejected nto the ionosphere [13, 14]. While the gas hypothesis can give an explanation for he observed altitude and roll dependence, the above considerations make it seem nlikely that this is the primary source of the bright glow.

This being the case, we are forced to the conclusion that by some mechanism the rocket itself, in moving through the ionosphere, produces the light. It should be noted that the altitude dependence of this light is very similar to the altitude dependence of the λ 5577 OI green line. The distributions are also similar, in that they have sharp lower boundaries and more gradual intensity changes at the upper boundary. If the OI green line is produced by chemically active atmospheric constituents, the rocket may release this energy through direct collisions and through a higher collisional frequency due to increased gas density created by flow around the rocket. Such processes have been experimentally verified in the laboratory at considerably higher pressures by flowing active nitrogen past bodies at velocities similar to that of the rocket. These experiments (for example, see [15]) also show different spectral distributions in different regions of the observed light. Electrical discharges have also been observed in the wake of various bodies in these experiments. This is another possible explanation for the rocket generated glow, but a discharge of this sort would probably have been modulated by the quarter-second on-off cycle of the magnetometer magnetic polarization field at the nose tip. This modulation was not observed.

While no intensely bright regions were seen above 112 km, Figure 5 shows that the descent intensities between 140 and 112 km are higher than those on the ascent. It seems reasonable, from the spectral similarity and gradation into roll modulated light, to also attribute this to a source associated with the rocket's wake. The source at these altitudes must have been diffuse.

We have not been able to attribute the bright glow to any specific emission or excitation process. This is largely due to the complicated nature of the spectra, as indicated by Table 1, and the lack of comparison spectra on band systems, other than those of N_2, which might have similar intensity ratios. For comparison, we have included in Table 1 the calculated intensities for the first positive system of N_2, using the results of Turner and Nicholls [16]. These ratios are strongly dependent on the conditions of excitation [17]. Another speculation is that the bright glow comes principally from NO_2. The triple collision

$$NO + O + M \rightarrow NO_2 + M + h\nu$$

produces a nearly continuous emission over the range λ 4200-λ 6700 [18, 19, 20]. This "continuous" spectra would not give the relative intensities of Table 1; however, the spectra is sensitive to gas composition, contaminates, and wall

Table 1

Wavelength	Bright glow relative intensities (*normalized volts*) (*a*)	(*b*)	(*c*)	First positive system of N_2 (*normalized volts*)
λ 5335	4.6	2.0	4.4	1.1
λ 5577	9.1	1.5	4.4	0.4
λ 5893	14.0	5.1	8.7	5.2
λ 6300	10.0	10.0	10.0	10.0

onditions. A particular example given by Newman [21] would give relative ntensities close to those of column (*a*), Table 1.

SUMMARY

λ 5577, OI *Green Line*: The columnar intensity curves of Figure 6 were differntiated to illustrate the layer distribution, Figure 8. The most striking feature f the OI green-line distribution is the sharpness of the lower and upper boundaries. The emission appeared abruptly near 90 km, rose rapidly to a maximum at 94 m, decreased rapidly from 100 to 104 km, and tailed off to zero at 118 km. The esults agree essentially with those obtained in previous rocket flights [1, 2], but ssign sharper boundaries to the emitting region.

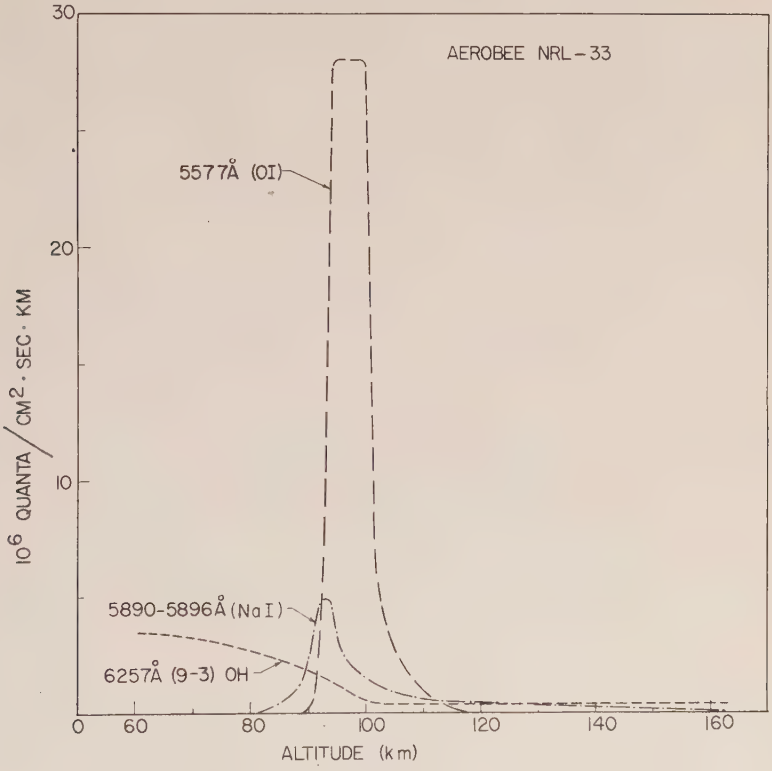

Fig. 8

λλ 5890-5896, *Sodium* D-*Lines*: As would be expected from statistics on the easonal intensity variation of the Na D-lines, the total intensity was very low. The 5 July firing date is coincident with the minimum of most annual intensity urves. The layer distribution is given in Figure 8. Cumulative errors due to the ow intensity and the subtraction of both "background" and OH band emissions nake the exact boundaries of this layer uncertain. The peak of the distribution t 93 km should be correct within ±3 km. The lower boundary is within the range

78 to 85 km. The tailing off of the intensity curve above 100 km makes the upper boundary indefinite. It appears probable that the D-line emissions exist at least as high as 140 km.

λλ 6300-6364, OI *Red Lines*: It was concluded that the emission of OI red lines originates primarily above 163 km. Possible errors do not exclude some emission below 163 km, but this at most would be a small fraction of the total. From the altitude separation of the regions of green and red line emissions, it must be concluded that electrons are supplied to the $^1D_2$ level of OI by other means than transitions from the $^1S_0$ level which give the OI green line. The same problem is encountered in explaining the enhancement of the red lines relative to the green line at twilight and in high altitude aurora [22].

The (9-3) *and* (8-2) *Meinel* OH *Bands*: The decrease in signal from the λ 6300 photometer between 56 and 100 km was, as discussed, attributed to the (9-3) OH band. The curve of Figure 6 has been differentiated to show the distribution of OH emission in Figure 8. Since the photometers were not "uncapped" until 55 km and the rocket turned over near 70 km on re-entry, the lower boundary of the OH region is unknown. The upper boundary is uncertain due to possible errors in analysis, but it is apparent that all but a small fraction of the OH emission originates below 100 km. The effective height of 70 km determined from ground observations and theoretical and spectrographic studies [7, 8, 9] is in good agreement with these observations.

Emissions near λ 5335: The λ 5335 photometer showed a decrease in signal with altitude which could not be due to the (6-2) OH band or λ 5577 contamination. The present results indicate that the atmospheric emission near λ 5335 is about equal in intensity to starlight and is most intense in the 100- to 110-km region. The previous rocket measurements [1, 2] showed a maximum intensity near λ 5200 and λ 5300 between 95 and 110 km. The identity of the atmospheric emission causing the decreasing signal is not known. On published spectrograms, the non-OH light near λ 5335 appears almost continuous. From the fact that the "background" subtraction led to no discrepancies in our analyses of the 100- to 110-km region, the present data give some indication that the same "continuous" airglow emission may extend over the pass bands of the other photometers. The mechanism,

$$O + NO + M \rightarrow NO_2 + M + h\nu$$

which produces a continuous glow from λ 4200 to λ 6700, has been suggested by Kaplan [18] and Nicolet [19] as a source of continuous radiation in the airglow. In view of the present results, indicating emission in a region of abundant O and possibly abundant NO and NO_2, suggested by the prominence of NO^+ and NO_2^+ in rocket measurements of ion spectra [23, 24], this suggestion should be given more serious consideration. It is unfortunate that emissions near the λ 5300 control region have so frequently been attributed entirely to OH, as this has led Krassovsky [25] to misinterpret rocket data in deducing mechanisms for OH excitation.

Bright Glow During Rocket Descent: During descent of the rocket through the 140- to 112-km range, a diffuse glow was created in the rocket's wake. At 112 km, the glow increased in intensity and became roll modulated. It reached its maximum intensity between 100 and 95 km. At 88 km, the glow extinguished. The glow was

doubtedly created by the release of energy stored in the ionosphere, but an planation as to exactly how the rocket caused the energy release has not been nd. Some preference is given to the hypothesis that the rocket's presence and tion in the ionosphere were sufficient. The alternative hypothesis is collisions ween atmospheric gases and gas from the rocket motor. Indications that the w spectra varied over their spatial distributions and uncertainties in comparison ctra do not permit identification of the emitting molecules. Two possibilities mentioned; these are the first positive system of N_2 and a modified "continuum" e to NO_2 .

Mr. H. M. Caulk provided the magnetic aspect instrumentation and analyzed aspect data. To him, and to J, F. McChesney and J. D. Stolarik, who assisted various ways, the authors wish to extend their appreciation.

References

[1] O. E. Berg, M. Koomen, L. Meredith, and R. Scolnik, J. Geophys. Res., **61**, 302 (1956).
[2] M. Koomen, R. Scolnik, and R. Tousey, J. Geophys. Res., **61**, 304 (1956).
[3] H. M. Caulk and L. R. Davis, description to be published in Rev. Sci. Instr.
[4] F. E. Roach and H. B. Pettit, J. Geophys. Res., **56**, 325 (1951).
[5] F. E. Roach, Washington, D. C., Nation. Bur. Stan., NBS Rep. No. 5006 (August 1956).
[6] W. A. Hiltner and R. C. Williams, Photometric Atlas of Stellar Spectra, University of Michigan Press, Ann Arbor (1946).
[7] F. E. Roach, H. B. Pettit, and D. R. Williams, J. Geophys. Res., **55**, 183 (1950).
[8] D. R. Bates and M. Nicolet, J. Geophys. Res., **55**, 301 (1950).
[9] A. B. Meinel, Astroph. J., **112**, 120 (1950).
[10] J. W. Chamberlain and F. L. Roesler, Astroph. J., **121**, 541 (1955).
[11] F. E. Roach and A. B. Meinel, Astroph. J., **122**, 530 (1955).
[12] J. W. Chamberlain and A. B. Meinel, The Earth as a Planet, Vol. II (G. P. Kuiper, Ed.), University of Chicago Press, Chicago (1954); chap. 11, p. 514.
[13] H. D. Edwards, J. F. Bedinger, and E. R. Manring, The Airglow and the Aurorae (E. B. Armstrong and A. Dalgarno, Eds.), Pergamon Press, Ltd., London (1955).
[14] J. F. Bedinger and E. Manring, J. Geophys. Res., **62**, 170 (1957).
[15] J. M. Benson, National Advisory Committee for Aeronautics, Tech. Note No. 2293 (February 1951).
[16] R. G. Turner and R. W. Nicholls, Can. J. Phys., **32**, 468 (1954).
[17] S. K. Mitra, Active Nitrogen —A New Theory, Indian Association for the Cultivation of Science, Jadavpur, Calcutta (1945).
[18] J. Kaplan, Mém. Soc. roy. sci., Liége, 4th Ser., **12**, 295 (1952).
[19] M. Nicolet, J. Atmos. Terr. Phys., **7**, 297 (1955).
[20] M. L. Spealman and W. H. Rodebush, J. Amer. Chem. Soc., **57**, 1474 (1935).
[21] F. H. Newman, Phil. Mag., **20**, 777 (1935).
[22] P. Swings, The Atmosphere of the Earth and Planets (G. P. Kuiper, Ed.), University of Chicago Press, Chicago (1949); chap. 6, p. 159.
[23] C. Y. Johnson, J. C. Holmes, and E. B. Meadows, presented at the Annual Meeting of the AGU, May 1957; abstract in Trans. Amer. Geophys. Union, **38**, 397 (1957).
[24] C. Y. Johnson and J. P. Heppner, J. Geophys. Res., **61**, 575 (1956).
[25] V. I. Krassovsky, J. Atmos. Terr. Phys., **10**, 49 (1957).

THE RANDOM OCCURRENCE OF METEORS IN THE UPPER ATMOSPHERE*

BY T. J. KEARY AND H. J. WIRTH

U. S. Navy Electronics Laboratory,
San Diego 52, California

(Received November 29, 1957)

ABSTRACT

This paper reports an experimental study of the distribution of time intervals between bursts of 43.5-Mc/s signals received over a 690-km path from Stanford, California, to San Diego, California, with the object of determining whether or not the bursts occurred completely at random.

The distribution of time intervals observed is consistent with the distribution expected if the bursts are produced by scattered radiation from the ionized trails of meteors which enter the upper atmosphere at random. The number of time intervals observed less than one second is appreciably less than the number calculated. This would be the case if some bursts were not observed when the interval between bursts is comparable to the duration of the bursts. The difference between observed and calculated values for large intervals for which the actual number of observations is small is not statistically significant. The observed number of triplets of equally spaced bursts substantially agrees with the number expected if the bursts occurred at random.

The data used in this analysis were the intervals preceding 778 bursts observed during 0400-0600 hours on 3 August 1956 and those preceding 446 bursts observed during 0500-0700 hours on 6 November 1956.

I. INTRODUCTION

Numerous investigators attempting to receive radio signals from distant, edium-power vhf transmitters have observed that, although normally no signals e received, occasionally signal bursts do erupt above the noise level. Such a gnal burst is now commonly interpreted as indicating that a meteor has entered e upper atmosphere and produced an ionized trail with suitable orientation and lequate linear electron density to scatter the transmitted radiation to the receiver. llard, Peterson, Manning, and Eshleman [see 1 of "References" at end of paper] d Forsyth and Vogan [2] have described observations of the forward scattering radio waves by meteoric ionization.

*Some of the material of this paper was presented as part of a talk given at a meeting of RSI on 12 October 1956 at University of California, Berkeley, California.

Several observers have examined the spacing between successive signal bursts to determine whether or not there is any regularity in the occurrence of the bursts.

Isted [3] observed in Great Britain the vhf sound carrier of a TV transmitter ($f = 53.25$ Mc/s) over a 530 km path. Signals arrived at the receiver in a succession of impulsive bursts. He found that many of the bursts were arranged in trains having a very rigid time separation between bursts, and he concluded that some mechanism is capable of producing regularly spaced bursts of signal. He proposed that upwardly directed electrical discharges from clouds produced patches of ionization in the E region.

Briggs [4] also observed in Great Britain short bursts of signal from a TV transmitter ($f = 53.25$ Mc/s) over a 480-km path. He studied the statistics of the time intervals between bursts and inferred provisionally that the majority of bursts occur at random, but a very small proportion may be grouped into trains.

Wylie and Castillo [5] monitored radio station WWV transmissions ($f =$ 20 Mc/s) over a 608-km path between Washington, D. C., and Springfield, Ohio. They recorded bursts from 0200 to 0300 hours on nine nights, and then counted the number of bursts in each half-minute interval on the record, using the first hundred good intervals on each night. They compared their observed frequency of intervals having various number of bursts with the predicted frequency of intervals with the same number of bursts. They concluded that for their observations during early morning hours on non-shower nights the distribution of meteors striking the upper atmosphere of the earth is not random, but clustered.

The varied conclusions obtained by the above investigators have stimulated the authors to examine more completely data which they have obtained. Since the summer of 1955, they have intermittently observed and recorded at the U.S. Navy Electronics Laboratory, San Diego, California, signal bursts from a vhf transmitter operated by the Radio Propagation Laboratory, of Stanford University, Stanford, California. It is the purpose of this paper to compare the distribution of intervals between signal bursts experimentally observed with the distribution which would be expected on the basis of random occurrence of meteors in the upper atmosphere.

II. CONSIDERATION OF SPACING OF SIGNAL BURSTS

Assuming the occurrence of meteors in the upper atmosphere to be completely random, one may calculate the distribution of intervals between starts of signal bursts.

Select a period of a few hours in which the average rate of occurrence of signal bursts does not change appreciably.

Let T be the average interval between starts of successive signal bursts.

Then $1/T$ is the average number of signal bursts per unit time.

Consider a time interval Δt which is very short compared with T.

Then the probability that a signal burst will occur in time Δt is $\Delta t/T$, and the probability that a signal burst will not occur in time Δt is $1 - \Delta t/T$. Assume that the chance that a signal burst occurs in a given interval Δt is independent of whether or not bursts occurred in previous intervals, then the probability that a signal burst will not occur in total time t is

$$\left.\begin{aligned} Q &= \lim_{\Delta t \to 0} \left(1 - \frac{\Delta t}{T}\right)^{t/\Delta t} \\ &= e^{-t/T} \end{aligned}\right\} \quad \ldots\ldots\ldots\ldots\ldots\ldots\ldots\ldots (1)$$

nd the probability that a signal burst will occur during time t is

$$P = 1 - e^{-t/T} \quad \ldots\ldots\ldots\ldots\ldots\ldots\ldots\ldots (2)$$

Here t may be considered as measured from the start of a signal burst.

The probability that a signal burst will occur during the time interval t to $+ \Delta t$ is

$$P(t + \Delta t) - P(t) = \frac{1}{T} e^{-t/T} \Delta t \quad \ldots\ldots\ldots\ldots\ldots\ldots\ldots\ldots (3)$$

f N is the total number of signal bursts in the sample, then the expected number f signal bursts in the interval t to $t + \Delta t$ is

$$n(t)\Delta t = N(t + \Delta t) - N(t) = \frac{N}{T} e^{-t/T} \Delta t \quad \ldots\ldots\ldots\ldots\ldots\ldots\ldots\ldots (4)$$

The exponential distributions given by Eq. (1) and Eq. (4) may be tested xperimentally by measuring the intervals between successive signal bursts for a arge number of bursts during a period in which the average rate of occurrence of ursts is approximately constant.

III. MEASUREMENT TECHNIQUE

The transmission path over which bursts of vhf radiation are observed extends or 690 km, from Stanford, California, to San Diego, California. The path is riented approximately NW to SE. A 43.5-Mc/s transmitter at Stanford is operated nmodulated at a power output of 1 kw, of which about 700 watts are radiated.

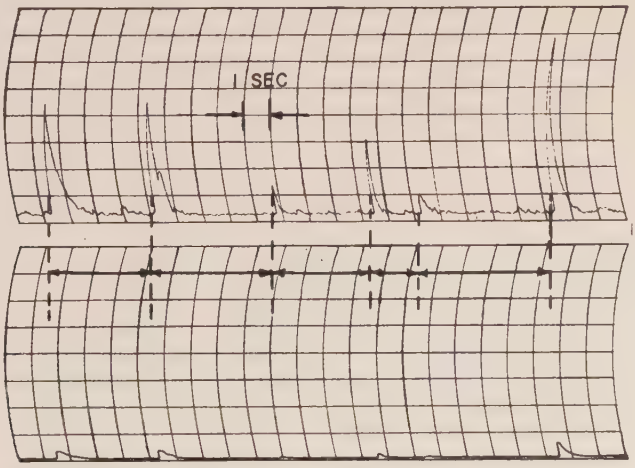

IG. 1—Sample record showing observed signal bursts; time intervals between starts of bursts are indicated.

The radiation is broadly directed toward San Diego by a horizontally polarized three-element Yagi antenna. Signals are received at San Diego with a similar three-element Yagi antenna, with its beam directed toward Stanford.

The receiving equipment consists of a *cascode* preamplifier, Hammarlund SP 600 receiver, with intermediate frequency bandwidth = 3 kc/s, deflection amplifier, and Brush recorder. The receiver is operated without automatic gain control and with the beat frequency oscillator adjusted to produce a beat note of convenient audio frequency. The deflection amplifier is made linear, so that the deflection on the recorder is proportional to the E field incident on the receiving antenna.

Figure 1 is a sample record showing bursts of signal received from the distant transmitter which was operating continuously. The time intervals between starts of bursts with peak amplitudes exceeding a set threshold are indicated. Only signals starting with a precipitous rise in amplitude above the noise level are considered as bursts for the purpose of this analysis.

IV. RESULTS

Data of 3 *August* 1956

Figure 2 shows the hourly rate of occurrence of signal bursts over a 26-hour period during 2-3 August 1956; the time shown is Pacific Daylight Time (PDT). During 0400-0600 hours on 3 August 1956, the rate of occurrence of signal bursts

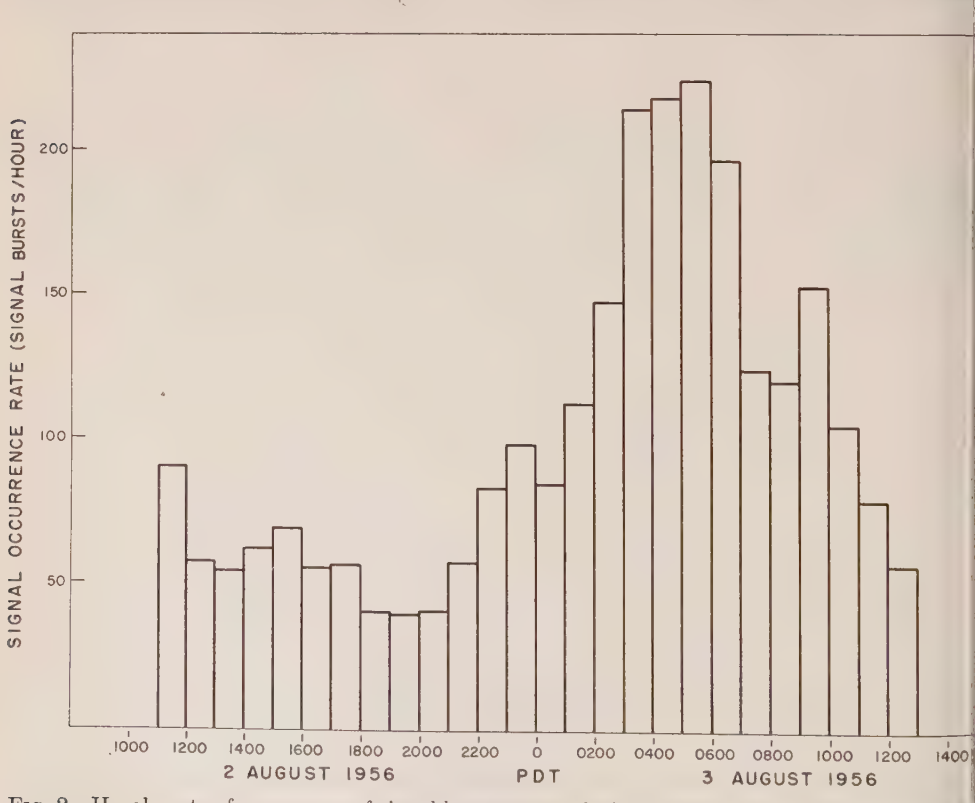

FIG. 2—Hourly rate of occurrence of signal bursts over a 26-hour period during 2-3 August 1956

was high and approximately constant. With the threshold for counting signals chosen as 0.5μv at the terminals of the receiving Yagi antenna, 778 signal bursts were counted in the two-hour period.

Figure 3 is a semilog plot of the number of instances in which the interval between successive signal bursts exceeds the interval shown on the abscissa. In accordance with the discussion culminating in Eq. (1), one should expect this plot to be essentially linear. The data are plotted only for small intervals, as the authors wish to direct attention to the departure of the curve from linearity for intervals of less than about a second. This departure does not mean that the exponential

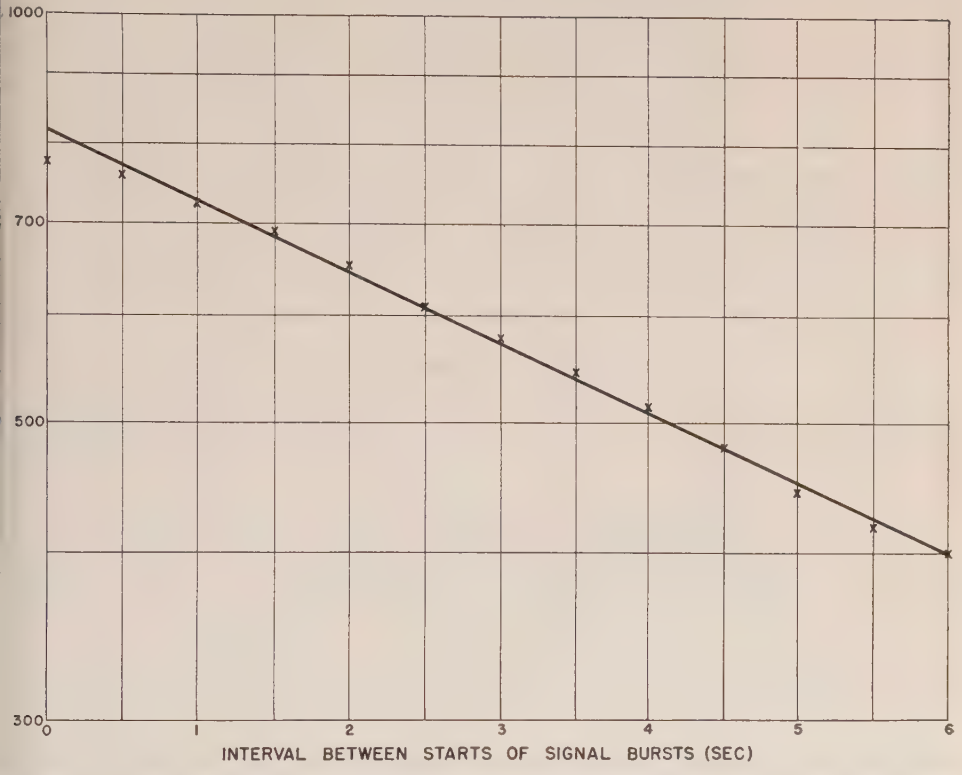

FIG. 3—Distribution of time intervals between signal bursts based on data of 0400–0600 hours on 3 August 1956. Regression line fitted to data to obtain corrected total number of bursts.

distribution fails to hold for small intervals, but rather indicates that, when the interval between signal bursts becomes comparable with the duration of the bursts, a number of signal bursts are missed. Thus, a large burst may hide a small burst occurring a fraction of a second later before the amplitude of the large burst has decayed to the noise level. As a consequence, the total number of signal bursts observed is less than the actual number which occurred. A corrected number may be obtained by fitting a regression line to the data by least-squares technique and extending this line back to a new intercept. The total number of intervals preceding the signal bursts is thus corrected from 778 to 825.

On the basis of the total number of intervals in the two-hour period, 825, the average interval between the starts of successive signal bursts T is 8.73 sec. The probability that a signal will not occur in time t as given by Eq. (1) becomes $Q = e^{-t/8.73}$ and is plotted as a line in Figure 4. The experimental points indicate

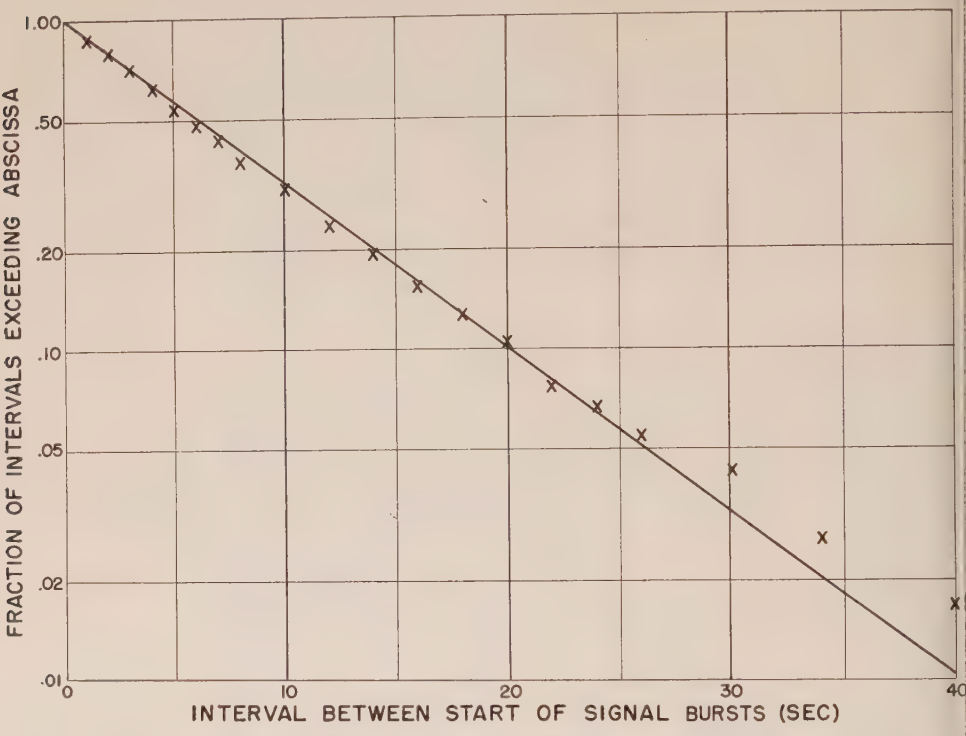

FIG. 4—Comparison of observed with expected normalized distribution of time intervals between signal bursts—based on data of 0400–0600 hours on 3 August 1956.

the fraction of observed intervals between the starts of successive signal spikes which exceed the interval shown on the abscissa. The experimental points follow closely the theoretical line based on random distribution of the occurrence of meteors, except for long intervals. Here the number of intervals is so few that the departure from the theoretical line is not statistically significant.

A somewhat more critical test of the random distribution is afforded by the plot of Eq. (4) and the corresponding experimental data. Again with $N = 825$ and $T = 8.73$ sec, Eq. (4) becomes

$$n(t)\Delta t = \frac{825}{8.73} e^{-t/8.73} \Delta t \quad \ldots\ldots\ldots\ldots\ldots\ldots\ldots\ldots (5)$$

and is plotted as a line in Figure 5. The experimentally observed numbers of intervals of value given by the abscissa are plotted as a histogram. One observes general agreement between experimental counts and the values calculated on the basis of random occurrence of signal bursts, except for the number of intervals under one second and except for large intervals. As explained earlier, the actua

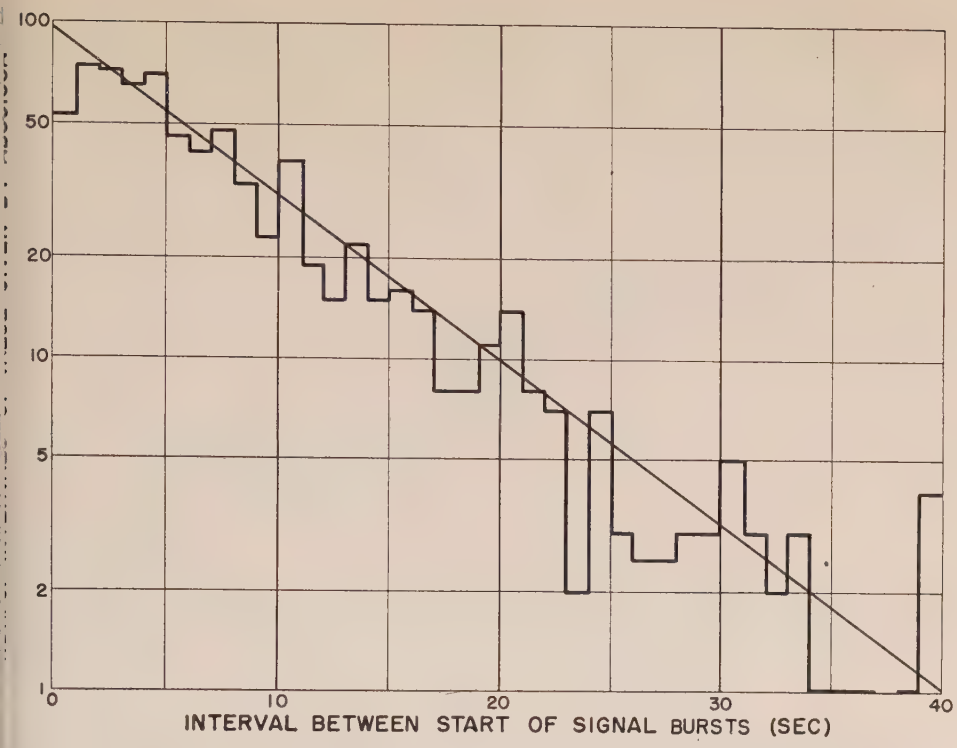

FIG. 5—Comparison of observed with expected frequency of time intervals between starts of signal bursts based on data of 0400–0600 hours on 3 August 1956.

umber of observed intervals under one second is less than that calculated, because, hen the interval between signal bursts is comparable with the duration of the ursts, some signals are missed and the count of short intervals is less than the rue count. For large intervals, the actual number of intervals is small and the eviations of the observed number from the calculated number is not statistically gnificant.

)ate of 6 November 1956

During 0500-0700 hours on 6 November 1956, the rate of occurrence of signal ursts was approximately constant. With the threshold for counting signals chosen s 0.5 μv at the terminals of the receiving Yagi antenna, 446 signal bursts were ounted in the two-hour period.

For 446 intervals and a usable time on the record of 6,829 seconds, the average iterval between the starts of successive signal bursts is 15.31 seconds. Correspondig to these values, Eq. (4) becomes

$$n(t)\Delta t = \frac{446}{15.31} e^{-t/15.31} \Delta t \quad \ldots\ldots\ldots\ldots\ldots\ldots\ldots\ldots (6)$$

nd is plotted as a line in Figure 6. The experimentally observed numbers of itervals of value given by the abscissa are plotted as a histogram.

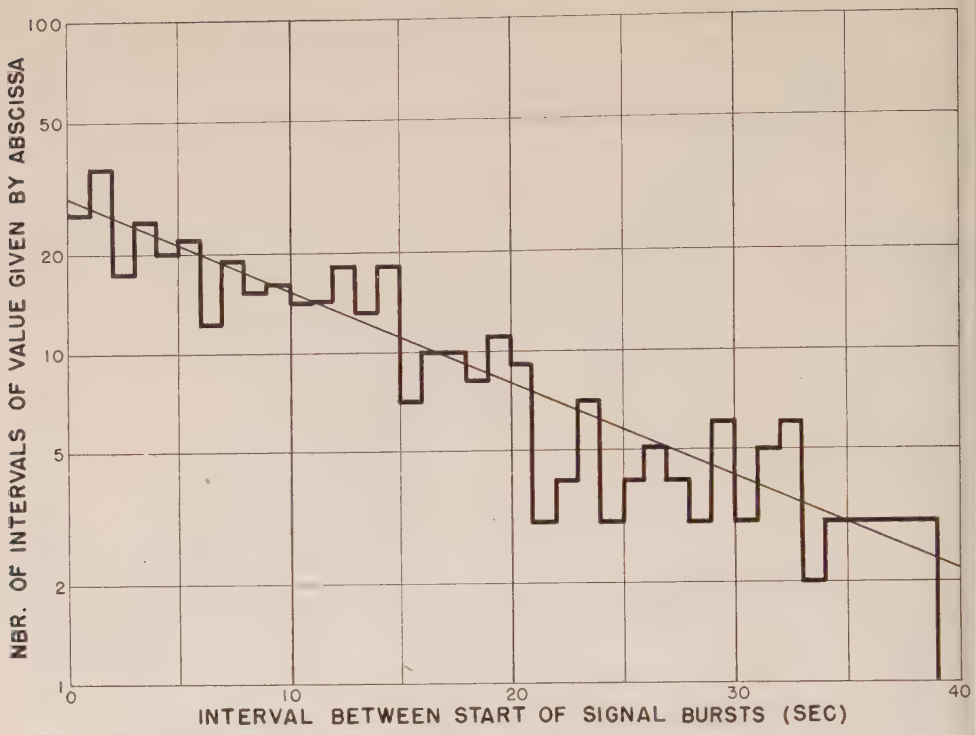

FIG. 6—Comparison of observed with expected frequency of time intervals between starts of signal bursts based on data of 0500–0700 hours on 6 November 1956.

Again there is general agreement between experimental counts and the values expected if the signal bursts occur at random.

V. TEST FOR GROUPING OF BURSTS

Following Briggs [4], one may test for the grouping of bursts by counting the number of pairs of successive equal time intervals between three equally spaced bursts, and comparing the number counted with that expected if the bursts occurred at random. Assume that a second interval will be counted equal to the first if it differs in length from the first interval by not more than $\pm\delta t$. The probability that a burst will occur in the interval t to $t + \Delta t$ is given by Eq. (3) as $(1/T)e^{-t/T}dt$, where T is the average interval between successive signal bursts. The probability that an interval t will be followed by a second interval in the time range $t - \delta t$ to $t + \delta t$ is given by the product

$$\left(\frac{1}{T}e^{-t/T}\,dt\right)\left(\frac{1}{T}e^{-t/T}2\delta t\right) \qquad (7)$$

Provided $\delta t \ll T$, the probability that two successive intervals are equal to each other, for all lengths of the first interval, is given by the integral of Eq. (7) over all values of t from 0 to ∞. Thus, for the intervals preceding the N bursts of the sample, the expected number of pairs of equal intervals and hence the number of

three equally spaced bursts is $N\ \delta t/T$. Table 1 compares the expected and observed number of pairs of equal intervals for two sets of observations and for three different values of δt.

TABLE 1—*Comparison of expected and observed number of pairs of equal intervals*

Hours	Date	N	T	δt	Number of pairs	
					Expected	Observed
	1956		*sec*	*sec*		
0400–0600	3 August	778	9.25	0.05	4.2	4
				0.15	12.6	13
				0.25	21.0	27
0500–0700	6 November	446	15.31	0.05	1.5	2
				0.15	4.4	4
				0.25	7.3	8

A comparison of the last two columns of Table 1 reveals substantial agreement between the observed number of pairs of equal intervals and the number expected if the bursts occurred at random. Thus, for the two samples of data examined here, each of two-hour length, the trains of three equally spaced bursts occur essentially at the rate expected.

VI. CONCLUSION

The distribution of intervals between the starts of signal bursts received over a vhf forward-scatter path compares favorably with the distribution of intervals calculated on the basis that the bursts occur at random. Trains of three equally spaced bursts occur at substantially the rate expected. The comparisons were carried out for the two periods of 0400-0600 hours on 3 August 1956 and 0500-0700 hours on 6 November 1956. For the samples of data analyzed, the occurrence of bursts of vhf signals is consistent with that expected if the bursts are produced by the scattered radiation from the ionized trails of meteors which enter the upper atmosphere at random.

VII. ACKNOWLEDGMENT

The authors are grateful to members of the Stanford University Radio Propagation Group, both for maintaining the transmissions necessary for the measurements and for their valuable comments.

References

[1] O. G. Villard, Jr., A. M. Peterson, L. A. Manning, and V. R. Eshleman, J. Geophys. Res., **58**, 83 (1953).
[2] P. A. Forsyth and E. L. Vogan, Can. J. Phys., **33**, 176 (1955).
[3] G. A. Isted, Marconi Review, **17**, 37 (1954).
[4] B. H. Briggs, J. Atmos. Terr. Phys., **8**, 171 (1956).
[5] L. R. Wylie and H. T. Castillo, Ohio J. Sci., **6**, 339 (1956).

GEOMAGNETIC DISTURBANCES ASSOCIATED WITH SOLAR FLARES WITH MAJOR PREMAXIMUM BURSTS AT RADIO FREQUENCIES $\leq$ 200 MC/S

By Helen W. Dodson and E. Ruth Hedeman

McMath-Hulbert Observatory of the University of Michigan, Pontiac 4, Michigan

(Received August 12, 1957)

ABSTRACT

Study of world-wide solar and geomagnetic data has shown a close association between flares with "major early bursts" at radio frequencies $\leq$ 200 Mc/s and sudden-commencement geomagnetic storms. Intercomparison of Hα and radio-frequency solar data for January 1949 to April 1956 has given positive evidence for such "major early bursts" with 115 of the approximately 3,000 flares observed during the 7-1/3 year interval. This type of radio-frequency event is, therefore, relatively rare. Geomagnetic storms were reported by at least one observatory within less than five days after the occurrence of 92 per cent of the 115 flares with "major early bursts." The average time interval between the flare and the start of the subsequent geomagnetic storm was slightly less than $2\frac{1}{2}$ days. Average superposed values of *Kp* and *Ap* were high on days 2, 3, and 4 after flares of importance 3 with "major early bursts," but this was not the case after flares of importance 3 when emission at frequencies $\leq$ 200 Mc/s was not present or occurred only in the post maximum phase of the flare.

The possibility of a "central meridian effect" has been investigated. The average, superposed values of *Kp* for the disk passage of the 77 regions concerned is very similar to that "predicted" for disk passage of active regions with storm-producing flares in random positions, and with double frequency and/or effectiveness for the five days nearest central meridian passage. The latter assumptions are in accordance with observations.

The geomagnetic effectiveness of each of the 115 flares with "major early bursts" was re-evaluated on the basis of all available world-wide solar data. Sixty-eight of the 115 flares were considered to be the most probable single solar cause of 68 geomagnetic storms. Study of these 68 cases of well-associated flares and geomagnetic storms indicated that storm-producing flares occurred at all meridian distances and in all importance categories. However, centrality of position and high flare importance favored greater severity in the subsequent storm. Again, the average time interval between flare and start of storm was 56 hours.

1. INTRODUCTION

During an earlier study of Cornell records of solar radiation at 200 Mc/s [see 1 of "References" at end of paper], it was observed that flares with sudden bursts of great magnitude during the *premaximum* phase of the flare were frequently followed within one to four days by sudden-commencement geomagnetic storms. Furthermore, certain important flares (importance 2 + or 3) without such "major early bursts" at 200 Mc/s were not followed by geomagnetic disturbances. The term "major early burst" (MEB) will be used in this paper to indicate a sudden, great increase in flux that begins at or close to the time of start of the Hα flare, lasts for at least several minutes, and is of such magnitude that it is generally off scale on the Cornell records. It is an early or "first part" of the flare-associated radio-frequency event and occurs primarily during the premaximum phase of the Hα flare. The "major early burst" may or may not be followed by a second or "late" radio-frequency event during the postmaximum phase of the Hα flare [1].

According to current thinking, emission at high radio frequencies provides information about the low level portions of the solar atmosphere, while low-frequency radiation indicates phenomena in the upper atmospheric levels and far out in the corona. It is possible, therefore, that the occurrence of a "major early burst" at radio frequencies of 200 Mc/s or less marks the passage of fast moving particles (or circumstances that permit their passage) through relatively high levels of the solar atmosphere. If these concepts are correct, the occurrence or absence of "major early bursts" may help to distinguish between flares that are associated with the ejection and successful escape of storm-producing particles, and flares without such ejections.

2. SOURCES OF FLARES, RADIO-FREQUENCY, AND GEOMAGNETIC DATA

In order to test the hypothesis that "major early bursts" at frequencies $\leq$ 200 Mc/s indicate the ejection from the sun of high velocity particles which may later impinge upon the earth and cause geomagnetic disturbances, a list was prepared of all flares with "major early bursts" known to the authors to have occurred during the time interval of January 1949 to April 1956. Flare information was compiled from the photographic records of the McMath-Hulbert Observatory, from the monthly reports of the Central Radio Propagation Laboratory of the U. S. National Bureau of Standards, and from the world-wide data in the Quarterly Bulletin of Solar Activity. Evidence for the radio-frequency phenomenon was secured by direct examination of the Cornell 200-Mc/s records, January 1949 to April 1956, and Cavendish 81-Mc/s records, January 1949 to August 1955. In addition, certain cases were deduced, sometimes with less certainty, from the radio-frequency data reported in the Quarterly Bulletin of Solar Activity, January 1949 to March 1955. No event was included in the list unless there was a known flare or ionospheric disturbance that provided reasonably good, positive evidence that the radio-frequency burst occurred during the premaximum phase of a flare.

The list includes 115 cases (see Appendix 1). For 112 of these, flares were observed by us or were reported in the documents referred to above. For three cases, we used ionospheric data to infer the approximate starting times of the

lares. For 77 of the "major early bursts," we have seen one or more of the original r published records at 200, 81, 97, or 18 Mc/s. The remaining 38 cases were nferred from the magnitude and time relationships of the radio-frequency data n the Quarterly Bulletin.

The Geomagnetic indices Kp and Ap, and the "musical diagrams" prepared y J. Bartels at the Geophysical Institute of Göttingen, have been used as measures f geomagnetic disturbance. In addition, reports from separate geomagnetic bservatories, published in the Journal of Geophysical Research, have been used s sources of information for starting times and types of geomagnetic storms. Constant reference was also made to the geomagnetic storm data in the Greenwich Observatory Publication (1955), "Sunspot and Geomagnetic-Storm Data," prepared under the direction of H. W. Newton [2]. For each of the 115 cases, the ime interval, ΔT, between the start of the flare with "major early burst" and hat of the next *reported* geomagnetic storm has been computed. Each storm in uestion has been designated as either sudden commencement or gradual. When vorld-wide information is considered, the storms do not fall unambiguously into hese two categories. In the moot cases, the designation for purposes of this study vas made on the basis of the "majority" report. Finally, each storm was classified s a non-recurrent storm, a "possibly" recurrent storm, or a member of a well-stablished 27-day recurrent sequence.

According to the purely statistical part of the study, the 115 flares with "major arly bursts" were followed by 81 separate geomagnetic storms. Of these, 43 are lassified as widespread "sudden-commencement" storms, and for 66 storms, or 1 per cent of the total, one or more geomagnetic stations reported the sudden-ommencement phenomenon. Only three of the storms were members of well-stablished 27-day recurrent series, and even these were "sudden-commencement vents."

Preliminary reports of this work have already been distributed to the IGY Regional Warning Centers through the CSAGI Reporter for World Days and Communications (A. H. Shapley) as part of the preparation for the International Geophysical Year. The reports are known as Circular Letters, RWC-2 (1956) nd RWC-26 (1957).

3. STATISTICAL STUDY OF GEOMAGNETIC DISTURBANCES FOLLOWING ALL KNOWN FLARES (115) WITH "MAJOR EARLY BURSTS"

a) Average values of Ap and Kp following flares with "major early bursts"

The association between solar phenomena and subsequent geomagnetic ffects is frequently demonstrated by increases in the averaged, superposed values f the geomagnetic indices Kp or Ap following the solar event in question. These lata for the 115 flares with "major early bursts" are given in Table 1 and Figure 1 top). For both Ap and Kp, the averaged, superposed values show a large in-rease, starting the second day after the occurrence of a flare with "major early urst." Maximum is on the third day, and the averages are still well above the re-flare level even on the eighth day.

TABLE 1—*Average geomagnetic indices, Ap and Kp, for days before and after all flares known to have had "major early bursts" at radio frequencies* $\leq$ 200 *Mc/s, January* 1949 *to April* 1956 (115 *cases*)

Days before and after flare	Average *Ap*			Average *Kp*		
	All cases (115)	Most imp. flares (21)	Least imp. flares (94)	All cases (115)	Most imp. flares (21)	Least imp. flares (94)
−7	17.3	14.1	18.0	21.0	18.8	21.5
6	15.2	11.7	15.9	19.7	17.4	20.3
5	14.7	13.2	15.1	18.9	18.6	19.0
4	13.9	11.4	14.4	18.8	17.3	19.1
3	14.0	11.7	14.5	19.2	17.6	19.6
2	15.1	12.8	15.6	19.9	19.6	20.0
−1	15.9	19.4	15.1	19.4	21.6	18.9
0	17.9	16.7	18.2	21.1	20.1	21.3
+1	17.4	17.6	17.3	20.7	20.6	20.7
2	25.0	37.8	22.1	22.9	27.0	22.0
3	29.2	34.2	28.1	25.8	28.7	25.1
4	27.0	27.3	26.9	24.4	25.8	24.1
5	23.5	17.3	24.9	23.8	21.5	24.3
6	22.8	18.2	23.9	24.2	21.7	24.8
7	20.0	16.3	20.9	22.0	19.9	22.5
+8	21.2	19.7	21.5	21.8	21.0	22.0

In order to examine the relationship between the importance of the Hα flares and the severity of the subsequent geomagnetic disturbances, the 115 cases have been divided into two groups. The first group contains the 21 most "important" flares in the study, namely, the 14 flares generally classified as of importance 3, and the seven additional flares for which at least one observer gave an estimate of importance 3. The remaining 94 cases include 61 flares of importance 1 and 1+, and 26 flares of importance 2. Table 1 and the graphs at the bottom of Figure 1 show that, on the average, the more important flares were followed by the more severe geomagnetic storms, and that these disturbances reached their maximum earlier and were concluded sooner than was the case for geomagnetic disturbances following the less important flares.

(*b*) *Time interval,* ΔT*, between flare and start of geomagnetic storm*

The assembled data show that for 29 per cent of the 115 flares with "major early bursts" geomagnetic storms were reported by at least one observatory within a time interval of less than 5 days. The time intervals between flare and start of storm are smoothly distributed about the average value of $2\frac{1}{2}$ days. See Table 2 and Figure 2. There were nine cases with $\Delta T > 5$ days. These intervals are so long that the flares in question are considered "failures" insofar as their association with a subsequent geomagnetic storm is concerned.

For comparison with the above data, our investigation was extended to all flares reported in the Quarterly Bulletin between January 1949 and April 1956,

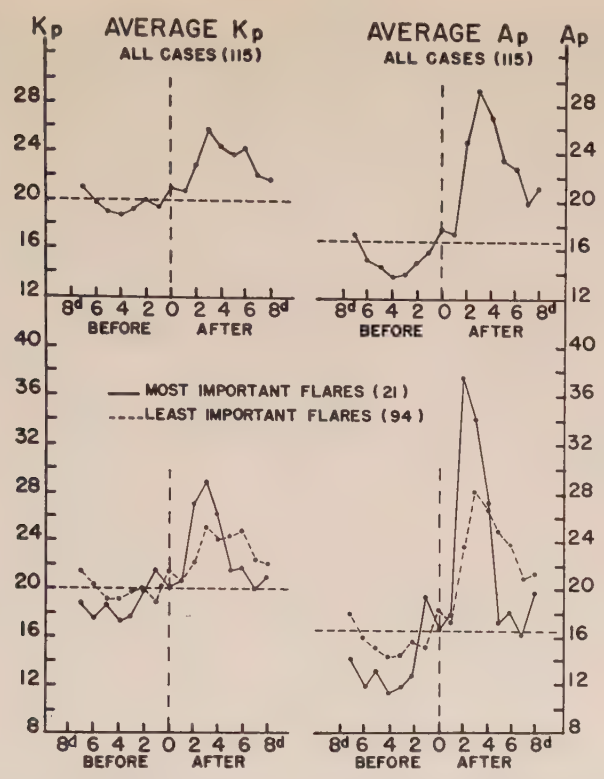

IG. 1—Average superposed values of *Kp* and *Ap* for 8 days before and after the 115 flares with major early bursts" at frequencies $\leq$ 200 Mc/s, January 1949 to April 1956. Dotted horizontal nes show average values of *Kp* and *Ap*, respectively, for the time interval studied, January 1949 to April 1956, inclusive.

TABLE 2—*Relation between importance of flare and* ΔT *for* 115 *flares in statistical study*

Importance of flare	Number		Average time interval between flare and start of geomagnetic storm	
	All cases	"Failures"	All cases	"Failures" excluded
3	14	0	$2^d5^h = 53^h$	$2^d5^h = 53^h$
2	33	5	$3^d0^h = 72^h$	$2^d7^h = 55^h$
1	61	4	$2^d22^h = 70^h$	$2^d15^h = 63^h$
Total	108*	9	$2^d21^h = 69^h$	$2^d11^h = 59^h$

*Excludes three cases with ionospheric data only; one flare for which importance is not nown; three cases that occurred during a geomagnetic storm and ΔT not determined.

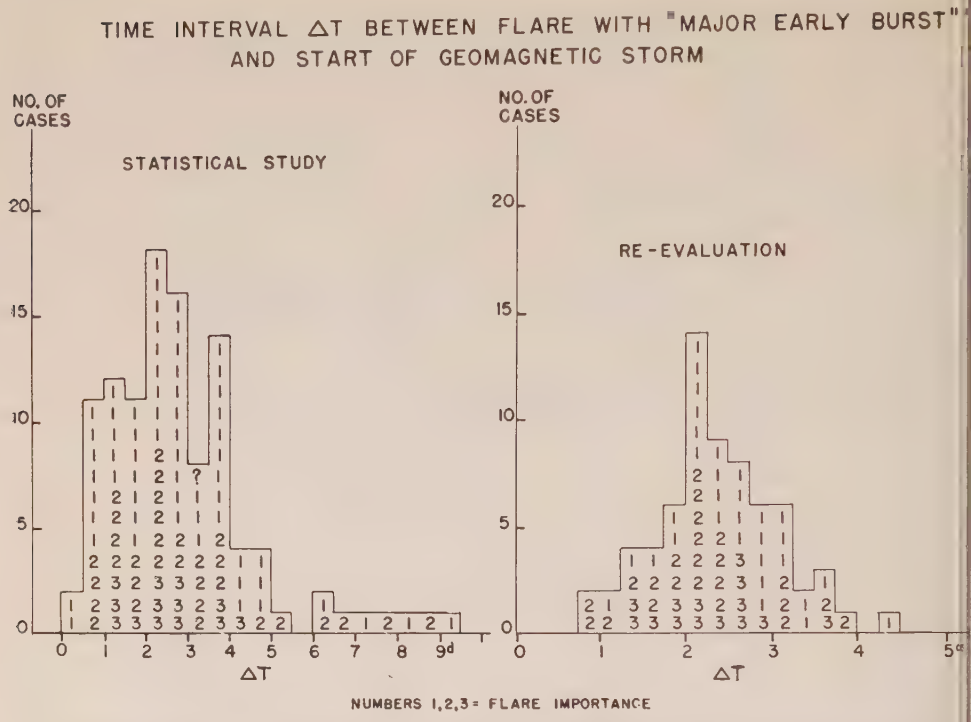

FIG. 2—Time interval ΔT between flare with "major early burst" and start of geomagnetic storm

without regard to radio-frequency emission. It showed that during this interval only 76 per cent of all flares were followed by onset of storms in less than five days. The frequency and distribution of geomagnetic storms were such that a mere chance phenomenon should have shown a similar association with geomagnetic storms in 65 per cent of the cases. See Table 3. The above calculations were carried out in units of a whole day (differences in calendar dates) rather than in the exact time interval in hours between starts of flares and storms, as had been done for the 115 flares with "major early bursts." The less exact calculation for the 11 MEB flares gives 93 per cent rather than the aforementioned 92 per cent. See Table 3.

There is limited evidence that high flare importance favors a slightly shorter than average time interval between the occurrence of the flare and the reported start of the geomagnetic storm. See Table 2 and Figure 2. For flares of importance 1, the average ΔT was 63 hours, but for flares of importance 2 and 3 the average was 54 hours. This difference is consistent with the difference in times of maximum Kp or Ap for the groups of more and less important flares, as shown in Figure 1.

According to the present study, evidence for a relationship between ΔT and the position of the flares on the solar disk is neither consistent nor convincing. See Table 4.

(c) *Disk distribution of flares with "major early bursts"*

The positions of the 112 flares known to have been associated with "major early bursts" are shown graphically in Figure 3. The distribution is similar to

TABLE 3—*Time interval Δt between date of (A) "MEB" flares, (B) all flares, (C) all calendar days (chance), and date of start of next geomagnetic storm for interval of January 1949 to April 1956*

Δt	(A)			(B)			(C)			Difference in percentage distribution of Δt		
	"MEB" flares			All flares			Calendar days			"MEB" and all flares	"MEB" flares and chance	All flares and chance
	No.	%	Σ%	No.	%	Σ%	No.	%	Σ%	(A - B)	(A - C)	(B - C)
0*	16	13.9	14	557	17.6	18	378	14.2	14	−3.7	−0.3	+3.4
1	25	21.7	36	515	16.3	34	357	13.4	28	+5.4	+8.3	+2.9
2	29	25.2	61	397	12.6	47	314	11.8	39	+12.6	+13.4	+0.8
3	19	16.5	77	398	12.6	59	272	10.2	50	+3.9	+6.3	+2.4
4	12	10.4	88	284	9.0	68	229	8.6	58	+1.4	+1.8	+0.4
5	6	5.2	93	247	7.8	76	192	7.2	65	−2.6	−2.0	+0.6
6	1	0.9	94	155	4.9	81	156	5.9	71	−4.0	−5.0	−1.0
7	1	0.9	95	134	4.2	85	129	4.8	76	−3.3	−3.9	−0.6
8	5	4.3	99	88	2.8	88	103	3.9	80	+1.5	+0.4	−1.1
9	..	....	..	66	2.1	90	92	3.5	84	−2.1	−3.5	−1.4
10	..	....	..	49	1.5	91	75	2.8	86	−1.5	−2.8	−1.3
11	1	0.9	100	58	1.8	93	56	2.1	88	−0.9	−1.2	−0.3
12				37	1.2	94	45	1.7	90	−1.2	−1.7	−0.5
13				39	1.2	96	38	1.4	92	−1.2	−1.4	−0.2
14				25	0.8	..	31	1.2	93	−0.8	−1.2	−0.4
15				24	0.8	97	27	1.0	94	−0.8	−1.0	−0.2
16				19	0.6	98	23	0.9	95	−0.6	−0.9	−0.3
17				14	0.4	..	19	0.7	..	−0.4	−0.7	−0.3
18				17	0.5	99	14	0.5	96	−0.5	−0.5	0.0
19				14	0.4	..	11	0.4	..	−0.4	−0.4	0.0
20				5	0.2	..	10	0.4	97	−0.2	−0.4	−0.2
21				6	0.2		9	0.3	..	−0.2	−0.3	−0.1
22				6	0.2		6	0.2	..	−0.2	−0.2	0.0
23				3	0.1		6	0.2	..	−0.1	−0.2	−0.1
24				...	....	100	4	0.2	98	....	−0.2	−0.2
25				2	0.1		4	0.2	..	−0.1	−0.2	−0.1
26				1	0.1		4	0.2	..	−0.1	−0.2	−0.1
27				...	....		3	0.1	..	....	−0.1	−0.1
28				2	0.1		3	0.1	..	−0.1	−0.1	0.0
29							3	0.1	..	....	−0.1	−0.1
≥30							52	1.9	100	....	−1.9	−1.9
Total	115	....	...	3162	....	...	2665	....	...	....	....	....

*$\Delta t = 0$ indicates that storm started on same calendar day as flare.

TABLE 4—*Relation between position of flare on solar disk and ΔT for 115 flares in statistical study*

Central meridian distance of flare	Number		Average time interval between flare and start of geomagnetic storm	
	All cases	"Failures"	All cases	"Failures" excluded
0 to 29°	59	5	$3^d0^h = 72^h$	$2^d14^h = 62^h$
30 to 59°	35	3	$2^d17^h = 65^h$	$2^d7^h = 55^h$
60 to 90°	15	1	$2^d16^h = 64^h$	$2^d11^h = 59^h$
Total	109*	9	$2^d21^h = 69^h$	$2^d11^h = 59^h$

*Excludes three cases with ionospheric data only, and three flares that occurred during geomagnetic storm and ΔT not determined.

that of flares in general, with the characteristic diminution in observed number near the solar limb [3]. More flares with "major early bursts" occurred in th

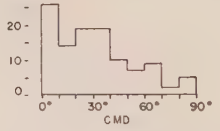

FIG. 3—Disk distribution of 115 flares with "major early bursts"

eastern than in the western hemisphere of the sun. However, an even greate north-south asymmetry exists in the data and casts doubt on the significance o these differences.

On the basis of the present data and assumptions, the flares that were followe by sudden-commencement storms had a higher concentration toward the cente of the solar disk than was the case for flares associated with gradual (but primaril non-recurrent) storms.

4. FLARES OF IMPORTANCE 3 WITH AND WITHOUT "MAJOR EARLY BURSTS"

In order to test further the significance of "major early bursts" as indicators o corpuscular ejection at the time of solar flares, we have made an additional studi of all great flares (importance 3 or 3+ according to at least one observer) betwee January 1949 and April 1956. There are 63 flares in this study, and we hav separated them into three categories: those for which there is reasonably goo evidence for the occurrence of a "major early burst" (25 cases), those definitel known *not* to have had major early bursts (15 cases), and those for which we hav no positive radio-frequency data (23 cases).

The upper section of Figure 4 shows the distribution of time intervals, Δt, between the start of these important flares and the start of the next geomagnetic storm. Eighty-eight per cent of the flares with "major early bursts" were followed by onsets of geomagnetic storms within three days. For the flares of importance

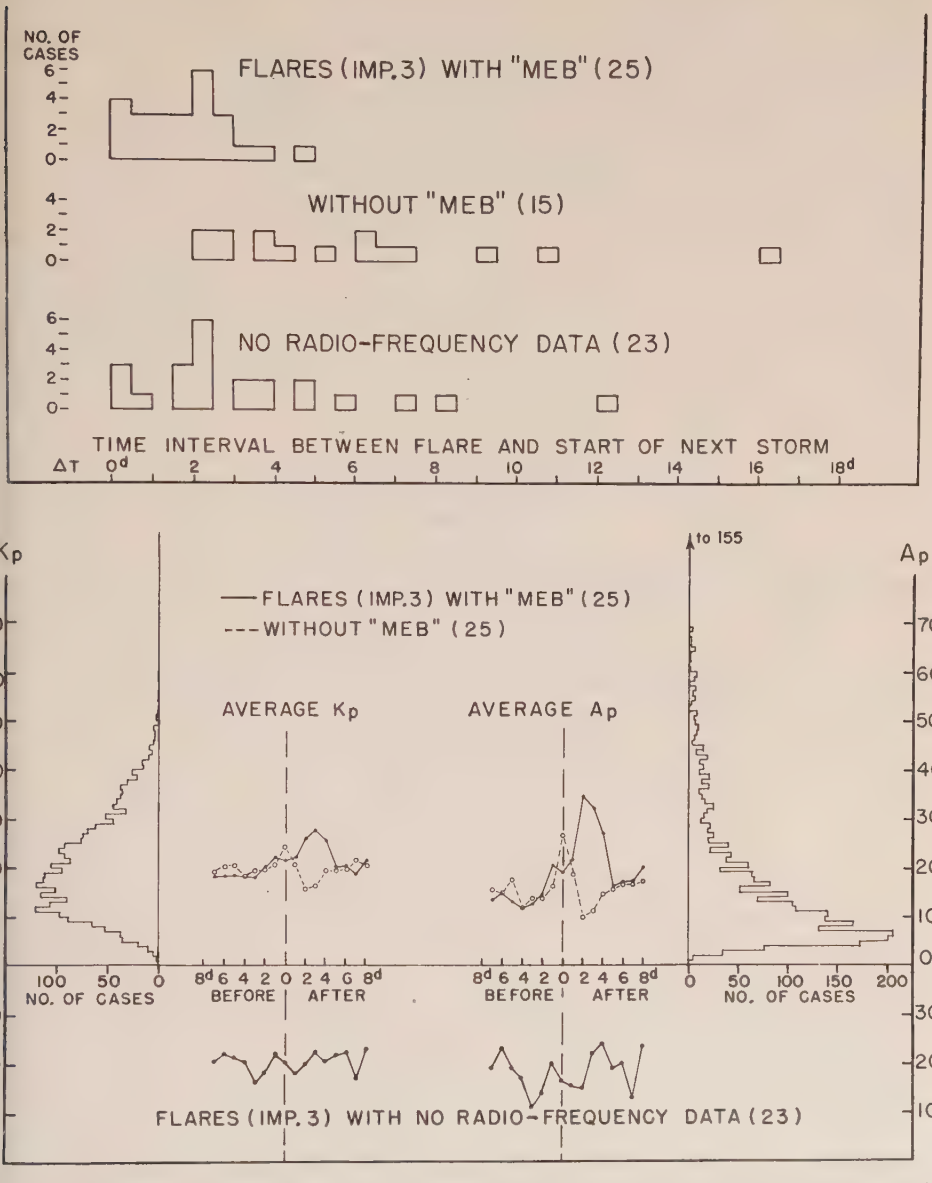

FIG. 4—Relationships between flares of importance 3, January 1949 to April 1956, and geomagnetic disturbances. *Upper section:* Time intervals between start of flares and onset of next geomagnetic storm. *Lower section:* Average superimposed values of Kp and Ap for eight days before and after flares of importance 3, and frequency distribution of the geomagnetic indices for interval studied, January 1949 to April 1956.

3 known *not* to have had this type of radio-frequency emission, the distributio of Δt is very different, with no reported geomagnetic storm within two days.

Average values of Kp and Ap before and after the flares in these three categorie also are given in Figure 4. The average values of Kp and Ap are high on days 3, and 4 after the occurrence of importance 3 flares with "major early bursts." They fall to a minimum on days 2 and 3 following the flares known not to hav had such radio-frequency accompaniments, and show primarily a scatter for th cases for which radio-frequency information is not available.

The minimum in Kp and Ap following flares of importance 3 without "majo early bursts" is similar to the diminution in geomagnetic activity after centra meridian passage of "Q-sunspot groups" and/or flares in such regions as show in the work of Denisse and Simon [4, 5]. The drop may be merely a "numbe effect" resulting from the sorting and separation at day "zero" of the storm-producing and non-storm-producing phenomena. In order to assist the reader i interpretation of the Kp and Ap curves, we give the frequency distributions o these indices for the interval studied, January 1949 to April 1956. These distr butions show that the minima referred to above, although low, drop only to th modal values of the geomagnetic indices.

The relatively high values of Kp and Ap on days -1 and 0 reflect the fa that great flares and great geomagnetic storms are not purely random phenomen but often occur repeatedly throughout the transit across the solar disk of certai great centers of activity. As a result, there is much overlapping of data, bot solar and terrestrial, and average values of geomagnetic indices can be misleadin when the number of cases is necessarily small. For example, in Figure 4, the hig values of Kp and Ap on day 0 for flares of importance 3 without "major ear bursts" should not be interpreted as evidence for a strong† geomagnetic effe coincident with the occurrence of great flares. The high values here in questio stem from geomagnetic storms already in progress before the flares of importan 3 under consideration took place.

5. COMPARISON WITH STUDIES BY DENISSE AND SIMON

Studies by Denisse [4] and Simon [5] have already shown that solar radiatio at radio frequencies is very helpful in improving the association between observe solar phenomena and geomagnetic disturbances. Their work lays stress upon hig radio flux with duration of hours or days (radio emission of the noise-storm type whereas the present study is concerned with the presence or absence of ver intense bursts with duration of the order of minutes that occur in the premaximu phase of certain flares. The two radio-frequency events are not mutually exclusiv phenomena, since large increases in flux or onsets of noise storms often occ during the postmaximum phase of flares, with or without "major early burst [1]. One of the most successful of the associations between solar phenomena an geomagnetic disturbances in Simon's studies [5] is shown by the average values Kp before and after the 27 flares of importance 3 or 3+ observed both in "radi

†"Solar flare effects" or crochets are of such small magnitude and short duration that th do not influence significantly the daily values of Ap or Kp.

oisy spots" and on "radio noisy days" during the years 1947 to 1951. The curve nowing this association is reproduced in Figure 5, where it can be compared irectly with a similar curve for the 25 flares of importance 3 with major early ursts, January 1949 to April 1956. The principal difference lies in the very broad

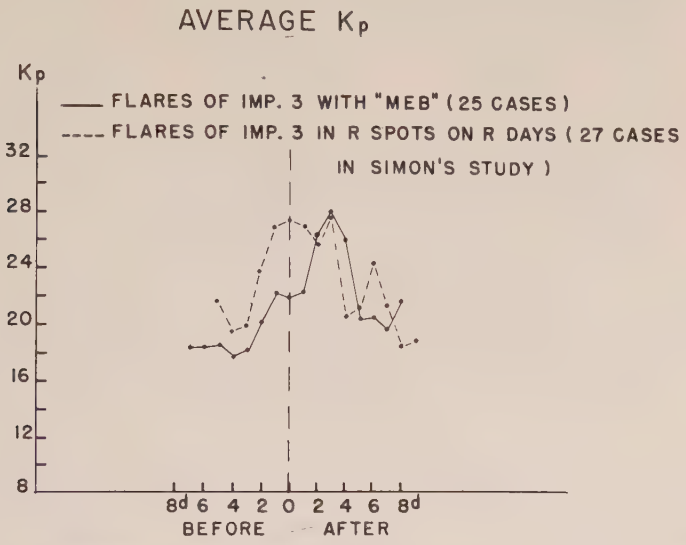

IG. 5—Average superposed values of *Kp* for 8 days before and after flares of importance 3 with major early bursts" compared to similar data for flares of importance 3 in "radio noisy spots" on "radio noisy days"

aximum that extends for several days on either side of day 0 in Simon's graph, nstead of the sharp maximum that follows the flare event in the present study. It nould be remembered that the two curves refer to somewhat different times in ne solar cycle and the average values of *Kp* can be greatly confused by multiple olar events.

6. TEST FOR "CENTRAL MERIDIAN EFFECT"

In order to explore the possibility of a "central meridian effect" as suggested y the work of several investigators (Denisse, Simon, Wood), we have formed ne averaged, superposed values of *Kp* for central meridian passage of the 77 ctive regions in which the 115 flares with "major early bursts" occurred. The verage values of *Kp* so formed are unsymmetrical with respect to the time of entral meridian passage. They rise to a broad maximum after central meridian assage and remain above normal through at least the 12th day. See Figure 6.

There is striking similarity between these average values and a "predicted" urve showing average values of *Kp* computed for central meridian passage of ctive regions in which storm-producing flares occur at all meridian distances. See dashed curve in Figure 6.) In deriving the "predicted" curve, it was assumed nat on the average, during the five days nearest to central meridian passage, torm-producing flares are twice as frequent as during the eight more limbward

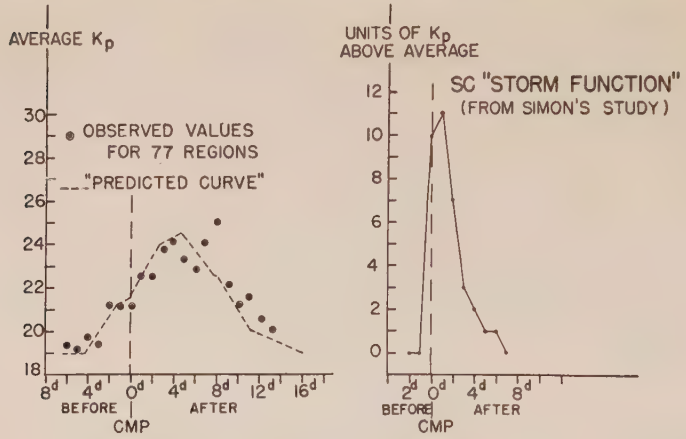

FIG. 6—Comparison of "predicted" curve of Kp with observed values of Kp for central meridian passage of the 77 active regions known to have had flares with "major early bursts," January 1949 to April 1956. *Note*: "Predicted curve" is shown for an average lag of 2½ days between flare and start of geomagnetic storm and for double frequency and/or effectiveness for flares on the five days nearest central meridian passage.

days. This represents a first approximation to the observed disk distribution of flares in general [3] and to the distribution of the 115 flares with "major early bursts" in this study (see Fig. 3). The storm function, or increase in Kp for the storm-producing flares, was based on the average sc storm as derived by Simon [5], with 19 as the average undisturbed value of Kp and an increase of 11 units in Kp for the maximum disturbance. It should be noted that the assumed double frequency of storm-producing flares within 35° of the central meridian in this computation is exactly equivalent to assuming a uniform flare distribution, but with a storm increase of 22 units in Kp instead of 11 for the central flares. Details of the computation are shown in Appendix 2.

The marked similarity between the observed and predicted values of Kp in the above curves for central meridian passage indicates that, for the 77 active regions here studied, it is not necessary to postulate a special central meridian effect beyond that implied by a greater "efficacy" and/or greater frequency, of storm-producing flares near the central meridian.

7. RE-EVALUATION OF ASSOCIATION BETWEEN FLARES WITH MAJOR EARLY BURSTS AND SUBSEQUENT GEOMAGNETIC STORMS

Finally, we have tried to evaluate the geomagnetic effectiveness of each of the 115 flares known to have been accompanied by a "major early burst." In order to do this, we have tried to decide, on the basis of all available world-wide solar data, the most probable single solar cause of each of the 81 geomagnetic storms statistically associated with the 115 flares in the foregoing study. In this work, we felt it wise, in a small number of cases, to divide a disturbance that had been reported as a single storm into two storms, on the basis of well-defined and well-separated maxima in the "musical" diagram of the three-hourly K indices [6].

Of the 115 flares with "major early bursts" in the statistical study, 68 were

considered to be the most probable, single solar cause of 68 geomagnetic storms. In addition, 28 more of the flares were felt to be "contributors" to these storms or to other storms for which the "most probable cause" was another more important flare without known radio-frequency data. There were seven well-observed cases of flares with major early bursts for which there was no evidence whatsoever of a subsequent geomagnetic disturbance within four days. For the remaining 12 flares, ambiguity in either the flare, radio-frequency, or geomagnetic data made further analysis inadvisable.

TABLE 5—*Relationships between position and importance of 68 Hα flares with "major early bursts" and the time and magnitude of subsequent geomagnetic storms*

	Central meridian distance of flare							
	−75°(*E*)	−45°	−20°	0°	+20°	+45°	+75°(W)	
Flare imp.	*Number of cases*							*Total*
1	4	6	3	10	3	4	1	31
2	1	3	5	4	3	5	2	23
3	2	2	1	2	3	2	2	14
Total	7	11	9	16	9	11	5	68
	Average number of hours between flare and start of storm							
1	62	65	65	60	54	55	67	61
2	54	50	54	58	56	42	56	52
3	49	63	35	61	57	56	48	54
Total	57	61	56	59	56	49	55	56
	Average value of MAXIMUM Kp in storm							
1	28	30	30	32	36	35	27	31
2	44	32	36	38	33	34	27	35
3	33	30	51	47	38	31	36	37
Total	32	31	36	35	35	34	31	34
	Average value of MAXIMUM Ap in storm							
1	24	29	28	39	49	38	21	34
2	64	40	49	65	34	46	26	47
3	32	49	150	113	56	38	62	65
Total	32	36	53	55	46	42	39	45

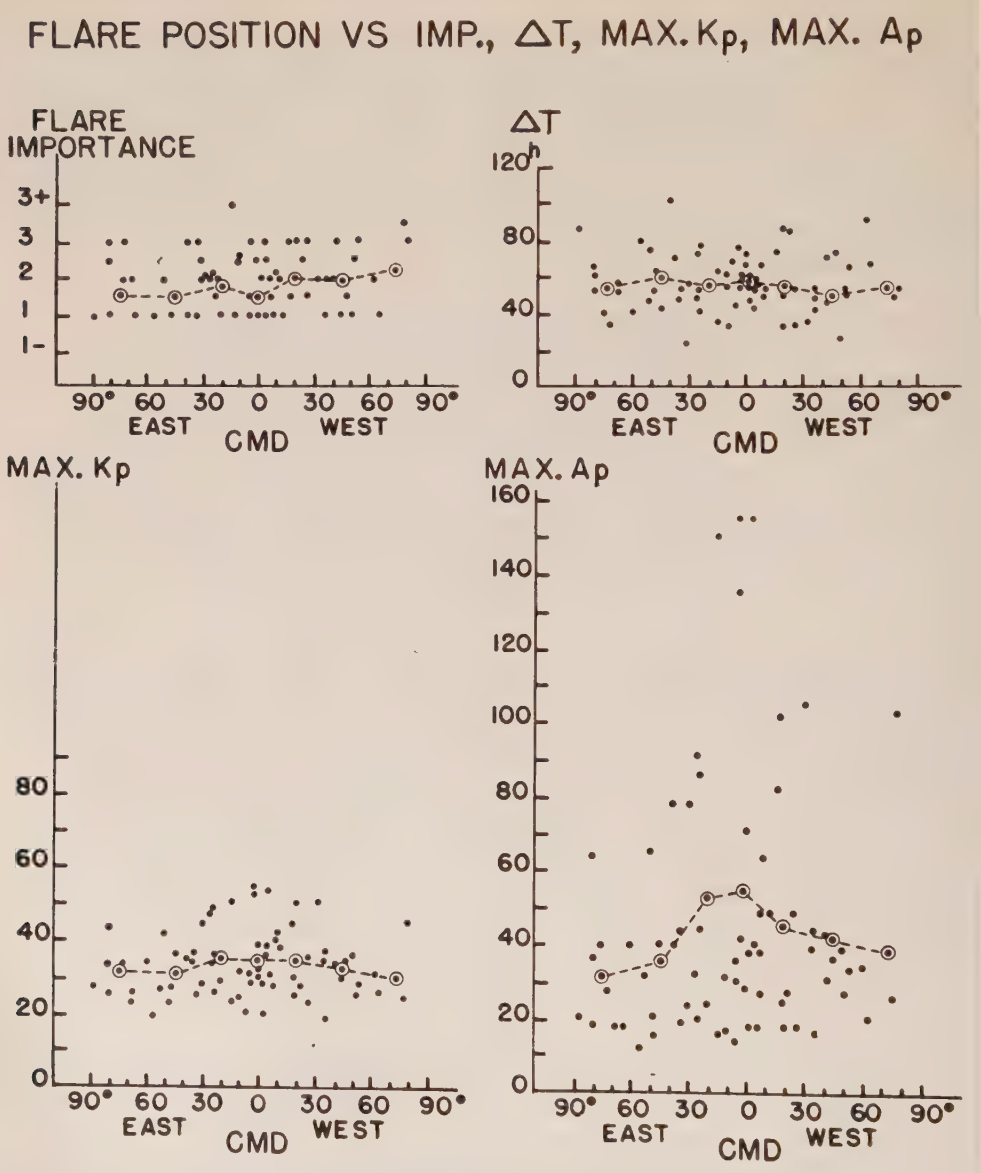

FIG. 7—Flare importance, time interval between flare and start of subsequent storm, and maximum values of Kp and Ap plotted *vs* flare position for 68 well-associated flares and geomagnetic storms, January 1949 to April 1956. *Note*: Circles and dotted lines show average values.

For the 68 cases of well-associated flares and geomagnetic storms, we have sought relationships between flare importance and position, the time interval between flare and start of storm, and the magnitude of the geomagnetic disturbance. The results of this study are presented in Table 5 and Figure 7. The authors regret that they were unable from available data to determine quantitative measures of the "major early bursts" associated with each of the 68 flares.

Study of these 68 most reliable cases again gives an average time interval, ΔT, between flare and start of storm of slightly less than $2\frac{1}{2}$ days. There is no evidence for a dependence of ΔT on the central meridian distance of the flare.

It should be pointed out again that the present study refers exclusively to the declining branch of the solar activity cycle and includes small as well as great storms.

The magnitude of the subsequent geomagnetic storm appears to depend on both the importance and the position of the Hα flare. Storms that followed flares of importance 2 and 3 had higher maximum values of Ap and Kp than storms that followed flares of importance 1. Furthermore, storms that followed flares near the central part of the disk were, on the average, more severe than storms that followed flares closer to the solar limb.

8. CONCLUSIONS

The present study has shown a close association between flares with "major early bursts" and sudden-commencement storms. It has confirmed the facts so often pointed out by Newton [7] that centrality of position and high flare importance play a large part in the probability of the occurrence of a severe geomagnetic storm. However, the average time interval of a little more than two days between flare and start of storm is longer than that usually considered in studies of solar-terrestrial relationships.

The occurrence or non-occurrence of a "major early burst" in the flare-associated radio-frequency event apparently provides assistance in identifying the small number of flares that are the potential causes of non-recurrent, sudden-commencement type geomagnetic disturbances of sufficient severity to be classified as "storms."

On the basis of the present study, it also appears that the number of flares with "major early bursts" is roughly comparable to the number of sudden-commencement and/or non-recurrent geomagnetic storms on the earth. Of the more than 3,000 flares of importance 1 or more between January 1949 and April 1956, only 112 are known to have been accompanied by "major early bursts." The list of such flares is necessarily incomplete, since radio-frequency coverage was relatively limited in 1949 and 1950. Furthermore, lack of flare data has kept us from including in the present study certain radio events that seem obviously of the type here considered. Nevertheless, the study indicates clearly that only small numbers of Hα flares, probably less than 10 per cent, are accompanied by *major*, early bursts at low radio frequencies. During the 7-1/3 year period of this study, 378 geomagnetic storms occurred on the earth; some were reported by a number of geomagnetic stations, others by only one. Of these storms, 150 were clearly members of well-established 27-day recurrent series. The remaining 228 storms constitute disturbances of the type that were probably associated with individual solar flares. The number of reported sporadic geomagnetic storms was thus of the same order of magnitude as the estimated number of flares with "major early bursts" at frequencies $\leq$ 200 Mc/s.

In the future, improved, more detailed geomagnetic data may permit investigators to recognize corpuscular ejections from a larger group of solar flares.

Likewise, more abundant information on "dynamic spectra," polarization, and magnitude of radio-frequency bursts should further improve the recognition and understanding of solar events that are associated with geomagnetic storms on the earth.

9. ACKNOWLEDGMENTS

The authors wish to express their appreciation of Dr. Robert R. McMath's interest in and strong support of this investigation throughout the more than five years in which it has been in progress, and their gratitude to Dr. Orren C. Mohler for his valuable discussion and advice on the many problems encountered during the course of the study. They also acknowledge with pleasure the encouragement given them at all stages of the work by Miss Virginia Lincoln and Mr. A. H. Shapley, of the Central Radio Propagation Laboratory of the National Bureau of Standards.

References

[1] H. W. Dodson, E. R. Hedeman, and L. Owren, Astroph. J., **118**, 169 (1953).
[2] Royal Greenwich Observatory, Sunspot and geomagnetic-storm data derived from Greenwich observations, 1874-1954, prepared by H. W. Newton (1955).
[3] L. Goldberg, H. W. Dodson, and E. A. Müller, Astroph. J., **120**, 83 (1954).
[4] J. F. Denisse, Paris, C.-R. Acad. sci., **232**, 2290 (1951); Ann. Géophys., 8, 55 (1952); Paris, C.-R. Acad. sci., **236**, 1856 (1953).
[5] P. Simon, Ann. Géophys., **12**, 167 (1956); Ann. Astroph., **19**, 122 (1956).
[6] J. Bartels and J. Veldkamp, Planetary magnetic three-hour-range indices *Kp*, Internat. Union Geod. Geophys., Assoc. Terr. Mag. and Aeronomy, Bull. No. 12.
[7] H. W. Newton and W. Jackson, Seventh Report of the Commission for the Study of Solar Terrestrial Relationships (Comm. Mixte, I.A.U., 1950), Paris (1951); p. 107.

APPENDIX 1

Date and reported times of start and maximum for 115 flares with "major early bursts"

Date		Start†		Maximum			Date		Start†		Maximum		
1949		*h*	*m*	*h*	*m*		*1949*		*h*	*m*	*h*	*m*	
Jan.	22	09	44	..	..	*	Oct.	13	<11	18	11	47	*
Jan.	23	01	03	..	..	*	Oct.	23	11	05	..	..	*
Feb.	1	<12	40	..	..	*	Nov.	5	18	27	18	29	?
Feb.	3	11	02	11	06	*C*	Dec.	8	03	11	..	..	*
Feb.	4	13	03	13	06	*C*	Dec.	8	11	36	11	43	*C*
Mar.	9	21	30	21	49	*	Dec.	8	<13	07	13	14	*C*
Mar.	14	<00	37	..	..	*	Dec.	9	12	43	12	50	?
Apr.	27	21	46	21	52	*	*1950*						
Apr.	28	<06	45	..	..	*C*	Jan.	22	<15	01	..	..	*
May	10	20	02	20	11	*	Jan.	30	<11	10	11	23	*
Jun.	4	16	08	16	20	*	Feb.	1	<22	15	..	..	*
Jul.	15	17	29	17	33	*	Feb.	16	00	48	..	..	*C*
Aug.	1	02	14	..	..	*	Feb.	17	<01	50	..	..	*
Aug.	5	00	36	00	40	*C*	Feb.	17	10	20	..	..	*C*
Aug.	5	07	54	08	09	*	Feb.	18	10	25	10	29	*C*
Aug.	30	01	10	..	..	*	Feb.	18	13	44	13	48	*C*
Sep.	5	02	18	..	..	*F*	Feb.	18	15	06	15	11	*C*
Sep.	9	00	15	..	..	*	Feb.	18	22	11	22	31	*C*
Sep.	13	<13	07	13	11	*F*	Feb.	21	23	40	23	46	*
Sep.	24	20	05	20	11	*	Apr.	26	17	50	17	52	*
Oct.	1	<10	12	..	..	*	Apr.	28	<15	03	..	..	*C*
Oct.	3	<03	14	..	..	*	May	5	05	48	06	11	?
Oct.	11	15	14	15	23	*	May	20	18	30	18	40	*

†The reported starting times of associated ionospheric disturbances have also been used to determine the probable starting time of the flare.

* = Most probable single cause of a subsequent geomagnetic storm or disturbance.

C = "Contributor" to a geomagnetic storm or disturbance.

F = Failure.

? = Ambiguity or uncertainty in interpretation of solar or geomagnetic data and therefore omitted from the re-evaluation.

Date and reported times of start and maximum for 115 flares with "major early bursts"—Concluded

Date		Start†		Maximum			Date		Start†		Maximum		
1950		*h*	*m*	*h*	*m*		*1951*		*h*	*m*	*h*	*m*	
May	23	13	55	14	01	*C*	Sep.	14	13	45	13	56	*
May	23	14	57	15	05	*C*	Sep.	15	15	08	15	10	*
May	23	21	55	21	59	*C*	Sep.	17	20	50	21	03	*
Jun.	20	<12	30	12	44	*	Nov.	27	<14	31	..	..	?
Jul.	21	05	18	05	25	*C*	Dec.	21	<11	50	11	56	*C*
Jul.	21	13	11	13	17	*	Dec.	30	15	15	15	22	*C*
Jul.	22	<09	50	09	58	*C*	*1952*						
Jul.	22	15	49	15	52	*	Jan.	2	20	26	20	31	*
Jul.	28	14	15	..	..	*	Feb.	16	<15	55	16	05	*C*?
Aug.	2	15	47	15	54	*F*	Jul.	12	04	43	04	50	?
Aug.	4	22	54	23	38	*	Jul.	12	<06	05	06	10	*F*
Aug.	11	00	34	01	00	?	Jul.	12	14	50	14	55	*F*
Aug.	15	17	48	18	01	*	Jul.	28	<16	35	..	..	*
Aug.	16	<06	34	..	..	*	Sep.	1	(SID 1235)		..	..	*
Sep.	20	03	05	..	..	*	Oct.	6	18	29	18	40	*
1951							Dec.	11	03	13	..	..	*
Jan.	22	16	25	..	..	*	*1953*						
Feb.	17	03	10	..	..	*C*?	Jul.	14	<05	50	05	51	?
Feb.	19	<14	10	14	10	*	Jul.	15	19	16	19	25	*F*
Feb.	25	<14	00	14	33	*	Aug.	11	15	36	15	42	*C*
Mar.	2	(SID 2058)		..	..	*	Oct.	14	<03	30	..	..	*C*
Apr.	2	17	06	17	18	*C*	Oct.	14	<09	46	..	..	*
Apr.	14	15	20	15	25	*C*	*1954*						
Apr.	26	<10	59	..	..	?	Aug.	26	<04	43	..	..	*?
May	23	<00	25	..	..	?	*1955*						
May	23	<01	08	01	25	*	Jan.	16	<21	30	..	..	*
Jun.	9	23	27	23	32	*C*	Jan.	30	17	40	17	49	?
Jun.	13	05	30	06	18	*	Jun.	18	19	05	..	..	*
Jun.	22	<04	05	..	..	*	Nov.	15	(SID 1735)		..	..	*
Jun.	28	20	24	20	55	*	*1956*						
Jul.	15	23	16	23	19	*	Jan.	23	14	44	14	49	*
Jul.	28	02	30	..	..	*	Feb.	13	14	38	14	50	?
Aug.	11	<02	11	..	..	*	Feb.	16	18	05	..	..	*
Aug.	11	<17	15	17	55	*C*	Feb.	19	<14	30	14	45	*
Aug.	13	13	18	..	..	*	Feb.	23	<03	34	..	..	*
Sep.	3	<13	08	13	15	*	Mar.	1	<17	30	..	..	*C*
Sep.	5	12	40	12	46	?	Mar.	15	<16	25	16	35	*F*
Sep.	13	<05	46	05	49	*?	Apr.	27	<20	50	21	00	*?

APPENDIX 2

In order to make entirely clear the manner in which the predicted curve given in Figure 6 was derived, we show below the computation on which it was based. Each value of "predicted" Kp is 19 plus the average of the 13 entries given in the following array:

"Smearing" of storm function for derivation of average values of Kp during central meridian passage of active region (double frequency for five central days)

	Minus						CMP	Plus													
	6	5	4	3	2	1	0	1	2	3	4	5	6	7	8	9	10	11	12	13	14
Day of flare																					
−6	10	11	7	3	2	1	2	1													
5		10	11	7	3	2	1	2	1												
4			10	11	7	3	2	1	2	1											
3				10	11	7	3	2	1	2	1										
2					20	22	14	6	4	2	4	2									
−1						20	22	14	6	4	2	4	2								
(CMP)0							20	22	14	6	4	2	4	2							
+1								20	22	14	6	4	2	4	2						
2									20	22	14	6	4	2	4	2					
3										10	11	7	3	2	1	2	1				
4											10	11	7	3	2	1	2	1			
5												10	11	7	3	2	1	2	1		
+6													10	11	7	3	2	1	2	1	
Σ(13)	10	21	28	31	43	55	64	68	70	61	52	46	43	31	19	10	6	4	3	1	
Average increase in *Kp*	0.8	1.6	2.2	2.4	3.3	4.2	4.9	5.2	5.4	4.7	4.0	3.5	3.3	2.5	1.5	0.8	0.5	0.3	0.2	0.1	
"Predicted" *Kp*	19.8	20.6	21.2	21.4	22.3	23.2	23.9	24.2	24.4	23.7	23.0	22.5	22.3	21.5	20.5	19.8	19.5	19.3	19.2	19.1	

The array is prepared for a delay of *zero days zero hours* between the occurrence of the storm-producing flare and the start of the geomagnetic storm, and for the special circumstances of double flare frequency (or storm intensity) for the five days nearest central meridian passage. Any desired average time interval between flare and start of subsequent storm can be introduced into the computation by increasing each time interval in the *horizontal* scale of days before and after central meridian passage by the chosen time interval. For the curve in Figure 6, the lag is made equal to $2\frac{1}{2}$ days, the value indicated by the present study.

The greater the time interval between flare and start of the subsequent geomagnetic storm, the greater will be the asymmetry about the time of central meridian passage in the averaged values of *Kp*. However, it should be noted that the shape and duration of the storm function alone, without any postulated delay between flare and start of storm, will introduce an asymmetry in the superposed curves for central meridian passage of active regions. This is evident in the "0" curve of Figure 8. In this Figure, we show a family of "predicted" curves for

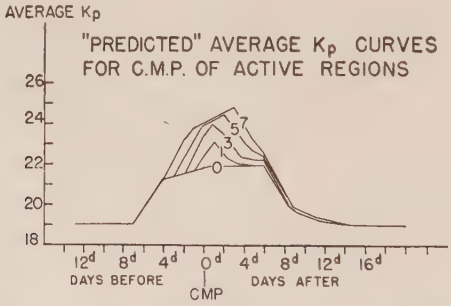

FIG. 8—"Predicted" values of *Kp* for central meridian passage of active regions with different assumed flare distributions (drawn for zero time lag between flare and start of geomagnetic storm). *Note*: Numbers 0, 1, 3, 5, 7 indicate number of days near central meridian with double flare frequency and/or double storm intensity.

central meridian passage of active regions with storm-producing flares. The successive curves show the effect of postulating either double flare frequency or double storm intensity for 0, 1, 3, 5, and 7 days, respectively, nearest central meridian passage.

CONCERNING IONOSPHERIC TURBULENCE AT THE METEORIC LEVEL*

BY HENRY G. BOOKER

School of Electrical Engineering, Cornell University, Ithaca, New York

(Received December 19, 1957)

ABSTRACT

Booker [see 1 of "References" at end of paper] and Booker and Cohen [2] have given reasons for thinking that application of fluid mechanics to meteoric phenomena leads to results in discord with previous thought. This has led to a discussion [3] that is continued in this paper. An underlying feature of the discussion is a phenomenon that may be described as the rough trail paradox. This arises from the fact that the turbulence velocity of the large eddies is about ten times greater than the turbulence velocity of the small eddies. For a trail that has been rendered rough by the small eddies, let us examine the echoes from two points, separated by a distance of the order of the large eddy size. Due to the motion of the large eddies, interference between these two points is taking place at a rate ten times faster than the rate at which the phase of the echo from either point is taking up random values due to the motion of the small eddies. The upshot is that, as already mentioned by Booker [1], the most obvious features of the fading of long-duration meteor echoes are controlled by the motion of the large eddies even when the mechanism of return is backscattering associated with the small eddies. Failure to appreciate this point seems to have led Manning and Eshleman [3] to claim as an antithesis to the Kolmogoroff-Heisenberg theory of turbulence results that, in fact, are consistent with it.

1. *Introduction*

In 1952, Kaiser and Closs [4] published a theory of long-duration radar echoes from meteor trails based on the assumption that spread of the trail is entirely due to molecular diffusion. The idea was that the initially straight trail was rendered sinuous by wind shear, and that the resulting multiple perpendiculars from the radar to the trail could be used to explain the observed fading of echoes. It was difficult to see how this theory could be the whole story, in view of the fact that long-duration visual meteor trails diffuse at a rate at least a thousand times the rate for molecular diffusion. Since the paper of Kaiser and Closs, the idea has grown that something more than simple wind shear is involved in the behavior of

*Published under U. S. Signal Corps Contract No. DA36-039-sc-74903.

long-duration meteoric phenomena. In particular, a study was made by Booker [1] of those features of fluid dynamics that are likely to be relevant at the meteoric level in the atmosphere, and on this basis Booker and Cohen [2] derived a theory of radar reflection from long-duration meteor trails applicable during the decay period after the trail has become underdense. These authors concluded that (*a*) the conditions necessary for the application of the Kolmogoroff-Heisenberg theory [7, 8, 5] of turbulence at the meteoric level in the ionosphere are satisfied; (*b*) the Kolmogoroff-Heisenberg theory of turbulence predicts that a meteor trail will be rendered rough on a scale comparable with VHF wavelengths in a time of somewhat less than a second; and (*c*) this result is quite inconsistent with the assumption that the spread of meteor trails is controlled purely by molecular diffusion for periods of many seconds, or even tens of seconds. Booker and Cohen, therefore, concluded that the disregard of turbulence in current thinking concerning meteoric phenomena was a fatal weakness, and set themselves the problem of bringing into line the accumulated researches of workers in fluid mechanics and the accumulated observations concerning meteor trails. They found that, if they applied well-established principles of fluid mechanics to meteoric phenomena, in defiance of the current thinking of workers on meteoric phenomena, they obtained results that were not in drastic disagreement with meteoric observations.

The fact that application of principles of fluid mechanics to meteoric phenomena led to results in discord with current thought in the field naturally led to heated discussion. The only such discussion to appear in print so far is that of Manning and Eshleman [3]. Perhaps the most significant sentence in their paper is the following. "However, the theoretical method in Booker and Cohen's paper appears sound." In other words, while the application by Booker and Cohen of well-known ideas in fluid mechanics leads to conclusions that Manning and Eshleman are unwilling to accept, nevertheless they are unable to find anything wrong with Booker and Cohen's derivation.

The position today seems to be the same as when Booker and Cohen did their work. On the one hand, we have a theory of turbulence which should be applicable at the meteoric level in the ionosphere and which leads to certain conclusions concerning meteoric phenomena. On the other hand, we have a body of experimental evidence concerning meteoric phenomena which has been interpreted, rightly or wrongly, in terms of ideas that appear to be inconsistent with fluid mechanics. We need to find some way of bringing the experimental observations concerning meteoric phenomena into line with the principles of fluid mechanics.

The main objection that has been made to the theory of Booker and Cohen is that, being a rough trail theory of long-duration meteor echoes, the fading of the echoes should be Rayleigh in character. While the fading of long-duration radar echoes from meteor trails is frequently irregular, experiments show that, particularly between one and ten seconds after the fall of the meteor, important and even drastic departures from Rayleigh fading occur. The statement that the rough trail theory necessarily implies Rayleigh fading is, in fact, incorrect. This is due to what in this paper will be called the rough trail paradox. The rough trail paradox was employed by Booker [1] in his analysis of the problem, but it was not referred to under this name. The rough trail paradox arises from the fact that the

turbulence velocity associated with the large eddies is about a power of ten larger than the turbulence velocity associated with the small eddies. This leads to a situation in which the occurrence of non-Rayleigh fading after the trail has been rendered rough by the small eddies is not only feasible but would, in fact, be expected for typical meteoric dimensions. Thus, the non-Rayleigh fading observed in practice in the earlier stages of long-duration radar meteor echoes is not a proof that the Kolmogoroff-Heisenberg theory of turbulence does not apply. On the contrary, this non-Rayleigh fading is predicted by the Kolmogoroff-Heisenberg theory of turbulence when account is taken of the finite length of meteor trails. This aspect of the problem is discussed in Section 2.

Another criticism made by Manning and Eshleman [3] is that there is an important discrepancy between the theory of Booker and Cohen and their observations. Manning and Eshleman plot a curve to illustrate this discrepancy, which, however, omits one term in Booker and Cohen's formula. They acknowledge the necessity for restoring this term, but the statements made in this connection are incorrect. This aspect of the matter is discussed in Section 3.

Another point made by Manning and Eshleman is that they can fit the data with a theory which is to be published by Manning and which is variously described as a "linear decay theory," a "large scale theory," and a theory based on an assumed "wind profile having the properties of Gaussian noise." A good way of defining turbulence is to say that it is a situation in which the variation of the velocity of the fluid as we move through it has the properties of noise. Manning's theory is, therefore, a theory based upon turbulence, but not upon turbulence obeying the customary laws of fluid dynamics. It is interesting, therefore, to inquire whether Manning's theory would be greatly modified if the somewhat peculiar assumptions regarding turbulence upon which it is based were replaced by ones more in keeping with the principles of fluid dynamics. This matter is discussed in Section 4.

Some other points raised by Manning and Eshleman are discussed in Section 5. The general conclusion is that, in their attempt to disprove the validity of the Kolmogoroff-Heisenberg theory of turbulence at the meteoric level in the ionosphere, Manning and Eshleman are in all probability attempting to destroy what must ultimately become the foundation of their own ideas.

2. *The Effect of the Large and Small Eddies Upon the Fading of Long-Duration Radar Echoes from Meteor Trails*

Manning and Eshleman [3] give the impression that Booker and Cohen have stated that the fading properties of long-duration radar echoes from meteor trails depend only upon the turbulence velocity of the small eddies. This is not the view of Booker [1], upon whose work Booker and Cohen [2] based their ideas. In fact, Booker used the fading rate of these echoes as one of the methods for estimating the turbulence velocity, not of the small eddies, but of the large eddies. The effect of the spectrum of turbulence upon the fading characteristics of meteor echoes involves a paradox that appears to be misunderstood. This paradox has been mentioned by Booker [1], but it appears that a more complete explanation is required.

According to Booker's application of the Kolmogoroff-Heisenberg theory of turbulence to the distortion of meteor trails, the trail becomes seriously distorted by the small eddies within the first second after the fall of the meteor. Successively larger eddies produce serious distortion of the trail in successively longer times, and it takes about a minute for a large eddy to rotate a section of trail through a radian. This means that, for radars of sufficiently short wavelength, the trail becomes rough quite quickly. This leads to what may be described as a rough trail theory of long-duration radar echoes from meteor trails in place of the smooth trail theory used by most other workers. It is tempting to argue that, if after a second the trail is rough, then contributions from the different parts of the trail must be randomly phased and, consequently, that the fading of the echo must be of Rayleigh type. As a matter of observation, long-duration radar echoes from meteor trails frequently do involve Rayleigh fading, particularly in their later stages. But, especially between one and ten seconds after the fall of the meteor, important and even striking departures from Rayleigh fading occur. It is argued that this is inconsistent with the estimate of less than one second for the time constant of the small eddies in the Kolmogoroff-Heisenberg theory of turbulence. The argument that the rough trail theory necessarily involves Rayleigh fading after about a second from the fall of the meteor sounds convincing, but is, in fact, fallacious. It is essential to avoid this fallacy if one is to bring established observations of the fading of long-duration radar echoes from meteor trails into line with well-known principles of fluid mechanics.

The paradox arises from the fact that the turbulence velocity of the large eddies is large compared with the turbulence velocity of the small eddies. To simplify the problem, let us imagine that the large eddies and the small eddies are the only eddies present and that the intervening spectrum of eddies is omitted. This simplifies consideration of the paradox without destroying it. For definiteness, let us think in terms of the numerical values derived by Booker [1]. We are, thus, to think of large eddies whose scale is of the order of 1.6 km and whose turbulence velocity is of the order of 35 m/s, and we are to think of small eddies whose size is of the order of 1.3 m and whose turbulence velocity is of the order of 3 m/s. We assume that an initially straight meteor trail is distorted by these eddies and inquire concerning the fading characteristics of radar reflections from the trail at a wavelength sufficiently short so that the small eddies render the trail rough.

To begin with, let us further simplify the problem by omitting from consideration even the large eddies, so that the trail is distorted only by the small eddies. Since, by assumption, the trail is rough, an echo from it is randomly phased. It is essential to inquire with some care what is meant by this statement. It does not mean that at any particular instant we have no idea what the phase of the echo is. It means that, if the phase of the echo is examined over a sufficiently long period of time, it is equally likely to take any value between 0 and 2π. We must now ask what is meant by a "sufficiently long period of time." This is a matter of calculating the fading period associated with the turbulence velocity of the small eddies and the radio frequency of the radar. Taking the latter to be 50 Mc/s, we deduce a fading period of about one second. Thus, the statement that the echo from the rough trail is randomly phased means that its phase changes substantially in one

second, and, examined over a period much longer than one second, the phase is equally likely to take any value. On the other hand, if examined over a period small compared with one second, the phase will have a value that is not only specifiable but also is scarcely changing over the short period concerned.

Now let us bring the large eddies back into the picture. Consider the echoes from two points of the rough trail, separated by a distance of the order of the large eddy size. These two points of the rough trail have a relative motion of the order of 35 m/s due to the turbulence velocity of the large eddies. The corresponding fading period for a 50 Mc/s radar is of the order of a tenth of a second. Now the phase of the echo from the rough trail, although it is random when examined over a period substantially greater than one second, hardly changes during so short an interval as a tenth of a second. It is erroneous, therefore, to argue that there can be no interference between the echoes from two points of the rough trail separated by a large eddy size on the grounds that the echoes from the two points are randomly phased. The interference between the two points of the trail is taking place at a rate ten times faster than that at which the phase of the echo from either point is taking up random values. The upshot is that the echo has a fading period of one-tenth of a second, but that, if this fast fading is smoothed out, the echo is randomly phased when examined over a period of many seconds.

We thus have a paradox in which the echoes from different parts of a rough trail can interfere with each other over limited periods of time. The secret lies in the fact that the relative motion of the different parts of the rough trail is ten times greater than the motion associated with the roughness. This paradox was mentioned by Booker [1] in connection with Eq. (28) of his paper. It was because of this paradox that Booker took the fast fading rate associated with the rough trail to indicate the turbulence velocity, not of the small eddies, but of the large eddies. It was also because of this paradox that Booker and Cohen [2] smoothed out the fading associated with the large eddies before comparing their experimental results with the rough trail theory.

It is an important consequence of the rough trail paradox that studies of the fading characteristics of long-duration meteor echoes give information most directly about the large eddies. In this particular respect, therefore, there is little difference between the rough and smooth trail theories, except, of course, the fact that it is the rough trail theory that is consistent with the principles of fluid mechanics. Manning and Eshleman [3] promise to publish experimental investigations that they have made of the fading characteristics of long-duration meteor echoes and to derive from them information concerning the large eddies. This is a thoroughly sound procedure. They will deceive themselves, however, if they imagine that, by interpreting their results in terms of the smooth trail theory, they will thereby disprove the rough trail theory, since this is a feature in which the two theories differ in only minor respects. If they interpret their results in terms of the smooth trail theory, it will require only editorial changes of wording to convert their statements into ones based on the rough trail theory and thereby bring their interpretation of the experiments into accord with the principles of fluid mechanics.

In terms of the rough trail paradox, it is easy to see why long-duration meteor echoes show important departures from Rayleigh fading. It follows from the para-

dox that those features of the fading that are most obvious to the eye depend upon the turbulence velocity of the large eddies. It is pertinent, therefore, to examine how many large eddies are covered by a typical meteor trail. Allowing for weakening of the trail near its upper and lower ends, the number of statistical wave components entering into the fading is approximately the ratio of the length of the trail to 2π times the scale of the large eddies. Using Booker's figure [1] for the scale of the large eddies, which agrees approximately with the estimate of Manning and Eshleman [3], 2π times the scale of the large eddies is about 10 km. For the fading of long-duration meteor echoes to be entirely Rayleigh in character, therefore, it would be necessary for the length of the trail to be large compared with 10 km. Most trails are, however, only about two or three times 10 km in length, so that important departures from Rayleigh fading are to be expected.

By examining the fading of long-duration radar echoes from meteor trails showing marked departures from Rayleigh fading, it may be possible to obtain direct evidence of the influence of the small eddies and from this to obtain a further estimate of the turbulence power per unit mass at the meteoric level. Thus, if sinusoidal fading persists for a period of time τ, then τ is a measure of the fading period associated with the turbulence velocity of the small eddies. Hence, an analysis of the durations of intervals of sinusoidal fading should make possible an estimate of the turbulence velocity of the small eddies and hence of the turbulence power per unit mass. The value thus obtained for the turbulence power per unit mass should agree with that derived from the effect of the large eddies in the manner already described by Booker [1].

3. *Comparison between Theory and Observation*

Booker and Cohen deduced from the available observations that disappearance of electrons from a trail follows an attachment law and that the attachment time is of the order of seven seconds. They pointed out that the attachment time should increase exponentially with height, and the figure of seven seconds applies to some average meteoric height. If we take this height to be 90 km and assume that the exponential variation of attachment time with height is determined by the scale height of the atmosphere at 90 km, we obtain a variation of attachment time with height such as that indicated in Figure 1. It should be noticed that, over the interval of height with which we are concerned in meteoric phenomena, the attachment time indicated varies from about one-tenth of a second to about 100 seconds. The attachment time appropriate to any particular trail varies enormously with the height of the trail. Indeed, there should be a marked variation of attachment time along the length of a particular trail, the ionization at the top of the trail persisting much longer than the ionization at the bottom of the trail.

These points do not seem to have been appreciated by Manning and Eshleman [3]. The discrepancy that they illustrate between the observations of Booker and Cohen and the theory of Booker and Cohen is obtained by neglecting the effect of attachment. This same discrepancy was pointed up by Booker and Cohen in their method of plotting, and it was this discrepancy that led them to consider the effect of attachment. Manning and Eshleman are conscious of the fact that in plotting their diagram they omitted one of the factors in Booker and Cohen's formula, but

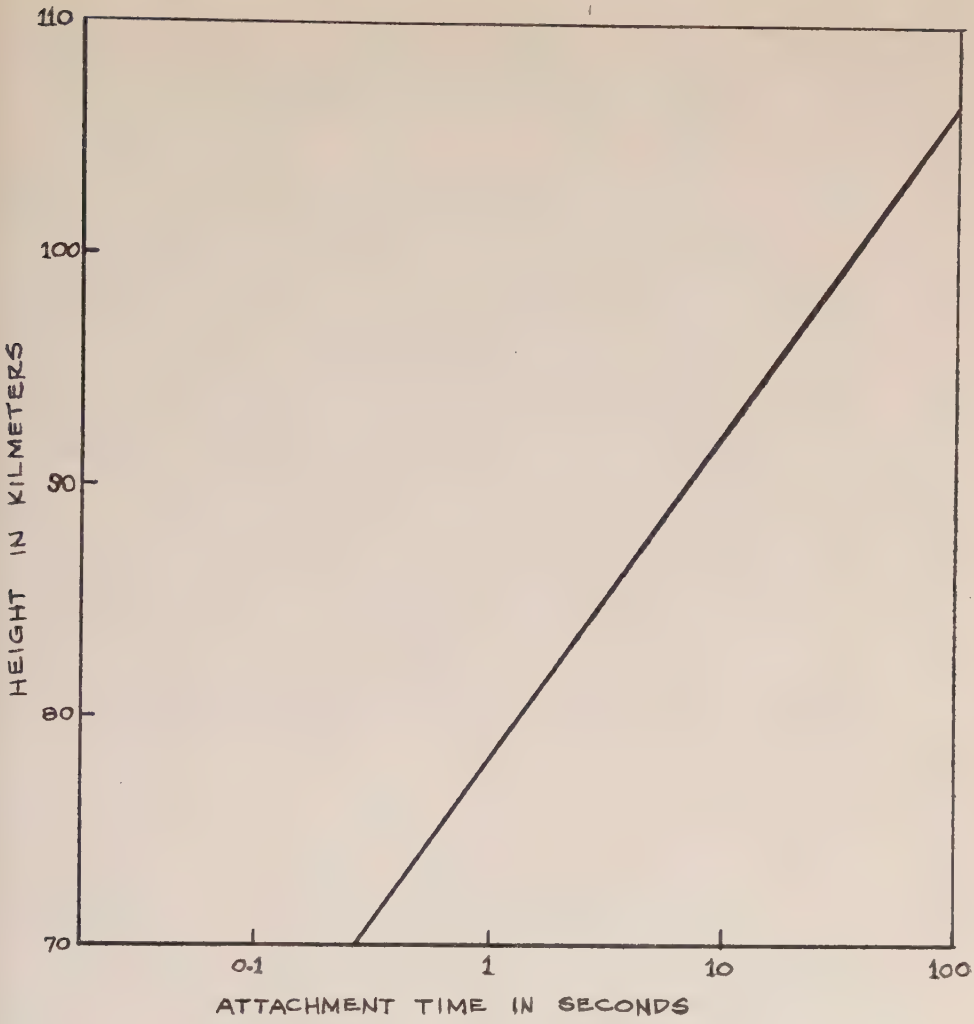

FIG. 1—Variation of attachment time with height according to Booker and Cohen

they argue that reinsertion of this factor would not cure the discrepancy. Manning and Eshleman reached this conclusion by omitting to notice that each meteor trail occurs at a different average height and that the attachment appropriate to this height must be used. Thus, for an individual meteor trail, we do not use the attachment time of 7 seconds applicable to some average height taken as 90 km in Figure 1. Instead, we find what attachment time is appropriate to this particular meteor trail and then deduce from Figure 1 the height to which it refers. If the theoretical curves associated with the meteoric observations illustrated in Figures 5 and 7 of Booker and Cohen's paper are modified to include the effect of attachment, we arrive at Figures 2 and 3, respectively. The attachment time used was simply guessed by eye, and corresponds to a height about 5 km less than the mean meteoric height to which Booker and Cohen's figure of 7 seconds refers. Since Booker and

Cohen's theory refers only to the decay period after the meteor trail has become underdense, it is only in the decay period that a comparison between the theoretical curves and the observational points is appropriate in Figures 2 and 3. Thus, when

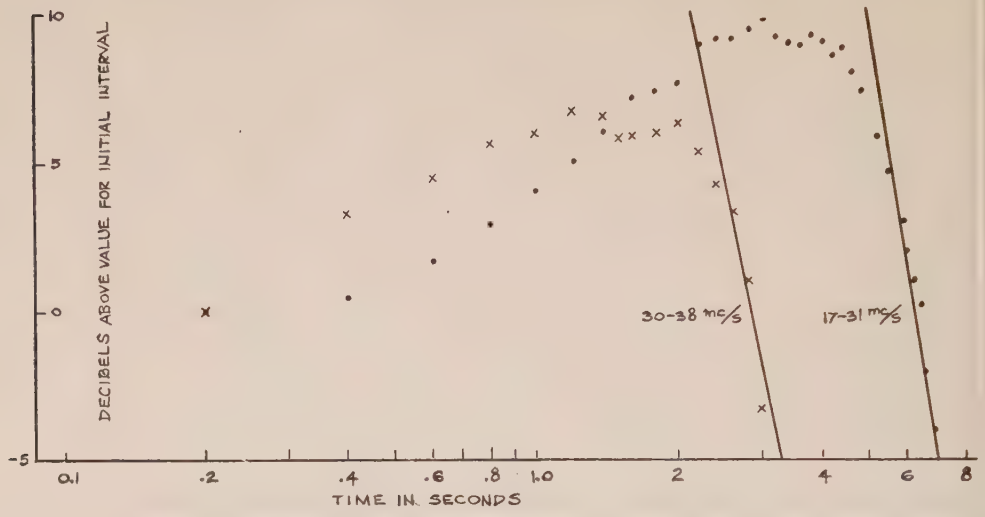

FIG. 2—Comparison between the theory and observations of Booker and Cohen for the meteor echo shown in Figure 5 of their paper [2] allowing for effect of attachment

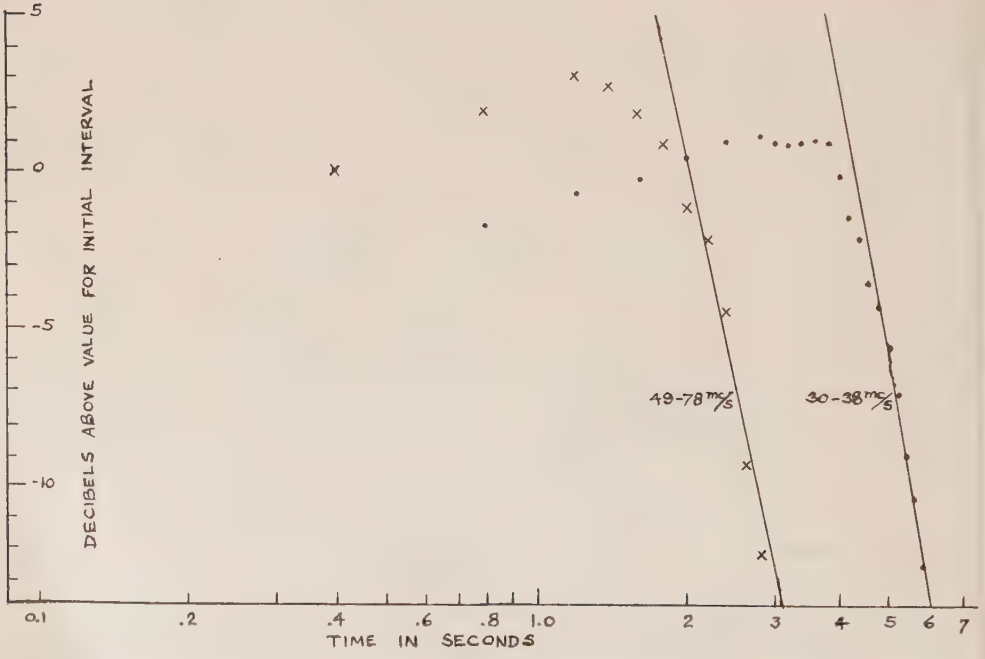

FIG. 3—Comparison between the theory and observations of Booker and Cohen for the meteor echo shown in Figure 7 of their paper [2] allowing for effect of attachment

the effect of attachment is included, the agreement is within the experimental error.

There are various respects in which the comparison made between theory and experiment by Booker and Cohen can be criticized. Probably the most important of these is their assumption that, as soon as the echo begins to decay, it is underdense. Manning and Eshleman do not, however, make minor criticisms of this type. Instead they deduce that the discrepancy between the theory and the observations, which is illustrated in Figures 2 and 3, is so drastic as to warrant the conclusion "that small scale turbulence of significant velocity does not exist in the ionosphere at meteoric heights." In contrast with this sweeping conclusion, Booker and Cohen did not even attempt to deduce attachment times from their own data because they did not regard the experimental accuracy as adequate to permit this refinement. It was for this reason that they used in this analysis data of McKinley and Millman [12], even though these data had not been handled in the most convenient way for the purpose. Thus, Eshleman and Manning were using discrepancies within the experimental error to draw the *a priori* unlikely conclusion that well-known principles of fluid mechanics, which ought to be applicable at the meteoric level, are completely wrong. For this conclusion, there is no basis whatever.

4. *Manning's Model of Turbulence at the Meteoric Level*

Manning and Eshleman [3] state that Manning will shortly publish a theory of long-duration radar reflection from meteor trails that will show good agreement with the observations of Booker and Cohen. It is presumed that this is the theory that Manning has presented at recent URSI meetings and which is based upon the assumption of a wind profile having the properties of Gaussian noise [13]. A situation in which the fluid velocity varies as we move through a medium in a manner having the properties of noise is a situation characteristic of turbulence. The assumptions that Manning has made concerning turbulence are, howeyer, different from those that would be made on the basis of the Kolmogoroff-Heisenberg theory of turbulence. The assumptions of Manning satisfy the equation of continuity of fluid mechanics, but in all probability they satisfy no other principle of fluid mechanics. From the standpoint of fluid mechanics, therefore, it is easy to criticize Manning's model. Nevertheless, it can probably be argued that, in spite of the shortcomings of Manning's model from the standpoint of fluid mechanics, it nevertheless contains a sufficient fraction of the truth to lead to interesting electrodynamic consequences. To justify Manning's model, it will be necessary first of all to exploit the rough trail paradox described in Section 2 of this paper in order to argue that omission of the tail in the Kolmogoroff-Heisenberg spectrum of turbulence is not serious. It will then be necessary to argue that, although turbulence is unlikely to have the one-dimensional character assumed by Manning, nevertheless incorporation of the other two dimensions would not have a major influence on the electrodynamic results of the theory. There seems to be a good likelihood either of justifying these assumptions or of extending Manning's theory to eliminate them. The theory is, therefore, of major interest in connection with the explanation of long-duration radar echoes from meteor trails. This interest does not, however, arise from a possibility that Manning's model may be an al-

ternative to the Kolmogoroff-Heisenberg theory of turbulence. On the contrary, Manning's theory in all probability will be of interest only in so far as it can be brought into line with the standard theory of turbulence. If and when Manning's theory leads to discrepancies with observations, attention will be focused upon the differences between Manning's model and the Kolmogoroff-Heisenberg theory of turbulence.

5. *Other Points Raised by Manning and Eshleman*

(*i*) The theory of backscattering from meteor trails developed by Booker and Cohen on the basis of the Kolmogoroff-Heisenberg theory of turbulence applies only after the trail has become underdense. The present author does not know how to calculate the echo from an overdense meteor trail that has been distorted in accordance with the Kolmogoroff-Heisenberg theory of turbulence. This author cannot satisfactorily solve the even simpler problem of total reflection from an ionospheric layer that is subject to turbulence at the level of reflection. It is anticipated that, when the theory of reflection from an overdense meteor trail subject to turbulence in accordance with the Kolmogoroff-Heisenberg theory of turbulence has been worked out, the results will fit the observations of McKinley and Millman [6] concerning the aspect properties of meteor echoes. That Manning and Eshleman do not anticipate this appears to arise from confusion about the rough trail paradox described in Section 2.

(*ii*) It is quite true that the data presented by Booker and Cohen in their Figure 12 can be fitted to laws described by Manning and Eshleman. It might be added that the paucity of data is such that yet other laws could be fitted to the results. Booker and Cohen, however, were interested in whether the data could be fitted by a theory based on the principles of fluid mechanics. They found that the data could be so fitted.

(*iii*) It is agreed that, in applying the data of McKinley [12] to VHF scatter transmission, no correction was made by Booker and Cohen for meteors smaller than those detectable by McKinley. It is not agreed, however, that the basis for making this correction used by Manning and Eshleman is satisfactory or even that the correction necessarily has to be made in the direction that they indicate. There is a fallacy in ascribing the background signal of VHF scatter transmission to specular reflection from meteor trails created by extremely small meteors. Extremely small meteors probably create their ionization at heights well above the level responsible for the main signal in ionospheric scatter transmission. The latter level is 90 km or less, according to Pineo [9], whereas according to the theory of Kaiser [10], backed up by the experimental results of Gregory [11], the tiny meteors create their ionization well above 100 km.

6. *Conclusion*

The papers of Booker and Cohen [2] and of Manning and Eshleman [3] appear at first sight to indicate two views that are poles apart. It is doubtful, however, whether in reality this is the case. Manning and Eshleman are convinced that they have important experimental information involving the fading of long-duration echoes from meteor trails that gives information about the large eddies and not

about the small eddies. In this, they are absolutely right. What they do not seem to appreciate is that this is predicted by the Kolmogoroff-Heisenberg theory of turbulence in spite of the wide spectrum of eddy sizes involved. So far as the author can determine, the confusion arises from the rough trail paradox previously mentioned by Booker [1] and described in greater detail in Section 2 of this paper.

References

[1] H. G. Booker, J. Geophys. Res., **61**, 673 (1956).
[2] H. G. Booker and R. Cohen, J. Geophys. Res., **61**, 707 (1956).
[3] L. A. Manning and V. R. Eshleman, J. Geophys. Res., **62**, 367 (1957).
[4] T. R. Kaiser and R. L. Closs, Phil. Mag., **43**, 1 (1952).
[5] G. K. Batchelor, The Theory of Homogeneous Turbulence, The Cambridge University Press, Cambridge, England (1953).
[6] D. W. R. McKinley and P. M. Millman, Proc. Inst. Radio Eng., **37**, 364 (1949).
[7] A. N. Kolmogoroff, C.R. Acad. Sci. URSS, **30**, 301; **32**, 16 (1941).
[8] W. Heisenberg, Zs. Physik, **124**, 628 (1948).
[9] V. C. Pineo, J. Geophys. Res., **61**, 165 (1956).
[10] T. R. Kaiser, Mon. Not. R. Astr. Soc., **114**, 52 (1954).
[11] J. B. Gregory, J. Geophys. Res., **62**, 383 (1957).
[12] D. W. R. McKinley, Can. J. Phys., **32**, 450 (1954).
[13] L. A. Manning, URSI Meeting, Washington, D. C., May 1957; URSI Assembly, Boulder, Colorado, September 1957.

BETWEEN THE ATMOSPHERICS

BY GROTE REBER

Research Corporation, New York 17, New York

(Received August 15, 1957)

ABSTRACT

Examination is made of the residual intensity of energy received between the atmospherics at a frequency of 520 kc. The nature of the junction between the earth's and the sun's atmosphere, and the manner in which an electromagnetic wave travels through an overdense ionosphere are briefly described. The way in which an ionospheric shutter opens and closes is explained, plus examples shown and reduced. A celestial component is found at declination $-6°$, which has a maximum at 2200 hours right ascension and a minimum at 0700 hours. The maximum intensity is 4×10^{-20} jansky per steradian. Unexpected variations at night may be due to auroral particles of low energy. Manifestations of strong precipitation static and local atmospherics are described. A few observations were made at 143 kc.

INTRODUCTION

Atmospherics have been studied for more than half a century in a wide variety of manners. However, the short periods of time between the atmospherics seem to have been overlooked. When these are investigated, a number of interesting phenomena are encountered.

Consideration was first given to making low-frequency observations of cosmic static early in 1953. A considerable number of listening tests were made in Hawaii, and it became obvious that if any success were possible it would be necessary to delete the atmospherics and measure only the spaces between the atmospherics. Using high-speed instruments, this appeared to be hopeful.

The problem of getting a ray of cosmic static through an overdense ionosphere looked much less promising, as only one vague suggestion could be found in the literature [see 1 of "References" at end of paper]. In the meantime, I learned that the values of *F*-layer critical frequency became low and remained low most of the night at Hobart. Thus, I decided to make an initial try at Hobart, using *O*-mode propagation above the critical frequency, as this seemed fairly certain. Success was immediately had at 2,130 kc and soon at somewhat lower frequencies [2]. However, the situation at 520 kc showed that this frequency was below what could be reasonably expected to produce satisfactory results, even near solar activity minimum, using *O*-mode propagation.

Critical examination of the records made it clear that there was still a smooth background at night below the atmospherics but still far above the day level.

This background was controlled by *D*-region absorption at sunset and sunrise. Further, the background sloped considerably downward during the early morning hours when the 2,130-kc records were doing the same thing. The symptoms looked interesting and peculiarly suspicious like cosmic static might be coming through at 520 kc in some manner other than *O* mode. One of these recordings, which I took, is shown in Figure 2*g* of reference [2]. The date is 14 July 1955.

On the basis of these hints, I decided to come back again to Hobart and have another try. To make significant progress, it would be necessary to find a better place and incorporate some direction-finding ability into the antenna system.

SPACE SURROUNDING THE EARTH

Interplanetary space has a material density far greater than interstellar space. Thus, the atmosphere of the sun may be thought of as extending throughout the solar system and merging with the zodiacal light. The pressure of light from the sun will exceed that of gravity for molecular size particles. Consequently, there is probably a general movement of such material outward from the sun. This tenuous gas is believed to be completely ionized, but the number of free electrons is probably a very small part of the total number of ions.

The earth will act as an obstacle to this outward movement and cause the material to flow around it in a shape similar to a raindrop, with the tail pointed in the direction of midnight. Figure 1 shows a variety of conditions. The material inside the drop may be considered part of the earth's atmosphere, while the material outside the drop belongs to the solar atmosphere.

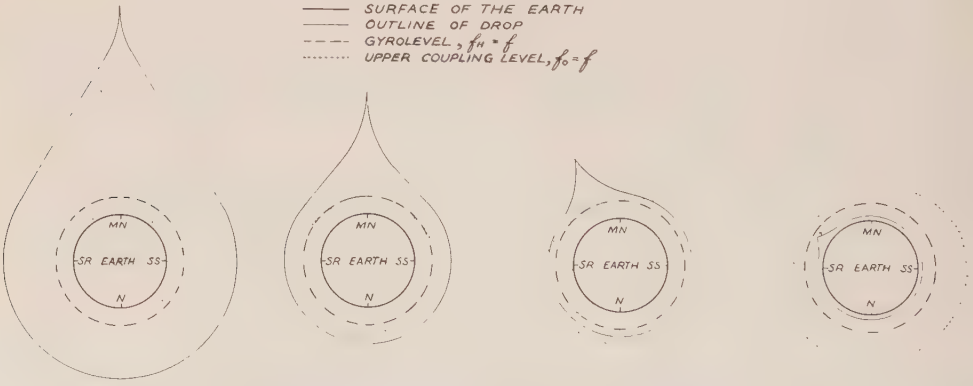

FIG. 1—Symbolic representation of extent of the earth's atmosphere during low, weak, medium, and strong solar activity. Solar atmosphere is outside the drop.

The size and shape of the drop will depend upon solar activity, both on a long and short time basis. When solar activity is low, the solar atmosphere becomes more tenuous. The drop will expand and become symmetrical as the earth's atmosphere extends farther from the planet, as shown in Figure 1*a*. Increasing solar activity will cause the drop to contract, as shown in Figure 1*b*. When the drop becomes small, the cross-component of the earth's magnetic field becomes effective. This drags some of the material from the sunset side of the earth around

to the rear of the earth and causes the drop to become unsymmetrical, with the tail pointed toward morning, as shown in Figure 1*c*. Figure 1*d* is an exaggerated example of this condition.

ELECTROMAGNETIC WAVES IN THE IONOSPHERE

An electromagnetic wave may travel through an ionized medium in a variety of manners. The two of interest here are the ordinary transverse or *O* mode and the extraordinary longitudinal or *Y* mode. The *O* wave can travel only in an underdense region where the critical frequency is less than the observing frequency $f_0 < f$. The *Y* wave can travel only in an overdense region where $f_0 > f$. Energy may transfer from one mode to the other at the boundary where $f_0 = f$, provided that this region is large enough for the electric fields of the two modes to be coincident over a significant distance. The lower coupling level will be at the base of the *E* region by day and may rise to just below the *F* region at night, depending upon the observing frequency.

An electromagnetic wave traveling through a medium containing free electrons in a magnetic field will cause the electrons to move in curved paths. The magnetic field of the earth becomes weaker farther out. Thus, at some level, the free electrons will be in resonance with the exciting wave. This level is the gyro level, where $f_h = f$. Near the gyro level, the *Y* wave will encounter a refractive index of infinity [3] and be totally absorbed. On the other hand, the gyro level will not have any perceptible effect upon an *O* wave, because the free electrons are turning in the wrong direction. Consequently, a shutter exists which may open or close, depending upon whether or not the upper coupling level occurs below or above the gyro level. At a given observing frequency and location on the earth, the gyro level will remain fixed both day and night. However, the upper coupling level may move higher or lower, depending upon the size and shape of the drop surrounding the earth.

Another door exists in the form of absorption in the *D* region. This door is closed during the day and open during the night. The effect may easily be seen on the records as rises near sunset and falls near sunrise. Such changes are quite abrupt, lasting on the order of half-hour to an hour.

Note:

The extraordinary longitudinal mode, I denote by the letter *Y* throughout the discussion. This is in line with the common practice of denoting the ordinary longitudinal mode by the letter *Z*. In some recent papers, the *Y* mode has been merely called the extraordinary or more poorly the *X* mode. This is unfortunate, as the letter *X* has, by long usage, been used to denote the extraordinary transverse mode above the gyro frequency. The *Y* mode cannot produce an echo on an ionosphere sounding machine, because the echo level of zero refractive index occurs above the absorption level of infinite refractive index.

I hereby suggest that the extraordinary transverse mode below the gyro frequency be denoted by the letter *W*, because its characteristics are quite different from the common *X* mode. The cusp frequency is independent of the ordinary transverse or *O*-mode cusp frequency when $f_0 > \sqrt{2}\, f_h$. Also, in the region

$f_h > f > f_h/2$, the f_w cusp is always sharp and clear, even on recordings showing great spread on the O and X cusps. Thus, the W echo must return from a very small region in the ionosphere, similar to the Z echo. This direction is probably to the south at Hobart. Furthermore [1], when $f_0 < \sqrt{2}\, f_h$, it seems probable that a ray of cosmic static might get through the ionosphere in the frequency range $f_h > f > f_w$. These are both matters worthy of future study.

SHUTTER OPENS AND CLOSES

Nearly continuous records at a frequency of 520 kc were secured from early August 1956 through May 1957. Due to sharply rising solar activity, the circumstances of Figure 1*a* were rarely encountered. An example may be seen in Figure 4*d*. Here the shutter was open from before sunset to after sunrise. The abrupt rise in base level coincident with the appearance of atmospherics near sunset indicates the removal of *D*-region absorption or the opening of the door at bottom. It closes with reverse manifestations near sunrise.

The situation of Figure 1*b* is more common, as shown in Figure 2*a*. Near sunset, the *D*-region absorption disappears and atmospherics begin. However, the shutter is closed as day level persists. Gradually the shutter opens and lets in celestial energy, which reaches a maximum near midnight. Then the shutter gradually closes, with a fall of the base-line toward sunrise, when *D*-region absorption again sets in and the atmospherics disappear. This gradual rise and fall from sunset to sunrise, centered on midnight, is a fundamental characteristic of the phenomenon, which could be found on the majority of the records secured.

The situation of Figure 1*c* is shown in three different amounts by Figures 2*b*, *c*, *d*. The shutter stayed closed most of the night and partially opened only a short time after midnight. The situation in Figure 1*d* is shown in Figure 2*e*, where the base-line is straight all night. This indicates the shutter did not open.

The records of Figures 2*a*, *b*, *c*, *d* have been reduced to relative intensity *vs* time, and the results are plotted in Figure 3. In all cases, there is a rapid, smooth rise and fall of intensity over great ranges, which is a sure sign of change in the size of the shutter and allows all such records to be deleted from those where the shutter remains open.

SHUTTER REMAINS OPEN

About three dozen records were secured where the shutter remained open for a period of four hours or longer. All of these showed a smooth base-line which was high compared to the daytime level, plus an abrupt rise at sunset or fall at sunrise, or both. During the open period, the base-line usually has a smooth variation over moderate ranges. Some of the recordings are shown in Figure 4. The data on these records and others were reduced to a common level and plotted against sidereal time. The results are shown in Figure 5.

The major maximum is near 2200 hours RA. Then a slight fall to 0000 RA, followed by a near flat level to 0200 RA. A second minor maximum probably exists near 0400 RA, followed by a steep fall to a minimum at 0700 RA. Then a slow rise sets in, with the intensity gradually building back up to the maximum near 2200 RA.

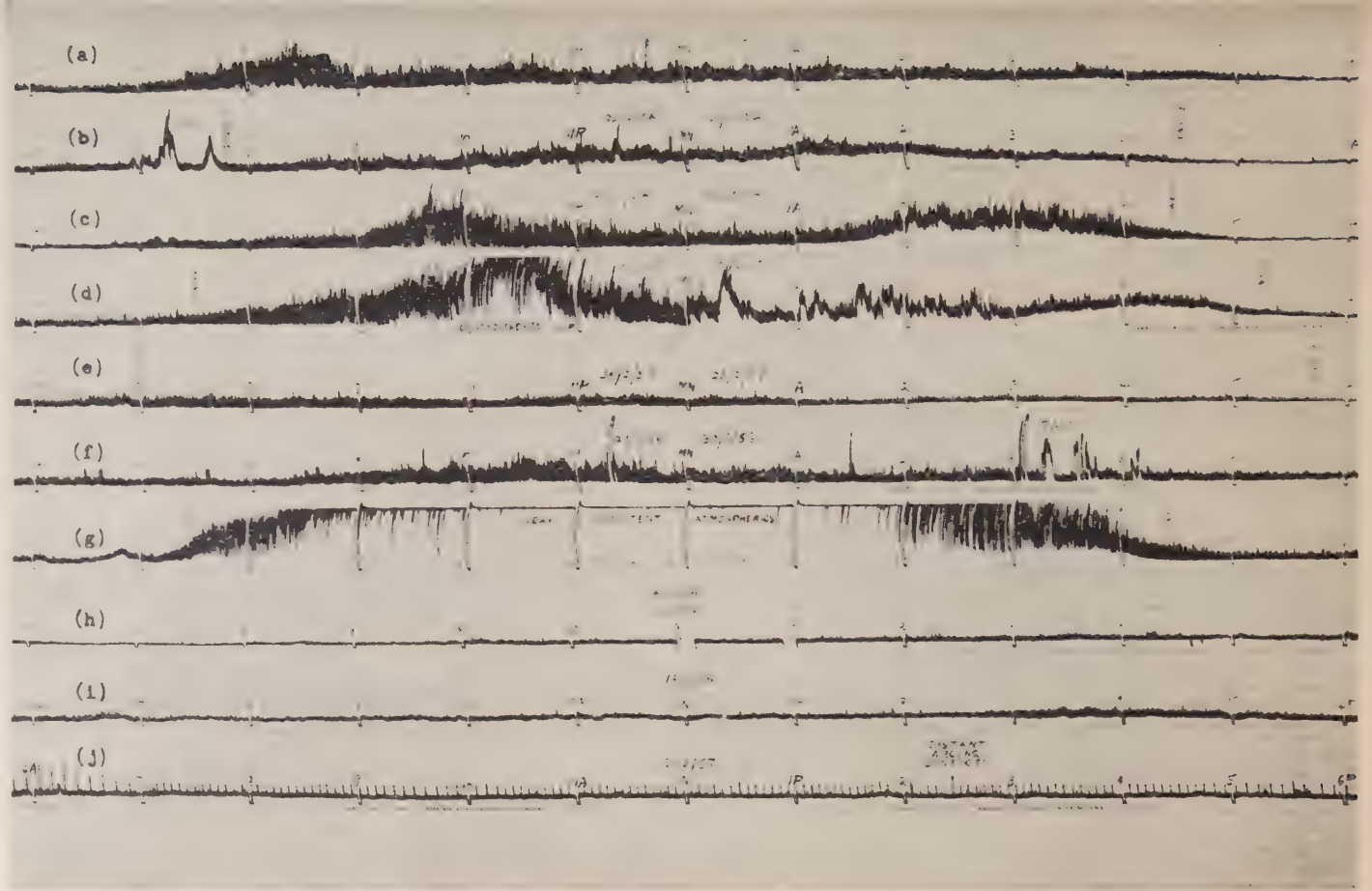

FIG. 2.—In *a*, *b*, *c*, *d* the shutter opens after sunset, near 10 p.m., midnight, and 3 a.m., respectively; *e* shutter remains closed all night; *f* antenna null 37° north of zenith; *g* persistent atmospherics most of night; *h* typical day record with gradual rise all day; *i* day record with peak in afternoon; *j* unusual flat day record.

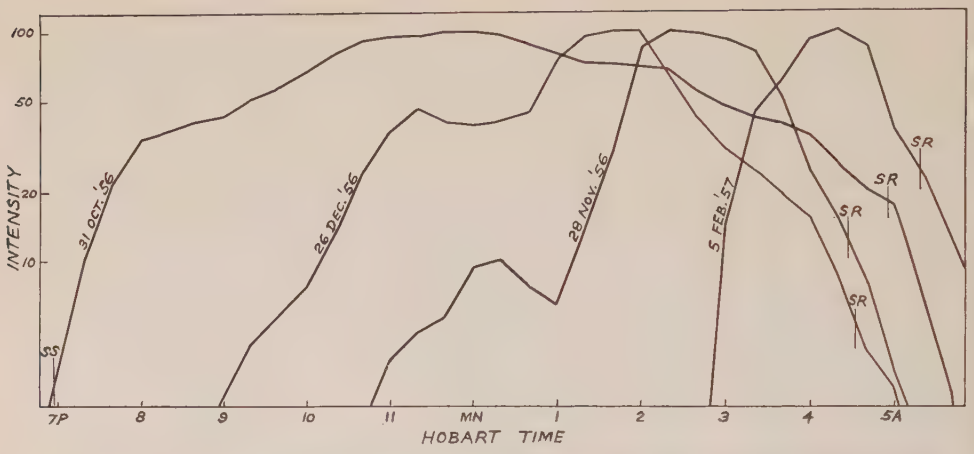

FIG. 3—Relative intensity *vs* time as shutter opens and closes; data taken from recordings 2*a*, *b*, *c*, *d*

Both the maximum at 2200 RA and the minimum at 0700 RA are shifted somewhat to the westward compared to similar data [2] taken at 2,130 kc. These features of the 2,130-kc data are also somewhat to the westward of similar features on data taken at still higher frequencies. Thus, it appears that there is a change in position of the apparent galactic plane, which progressively increases as the frequency is decreased.

Current popular ideas suggest that the low-frequency radiation originates in a region of the galaxy fairly close to the sun, while cosmic static at meter waves originates at much greater distances. Thus, it seems quite likely that the local region which produces cosmic static at kilometer waves may be at a marked angle to the plane of the entire Milky Way system.

The great ratio of intensity from maximum at 2200 RA to minimum at 0700 RA is an unexpected feature when compared to the results at 2,130 kc. It is undoubtedly due to the much better resolution at 520 kc in comparison with 2,130 kc, at which frequency the antenna integrated over an area of more than a steradian.

Listening tests always showed the sounds between the atmospherics to be short bursts of a smooth continuum. They might last from a fraction of a second to several seconds and sounded like "Pish-Pish-sh". Very sensitive examination with a beat oscillator confirmed that no carrier was present.

LOCATION AND SIZE OF SHUTTER

The connections of the various antennas may be changed to produce a variety of nulls. These are shown in Figure 6, plotted in terms of amplitude squared. Thus, intensity is proportional to the area under the curve. The sharp computed nulls are not available in practice because the various impedances cannot be perfectly equalized. However, by attention to detail, the impedances of the lines can be made to appear at the receiver within three per cent or less of one another. Thus, minimums of about one-tenth per cent in power may be achieved. This accuracy is still insufficient to take advantage of the sharpest null. Further limitations are introduced by the large varying component of the energy frequently encountered.

FIG. 1—Smooth slow variations of intensity when shutter remains open several hours

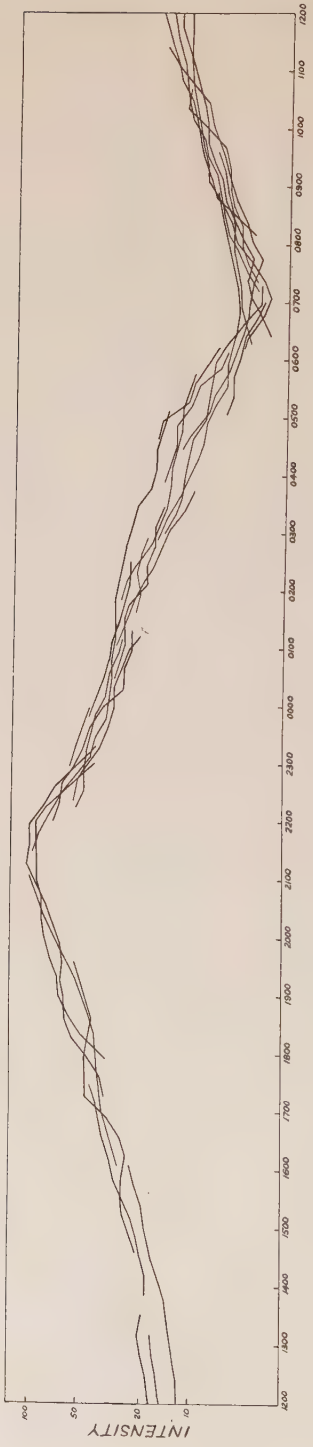

FIG. 5—Relative intensity *vs* right ascension for records of Figure 4 and others; declination about −6°

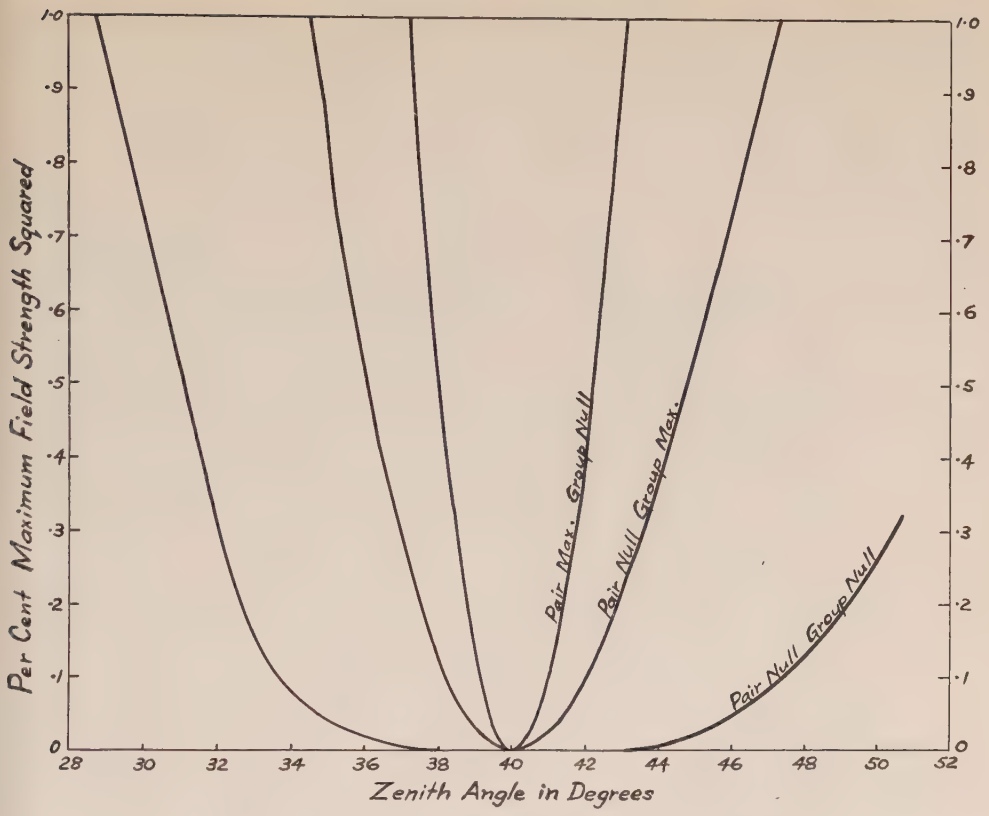

FIG. 6—Types of nulls available by adjusting antenna connections

By selecting quiet circumstances, it is clear that the radiant, by which the energy is arriving, is definitely between 35° and 40° north of the zenith, with an estimated center around 37°. This refers to the steady celestial component previously discussed. Figure 2*f* shows a record taken with the broad null at 37°. It is much the same as one taken when the shutter was closed, as in Figure 2*e*. The angle is about what might be expected if the upper coupling level is at 3,000 km with a magnetic dip of 72° at ground level at Hobart.

To suppress the cosmic static by a factor of 10^3 or greater, the shutter must be three degrees or less in north-south direction when open. No information is available on the east-west extent of the shutter. It could be a long slit, but this seems unlikely. Most probably the shutter is nearly circular. Hobart is 43° south latitude, so the radiant is in the direction of −6° declination. How much bending the ray will encounter from space down to the upper coupling level is not known, but is probably only on the order of a few degrees.

INTENSITY

The maximum intensity at 2200 hours RA may be estimated in the following manner.

The antenna extracts energy from the wavefront over an area approximately 3,000 feet east-west by 4,000 feet north-south, equal to 1.1 square kilometers. Area $A = 1.1 \times 10^6$ square meters.

Losses in ground, steel antenna wire, and tuner box are each 1 db, plus 3 db in buried cable, for a total loss of 6 db. System efficiency $\varepsilon = 0.25$.

The energy arriving in wavefront above antenna is via O mode only, so a correction-factor of two is needed to cover the W mode above the upper coupling level which cannot penetrate the ionosphere. The antenna is susceptible only to east-west polarized energy, so a further correction-factor of two is needed to cover the north-south components of a random polarized wave-front. Propagation-factor $F_p = 4.0$.

The receiver bandwidth is six kilocycles, $\Delta f = 6 \times 10^3$ cps.

The four buried coaxial lines in parallel present an apparent antenna radiation resistance of 12.5 ohms at input to receiver, which is closely matched for maximum energy transfer, giving $R_a = 12.5$ ohms.

The maximum apparent induced voltage caused by cosmic static at 2200 RA, in series with R_a, is 0.65 microvolt. Thus, $E_a = 0.65 \times 10^{-6}$ volt.

The apparent antenna power is thus

$$P_a = \frac{E_a^2 F_p}{R_a \varepsilon} = 0.54 \times 10^{-12} \text{ watt}$$

The size of the shutter is probably about three degrees in diameter. Sky area $\psi = 2.1 \times 10^{-3}$ steradian.

The maximum surface brightness of the galaxy at 520 kc near 2200 RA and $-6°$ declination averaged over 2.1×10^{-3} steradian becomes

$$I_s = \frac{P_a}{A \Delta f \psi} = 3.9 \times 10^{-20} \text{ jansky/steradian}$$

The error may easily be a factor of two, but rather unlikely a factor of ten.

If the surface brightness is averaged over a large area, such as a steradian, the value of I_s will probably drop by a factor of two or more.

Recent examination of the data taken at 2,130 kc during the winter of 1955 indicates that a better value of maximum intensity is $1.5 \pm 0.3 \times 10^{-19}$ jansky per steradian, when averaged over an area of 1.2 steradians near 1900 RA and $-43°$ declination. While this position is somewhat different from that quoted for 520 kc, it seems that the surface brightness of the galaxy is decreasing with frequency.

DAYTIME BACKGROUND

The daytime level is nearly always considerably above the amount expected from D-region absorption. Sample records are shown in Figure 2*h*, *i*, *j*. A characteristic daily variation is present, which begins as a minimum about an hour after sunrise. Then a gradual smooth increase sets in, which reaches a maximum in the afternoon. This is followed by a slow decline all night long to the next minimum after sunrise. See Figure 2*e*, *f*. The minimum follows the sunrise time closely throughout the year. However, the maximum changes its position with the seasons.

In winter, the maximum occurs after sunset, and can only be seen on occasional records where the shutter remains closed and fluctuation disturbances are absent. With the coming of spring, the maximum moves forward in time, and about the vernal equinox it may usually be seen an hour or so before sunset. It continues to move forward and reaches about 2 p.m. at the summer solstice. Thereafter, it moves backward, and merges with the night record shortly after the autumnal equinox.

Direction-finding tests show the sky to be fairly evenly illuminated during the day and often a bit brighter high in the south. The sounds are characteristic of a thermal continuum, with occasional feeble man-made disturbances of sparking type. Perhaps once a month, the morning minimum drops to about 300° absolute temperature for an hour or less, so that one time-mark may disappear.

Fortunately, when the antennas look upward, there is very small response at low angles. Thus, even at the galactic minimum near 0700 hours RA, the level of cosmic static is well above the daytime background; see Figure 4*d*.

PRECIPITATION STATIC AND ATMOSPHERICS

Tasmania has a maritime climate. Thus, violent thunderstorms with blinding displays of lightning are unknown. The prevailing winds are from the southwest and sharp cold fronts bring intense examples of precipitation static, particularly in the winter. This energy does not seem to radiate many miles out of the front, but is exceedingly intense when directly overhead. In a few cases, enough radio-frequency energy on a bandwidth of 30 kc was extracted to cause the input tuning condenser at the receiver to flash over. Such displays only last ten minutes or less; however, they are new to me. I suggest that some similar disturbances in the atmosphere of Jupiter may account for the peculiar transients emitted from time to time on that planet. Listening to more moderate examples discloses a slowly varying frying sound, often having squeals and screeches of several seconds duration. These sounds usually ascend in pitch and may rise from below audible pitch in the general frying up to above audible pitch. Often they gain coherence and become purer and end as a whistle. Perhaps they are due to sheets of rain intersecting.

Four recordings were secured similar to Figure 2*g*. In all cases, a moderate local thunderstorm was found to be in progress somewhere over Tasmania. Examination of the Figure shows that even during local electrical storms there occur short intervals when the snapping momentarily abates and the pen finds its way to the celestial background level. A statistical investigation of these matters might provide new information about electrical storms. The apparatus seems well able to cope with normal distant atmospherics.

FLUCTUATIONS, SWELLS, AND RIPPLES

The majority of the recordings show different amounts of high variable background. This is an unexpected and disconcerting discovery compared to the situation during the winter of 1955, when the recordings were mainly quite smooth. About half of the records with high background showed more or less coherence, varying from long swells to short ripples. Selected samples are shown in Figure 7.

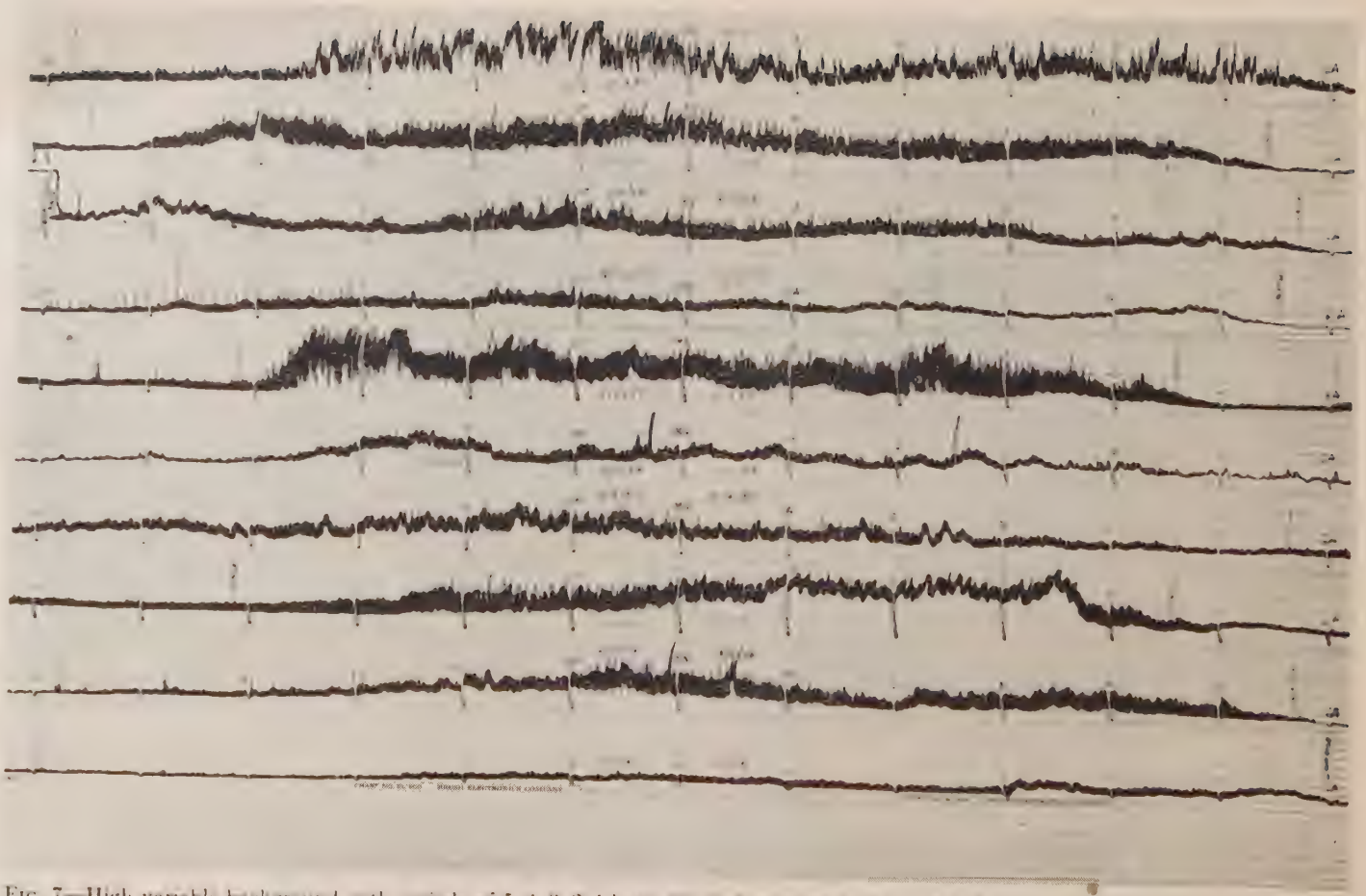

FIG. 7—High variable background with periods of 5, 4, 3, 2, 1 hour, 30, 10, 5 minutes; also samples of shutter opening briefly near midnight with abrupt onset of fluctuations near 2 a.m. and 3 a.m.

It has been suggested [4, 5] that auroral particles might produce radio-frequency radiation by the Čerenkov effect when traveling through regions of high refractive index. No visible aurora was seen in Tasmania or Australia on any of the nights shown in Figure 7. The 520-kc records taken during several minor displays showed the usual weak to moderate irregular swells, but nothing to distinguish these nights particularly.

On 24th February, 2nd and 10th March 1957, great auroral displays occurred with bright arcs and rays high overhead and to the north in Tasmania. These displays were also seen in Victoria and South Australia. On all three nights, the 520-kc equipment recorded steady smooth daytime level until the auroral display was over. Apparently, intense displays in the direction of the lower coupling level cause abnormal *D*-region absorption at night. It is clear that the auroral particles which produce the visible displays are not important in producing 520-kc radiation. This is probably because their number is too small.

It may well be that the earth is flooded with low-energy particles incapable of producing a visible aurora. During 1955, the upper coupling level was far below the gyro level, so that no regions of high refractive index were effective. During 1956 and 1957, the increase in solar activity seemed to cause the upper coupling level to hover around the gyro level and its associated very high index of refraction. Thus, these low-energy particles, which may always be present, are now effective in producing 520-kc radiation. Such was not so in 1955. It appears as though these unknown particles get bunched by a process similar to that in a klystron tube. This may account for the regular features of Figure 7. The fourth trace is particularly interesting, as the amplitude builds up over several hours until cut-off at dawn.

This high variable background also arrives from north of the zenith. The radiant is quite difficult to measure. However, the best estimate indicates a patch 10° to 15° in diameter, with a center somewhere around 30° north of the zenith. The intensity rarely exceeds ten times that of the cosmic static near 2200 hours RA as measured on the recordings. Listening discloses sounds which are typical of a smooth continuum.

Another type of fluctuation exists, which at first was confused with examples of Figure 7. This second type, however, is much smoother along the base and tends toward pointed instead of rounded tops. Most important, it passes across a sunset or sunrise time with no discontinuity whatever. It exists in an attenuated form during the day, even at noon; a couple of long-term examples show it gradually weakens from dawn to noon and then strengthens from noon to dusk. Listening discloses a steady continuous low frying sound about half-way between thermal continuum and precipitation static. The few cases tested all showed the source to be high, on the order of 45° up, in the south. Perhaps this disturbance is associated with intense examples of moderately distant precipitation static. It seems to be generated well below the *D* region, as it is only weakly influenced by such absorption during its travel to the observer.

OBSERVATIONS AT 143 KC

During June, July, and August, 1957, records were secured at 143 kc. The

results confirm the above in a general way. *D*-region absorption is markedly less. Fluctuations have a wider range of intensity which varies rapidly in an irregular fashion. The cyclic character frequently encountered at 520 kc is only found occasionally at 143 kc. The fluctuations come and go in an irregular manner. Several days of strong fluctuations may be followed by a couple of days with a complete absence of the phenomenon. No better correlation between fluctuations and the visible aurora could be found.

During quiet periods, the background level shows a characteristic diurnal pattern which begins as a minimum in the early afternoon. This is always far in excess of 300° absolute temperature. The level then rises very slowly and steadily until a couple of hours after sunset. Thereafter, a rapid increase in an hour or two brings the background up to over a hundred times the daytime level. This high level persists all night to near dawn, after which a slow and steady decline brings the background level down to a minimum the next afternoon. The only feature of the high night-time background which might be construed as of celestial origin is a small minimum near 2100 hours RA, which moved forward in mean solar time during the above limited collection of records. This night-time energy comes in from north of the zenith.

The daytime sky is bright all over, but usually brightest north of the zenith. Thus, a bit of the night-time energy is probably leaking through during the day. On some days, the bright northern patch may disappear in a period of three hours, leaving a uniformly illuminated sky. The sounds are characteristic of a smooth thermal hiss. No significant discontinuity exists in the background level at either sunset or sunrise. Fluctuations are nearly always limited to the period of high night-time background. Man-made interference appears weaker, probably because of the poorer radiating ability of the various electrical appliances.

The substantial lag between sunset and the beginning of the night-time rise in background may be due to the proposed jet [6] of gas streaming off the sunset side of the earth. No cosmic static could be seen by the observer until his radiant passes out from under the jet. Perhaps, by making simultaneous measurements at several frequencies, both higher and lower, from a variety of latitudes over the entire year, it would be possible to deduce the physical size, shape, and density throughout the stream, even beyond the counterglow. A few likely places which suggest themselves are Port Davey (Tasmania), Sawyer Creek (Macquarie Island), and some place in South Australia. Probably the celestial component can be traced down to markedly lower frequencies near solar activity minimum.

INSTALLATION

A north-south valley containing very few trees was selected about 30 miles north of Hobart. Four steel wires, each about 3/4 mile long, were strung across the valley, about 1,000 feet apart. The antennas consist of the near-center 2,200 feet of each wire. This working part is 300 feet above the bottom of the valley at the center and about 200 feet at the ends. A tuned down lead goes from the center of antenna to a tuning-box on a post directly below. A 50-ohm coaxial line from each tuner-box to the building, which is in the center of the array, is buried a few inches in the ground for protection from animals. Phase adjustment between the various antennas is made with a variety of patch cords.

The electronic equipment uses entirely 1.4-volt tubes. A minimum reading circuit between receiver and the recorder provides a downward time of 0.05 second from full to zero scale and an upward time of 50 seconds from zero to full scale. Thus, the height of the marks above the minimum are a measure of the persistence and not the strength of the atmospherics. The Brush recorder is clock-driven by the works of an Esterline-Angus instrument. A speed of 2-3/8″ of chart paper per hour has been found satisfactory.

Horizontal dipole antennas are much more desirable than loop antennas, because a well-balanced dipole is quite insensitive to vertical polarized energy such as precipitation static, atmospherics, radio transmitters, and power-line radiation. Investigation has shown that nearly all the spurious radiation from faults in the power system is vertically polarized. The entire grid system acts as an immense multiple-tuned Beverage antenna. The power-line wires form the capacity flat top. A vertical down lead in the form of an earth wire exists at each distribution transformer. Each small fault is an oscillator. Thus, the whole grid is driven by innumerable small incoherent oscillators, all synchronously modulated in a three-phase manner.

Recent extensive tests have demonstrated that all man-made electrical disturbances perceptible at 143 kc originate within a radius of 15 miles from Kempton. This was done by having the power authorities disconnect all lines within this radius, at which time only a very smooth hiss of a thermal continuum could be heard.

ACKNOWLEDGMENT

This experiment was conducted upon the properties of Neil T. Johnson and Cecil E. Johnson, at Kempton, Tasmania. The prompt and able assistance of these men in planting of anchor-posts, cutting trees, ploughing ditches, erecting sheds, adjusting fences and culverts, providing for charging of batteries, storing of equipment, and use of tractors, greatly facilitated the securing of results. It is a pleasure to record their full and free cooperation, which greatly expedited the undertaking.

The University of Tasmania is thanked for provision and use of technical and clerical facilities.

References

[1] H. Bremmer, Terrestrial Radio Waves, Elsevier Publishing Co., Amsterdam (1949); p. 284.

[2] G. Reber and G. R. Ellis, Cosmic radio-frequency radiation near one megacycle, J. Geophys. Res., **61**, 1-10 (1956).

[3] G. R. Ellis, On the propagation of radio waves through the upper ionosphere, J. Atmos. Terr. Phys., **9**, 51-55 (1956).

[4] A. A. Kolomenski, Radiation emitted by a uniformly moving electron in an electron plasma and a magnetic field, Compt. Rend. Acad. Sci. USSR, **106**, 982-985 (1956).

[5] G. R. Ellis, Low frequency radio emission from aurora, J. Atmos. Terr. Phys., **10**, 302-306 (1957).

[6] E. R. Hope, The earth's exterior atmosphere and the counterglow, translations from Russian, Defence Research Board of Canada, Pub. No. T 65 R, 3rd ed. (April 1957); particularly Figure opposite p. 16.

AN EXTENSION TO THE MODE THEORY OF VLF IONOSPHERIC PROPAGATION

By James R. Wait

National Bureau of Standards, Boulder, Colorado

(Received August 15, 1957)

ABSTRACT

The wave-guide mode theory of VLF propagation for a sharply-bounded homogeneous ionosphere is refined to include stratification at the lower edge of the ionosphere. The numerical results for a two-layer model are discussed in detail. By choosing the upper medium to have a conductivity with a factor of 10 greater than the lower medium, the attenuation *vs* frequency characteristic of the model is consistent with experimental data from 1.0 to 20 kc. The effect of the finite thickness of the *E* layer, important for frequencies less than 1.0 kc, is treated by an ionospheric model which has a sharp lower edge and an exponential taper to zero at greater heights.

Introduction

The theory of ionospheric propagation of VLF waves has received considerable attention in recent years. The representation of the field as a sum of wave-guide type modes has been quite successful in predicting field strengths of VLF transmitters at great ranges. At the original suggestion of Budden [see 1 of "References" at end of paper], the ionosphere is taken to be a plane sharply-bounded ionized medium. The author [2] has reformulated the problem in spherical coordinates, with the earth defined by a homogeneous sphere of radius a and the ionosphere represented by concentric spherical layers of differing electrical properties.

In this work, it was discovered that the so-called negative-order modes are not excited by a vertical dipole source. While this does not affect the important conclusions in Budden's papers, it does modify the numerical magnitude and variation of the field with distance from the transmitter. The nonexistent negative-order modes have been employed very recently by Hepburn [3] to explain the variation with distance of atmospheric wave-forms. This reasoning would seem to require revision.

Some confusion has also arisen as a result of the various (usually undefined) conventions of numbering modes. In the work of Wait [2] and Howe [4], the numbering is to be assigned in a way which is consistent with standard wave-guide practice. Namely, for bounding walls of very high conductivity, the mode numbering is related to the periodic variation of the field across the width of the guide. Retaining these numbers, the conductivity of the upper medium and then that of the lower medium is continuously decreased to their prescribed values. Since Budden uses a different convention, his mode numbering may differ from that of Wait and Howe.

Fortunately, mode numbering is rather an academic matter; the important thing is to sum over all modes that are excited by the source.

Most of the calculations of wave-guide modes in VLF propagation have been restricted to a sharply bounded ionosphere. The ionized region is assumed to be semi-infinite in extent. Such a model was fairly satisfactory in explaining a large body of experimental data in the frequency range from 1 to 20 kc [2]. It is the purpose of this paper to refine the model in two ways; first, the ionosphere is represented by two discrete layers, and, secondly, by an exponentially tapered layer. The two-layer model removes the objection that effective conductivity of the homogeneous ionosphere is a constant with respect to frequency, and the tapered layer is to account for the effect of the finite thickness of the E layer.

The Two-Layer Model

The earth is taken to be a homogeneous sphere of conductivity σ and dielectric constant ϵ. The lower edge of the ionosphere is taken to be at a height h and the collisional frequency ν_1 and the plasma frequency ω_1 are homogeneous up to a height $h + d$, whereupon they change abruptly to ν_2 and ω_2 , respectively. The situation is illustrated in Figure 1*A* and 1*B*.

Assuming that the source is a vertical dipole radiating P kilowatts, the vertical electric field in millivolts per meter at the great-circle distance $\bar{d}$ in kilometers is given by the mode sum [2].

$$E = E_0 W$$

where

$$\left.\begin{aligned} W &= \left[\frac{(\bar{d}/a)}{\sin(\bar{d}/a)}\right]^{1/2} \frac{(\bar{d}/\lambda)^{1/2}}{(h/\lambda)} \exp\left\{i\left[\frac{2\pi\bar{d}}{\lambda} - \frac{\pi}{4}\right]\right\} \sum_{n=0}^{\infty} \delta_n S_n^{3/2} \exp\{-2\pi S_n(\bar{d}/\lambda)i\} \\ E_0 &= \frac{300\sqrt{P}}{d}, \qquad \delta_n = \left[1 + \frac{\sin(4\pi C_n h/\lambda)}{(4\pi C_n h/\lambda)}\right]^{-1} \end{aligned}\right\} \quad (1)$$

where $S_n = (1 - C_n^2)^{1/2}$ and C_n is a solution of

$$R_g(C)\bar{R}_i(C) \exp(-4\pi i C h/\lambda) = \exp(-i2\pi n) \quad (2)$$

where $R_g(C)$ is the Fresnel reflection coefficient at the ground for a plane wave whose (complex) angle of incidence is the arc cosine of C and $\bar{R}_i(C)$ is the corresponding Fresnel reflection coefficient at the lower edge of the ionosphere.

It follows from a previous analysis [6] that

$$R_g(C) = \frac{(KG - i)C - [(K - 1)G^2 - iG + C^2G^2]^{1/2}}{(KG - i)C + [(K - 1)G^2 - iG + C^2G^2]^{1/2}} \quad (3)$$

where $K = \epsilon/\epsilon_0$ and $G = (\epsilon_0\omega)/\sigma$ and

$$\bar{R}_i(C) = \frac{N_1^2 C - (N_1^2 - S^2)^{1/2} Q}{N_1^2 C + (N_1^2 - S^2)^{1/2} Q} \quad (4)$$

with

$$Q = \frac{N_1^2(N_2^2 - S^2)^{1/2} + N_2^2(N_1^2 - S^2)^{1/2} \tanh[i2\pi(d/\lambda)(N_1^2 - S^2)^{1/2}]}{N_2^2(N_1^2 - S^2)^{1/2} + N_1^2(N_2^2 - S^2)^{1/2} \tanh[i2\pi(d/\lambda)(N_1^2 - S^2)^{1/2}]} \quad (5)$$

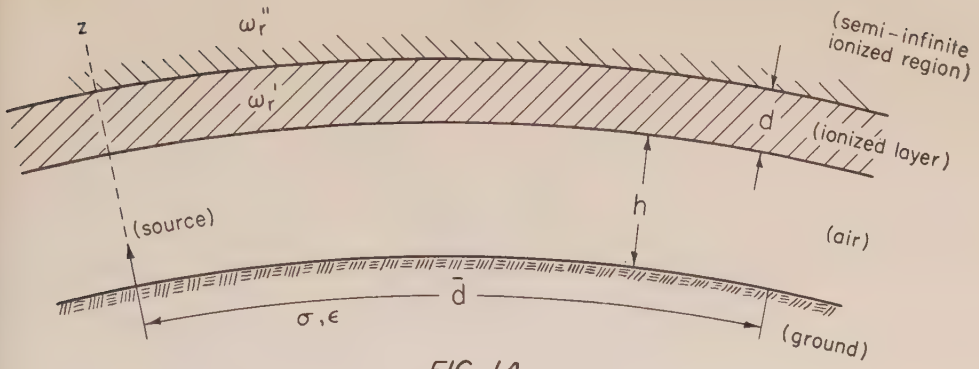

FIG. 1A

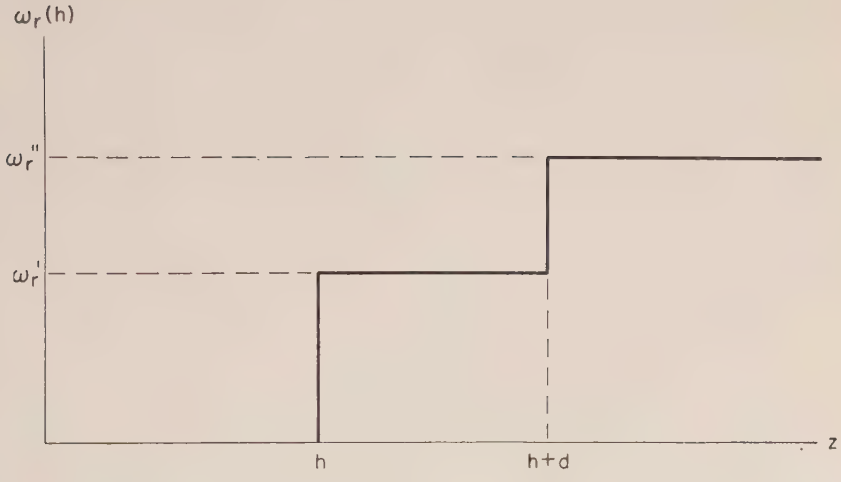

FIG. 1B

FIG. 1—(*A*) Stratified model for ionosphere; (*B*) ω_r as a function of height for stratified model

where*

$$N_1^2 \cong 1 - i/L_1 = 1 - i(\omega_r'/\omega), \qquad \omega_r' = \omega_1^2/\nu_1$$

$$N_2^2 \cong 1 - i/L_2 = 1 - i(\omega_r''/\omega), \qquad \omega_r'' = \omega_2^2/\nu_2$$

The complex values of S_n ($n = 0, 1, 2, \cdots$) satisfying equation (2) have been obtained from an automatic computer, using a program devised by Dr. H. H. Howe.

*These expressions for the effective refractive index which tacitly neglect the earth's magnetic field are valid for VLF and small values of C.

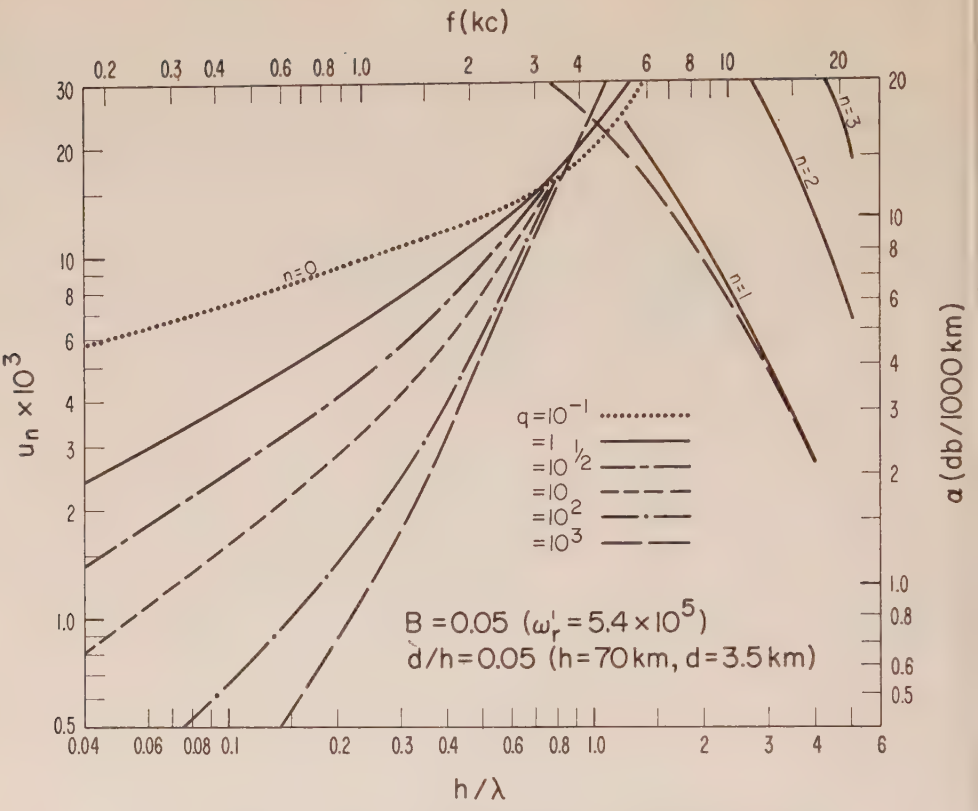

FIG. 2—Values of u_n as a function of h/λ, for $B = 0.05$ and $d/h = 0.05$

When L_1 and L_2 are small compared with unity, it was shown previously that

$$S_n \cong \left[1 - \left(\frac{\lambda n}{2h}\right)^2\right]^{1/2} - \frac{\lambda}{4\pi h} e^{i3\pi/4}(G^{1/2} + Q_0 L^{1/2}) \frac{\bar{\epsilon}_n}{\left[1 - \left(\frac{\lambda n}{2h}\right)^2\right]^{1/2}} \quad \ldots\ldots(6)$$

where $\bar{\epsilon}_0 = 1$, $\bar{\epsilon}_n = 2$ $(n \neq 0)$ and

$$Q_0 \cong \frac{N_1 + N_2 \tanh [i2\pi N_1 d/\lambda]}{N_2 + N_1 \tanh [i2\pi N_1 d/\lambda]} \quad \ldots\ldots(7)$$

and $N_1 \cong e^{-i\pi/4}/\sqrt{L_1}$ and $N_2 \cong e^{-i\pi/4}/\sqrt{L_2}$.

The above formula for S_n is particularly suitable for very low frequencies, in which case only the zero mode is of any consequence.

The exponential term inside the summation of equation (1) determines, in the main, the propagation characteristics of the modes. It can be rewritten as follows:

$$| \exp [-i2\pi S_n(\bar{d}/\lambda)] | = \exp\left[-\frac{2\pi\bar{d}}{h} u_n\right] \quad \ldots\ldots(8)$$

where $u_n = -$ Im $S_n(h/\lambda)$, u_n is a dimensionless measure of the attenuation per unit distance, and Im indicates that the imaginary part is to be taken.

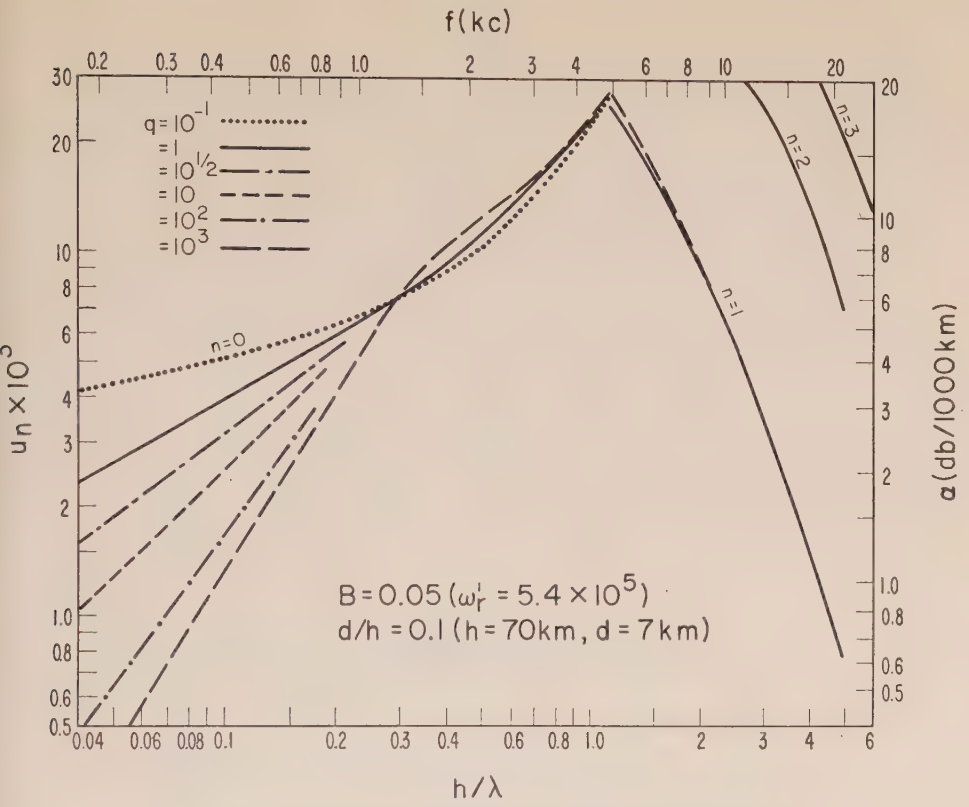

FIG. 3—Values of u_n as a function of h/λ, for $B = 0.05$ and $d/h = 0.1$

Values of $u_n (n = 0, 1, 2, \text{and } 3)$ are plotted in Figures 2 to 7 as a function of h/λ, for various values of B [$= L_1\lambda/h = 2\pi c/(\omega_r' h)$] and the ratio d/h. For these results, the earth is assumed to be perfectly conducting. This is justified for propagation over sea water [2].

In each Figure, the solid line corresponds to the sharply-bounded homogeneous ionosphere and the other curves are for the two-layer ionosphere. The ratio of ω_r''/ω_r' is denoted by q and varies from 10^{-1} to 10^3 in each Figure. When the height is specified, u_n can be converted to decibels per 1,000 km of path length and h/λ can be converted to frequency in kilocycles per second. Such scales are appended in Figures 2 to 7 for $h = 70$ km, where B values of 0.05, 0.1, and 0.2 now correspond to ω_r' values of 5.4, 2.7, and 1.35 $\times 10^5$, respectively. The two values of d are then 3.5 and 7.0 km. For any other assumed height, h, the scales for frequency and attenuation are changed correspondingly.

Some interesting observations can be made from the numerical results. At the higher frequencies (8 to 18 kc), the attenuation rate is determined almost entirely from the electrical properties of the medium between heights h and $h + d$. Physically, this means that the incident energy does not penetrate to the upper medium above $h + d$. On the other hand, at the lower frequencies (less than 3 kc), the attenuation rate is almost entirely controlled by the electrical properties of

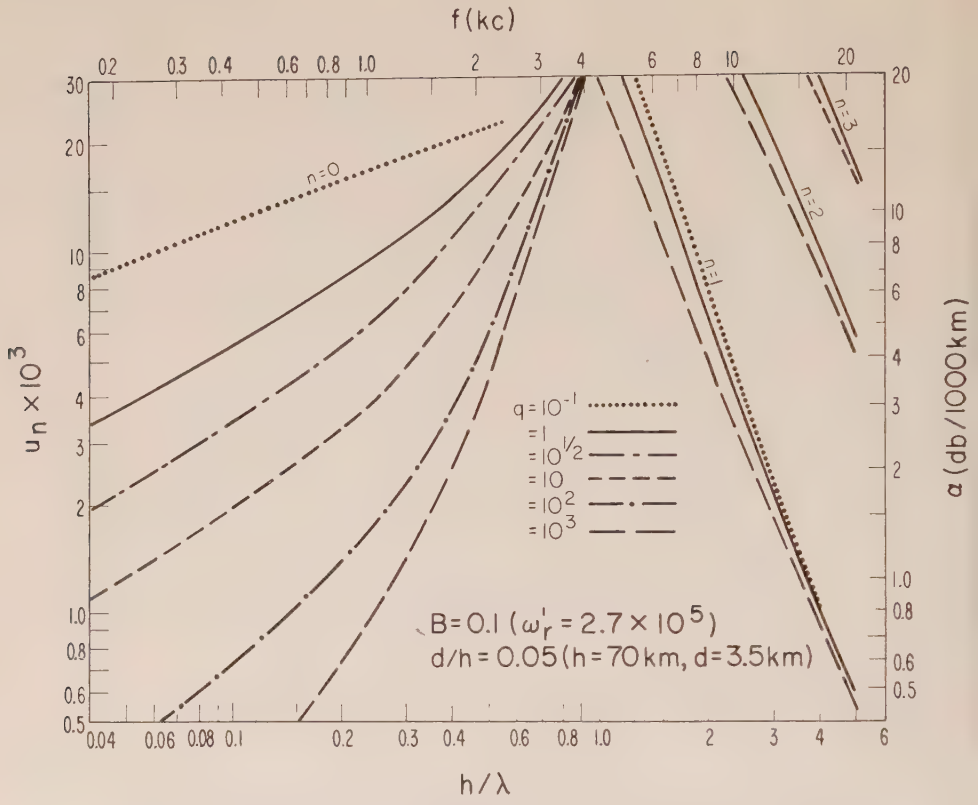

FIG. 4—Values of u_n as a function of h/λ, for $B = 0.1$ and $d/h = 0.05$

the upper medium. In this case, the incident energy penetrates through the lower medium with negligible loss and the reflection takes place almost wholly at $h + d$.*

Experimental data [5, 7] on the attenuation rates of VLF waves in daytime indicate that α is about 2 db/1,000 km at 10 kc, greater than 10 db between 3 and 4 kc, and again about 2 db at 500 c/s. The two-layer model that best fits this data is shown in Figures 4 and 5, where $\omega_r' = 2.7 \times 10^5$ and either $d = 3.5$ km and $q = 10$ or $d = 7$ km and $q = 100$. This removes the first objection to the single-boundary homogeneous ionosphere, namely, that the effective value of ω_r was different at the high and low end of the VLF spectrum.

Unfortunately, extensive and reliable experimental data on attenuation rates at frequencies in the range below 1 kc are not available. It is possible that new experimental data will modify our present choice of a suggested two-layer model.

The Exponentially Tapered Model

In general, the attenuation rate at extremely low frequencies (less than 1 kc) varies as the square root of frequency. There is some evidence [8] indicated, however, that this law does not hold as the frequency becomes even lower. For example,

*L. N. Lieberman [7a] reasons that the higher frequencies (>10 kc) exhibit greater penetration than the lower frequencies. This is not substantiated by the present results.

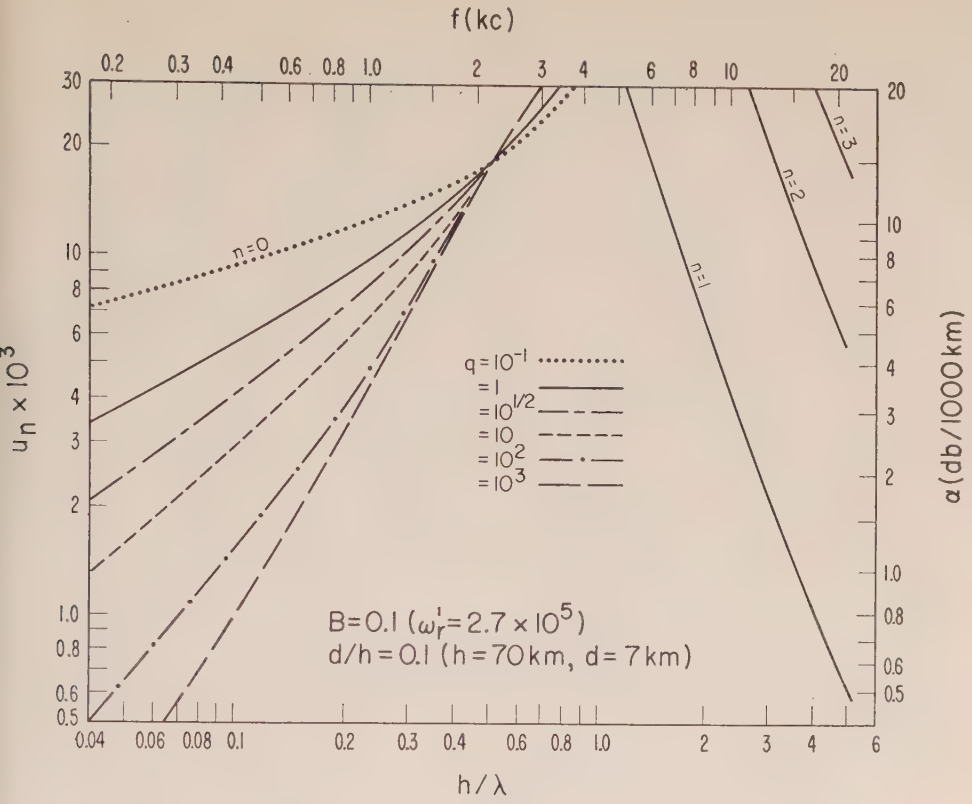

FIG. 5—Values of u_n as a function of h/λ, for $B = 0.1$ and $d/h = 0.1$

the attenuation rate seems to reach a minimum value around 100 c/s. A possible explanation is that the E layer is no longer behaving as a semi-infinite medium. A suggested model for propagation in this extremely low frequency range is an ionosphere with a sharply-bounded lower edge at a height h; above this value, the value of $\omega_r(z)$ at height z is to taper exponentially from an initial value $\tilde{\omega}_r$ to a final value of zero at infinite height, such that

$$\omega_r(z) = \tilde{\omega}_r e^{-2z/s} \quad \text{for} \quad z > h, = 0 \quad \text{for} \quad z < h$$

The situation is illustrated in Figure 8*A* and 8*B*.

By a straightforward extension of the two-layer model, it is not difficult to show that the solution for the zero mode for $\bar{L} \ll 1$, is given by **

$$S_0 \cong 1 - i\frac{\lambda}{4\pi h}(\sqrt{\bar{L}}\, e^{i\pi/4}\bar{Q}) \qquad (9)$$

**The reflection coefficient for an exponentially varying medium can be expressed in closed form [9].

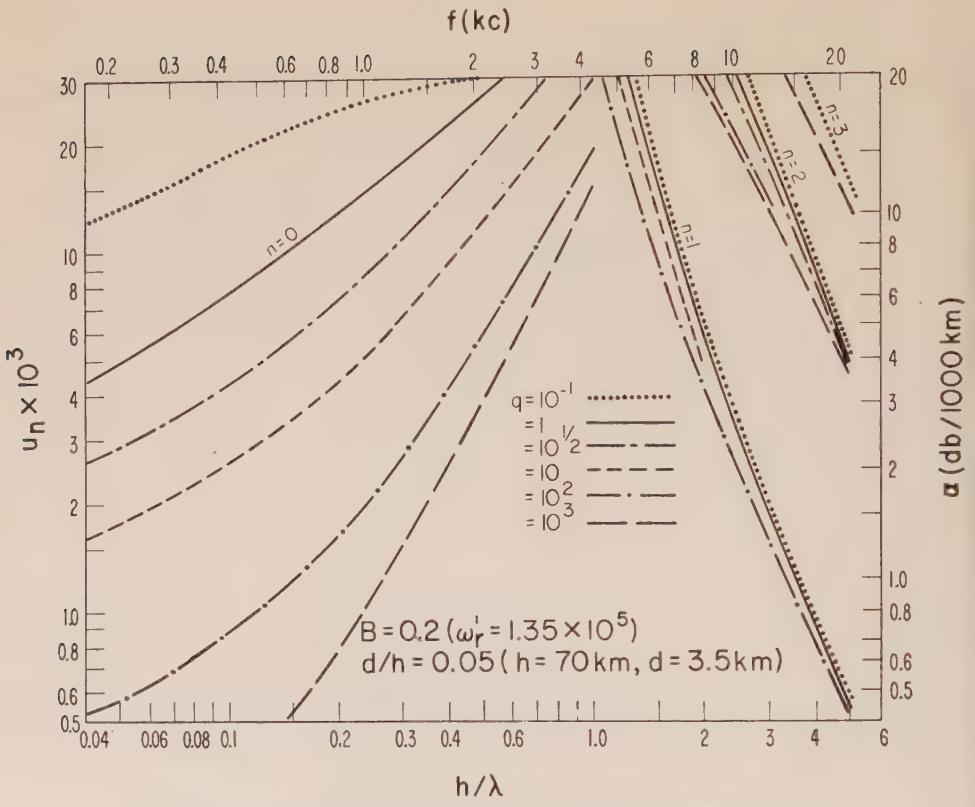

FIG. 6—Values of u_n as a function of h/λ, for $B = 0.2$ and $d/h = 0.05$

where

$$\bar{L} = \frac{\omega}{\bar{\omega}_r}, \qquad \bar{Q} = \frac{I_0(\sqrt{i}\beta)}{I_1(\sqrt{i}\beta)} \quad \text{and} \quad \beta = (\bar{L})^{-1/2}\frac{\omega}{c}s$$

In the above, I_0 and I_1 are modified Bessel functions of the first type and the quantity s is a scale factor which represents a scale thickness of the E layer. For purposes of computation, the following formula is used

$$u_0 \cong \frac{\sqrt{\bar{L}}}{4\pi\sqrt{2}} P(\beta) \qquad (10)$$

where

$$P(\beta) = \frac{\text{ber}\,\beta\,\text{bei}'\,\beta - \text{bei}\,\beta\,\text{ber}'\,\beta}{(\text{ber}'\,\beta)^2 + (\text{bei}'\,\beta)^2}$$

in terms of the Thomson ber and bei functions and their derivatives. Assuming that $h = 90$ km, the attenuation rate in db/1,000 km is shown plotted in Figure 8 as a function of frequency from 50 c/s to 1 kc for values of s from 10 km to ∞ and $\bar{\omega}_r$ values of 10^5 and 10^6. It is seen that as s approaches infinity the attenuation rate becomes identical to that for a semi-infinite ionosphere. Smaller values of s

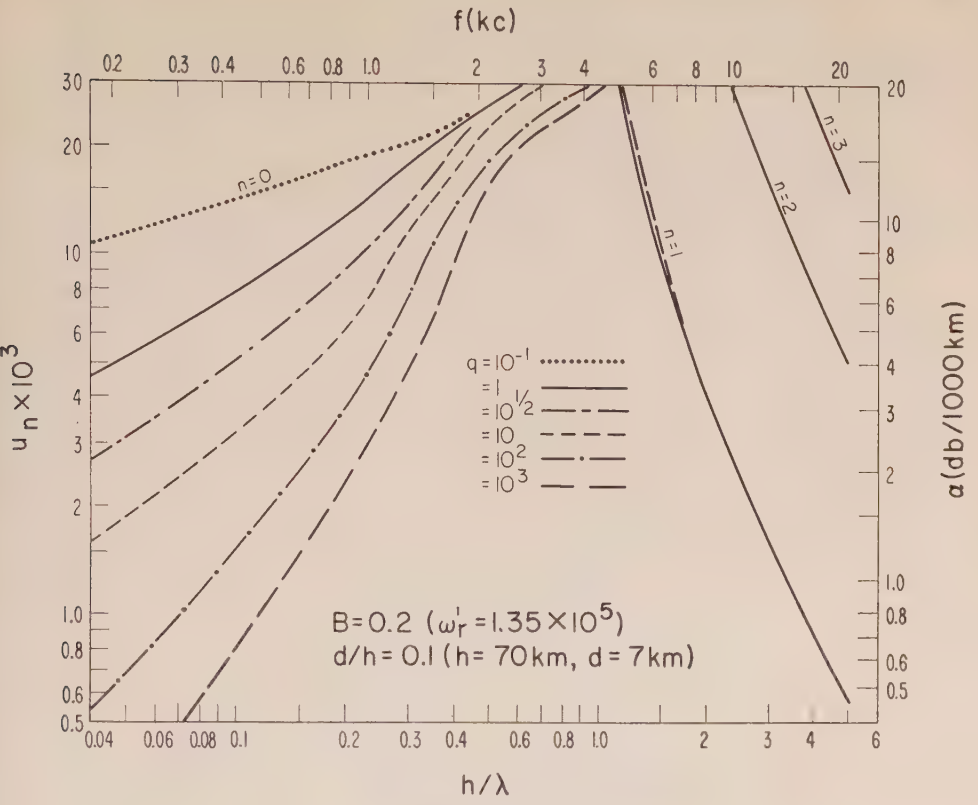

FIG. 7—Values of u_n as a function of h/λ, for $B = 0.2$ and $d/h = 0.1$

correspond to a more rapid decline of ω_r with height. On the basis of Holzer's [8] results, it could be expected that s should be of the order of 30 km. It is interesting to note that this exponential model would predict that the attenuation rate is essentially independent of frequency at the lower end of the VLF band. Further experimental data will no doubt revise this initial estimate of the value of the scale distance s.

Conclusion

The numerical results presented here for the two-layer model should be useful in interpreting experimental data for attenuation rates of VLF waves in the frequency range from 1 to 20 kc. Until more direct measurements are available for electron densities and collisional frequencies at the lower edge of the ionosphere, it would seem hardly justified to assume a more elaborate model. At the extremely low frequencies (less than 1 kc), however, it is expected that, while the E layer has a sharp lower boundary, the effective conductivity will taper to zero for greater heights in a gradual manner. It is possible that the finite thickness of this layer is an explanation for the minimum attenuation at frequencies of the order of 200 c/s, although it is admitted that the influence of the F layer could also be important.

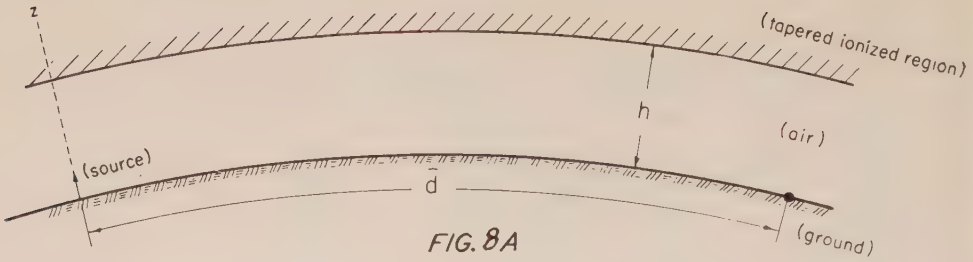

FIG. 8A

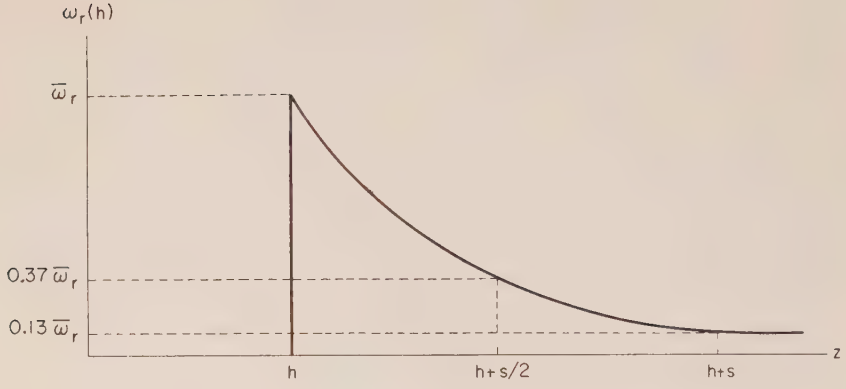

FIG. 8B

FIG. 8—(*A*) Exponential model for ionosphere; (*B*) ω_r as a function of height for exponential ionosphere (ω_r tapers to e^{-1} at $z = h + s/2$ and e^{-2} at $z = h + s$)

Acknowledgment

I would like to thank Dr. H. Bremmer for reading the manuscript and his helpful suggestions.

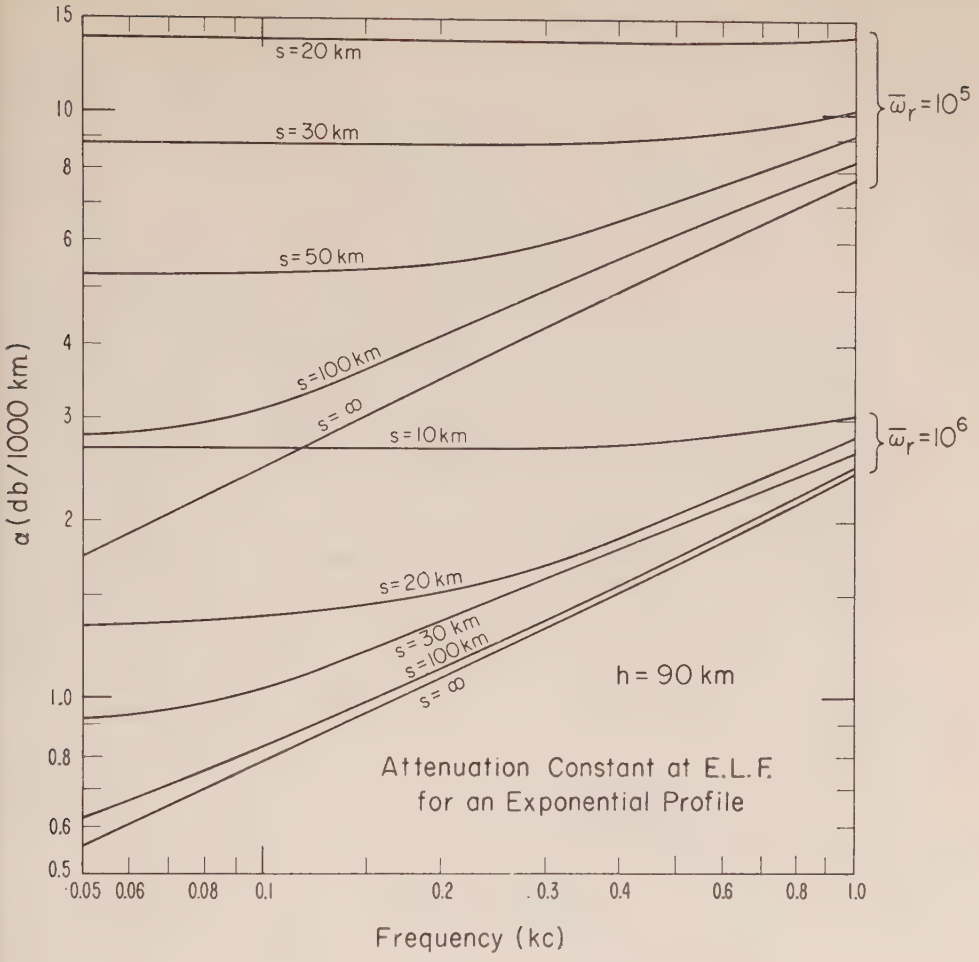

FIG. 9—Attenuation rate as a function of frequency, assuming $h = 90$ km

References

[1] K. G. Budden, Phil. Mag., **42**, 833 (1951) and **43**, 1179 (1952).
[2] J. R. Wait, Paper No. 6, Proceedings V.L.F. Symposium, Boulder, Colorado, January 1957; also Proc. Inst. Radio Eng., **45**, 760 and 768 (1957).
[3] F. Hepburn, J. Atmos. Terr. Phys., **10**, 121 (1957).
[4] H. H. Howe and J. R. Wait, Paper No. 36, Proceedings V.L.F. Symposium, Boulder, Colorado, January 1957.
[5] A. D. Watt, Proc. Inst. Radio Eng., **45**, 787 (1957).
[6] J. R. Wait, Paper presented at Wave Propagation (URSI) Meeting, Paris, September 1956, Geofisica pura e appl., **37**, 103 (1957).
[7] F. W. Chapman and R. C. Macario, Nature, **177**, 930 (1956).
[7a] L. N. Liebermann, J. Appl. Phys., **27**, 1477 (1956).
[8] R. E. Holzer, O. E. Deal, and S. Rutlenberg, Paper No. 45, Proceedings V.L.F. Symposium, Boulder, Colorado, January 1957.
[9] J. R. Wait, J. Appl. Phys., **23**, 1403 (1952).

INFERENCES CONCERNING THE DYNAMICS OF THE MESOSPHERE*

BY ROBERT G. FLEAGLE

University of Washington, Seattle 5, Washington

(Received September 24, 1957)

ABSTRACT

In earlier work, the development of large-scale atmospheric disturbances has been shown to depend in an explicit manner on horizontal density gradient, static stability, latitude, and dimensions of the disturbance. This theoretical analysis is generalized by eliminating the dimensions of the disturbance. The result is verified by comparing theory with tropospheric observations; then, on a reasonable postulate, the theory is applied to determination of the instability of small disturbances in the region between heights of 20 and 80 km, the mesosphere. The results indicate that in the statically stable mesoincline large-amplitude disturbances are limited to the polar regions and must develop slowly. In the statically less-stable mesodecline, disturbances also are limited to the middle and high latitudes, but they may grow much more rapidly. The marked selectivity which the troposphere exhibits for disturbances three to five thousand kilometers in length occurs in the mesodecline in winter, but in summer there is only very weak preference for a wave number of two at about 65° latitude. It is inferred that summer disturbances in the mesodecline probably develop more rapidly than do disturbances in the troposphere, but that they undergo rapid change in form and size, so that they may quickly lose their identity.

Introduction

Recent developments in upper-air sounding techniques are providing more and more reliable data from which the structure and the behavior of the upper atmosphere may be determined. Direct observation, however, has far to go before it can yield detail comparable to the detail with which we regularly observe the lower atmosphere. The ceiling of our observations is rising, but we have not gone much beyond the state where, like rational but naive fish, we inspect the hulls of ships moving above us and speculate on the nature of the ships, their engines, and their crews. This paper, then, represents a particular fish's deductions as to what is going on above him.

Certain deductions concerning the mean velocity field in the upper atmosphere

*Contribution No. 30, Department of Meteorology and Climatology, University of Washington. Read at the Eleventh General Assembly, International Union of Geodesy and Geophysics, Toronto, September 6, 1957.

have been made by Kellogg and Schilling [See 1 of "References" at end of paper], Brasefield [2], Palmer [3], Pant [4], and others. Their results are applied here to the problem of determining the dominant forms of the large-scale disturbances, if any, which may be superimposed on the mean velocity field in the region between about 20 km and 80 km, the region known as the mesosphere. To determine these forms from observation would require for the mesosphere synoptic observations of wind velocities at regular intervals and over large areas. These observations will certainly not be available in the immediately foreseeable future. At the same time, one should recognize that definitive answers to questions concerning the effect of extra-terrestrial events on tropospheric weather may require just this sort of detail. For this reason, as well as for the general interest of the problem, the attempt will be made to apply the theory of planetary aerodynamics to the conditions of the upper atmosphere. Successful application of the theory should provide a far more accurate description of the velocity field than is now known from observations alone and it should provide an understanding of the behavior in terms of fundamental physical principles.

To extend quite generally the theory of planetary aerodynamics to the upper atmosphere would require description of the undisturbed temperature field as a complicated function of height and latitude. The difficulty encountered by Kuo [5] and others in the linear problem and by Phillips [6] in the non-linear problem for the much simpler case of a constant lapse-rate makes this procedure unattractive, although eventually it will have to be followed. The objective of this paper is much more modest; it rests on, instead of a general mathematical treatment, a postulate which appears to be plausible. Separately stratified layers like the troposphere, the mesoincline, and the mesodecline will be assumed to behave independently of one another in so far as disturbances which grow to maturity in less than a few days are concerned. More exactly, the postulate requires that the boundaries between these layers might be replaced by horizontal rigid boundaries without invalidating the major results as they apply to unstable periodic solutions which double in amplitude in roughly one day. The evidence which supports the postulate comes from observations in the region of the boundary between troposphere and stratosphere, from a recent theoretical study of the effect of the stratosphere by Gates [7], and from intuitive considerations of the energy transformations required if the pattern of vertical velocity in one layer were to extend to a layer of contrasting baroclinity.

The Method

Recent studies of the general circulation of the troposphere have been successful in explaining for the first time certain dominant features of the circulation as consequences of the baroclinity and static stability of the atmosphere. The interrelation of papers which have contributed to this advance is so complex that the direct antecedents of the ideas expressed in this paper cannot be adequately cited here. However, neither can one fail to mention the seminal work of Eady, Bolin, Starr, Kuo, Lorenz, Fultz, and Phillips, whose studies of the general circulation have in the past eight years brought that important subject from the

level of primitive speculation to the level of reasonably complete description and understanding.

In a study of the dynamics of the general tropospheric circulation, the author (Fleagle [8]) has suggested that small tropospheric disturbances poleward of a critical latitude should increase in amplitude and form vortices roughly 4,000 km in horizontal extent, whereas disturbances in the tropics should develop only in areas of neutral static stability and should be limited to small horizontal extent. The middle- and high-latitude disturbances should grow at rates such that they may double in amplitude in time intervals of a day or so. "Jet streams" should form just poleward of the critical latitude. Because these baroclinic disturbances are rather highly selective with respect to horizontal dimension, one may consider that the dimension of greatest instability grows most rapidly and therefore dominates. On this basis, the number of disturbances at any one latitude (wave number) should decrease from about 10 at 45° latitude to 3 at 70° and 2 at 80°. These results arose from the linearized hydrodynamic equations for a spherical earth applied to a stream-surface of greatest slope.

The correspondence between the results just summarized and certain of the most characteristic features of tropospheric disturbances suggests that the theory may be of general validity so that it might be applied to the upper atmosphere or to planetary atmospheres other than our own. These applications require consideration of a wide range of static stability and of baroclinity.

Application to Upper Atmosphere

In the work referred to (Fleagle [8]), the amplitude of unstable disturbances is characterized by an exponential increase with time. The time coefficient has been shown to be given by

$$\sigma_i = \frac{ml\gamma(lU_z + \beta s_z/l\gamma)^{1/2}}{a\cos\varphi(2s_z\alpha^2 + g\gamma^2 l^2)}\,[lU_z - \beta(s_z/l\gamma + g\gamma l/\alpha^2)]^{1/2} \quad \ldots\ldots\ldots (1)$$

where the following notation is used:

m = zonal wave number
l = absolute vorticity of the undisturbed current about a vertical axis (roughly the Coriolis parameter)
γ = coefficient of piezotropy
a = radius of earth
φ = latitude
s_z = static stability
U_z = vertical shear of the undisturbed zonal wind (baroclinity)
β = $(1/a)\partial l/\partial\varphi$
g = gravitational acceleration
$\alpha^2 = \left[\dfrac{m^2 - \sin^2\varphi}{\cos^2\varphi} + \nu^2\right] \Big/ a^2$
ν = meridional wave number
c = wave speed toward the east

In Figure 1, σ_i computed from equation (1) is represented as a function of baroclinity and wavelength or wave number for latitude of 45° and a vertical gradient of potential temperature of four and a half degrees per 100 mb. The region of positive baroclinity has been discussed by Charney [13], Kuo [5, 12], and others, as well as by the author; however, the finite baroclinity required for instability has not always been recognized. The region of negative baroclinity has not previously been described, so far as is known to the author. In this region, the same critical baroclinity is required at all wavelengths, and, except for the fact that short waves are relatively stable, there is very little variation of instability with wavelength. For very large negative baroclinity, the wavelength of maximum instability decreases with baroclinity rather sharply. If instabilities of opposite sign are compared, it is evident that, for the same absolute values, negative baroclinity yields greater rate of growth than does positive baroclinity.

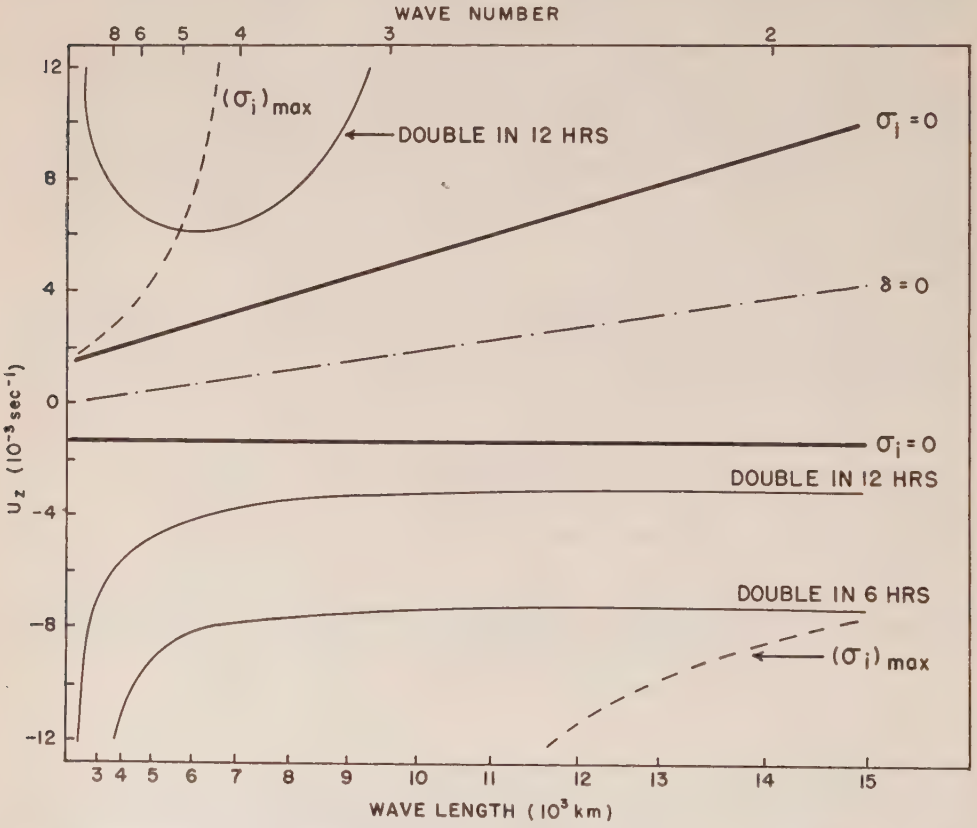

FIG. 1—Distribution of amplification of unstable waves (σ_i) calculated from equation (1) as a function of vertical wind shear (U_z) and wavelength or wave number

Equation (1) differs from similar equations developed by Fjörtoft [9], Thompson [10], and others in several respects. For example, as pointed out in an earlier paper (Fleagle [11]), Fjörtoft and Thompson found that short waves are stable,

whereas equation (1) shows that short waves are unstable. On the other hand, Kuo [5, 12], in the most general of the various studies of this subject, found that short waves are unstable. This difference in results probably is to be attributed to the fact that Fjörtoft and Thompson assumed the existence of characteristic horizontal surfaces on which the vertical velocity was prescribed, whereas Kuo and Fleagle made no such assumption. A second difference is of interest here; namely, Fjörtoft's and Thompson's equations indicate identical instability for positive and negative baroclinities of equal absolute magnitude, whereas equation (1) and Kuo's [12] equations indicate different degrees of instability in the two cases. Presumably, the behaviour of Fjörtoft's and Thompson's models in this case also is to be attributed to the characteristic horizontal surfaces assumed in their models, although it would be very difficult to demonstrate this in a thoroughly convincing manner. It is surely preferable to avoid the introduction of such surfaces wherever possible.

The line labeled $\delta = 0$ separates positive stream-surface slope from negative. One may visualize the slope as increasing positively as one moves counter-clockwise and as increasing negatively as one moves clockwise from $\delta = 0$; for instability, slope exceeding a critical value $(\beta/gl\gamma)$ is required. Along the curves $(\sigma_{i\ max})$, the slope of the stream-surface is about one-half the slope of the isentropic surface; and, as the vertical axis is approached, the stream-surface slope approaches the slope of the isentropic surface.

The clear inference to be drawn from Figure 1 is that in layers where temperature increases toward the pole there is a possibility of rather rapid development of large-scale disturbances which have only very weak wavelength selectivity.

If equation (1) is differentiated with respect to α^2, the wave number of greatest instability is found to be, for ν equal to zero,

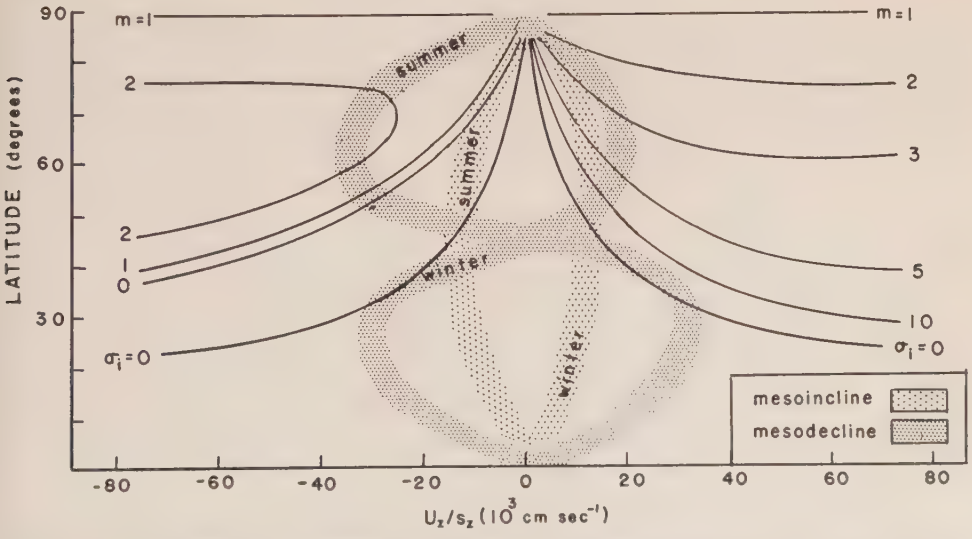

FIG. 2—Wave number (m) of greatest amplification calculated from equation (2) as a function of latitude and vertical wind shear divided by static stability (U_z/s_z). The stippled lines indicate approximately the ratio U_z/s_z given by Pant [4].

$$m_{\max} = a\gamma l \cos\varphi \left[\frac{g}{2s_z}\frac{U_z/s_z + 3\beta/\gamma l^2}{U_z/s_z - \beta/\gamma l^2}\right]^{1/2} \quad \ldots\ldots\ldots\ldots\ldots\ldots (2)$$

In Figure 2, the wave number of greatest instability is shown as a function of U_z/s_z and latitude. A value of 10^{-7} sec^{-1} has been used for s_z where it appears other than in combination with U_z. The decrease of tropospheric wave number with latitude is indicated clearly on the right side of the diagram. The bounding lines represent the critical latitudes below which small amplitude disturbances are stable. Unstable disturbances may form in the region between the critical curve on the left and the curve $m = 0$, but in this region instability increases with wavelength without limit.

In the mesoincline, between 20 and 55 km, according to Kellogg and Schilling [1], Pant [4], and others, U_z is positive in winter and negative in summer. The ratio U_z/s_z is probably no greater than 5 to 10 $\times$ 10^3 cm sec^{-1} in either season. Figure 2 shows that in both seasons, the critical latitude is situated in the polar regions; in summer, instability increases with wavelength, so that a wave number of only one is probable. In the mesodecline, between 55 and 75 km, Pant indicates that in winter U_z/s_z is probably negative at low latitudes and positive at high latitudes; whereas in summer the signs are reversed. The absolute values are much larger than 10^4 cm sec^{-1}. The hatched lines indicate approximate distributions of U_z/s_z in the mesoincline and mesodecline, according to Pant [4]. The intersections of the hatched lines with wave-number lines show the wave numbers to be expected at particular latitudes.

If m or α is eliminated from equation (1) by use of equation (2), the time coefficient of growth is expressed by

$$(\sigma_i)_{\max} = \pm\frac{lU_z/s_z - \beta/\gamma l}{2\sqrt{2g/s_z}} \quad \ldots\ldots\ldots\ldots\ldots\ldots (3)$$

where the positive sign is taken with positive U_z and the negative with negative U_z. In Figure 3, the time coefficient computed from equation (3) is shown as a function of U_z/s_z and latitude. Doubling of amplitude in 24 hours is represented by lines labeled "2", etc. Figure 3 shows that, holding U_z/s_z constant, in the region of positive U_z, instability increases from the critical latitude poleward; in the region of small negative U_z, instability decreases with latitude; and for large negative U_z, instability exhibits a maximum at 70° to 80°. From Figure 3, one may infer that in the troposphere greatest instability should occur at 60° to 70° latitude, and the characteristic increase in amplitude should be doubling in about a day. In the mesoincline, instability is possible only poleward of 50° in both winter and summer, and is small in magnitude. In the mesodecline, maximum instability occurs at roughly 60° in both winter and summer, but rate of growth should be larger in summer than in winter. Because the region of negative baroclinity is very weakly dependent on dimension, one should not expect accurate verification of equation (3) in the summer.

Accompanying the seasonal change from positive to negative baroclinity is a seasonal change from west winds in winter (for the most part) to east winds in summer. According to the theory used here, rate of growth is unaffected by the sign or magnitude of the zonal speed; but the wave speed is affected by both the

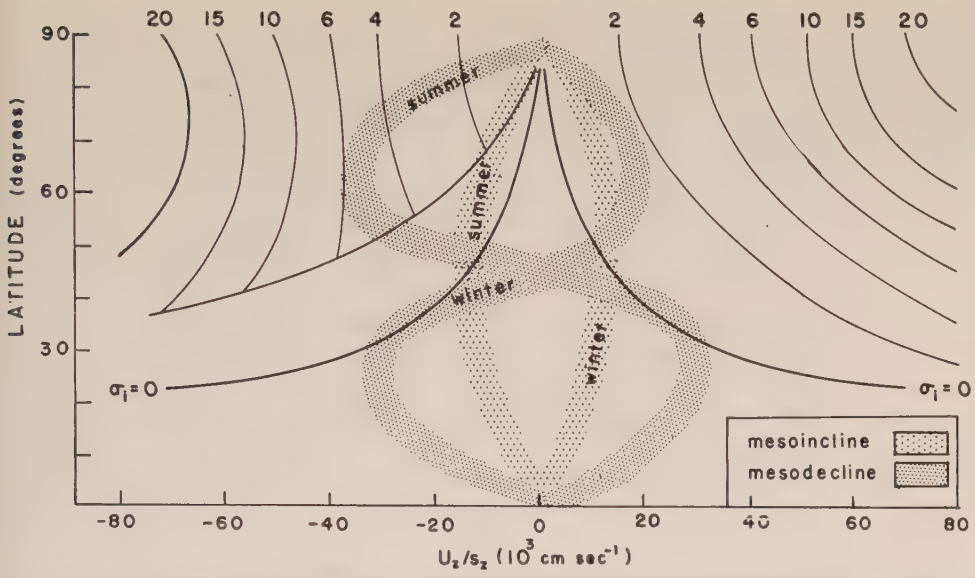

FIG. 3—Amplification in 24 hours calculated from equation (3) as a function of latitude and vertical wind shear divided by static stability (U_z/s_z). The stippled lines indicate approximately the ratio U_z/s_z given by Pant [4].

baroclinity and the zonal speed. Equation (29) given by Fleagle [8] expresses the wave speed in terms of U_z/s_z, φ, and α^2. If α^2 is eliminated by use of equation (2), the wave speed of maximum rate of growth for the case where meridional wave number can be neglected compared to zonal wave number is

$$c_{max} = U - \frac{U_z/s_z - \beta/\gamma l^2}{2g\gamma/s_z} \quad \ldots\ldots\ldots\ldots\ldots\ldots\ldots\ldots (4)$$

Figure 3 may be used as a rough indication of the dependence of U-c_{max} on latitude and baroclinity. From equation (4), one may conclude that, in winter, disturbances in both mesoincline and mesodecline should move more slowly than the positive zonal current, as they do in the troposphere. An exception should be noted at about 30° latitude, where weak disturbances may move faster than the zonal wind.

In summer, mesoincline and mesodecline should be distinguished. In the mesoincline, at high latitude the zonal current is small and the two terms in the numerator of equation (4) yield a small negative value, so that disturbances should move slowly toward the east. In the mesodecline, at high latitude the fractional term on the right should be large and negative and the zonal wind is large and negative. Therefore, the speed of disturbances probably is small, but the direction of movement is uncertain.

The meridional slope of the stream-lines which permit maximum conversion of potential to kinetic energy may be shown to be equal to one-half the slope of the potential temperature surfaces. It is given by

$$\delta = \frac{lU_z}{2gs_z} \quad \ldots\ldots\ldots\ldots\ldots\ldots\ldots\ldots\ldots\ldots (5)$$

Equation (5) approximates with sufficient accuracy for this discussion the slope given by more accurate, but more complex, equations. In Figure 4, the projections of stream-lines on a vertical meridional cross-section are shown for troposphere, mesoincline, and mesodecline. The outstanding feature shown in Figure 4 is the shift from marked subsidence toward the pole (ascent toward the equator) in summer to subsidence toward the equator (ascent toward the pole) in winter.

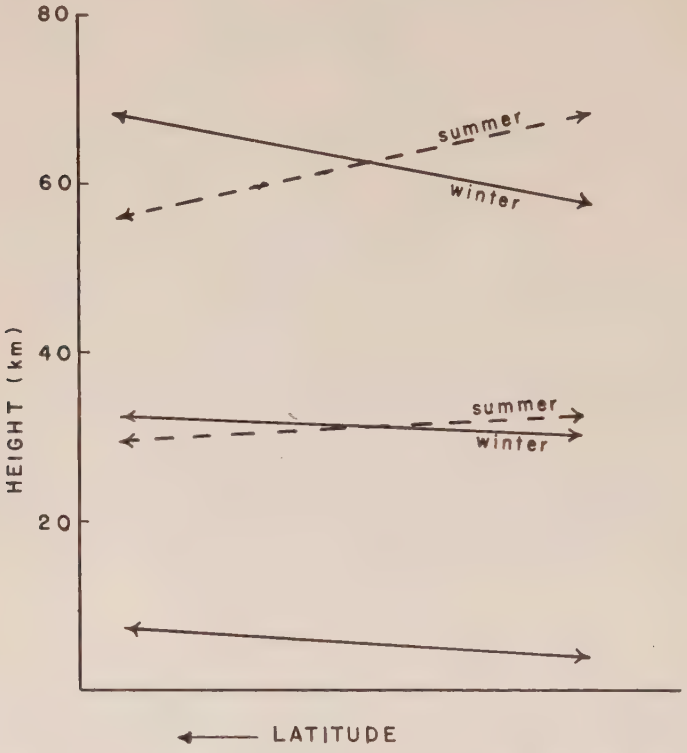

FIG. 4—Approximate slopes of the stream-lines of unstable disturbances projected onto the vertical-meridional plane calculated from equation (4), using U_z/s_z given by Pant [4]

Inferences and Discussion

Certain generalizations regarding the mesosphere are permitted, indeed invited, by the results shown in Figures 1, 2, 3, and 4. In the mesoincline, where U_z is negative in summer and positive in winter and s_z large and positive, unstable disturbances should be infrequent, but should be expected occasionally at high latitude, particularly in winter when latitudinal temperature gradient is large and static stability relatively small. There should be only one or two major disturbances in the northern hemisphere at any one time, and these should grow in amplitude very slowly.

In the mesodecline, where at latitudes above 40° U_z/s_z is assumed to be large and negative in summer, smaller and positive in winter, conditions should be very different. In summer, wave numbers should be small and disturbances should

double in amplitude in something like 10 hours. In winter, wave numbers should decrease with latitude and rate of growth should be considerably less than in summer. The preference for small wave numbers (one or two) in summer is very weak, so that rather rapid transitions from one wave number to another may occur. Each wave number must have a characteristic and different speed, which may differ in sign as well as in magnitude. One may imagine a rapidly changing circulation rather different from the circulation of the troposphere. The tropospheric time scale is accelerated and the dimensions of the disturbances change between, say, 4,000 and 16,000 km.

Small-scale vertical convection probably occurs in the mesodecline; but the effect of this convection is only to distribute energy vertically, thereby producing the baroclinic fields described by Pant [4] and summarized in Figure 2. In middle and high latitudes, energy is then transported from south to north or north to south by the quasi-horizontal baroclinic disturbances; overturning in a vertical plane on a planetary scale should be effectively limited to the lower latitudes, if it occurs at all.

Finally, one should recall the postulate on which all these inferences rest, namely, that between troposphere, mesoincline, and mesodecline, flow is somewhere roughly horizontal, so that rigid boundaries may be imagined at these stream-surfaces. This is an important condition, but it is probably not so stringent that one must assume no interaction between layers. Thus, one does not have to choose between believing in a relation between geomagnetic activity and tropospheric weather on the one hand and the inferences stated here concerning the dynamics of the upper atmosphere on the other. It may be that particularly great baroclinic instability in the mesodecline or in the higher thermosphere may initiate a disturbance in the mesoincline which then exhibits the characteristic slow growth; this disturbance, in turn, may initiate growth of tropospheric disturbances. In this way, a time lag of a week or two could be accounted for between geomagnetic activity and tropospheric weather changes.

Most of what has been stated here must await verification by independent theory or by observation before it can achieve general acceptance. In fact, the author will reserve his judgment until verification appears. In the meantime, however, this is the sort of fun which, one hopes, will keep us thinking and pressing on toward solutions of the fundamental problems.

Acknowledgment

The study reported here has been supported in part by a grant from the National Science Foundation.

References

[1] W. W. Kellogg and G. F. Schilling, J. Met., 8, 222 (1951).
[2] C. J. Brasefield, J. Geophys. Res., **59**, 233 (1954).
[3] C. E. Palmer, Weather, **9**, 341 (1954).
[4] S. P. Pant, J. Geophys. Res., **61**, 459 (1956).
[5] H. L. Kuo, J. Met., **9**, 260 (1952).
[6] N. A. Phillips, Q. J. R. Met. Soc., **82**, 123 (1956).

[7] W. L. Gates, Q. J. R. Met. Soc., **83**, 141 (1957).
[8] R. G. Fleagle, Q. J. R. Met. Soc., **83**, 1 (1957).
[9] R. Fjörtoft, Geofys. Pub., Oslo, **17**, No. 5, 52 pp. (1950).
[10] P. D. Thompson, Q. J. R. Met. Soc., **79**, 51 (1953).
[11] R. G. Fleagle, Tellus, **7**, 168 (1955).
[12] H. L. Kuo, J. Met., **10**, 235 (1953).
[13] J. G. Charney, J. Met., **4**, 135 (1947).

JOURNAL OF GEOPHYSICAL RESEARCH VOLUME 63, No. 1 MARCH, 1958

THE IONIZATION DUE TO BETA RADIATION FROM THE ATMOSPHERE

BY HENRY A. MIRANDA, JR.*

Physics Department, Fordham University, New York 58, New York

(Received August 1, 1957)

ABSTRACT

Measurements of the ionization due to beta radiation from the air, employing two thin-walled ionization chambers in a differential arrangement, are described. Corrections for geometry, absorption of beta and gamma radiation in the shield, formation of secondary betas in the shield, and back-scattering of betas within the chamber are discussed.

The results of 73 measurements, taken throughout the summers of 1955 and 1956, are reported. Two-thirds of all the measurements fall within a range extending over one order of magnitude. The weighted mean of all the measurements is $0.67I$. This is roughly ten times the expected value, computed from random and thoron concentrations measured at this locality. Wide (and rapid) fluctuations in ionization current were also noted.

All the mechanisms coming to mind which might account for the excess ionization observed over that expected are discussed, and rejected on various grounds. By process of elimination, the possibility of the existence of a "very soft" cosmic-ray component is suggested.

INTRODUCTION

One of the parameters fundamental to the study of terrestrial atmospheric electricity is the ion content of the atmosphere. Formed by the various ionizing radiations originating both in the ground, in the air, and from outer space, those ions which escape recombination account for the finite conductivity of the atmosphere, and are intimately related to all atmospheric-electric phenomena.

In this connection, the rate of ion production in the lower atmosphere is of rather singular importance. While a considerable number of measurements of the total ionization observed in closed vessels have been carried out in the past, much less emphasis has been placed on the problem of isolating the various ionizing components.

This is particularly true of the ionizing radiations from the air. The effect of alpha radiation from radon, thoron, and their decay products in the air was determined by Hess and Vancour [see 1 of "References" at end of paper], by means

*Now at Columbia University, Hudson Laboratories, Dobbs Ferry, New York.

of introducing the air sample into a thick-walled ionization chamber made of brass. An error was found in the computations, and the corrected value of $1.2I$ was reported subsequently by Hess [2]. Cotton [3], using a cellophane-walled ionization chamber designed by the late R. G. Wait, found a value of $1I$ for the alpha-ray ionization from the air.

As regards the gamma-ray ionization from the air, a long series of determinations was carried out by Burns [4] on the grounds of the Seismological Station of Fordham University. The value obtained was $0.7I$. This was five times higher than the value calculated on the basis of concentrations of radon and thoron known to be present in the air at this locality. In discussing this discrepancy, Hess [5] has pointed out the need for further measurements.*

With the completion of other work at this laboratory, two thin-walled aluminum ionization chambers of identical construction were made available. These had been designed for measuring the beta radiation from radioactive sources in the ground, and it was felt that with proper modification they could be adapted for measuring the beta radiation from the air as well.

Because of the above-mentioned discrepancy for gamma radiation from the air, and also because to our knowledge determinations of the beta radiation from the air had never been carried out, it was decided to attempt such a measurement.

APPARATUS

The chambers were constructed of aluminum, with dimensions 28.5 cm × 28.5 cm × 8.5 cm, having a volume of 7,000 cm^3. The side walls were 3 mm (850 mg/cm^2) thick.† The upper and lower surfaces, each comprising a "window" area of 800 cm^2, were made of aluminum foil of thickness 5 mg/cm^2. Each "window" could be covered with a removable aluminum shield of thickness 850 mg/cm^2.

The inner electrode of each chamber consisted of an aluminum rod about 3 mm in diameter, bent to the form of a square, and mounted within the chamber in a plane parallel to the upper and lower surfaces, midway between each. The electrode protruded through an amber plug, which was mounted in a suitable guard-ring arrangement.

The electrodes were joined by means of a brass rod about 25 cm long, which was provided with a "T" fitting to allow connection with the probe of a vibrating reed electrometer. The interconnecting "T" arrangement was enclosed in a grounded metal shield making contact with both guard rings. The electrometer was operated in conjunction with an Esterline-Angus 0-1 ma recording galvanometer.

A 22.5-volt battery provided the sweep voltage for each chamber. This was found to be sufficient for saturation at these levels of ionization. Opposite polarity was applied to each chamber, so that the measured current was proportional to the difference in ionization current between the two chambers. With this arrangement, the chief source of background current was that due to the difference in wall radiation between the two chambers.

*A new technique, suggested in the same paper, has been employed for the measurement of the "air radiation" more recently by A. Manning. The results, yet to be published, are in good agreement with those of Burns.

†This is a sufficient thickness to cut out virtually all the beta radiation.

The lower "window" of each chamber was completely covered by an aluminum shield, 3 mm thick. Thus, only the beta radiation from the hemisphere above the chambers was able to cause ionization within.

Some of the earlier measurements were carried out using a Lindemann electrometer in place of the vibrating reed electrometer. For the earlier Lindemann measurements, the apparatus was placed upon a table, about one meter above the ground. In its final form, both chambers and the vibrating reed electrometer head were firmly mounted as one unit on a rigid welded iron frame. This was placed directly on the ground, with only a sheet of foam rubber interposed.

In the later experiments, a thin film of saran-wrap was placed atop the aluminum foil, so as to better seal the chambers. This was not stretched tightly, with the result that fluttering of the aluminum foil in the presence of wind was reduced somewhat.

CALIBRATION

The ionization current q (measured in ion pair/cm^3/sec) is usually given by the well-known relation

$$qev = C\frac{dV}{dt} \quad \ldots\ldots\ldots\ldots\ldots\ldots\ldots\ldots\ldots\ldots\ldots\ldots (1)$$

where all quantities are measured in the proper units, and e is the electronic charge, C is the capacity of the system,* dV/dt is the rate of change of voltage due to the ionization current, and v is the actual volume of the chamber.

The relation (1) implies that every point within the chamber "sees" an entire hemisphere through the upper "window" of the chamber; in other words, that the upper "window" of the chamber subtends a solid angle of 2π steradians at every point within. Since this is not the case, the factor v in relation (1) must be replaced by $v(\bar{\Omega}/2\pi)$ (where $\bar{\Omega}$ is the mean solid angle subtended by the window throughout the chamber). Thus, the factor $v(\bar{\Omega}/2\pi)$ can be considered an effective volume.

The factor $v(\bar{\Omega}/2\pi)$ was computed numerically, and found to be 0.58. Thus, the effective volume of the chamber was 3,990 cm^3.

Other factors affecting the differential ionization current measured in the apparatus are

(1) Absorption of gamma radiation by the shield
(2) Absorption of cosmic radiation by the shield
(3) Production of secondary beta particles by the gamma radiation traversing the shield
(4) Back-scattering of betas by the inner walls of the chamber
(5) Absorption of beta radiation by the upper window of the chamber

Taking the measured value of gamma radiation as observed both in 1952 and again in 1956 at this location as $0.7I$, and assuming an average energy of 0.5

*The electrical capacity of the system, measured with a Harmes condenser, was found to be 13.2 cm. For the earlier measurements, a Lindemann electrometer was used, as mentioned above. This yielded an altogether different capacity for the system (38.5 cm).

MEV,** it can easily be computed that effect (1) contributes $0.03I$ to the measured ionization current in the given apparatus. Therefore, in order to correct for this effect, $0.03I$ must be subtracted from each measurement.

To evaluate effect (2), consider only the soft components of cosmic radiation. These amount to one-fourth of the total cosmic radiation at sea-level in this locality. Taking the mean value of the linear absorption coefficient for this radiation in aluminum from the data of Steinke [6], it can be shown that effect (2) contributes $0.01I$ to the measured ionization current in the given apparatus.

While it is exceedingly difficult to assess accurately effect (3), rough tests showed that this is perhaps equal to, but certainly not greater than, effect (2).

Effects (4) and (5) have been studied for a similar chamber by Weller [7], who showed that each of these effects involves a correction of about 10 per cent. Since effect (4) tends to increase the measured current, and (5) tends to decrease the same, the net correction for these two effects is negligible.

It will also be noted that effects (2) and (3) tend to cancel each other. Thus, we see that the net result of effects (1) through (5) is simply that due to (1) alone.

EXPECTED IONIZATION CURRENT

From Eve's law, the ionization dq at a point due to an element of volume dv at a distance r from the point is given by

$$dq = (KM/r^2)e^{-\mu r}\, dv \qquad (2)$$

where K is Eve's constant for beta radiation from radium B and radium C, M is the concentration of radon in curie/cm^3, and μ is the linear absorption coefficient for beta radiation in the air.

If dv is taken as a hemispherical shell of area $2\pi r^2$ and thickness dr, centered about the point of interest, then

$$dq = 2\pi KMe^{-\mu r}\, dr \qquad (3)$$

from which

$$q = 2\pi KM \int_0^\infty e^{-\mu r}\, dr = 2\pi KM/\mu \qquad (4)$$

For K, we insert the mean value of 1.7×10^{11} ion pair cm^{-1} sec^{-1} curie^{-1}, as given by Eve [8]. Since the average mass absorption coefficient (μ/ρ) for this radiation is 4.9, μ is taken as 4.9 ρ, or 6.3×10^{-3} cm^{-1}. Finally, choosing an upper limit for the radon concentration in this locality of 2×10^{-16} curie/cm^3, q is found to be $0.034I$. And, if we estimate an equal contribution from thoron products in the atmosphere (which is a very generous estimate), the expected value is $0.068I$.

Although equation (2) holds strictly for a point source and point detector only, it can be shown that it is correct to within 6 per cent for the apparatus in question.

**We know little about the spectrum of energies comprising the measured gamma-ray ionization, except that it is capable of penetrating 3 mm of brass with only 8 per cent absorption, and that it is virtually all absorbed by 10 cm of iron.

PROCEDURE

A single determination of the beta radiation from the air consists of two successive measurements. The first measurement is carried out with the upper window of chamber A unshielded, while an aluminum shield 3 mm thick is placed above the upper window of chamber B. This gives rise to an ionization current Q_1 . For the second measurement, the shield is removed from above chamber B, and placed above the upper window of chamber A, giving rise to an ionization current Q_2 .

If we adopt the convention that, whenever Q is in the direction opposite to that expected, it is prefixed by a negative sign, the ionization current due to beta radiation in the air is given by

$$q = (Q_1 + Q_2)/2 \text{ (neglecting effects 1 through 5 discussed above)}$$

Since the chambers could not be made airtight, continuous rinsing with radon-free air had to be employed throughout the measurements. The air was introduced at a flow rate of about $\frac{1}{4}$ liter per minute.

An exploratory set of measurements was carried out, both on the fourth-floor roof of the physics building and in the seismic garden at Fordham University, from September through October, 1954. Rather wide fluctuations were observed, and pointed to the necessity of taking many measurements, although it was quite evident even from these few measurements that the effect was greater than expected. It was further noted that the roof measurements tended to be higher than the garden measurements.

A second set of measurements was taken through the summer of 1955, near the center of an open field of grass, measuring about 150 yards on each side, located near the physics building. These measurements were made using the Lindemann electrometer.

A final set of measurements was carried out in the same location through the summer of 1956, using the vibrating reed electrometer.

RESULTS

The single dominant feature of all the measurements was the wide fluctuations noted from day to day, and from hour to hour. In fact, all but a few of the traces exhibited a very jagged character.

On more than one occasion, we were fortunate enough to be observing the instrument at the onset of a sudden increase of the differential ionization current, which amounted to a factor of perhaps 4 or 5 over the previous current. Switching the shield a minute or two following the onset of the increase resulted in a differential current of the same magnitude, but of opposite sign. The effect lasted about 15 minutes, diminishing slowly through this period.

It is not unreasonable, therefore, to ascribe a good part of this jaggedness to short-period fluctuations in beta radiation.

Table 1 gives a summary of 73 measurements taken during the summers of 1955 and 1956. In striking the mean value, each measurement was weighted according (1) to its duration as compared with an arbitrarily chosen length of time, and (2) to its degree of uncertainty, assigned on the basis of the jaggedness of the trace.

TABLE I—Summary of the results of 73 measurements taken during 1955 and 1956

Range of measured differential ionization current	Frequency of occurrence for respective range
(*ion pair/cm³/sec*)	
0.0–0.1	6
0.1–0.2	3
0.2–0.3	6
0.3–0.4	8
0.4–0.5	6
0.5–0.6	9
0.6–0.7	6
0.7–0.8	4
0.8–0.9	4
0.9–1.0	3
1.0–1.1	8
1.1–1.2	2
1.2–1.3	3
1.3–1.4	1
1.4–1.5	1
1.5–1.6	1
1.6–1.7	0
1.7–1.8	0
1.8–1.9	0
1.9–2.0	1
2.0–2.1	1

The weighted mean of all the measurements is $0.67I$. Two-thirds of all measurements fall between the value $0.10I$ and $1.00I$.

DISCUSSION OF RESULTS

Since the expected ionization current due to beta radiation from radon and thoron products alone is less than $0.07I$, we are faced with a discrepancy amounting to about $0.6I$ (that is, the observed ionization is nine times greater than expected).

One might at first suspect that the observed excess can be explained by the presence of radioactive debris from nuclear explosions. However, Blifford, *et al.* [9], report the fission product concentration in air as being at all times less than 1.0×10^{-18} equivalent curie/cm^3 at Washington, D. C., throughout the period of our 1955 measurements. This is two orders of magnitude less than the highest measured radon content at Fordham, and can be neglected. Furthermore, samplings of airborne radioactive matter near the ground by means of an AEC-type paper filter were carried out at Fordham on a number of days during the summer of 1956, in connection with other work.* These measurements indicate that the concentration of airborne radioactive debris at this location was never more than 30 per cent of the radon and thoron products concentration during this period. (Confirmation of this has also been obtained by private communication

*We are indebted to F. X. Roser, S.J., for allowing us to publish these results.

with Dr. John H. Harley, Health and Safety Division, New York Operations Office, U. S. Atomic Energy Commission, New York, N. Y.)

It appears, therefore, that contamination of the lower atmosphere cannot be invoked to explain the observed excess.

Also, any airborne radium D could not affect the measurements, since the weak beta radiation from this source would be completely stopped by the thin aluminum foil of the window.

The radium E content of the atmosphere (if we assume equilibrium with radium D) would exhibit a very long half-life, and be included with the radioactive debris in all of the filter-type measurements quoted above. Radium E, therefore, is to be discarded as a possible source of the observed discrepancy.

The possible effect of the weak beta radiation from C^{14} in the atmosphere has also been considered. It is known that neutrons can produce C^{14} by the reaction N^{14} $(n, p)C^{14}$. Neutrons of cosmic-ray origin can be expected, therefore, to yield quantities of atmospheric radiocarbon at altitudes of 30,000 feet and higher. This radioactive carbon forms CO_2, which would diffuse downward.

Taking the value of atmospheric radiocarbon content as given by Anderson and Libby [10] (0.12 gram/cm^2 of earth's surface), and the value for the specific radioactivity of inorganic carbonate carbon quoted in the same paper (16.2 dis./min./gram carbon), one can easily compute the expected ionization from this source. This turns out to be $0.001I$, which is entirely negligible.

There remains only one possibility which has not been considered so far, namely, that the beta particles giving rise to the observed excess ionization currents originate from scattering processes taking place in the air above the chambers. Whatever the process may be, it must occur within a hemisphere of about 12 meters above the chambers.

Three processes able to yield scattered radiation come to mind: (1) Compton scattering of gamma radiation from the ground, (2) Compton scattering of gamma radiation from the air, and (3) a hitherto undetected "very soft" component of cosmic radiation.

Of these, the first effect can be excluded, in view of the large scattering angles involved. In addition, it must be pointed out that if this effect were at all in evidence, the preliminary measurements taken on the roof of the physics building would have been much lower. As mentioned above, these actually tended to be higher than the ground measurements.

The second effect must also be small, since the "primary" gammas themselves give an ionization current of only $0.7I$.

We are left with the third effect as the only convenient hypothesis, since, as stated before, measurements of this kind have never, to our knowledge, been carried out before.

This is not at all as surprising as might at first appear. It must, after all, be remembered that nearly all previous ionization-chamber measurements of cosmic radiation have been made with chambers having walls thick enough to stop virtually all beta radiation.

There is some possibility that the discrepancies in absolute value of cosmic-ray ionization at sea-level reported in the literature by Hess [11] can be resolved by considering this "very soft" component.

Although there is some reluctance on the part of many investigators to consider the ionization "balance" of the atmosphere as a true balance, a knowledge of the rate of ion production is of some importance in the study of atmospheric electricity. It would be of interest, therefore, to repeat the measurements with a more sensitive technique, with a view towards studying the spectrum of this radiation, if possible.

SUMMARY

An excess of observed gamma-ray ionization from the air over that expected on the basis of known radon and thoron concentrations of the air led to an investigation of the beta-ray ionization from the air.

Two identical rectangular beta-ray ionization chambers were combined in a single differential ionization apparatus for the purpose of reducing or eliminating the effects of the residual ionization, gamma radiation, and ordinary cosmic radiation. Each had a "window" of thin aluminum foil, having an area of about 800 cm^2.

Corrections for geometry (effective chamber volume), absorption of gamma and cosmic radiation by the shield, production of secondary beta particles by gamma radiation traversing the shield, back-scattering of betas by the inner walls of the chamber, and absorption of betas by the thin aluminum "window" of the chamber are discussed.

The expected ionization is computed from radon and thoron concentrations measured at this locality. It is certainly less than $0.072I$.

The observed ionization current from the air is $0.67I$ (weighted average of 73 measurements). Two-thirds of all measurements fall within the range 0.10 and $1.00I$. These were taken over the summer of 1955 and 1956.

Moreover, there were noted large fluctuations in the ionization current from day to day, and from hour to hour.

The observed beta-ray ionization current is roughly ten times the anticipated value. Many possible explanations for this discrepancy have been explored, namely, (*a*) contamination of the atmosphere by radioactive debris from nuclear explosions, (*b*) radium D and E carried along in the atmosphere, (*c*) C^{14} content of the atmosphere caused by cosmic-ray neutrons, (*d*) Compton scattering of gamma radiation from the air and from the ground which gives rise to scattered betas that subsequently enter the chamber through the upper window, and (*e*) a "very soft" component of cosmic radiation.

All of the above possible explanations are found wanting on various grounds, with the exception of the last. The possibility of the existence of a very soft cosmic-ray component is inferred by process of elimination.

ACKNOWLEDGMENTS

I am, indeed, grateful to Prof. V. F. Hess, who suggested the study initially, for his continued interest during its progress.

Special thanks are due also to Messrs. V. J. Kisselbach and D. J. Michaels, who did much of the experimental work.

The research reported herein was supported in full by the Geophysics Research Directorate, Air Force Cambridge Research Center, Air Research and Development Command, under Contract No. AF 19(122)-409.

References

[1] V. F. Hess and R. P. Vancour, J. Atmos. Terr. Phys., **1**, 13 (1950).
[2] V. F. Hess, J. Atmos. Terr. Phys., **3**, 172 (1953).
[3] E. S. Cotton, J. Atmos. Terr. Phys., **7**, 90 (1955).
[4] W. F. Burns, Thesis, Fordham University (1952).
[5] V. F. Hess, J. Geophys. Res., **58**, 67 (1953).
[6] E. G. Steinke, Ergebn. Exakt. Naturwissen, **13**, 89 (1934).
[7] R. I. Weller, J. Atmos. Terr. Phys., **5**, 1 (1954).
[8] A. S. Eve, Phil. Mag., **22**, 551 (1911).
[9] I. H. Blifford, Jr., H. Friedman, L. B. Lockhart, Jr., and R. A. Baus, J. Atmos. Terr. Phys., **9**, 1 (1956).
[10] E. C. Anderson and W. F. Libby, Phys. Rev., **81**, 64 (1951).
[11] V. F. Hess and J. Eugster, Cosmic radiation and its biological effects, Fordham University Press (1949).

VARIATIONS IN THE HEIGHT OF IONOSPHERIC LAYERS DURING MAGNETIC STORMS*

BY EINAR TANDBERG-HANSSEN

High Altitude Observatory, Boulder, Colorado

(Received August 26, 1957)

ABSTRACT

The variations of the virtual heights of the $F1$ and E layers of the ionosphere are studied and it is found that, in general, the E layer remains unchanged, while the $F1$ layer rises during geomagnetic storms. This is applied to Parker's theory for magnetic storms and it is concluded that the absorption of the storm-associated solar energy takes place at a height between 100 and 200 km.

I. *Introduction*

Extensive studies have been carried out correlating changes in the $F2$ layer with the occurrence of geomagnetic storms. Already in 1935, Kirby, Gilliland, and Judson [see 1 of "References" at end of paper] found that the height of the $F2$ layer increased during magnetic storms, and this has been well confirmed by Lewis and McIntosh [2].

On the other hand, very little has been published concerning the simultaneous behavior of the $F1$ layer. Now there are reasons to believe that the virtual height of the $F1$ layer is more often a reliable measure of its true height than is the virtual height of the $F2$ layer in determining its true height. Even though spurious effects may sometimes invalidate our assumptions, we will here adopt the attitude that a rise in the virtual height, $h'F1$, of the $F1$ layer portrays a real rise of the layer.

The virtual heights used in this investigation are those observed in Washington, D. C. [3], and the magnetic planetary Kp figures—as indicators of magnetic storms—are also taken from CRPL publications [3]. The period considered covers the years 1952 through 1956. One might argue that the occurrence of sporadic E should be taken into account in selecting the individual days because of blanketing. This has not been done, since it is found [4] that the occurrence of sporadic E at middle latitudes peaks up about the low Kp periods.

II. *The Height of the F1 Layer*

First, a superposed-epoch analysis has been carried out for 40 major magnetic storms with good simultaneous ionospheric data, thereby relating the $h'F1$ to the Kp figures. Days when $\sum Kp$ was a maximum were taken as zero days. The results are shown in Figure 1 and indicate a distinct rise of some 10 km of the $F1$ layer around the time of magnetic storms.

*This research was supported by the Central Radio Propagation Laboratory of the National Bureau of Standards.

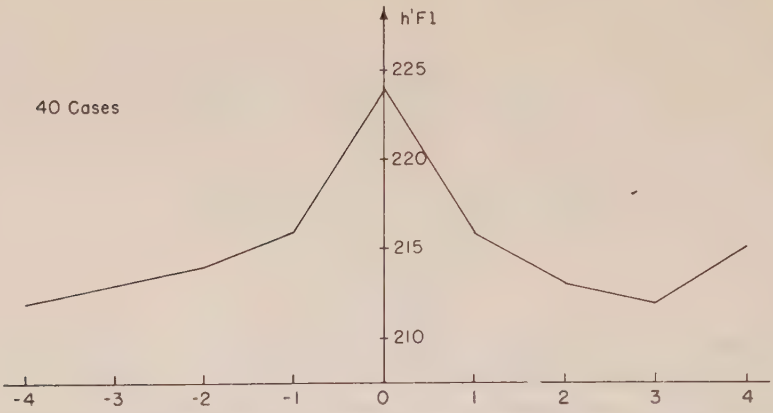

Fig. 1—Superposed epoch analysis of the virtual height of the $F1$ layer, $h'F1$, during magnetic storms. Zero days are days when ΣKp was a maximum, 40 cases.

In order to establish the reverse correlation, we then did a second superposed-epoch analysis, using as zero days those days when the virtual height of the $F1$ layer was significantly above the monthly median value.

If $\overline{h'_T F1}$ denotes the monthly median value of the virtual height in kilometers at time T and $h'_T F1$ the actual value for a particular day at time T, then a day was picked as zero day if

$$\sum_T h'_T F1 - \sum_T \overline{h'_T F1} \geq 100 \quad \ldots\ldots\ldots\ldots\ldots\ldots\ldots\ldots (1)$$

The summation was generally taken between 0900 and 1500 local time. The mean magnetic Ap figures (for our purposes equivalent to $\sum Kp$) before and after the selected days are given in Figure 2, and indicate that the geomagnetic conditions are significantly disturbed at times when the $F1$ layer is markedly higher than normal. There were 100 cases that fulfilled the requirements of equation (1).

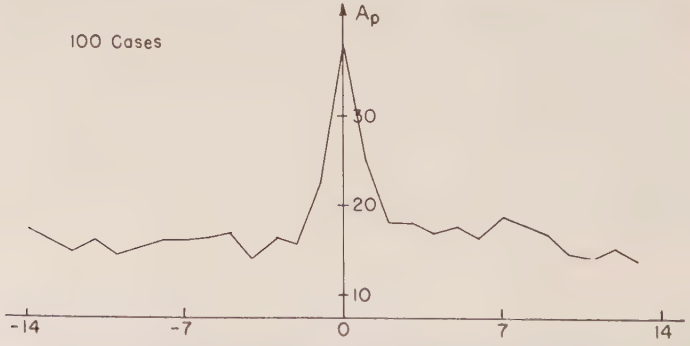

Fig. 2—Superposed epoch analysis of the magnetic Ap figure during times of increased virtual height of the $F1$ layer. Zero days are days when the virtual heights satisfied the inequality (1), 100 cases.

Since the criterion by which we picked a day as zero day depends on the numerical value of the term on the right side of equation (1), and consequently

is somewhat arbitrary, an analysis was also made with the right side set equal to 70; see Figure 3.

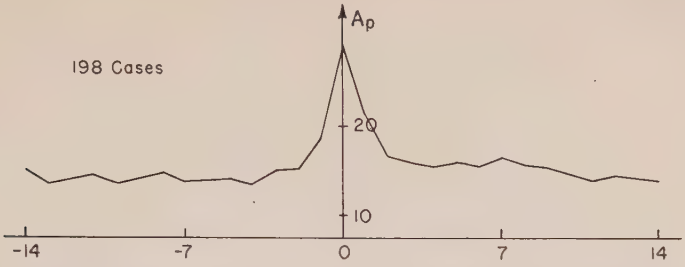

FIG. 3—Same as Figure 2, except the virtual heights satisfied the inequality (1) with the right side set equal to 70 km, 198 cases

Now, to get a feeling for what numerical value one should use in equation (1), we have plotted the 98 cases where

$$70 \leq \sum_T h'_T F1 - \sum_T \overline{h'_T F1} < 100 \quad \ldots\ldots\ldots\ldots\ldots\ldots (2)$$

separately in Figure 4. One sees that there is a small peak at zero day. However, the material giving the curve in Figure 2 consists of essentially the same number of cases, so it is evident that in using 70 km as a lower value one includes cases with a small rise of the virtual height of the $F1$ layer that have nothing to do with magnetic storms. On the other hand, since there is a small peak at day zero, one is apt to overlook some cases of actual increase in the virtual height if 100 km is used as a lower limit.

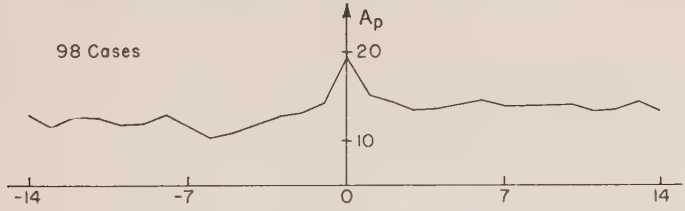

FIG. 4—Superposed epoch analysis of the magnetic Ap figure for those cases where the virtual heights satisfied the inequalities (2), 98 cases

III. *Application to Parker's Theory*

Kirby, *et al.* [1], attributed the increased height of the $F1$ layer during magnetic storms to some sort of heating taking place in the atmosphere. At that time, there was no convincing physical argument that this should really lead to the magnetic-storm main-phase phenomenon. After the formulation of hydromagnetic conceptions, Parker [5] had better reasons to attribute the main phase to effects produced by the lifting up of some part of the ionosphere, thereby dragging the magnetic lines of force with it. If this lifting is produced by a heating of underlying air masses, the absorption of heat must, according to this analysis, take place below the $F1$ layer, say below 200 km. This is not a proof for Parker's theory, but if one had found no effect in the $F1$ layer, it might have had serious conse-

quences, because it is easy to see that absorption of solar energy cannot take place much higher. A change ΔB of say 0.2 per cent in B (= 0.5 gauss) requires a stress variation of

$$\frac{B \cdot \Delta B}{8\pi} \approx \frac{0.01}{25} = 4 \times 10^{-4} \text{ dyne/cm}^2 \quad \ldots\ldots\ldots\ldots\ldots\ldots (3)$$

Now, at 220 km, $\log p = -3.7$, according to Whipple [6], or $p = 2 \times 10^{-4}$ dyne/cm^2, so that already at this height the gas pressure is marginal.

In order to try to pin down more accurately the height where, in this picture, absorption takes place, we then carried out an analysis of the virtual height of the E layer, $h'E$, as was done for $h'F1$, and on the same assumption that the virtual height is a good measure of the true height of this layer. The results are presented in Figure 5, and refer to the same 40 storms as Figure 1.

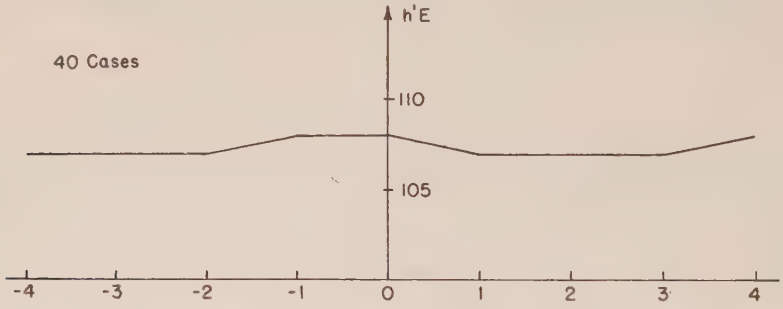

Fig. 5—Superposed epoch analysis of the virtual height of the E layer, $h'E$, during magnetic storm. Zero days are the same as in Figure 1.

Apparently no significant change takes place in the height of the E layer during magnetic storms. This indicates that, since the E layer is not being lifted up, the absorption of heat takes place higher up. We are consequently led to the conditions:

$$200\ km > h_1 > 100\ km \quad \ldots\ldots\ldots\ldots\ldots\ldots\ldots\ldots (4)$$

h_1 is here the height where absorption of solar energy takes place and above which the lifting of the ionospheric matter occurs.

V. *Acknowledgment*

In conclusion, it is a pleasure to acknowledge the stimulating discussions with Dr. C. Warwick. I am also indebted to the National Bureau of Standards for making their computing facilities available.

References

[1] S. S. Kirby, T. R. Gilliland, and E. B. Judson, Phys. Rev., 48, 849 (1935).
[2] R. P. W. Lewis and D. H. McIntosh, J. Atmos. Terr. Phys., 4, 44 (1953).
[3] Nation. Bur. Stan., Rep. CRPL-F series.
[4] E. K. Smith, Jr., Nation. Bur. Stan., NBS Circ. No. 582 (1957); p. 162.
[5] E. N. Parker, J. Geophys. Res., 61, 625 (1956).
[6] G. P. Kuiper (Ed.), The Earth as a Planet, University of Chicago Press, Chicago (1954); chap. 10, p. 500. [Vol. 2, The Solar System series.]

THE AIRBORNE MEASUREMENT OF ATMOSPHERIC CONDUCTIVITY

By J. H. Kraakevik

*U. S. Naval Research Laboratory, Washington 25, D. C., and University of Maryland, College Park, Maryland**

(Received September 26, 1957)

ABSTRACT

The simultaneous measurement of both polar conductivities from a P4Y airplane using two Gerdien-type condensers is described. An altitude distribution of conductivity representative of clear arctic air is presented. From this distribution, a columnar resistance of 6.0×10^{16} ohm-m^2 is obtained by integration from the earth's surface to 6 km. The average ratio of negative to positive conductivity was found to be 1.1.

The charge on the aircraft was found to have negligible effect on the conductivity measurement for fair weather conditions. Triboelectric charging of the conductivity chamber central electrodes by aerosols was observed on most fair weather flights. Concurrent observations at the earth's surface occasionally exhibited the same effect. Even in its presence, techniques were used which permitted valid measurements of conductivity to be made. It is suggested that this effect may have been responsible for unusually high positive-to-negative conductivity ratios reported by others.

INTRODUCTION

The variation in atmospheric conductivity with altitude has been obtained from balloon and aircraft measurements, and the results are in general agreement with the theoretical curves based on cosmic-ray data. Balloon measurements by Stergis and others [see 1 of "References" at end of paper] showed a monotonic increase in conductivity with altitude above the exchange (or "austausch") layer by approximately a factor of three for every 6 km. Airplane measurements of conductivity over New England by Sagalyn and Faucher [2] demonstrated the variability of conductivity within the exchange layer and its qualitative relation to several meteorological factors. Nevertheless, there remained a need for airborne conductivity measurements in areas remote from contamination sources, such as over the oceans, and in the arctic and tropics.

Consequently, in 1954, a P4Y aircraft was instrumented to measure simultaneously both polar conductivities, in addition to other atmospheric electric and meteorological variables, in order to study space and time variations in these quantities. Altitude distributions of conductivity are obtained from measurements

*Part of this work was submitted to the University of Maryland in partial fulfillment of the requirements for the Doctor of Philosophy degree in Physics. Other portions of the dissertation will be published separately.

between 0.03 and 6 km, and are used to derive values of columnar resistance. It is the purpose of this paper to give typical results from measurements in the arctic, and to show how several disturbing effects were evaluated and overcome to provide valid measurements of conductivity.

INSTRUMENTAL TECHNIQUE

The general instrumentation of the P4Y as an airborne atmospheric electricity laboratory is described elsewhere [3]. The conductivity experiment consists of two Gerdien-type cylindrical condensers mounted in the nose of the aircraft, together with their associated vibrating-reed electrometers and recorders. The location of

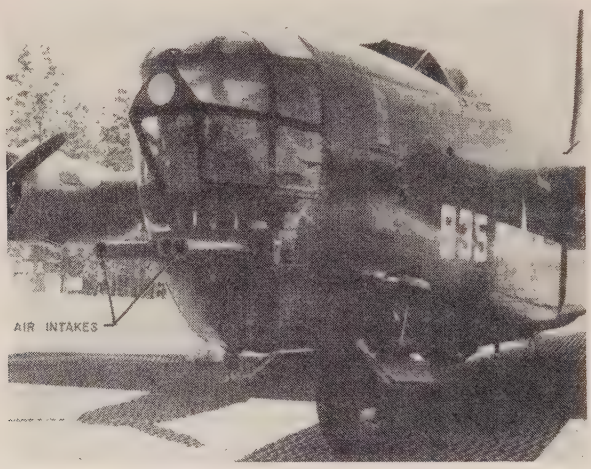

FIG. 1—Nose of P4Y airplane

the intake ducts to the conductivity chambers is shown in the photograph of the aircraft nose in Figure 1. A block diagram of the conductivity meters is given in Figure 2. The positive conductivity in mks units is given by

$$\lambda_+ = \frac{\epsilon i}{CV} \qquad (1)$$

Here ϵ is the atmospheric permittivity; i is the positive ion current to the central electrode; C is the effective capacitance between the inner and outer electrodes; and V is the positive voltage applied to the outer cylinder. A similar expression is valid for the negative conductivity, where V is negative. The total conductivity λ is the sum of the two polar conductivities.

If the applied voltage is not too great, nor the air flow through the chamber too small, the current i through the electrometer input resistance R increases linearly with V and is proportional to the conductivity. However, at some critical voltage V_k, corresponding to the largest ionic mobility k, the current-voltage characteristic becomes non-linear. This characteristic has been checked experimentally in flight and found to be linear out to at least 300 v. Consequently, the use of only ± 90 v on the chambers insured that the instruments were operated on the linear portion of the characteristic under all conditions.

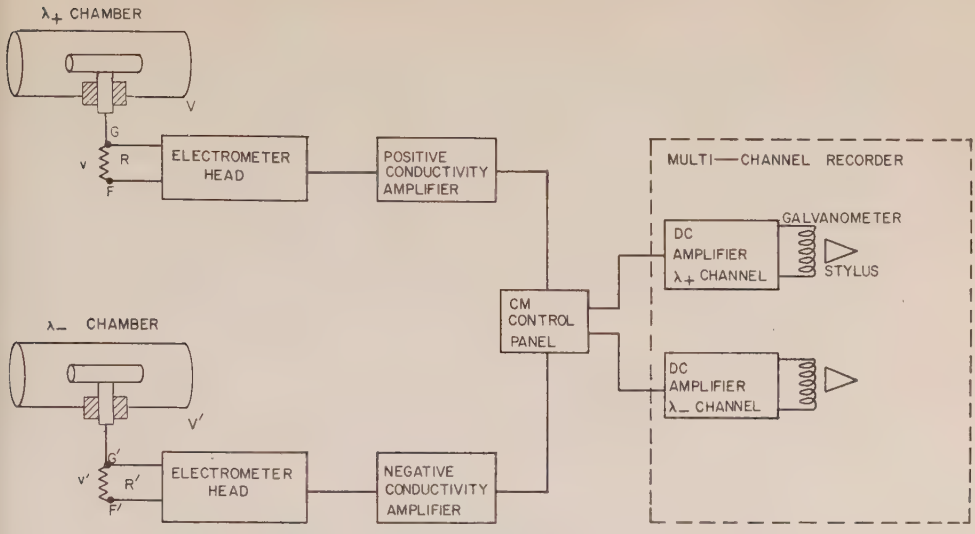

FIG. 2—Block diagram of conductivity meter and recorder

Since the intake duct to the conductivity meter extends some 1.6 m in front of the chamber, the effect of diffusion of small ions to the walls of the duct was investigated. This effect would tend to reduce the measured conductivity from the ambient. From a solution of the diffusion equation by Gormley and Kennedy [4], the reduction in conductivity due to diffusion was found to be less than 0.5 per cent under all conditions. This may be neglected, since the over-all accuracy of the airborne conductivity measurement is approximately ±5 per cent.

CHARGE ON THE AIRCRAFT

The effect of airplane charge on the airborne measurement of conductivity has been investigated by Coroniti and others [5]. Their results are presented in Figure 3(*a*). An electric field meter was mounted at the nose of a B-17 airplane to measure the electric field due to the aircraft charge. The air velocity u in the conductivity chamber was about one-tenth the aircraft velocity u_a. In agreement with the theory, the conductivity of each sign is unaffected by a substantial aircraft charge of the opposite polarity. However, the reduction in both polar conductivities for zero plane charge is in disagreement with the theory and also a later statement by Coroniti [6]. In addition, Gunn [6] questions the soundness of these experimental results because the measured values on which the smooth curves of Figure 3(*a*) are based show a scatter of some ±25 per cent.

Consequently, a similar experimental study was made on the P4Y airplane, where the aircraft charge was measured by means of electric field meters at each wing tip. Clark [7] has shown that the airplane potential in volts is 57 per cent of the average wing-tip field in volts per meter, and with a capacity of 740 $\mu\mu$f for the P4Y the wing-tip field can be related directly to the aircraft charge. The variation in measured conductivity with the average wing-tip field is shown in Figure 3(*b*). The solid curves (for $u = 0.1\ u_a$) are similar to those obtained on the B-17, with the major exception that there is no reduction in measured conductivity

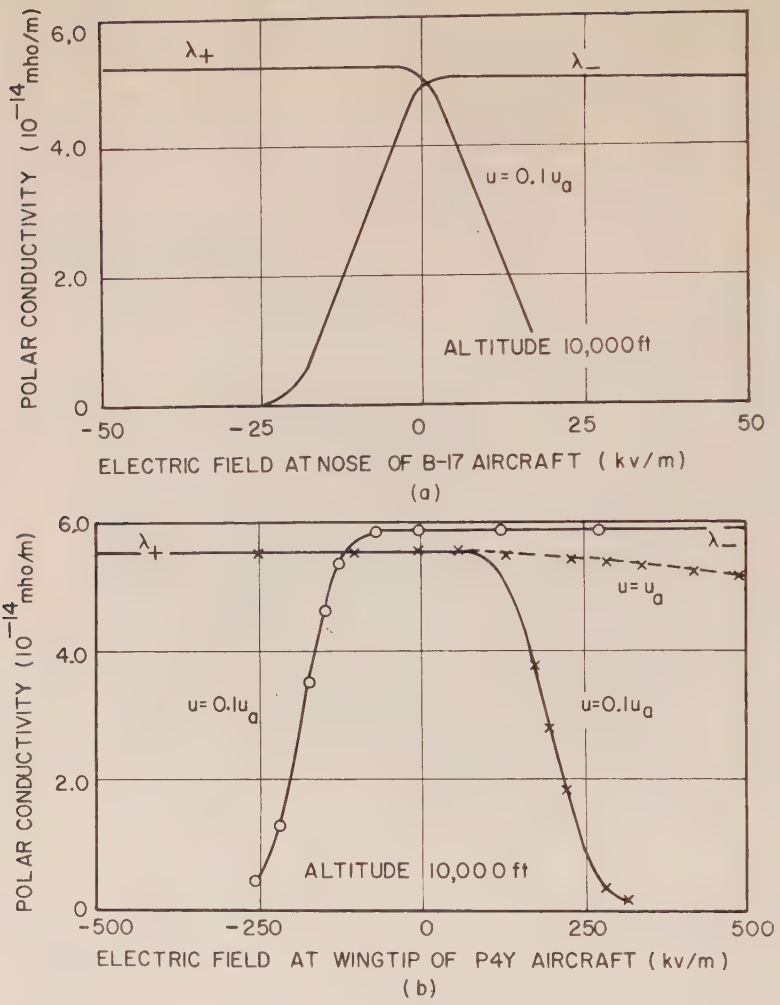

FIG. 3—Effect of aircraft charge on airborne conductivity measurement

up to an aircraft charge of the same polarity corresponding to 60 kv/m. The fact that the wing-tip field on the P4Y corresponds roughly to ten times the field at the nose of the B-17 is undoubtedly due to the difference in electric field augmentation at the two locations. The dashed curve in Figure 3(*b*) shows that for the normal operating condition of $u = u_a$ the conductivity decreases only 7 per cent with a wing-tip field of 500 kv/m. It is evident that for the normal fair-weather plane charge corresponding to less than 1 kv/m at the wind tips the conductivity measurement is a valid one, even with the air velocity through the chamber as low as one-tenth the aircraft velocity.

TRIBOELECTRIC CHARGING EFFECT

Since the conductivity is proportional to the slope of the current-voltage characteristic, the measurement has usually been made with a fixed voltage

applied to the chamber and a periodic check of the conductivity zero. Several methods are available for obtaining this zero. The simplest one is to short-circuit the input resistance R (see Fig. 2) and measure the residual electrometer output voltage. This technique eliminates any effect due to electrometer drift and has the advantage of being extremely simple.

The second method reduces the air flow rate to zero by means of remotely operated valves. This represents an improvement over the first method, in that any leakage resistance between the central electrode and the system ground is indicated by an "offset" current, due to the negative feedback voltage to the electrometer input.

The third technique is to change the applied voltage on the chamber and measure the change in current. This provides an advantage over the first two methods, because there is often an offset current for zero applied voltage only when air is flowing through the chamber. This is probably a triboelectric charging of the central electrode by large aerosols. Such an effect has been reported by Gish [8], who observed that in haze the *apparent* conductivity of one sign rose while that of the other sign fell. He emphasized the need for measuring both polar conductivities simultaneously from aircraft and questioned the accuracy of such measurements except on "clear" days.

The present conductivity measurements on the P4Y are in general agreement with Gish's observations with two exceptions. First, conductivity offsets have been observed on clear days, particularly within the exchange layer, within which no clouds or haze were visible. Second, valid conductivity measurements can be obtained in the presence of this effect, whether in visible haze or on clear days, by changing the applied voltage and observing the corresponding current change.

A sample section of a conductivity record taken in flight illustrating this effect is shown in Figure 4. The first method of obtaining the conductivity zero gives the current indicated in column (1). The second method is represented in column (2). Column (3) shows the offset current from triboelectric charging. It is to be noted that the only valid measurement of conductivity is obtained by taking the difference between the currents measured during conditions (3) and (4). Since the voltage increment method of obtaining the conductivity includes most of the advantages of the other two techniques, it was used exclusively on all the flights.

The possibility of space charge producing this effect has been rejected. For if it is assumed that the frontal area A of the central electrode collects all ions of both signs, the current to the probe is

$$i = \rho u A \quad \ldots\ldots\ldots\ldots\ldots\ldots\ldots\ldots\ldots\ldots (2)$$

where ρ is the space-charge density. But on a representative flight, the measured offset current was 100 times greater than that given by Eq. (2), where ρ was obtained from the altitude distribution of potential gradient.

The proportionality of this current offset to air flow has also been investigated in the P4Y airplane. The anticipated reduction in current offset was observed when the air flow rate was reduced by a factor of three by means of the remotely operated valves, with no change in measured conductivity.

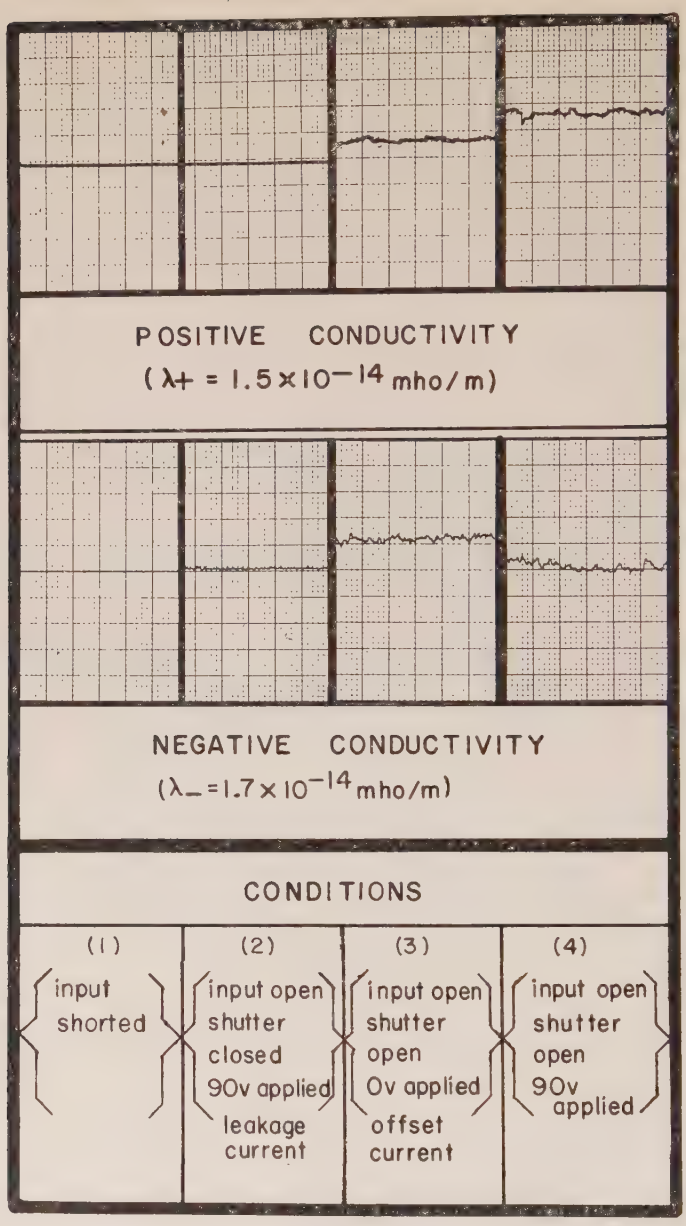

Fig. 4—Sample record of effect of triboelectric charging on conductivity measurement

This offset current due to triboelectric charging occurred on a majority of the flights. It was observed primarily within the exchange layer and was most severe on days of high turbulence and at the lowest altitudes. The polarity of the current produced was almost invariably positive, the maximum observed value being some 10^{-12} amp. This is a larger current than that usually resulting from the conductivity at the lower altitudes.

One notable exception to a positive current offset was obtained in Greenland

at altitudes between 5.3 and 6.1 km. There, a very large negative offset current greater than 10^{-10} amp was produced. Although no clouds were apparent, upon close examination a faint halo was observed about the sun, indicating the presence of thin cirrus clouds. The conductivity offset, and a corresponding change in the aircraft charge observed on the electric field meters, were undoubtedly due to triboelectric charging of the metal surfaces by ice crystals. The sign of the charge on the aircraft and on the conductivity central electrode was negative, in agreement with that reported by previous investigators [9].

Measurement of atmospheric conductivity at the earth's surface have been made at a number of different locations concurrently with the airborne measurements. For surface measurements, the air flow rate and the applied voltage are only 0.04 times as great as in the airborne case, the resultant current being correspondingly lower. The triboelectric charging effect was also present in some of these surface conductivity measurements, particularly those made in Kansas, when dust was prevalent and turbulence was high. Perhaps some past surface results showing high ratios of positive-to-negative conductivity, which have been attributed to the electrode effect, such as those of Pluvinage on the Greenland ice-cap [10], may in reality be due to triboelectric charging from snow or dust particles. The correspondence between frictional charging effects from ice and dust particles has been noted by Chalmers [11].

A fourth method of obtaining a conductivity zero, that used by Sherman [12], utilizes a separate condenser in front of the Gerdien condenser to remove all the small ions, while maintaining the air flow constant. This technique should also provide a valid conductivity zero in the presence of triboelectric charging.

EXPERIMENTAL RESULTS

The variation in conductivity with altitude representative of a cloudless sky and clear air was obtained over Söndre Strömfjord, Greenland, at 1100 GMT 11 September 1955. An ascent was made to 6 km and the altitude distribution was obtained on the descent. The time indicated is the quarter-hour nearest the middle of the 70-minute descent. A plot of the conductivity distribution is given in Figure 5 on a semi-logarithmic scale. Above 0.2 km, the exponential curve which best fits the experimental data is

$$\lambda = 27.2 \exp [(Z - 6)/3.5] \times 10^{-14} \text{ mho/m} \quad \ldots\ldots\ldots\ldots (3)$$

where Z is the altitude in kilometers. The standard deviation of the experimental points from the line is 3.4 per cent.

The exponential increase in conductivity with altitude is indicative of the cleanliness of arctic air. Since the conductivity in clean air is directly proportional to the product of the mobility and the square root of the ion production rate, which product increases approximately exponentially over this altitude range, then such a variation in conductivity with altitude is evidence that the condensation nuclei content is low. Spot measurements, using a photoelectric nucleus counter [3], support this with an average density of less than 500 nuclei per cubic centimeter. The small departure from an exponential curve below 0.2 km shown in Figure 5 is probably due to the small exchange layer effect which is present.

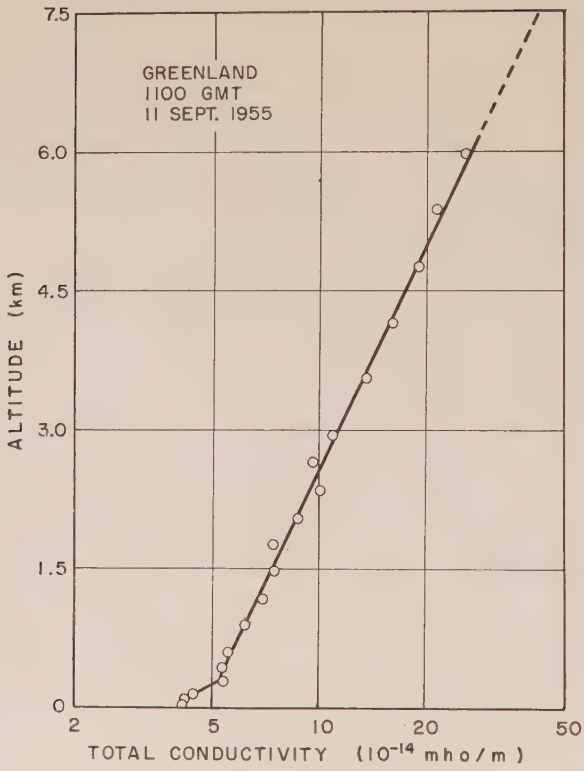

Fig. 5—Altitude distribution of conductivity above Greenland fjord

The columnar resistance up to 6 km, obtained by integrating the reciprocal of conductivity with respect to altitude, is 6.0×10^{16} ohm-m^2. Assuming the conductivity above 6 km in Greenland is approximately the same as that measured on the Explorer II balloon flight [13], the columnar resistance of the entire atmosphere is 8.0×10^{16} ohm-m^2. This is lower than the 9 to 25×10^{16} ohm-m^2 range of values obtained over the continental United States [2].

The ratio of negative to positive conductivity varied from 0.90 to 1.27 on this flight, with an average value of 1.10. This is in disagreement with the results of Callahan (Sagalyn) and others [14], who found the average ratio to be unity throughout this altitude range. The disagreement may be due to the results of Callahan and others having been obtained in more polluted air than is found in Greenland [15]. The dependence of the conductivity ratio on pollution has been studied by Phillips [16].

The conduction current density is obtained by multiplying the values of conductivity with Clark's [7] simultaneously measured values of potential gradient at each altitude. It is found that the current density is approximately constant with altitude, having an average value of 3.7×10^{-12} amp/m^2, and a standard deviation of 7.8 per cent.

CONCLUSIONS

The effect of aircraft charge on the conductivity measurement during fair weather is negligible, even with an air velocity through the chamber as low as one-tenth the aircraft velocity. On a majority of the flights, a positive offset current was observed on both polar conductivity meters and is attributed to triboelectric charging of the central electrode by aerosols. Valid measurements of conductivity were made in the presence of this effect by varying the chamber voltage at a constant air flow rate.

An exponential increase in conductivity with altitude from 0.03 to 6 km obtained over Söndre Strömfjord, Greenland, during cloudless weather is representative of clean air. From this, and a simultaneously measured potential gradient distribution, the 6-km columnar resistance is 6.0×10^{16} ohm-m^2 and the average conduction current density is 3.7×10^{-12} amp/m^2. The average ratio of negative to positive conductivity is 1.1.

ACKNOWLEDGMENTS

The author wishes to thank Dr. H. O. Curtis, of the Air Force Cambridge Research Center, for the loan of the conductivity instruments used during this investigation. Thanks are also due Dr. J. F. Clark for many stimulating discussions; to Messrs. G. P. Serbu, R. V. Anderson, and E. C. Whipple, Jr., for their cooperation in the flight program; and to Prof. Jules de Launay, of the University of Maryland, who supervised the thesis.

References

[1] C. G. Stergis and others, J. Atmos. Terr. Phys., **6**, 233 (1955).
[2] R. C. Sagalyn and G. A. Faucher, J. Atmos. Terr. Phys., **5**, 253 (1954).
[3] J. H. Kraakevik and J. F. Clark, Report of NRL Progress, March 1957; p. 1.
[4] P. G. Gormley and M. Kennedy, Proc. R. Irish Acad., A, **52**, 163 (1949).
[5] S. C. Coroniti and others, J. Geophys. Res., **57**, 197 (1952).
[6] R. E. Holzer and W. E. Smith, Editors, Proceedings of the Conference on Atmospheric Electricity, Air Force Cambridge Research Center, Bedford, Massachusetts, Geophysical Research Paper No. 42, 244 (1955).
[7] J. F. Clark, J. Geophys. Res., **62**, 617 (1957).
[8] R. E. Holzer and W. E. Smith, *op. cit.*, p.,79.
[9] R. G. Stimmel and others, Proc. Inst. Radio Eng., **34**, 167P (1946).
[10] R. E. Holzer and W. E. Smith, *op. cit.*, p. 109.
[11] J. A. Chalmers, Atmospheric Electricity, Clarendon Press, Oxford (1949); p. 160.
[12] K. L. Sherman, Terr. Mag., **42**, 371 (1937).
[13] O. H. Gish and K. L. Sherman, Nation. Geog. Soc., Contrib. Tech. Papers, Stratosphere Ser., No. 2, 94 (1936).
[14] R. C. Callahan and others, J. Geophys. Res., **56**, 545 (1951).
[15] J. H. Kraakevik, The electrical conductivity and current density in the troposphere, University Microfilms, Ann Arbor, Michigan, 1957; Doctoral Dissertation Series, Pub. No. 21,526, pp. 111 and 124.
[16] B. B. Phillips and others, J. Geophys. Res., **60**, 289 (1955).

SIMULTANEOUS MEASUREMENTS OF THE POSITIVE AND NEGATIVE LIGHT-ION CONDUCTIVITIES TO 26 KILOMETERS

By R. H. Woessner, W. E. Cobb, and Ross Gunn

Office of Physical Research, U. S. Weather Bureau, Washington 25, D. C.

(Received October 26, 1957)

ABSTRACT

Continuous simultaneous measurements of the positive and negative light-ion conductivities have been made to altitudes of more than 26 km. Balloons carried aloft two nearly-identical self-ventilated Gerdien tubes, 60 cm in diameter and 120 cm long, each connected to utilize new circuits which modulated a standard radiosonde transmitter. The operating signals for the positive and negative units are arranged to provide two different characteristic pulses. Critical tests showed that saturation effects in the measurement have been eliminated. A number of successful flights have provided more than a thousand simultaneous measurements. It is found that the negative conductivity normally exceeds the positive conductivity at levels between 5 and 18 km. The altitude of the level of equal conductivity depends critically upon the cleanliness of the air and is commonly observed between 3 and 7 km. Below this level, the positive conductivity is normally in excess. It is found that the conductivity is represented by an expression of the form

$$\lambda = A \exp [\beta Z - \varphi Z^2 + \Omega Z^3]$$

where the constants are different for the positive and negative conductivities.

1. *Introduction*

A recent series of important investigations has emphasized the necessity for knowing the electrical conductivity at every level in the atmosphere and, in particular, the ratio of the conductivities due to the positive and negative light ions. It has been found that the electrical conductivities determine the charges accumulated on rain droplets as well as their subsequent rate of discharge [see 1 of "References" at end of paper]. Accordingly, the electrical conductivity of both the positive and negative ions and their ratio are important physical characteristics of the atmosphere and deserve special consideration. Earlier measurements by A. Wigand [2] and Gish and Wait [3] showed clearly that the conductivity, in general, increased more or less regularly with altitude, but Gish and Sherman's measurements on the Explorer II [4] exhibited peculiar decreases at the higher altitudes. None of our measurements confirms such a decrease. The later measure-

ments of Gish and Wait [3] made in aircraft extended only to 14 km. More recently, Callahan, *et al.* [5, 6], measured the conductivities in aircraft and concluded that the positive and negative light-ion conductivities were essentially the same at all measured altitudes. This conclusion is not fully consistent with their data. More recently, Stergis, *et al.* [7], measured the conductivity to 100,000 feet by the use of balloons. Except for the aircraft measurements of Gish and Wait [3], the conductivity of one polarity only was measured at a time and, therefore, the relative values were subject to considerable uncertainty. Recognizing the urgency of obtaining reliable and coherent data, we have made a large number of simultaneous measurements by the use of balloons released over a period of several months from Silver Hill, Maryland, on the outskirts of Washington, D. C. These new results are summarized in this article.

2. *Theoretical Considerations*

In order to clarify the analysis, it is assumed that cosmic rays are the only source of ionization in the atmosphere. This is not exactly true and the following expressions are therefore only applicable several kilometers above the earth. Consider particularly the altitude range from 10 to 26 km, where the temperature is approximately constant and approaches 218°K. In this range, pollution is thought to be small.

Let the cosmic-ray intensity obey the relation

$$dI = \delta \rho I dZ \quad \ldots\ldots (1)$$

where I is cosmic-ray intensity, δ is an average mass absorption coefficient, ρ is air density, and Z is the height above sea level. The air density is related to altitude by the expression

$$\rho = \rho_0 e^{-\alpha Z} \quad \ldots\ldots (2)$$

where ρ_0 is the air density at sea level.

$$\alpha = \frac{mg}{kT} \quad \ldots\ldots (2a)$$

and m is the mass of the mean equivalent air molecule, g is acceleration due to gravity, k is Boltzmann's constant, and T is the absolute temperature.

The following well-known equation relates the number of ion pairs formed per cubic centimeter per second, or q, with the cosmic-ray intensity I at an altitude Z'

$$q_{Z'} = B \rho_{Z'} I_{Z'} \quad \ldots\ldots (3)$$

where B is the mass ionization coefficient. From the preceding expressions, it follows that

$$ln \left(\frac{q}{q_{Z'}} \right) = -\alpha (Z - Z') - \frac{\delta \rho_0}{\alpha} (e^{-\alpha Z} - e^{-\alpha Z'}) \quad \ldots\ldots (4)$$

The electrical conductivity of the atmosphere may be represented by the equation

$$\lambda = neu = \left[\frac{q}{\alpha} \right]^{1/2} eu \quad \ldots\ldots (5)$$

where λ is electrical conductivity, n is number of ions per cubic centimeter, e is elementary electrical charge, u is the electrical mobility, and α is the recombination coefficient. From J. J. Thomson's theory of recombination [8, 9], the recombination coefficient for pressures in the lower atmosphere is approximately

$$\alpha = K\rho^{1/3} \quad \ldots\ldots\ldots\ldots\ldots\ldots\ldots\ldots\ldots\ldots (6)$$

where K is a constant. Using the additional relation that the mobility of an ion is inversely proportional to the density of the gas, one may substitute into Eq. (5), and after collecting terms and expanding it is found that

$$\left.\begin{aligned} ln\frac{\lambda}{\lambda_{Z'}} = &\left(\frac{2a}{3} + \frac{\delta\rho_0}{2}\exp\left[-aZ'\right]\right)(Z - Z') \\ &- \frac{\delta\rho_0}{4}a(Z - Z')^2\exp\left[-aZ'\right] \\ &+ \frac{\delta\rho_0}{12}a^2(Z - Z')^3\exp\left[-aZ'\right] \end{aligned}\right\} \quad \ldots\ldots\ldots\ldots (7)$$

Thus, it is anticipated that the electrical conductivity of the atmosphere can be expressed by an equation of the form

$$\lambda = A\exp\left[\beta Z - \varphi Z^2 + \Omega Z^3\right] \quad \ldots\ldots\ldots\ldots\ldots\ldots (8)$$

where A, β, φ, and Ω are constants having different values for the positive and negative light ions.

It is clear from Eq. (7) that one may divide the coefficient of the cubic term by the coefficient of the quadratic term to determine a. From the least-square values of the coefficients, it is calculated that a approximates $14.0 \times 10^{-7}\text{cm}^{-1}$ and $16.2 \times 10^{-7}\text{cm}^{-1}$ for λ_+ and λ_-, respectively. These values may be compared with the value calculated from Eq. (2a), or $15.7 \times 10^{-7}\text{cm}^{-1}$. Further, from Eq. (7), δ may be calculated to have values of $14.5 \times 10^{-3}\text{cm}^2/\text{gm}$ and $9.6 \times 10^{-3}\text{cm}^2/\text{gm}$ for λ_+ and λ_-, respectively. Available information on cosmic rays [10] suggests that δ has a value lying between 7 and $10 \times 10^{-3}\text{cm}^2/\text{gm}$. The agreement with estimates from other sources is, therefore, considered satisfactory.

3. *Apparatus*

The apparatus consists of two nearly-identical cylindrical condensers, mounted side by side. The outer cylinder of each condenser is fabricated out of light-weight aluminum tubing and wire, disposed to form a coarse screen. The outer cylinders were 120 cm long and 60 cm in diameter, while the inner cylinder consisted of a light paper tube covered with aluminum foil and is 90 cm long and 10 cm in diameter. The large size was adopted to insure free circulation of the environmental air and freedom from saturation. The inner cylinder is insulated from the outer by Teflon. The electronic circuits for each polar conductivity apparatus is mounted at the top of the condensers, as shown in Figure 1. The highly insulated grid of an electrometer tube is connected to the center cylinder for the positive conductivity apparatus and to the outer cylinder of the other condenser for the negative conductivity apparatus. A predetermined voltage (approximately 34

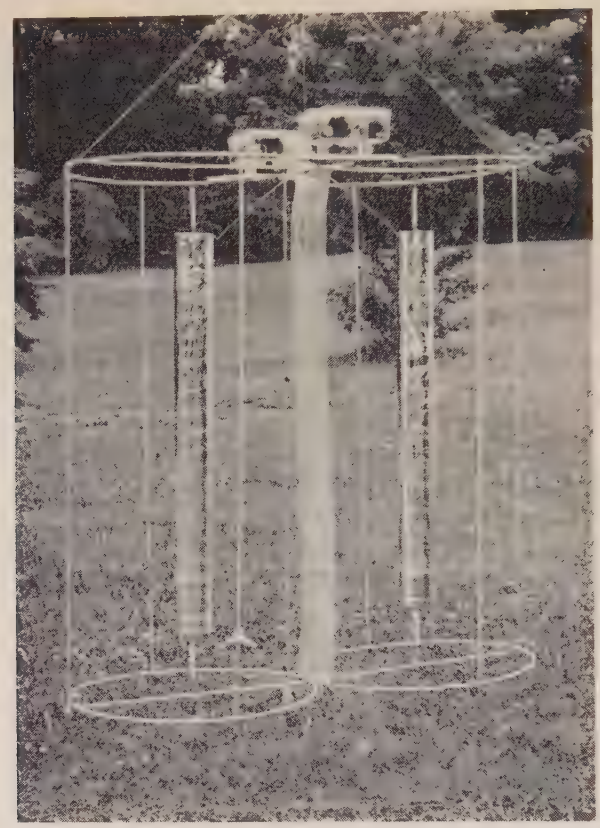

Fig. 1—Photograph of conductivity apparatus. The outer cylinder of each condenser is fabricated of single strands of aluminum wire, spaced about every 3 cm around the perimeter. Electronic circuitry is shown mounted on top of the condensers. Between the condensers, there is a strip of fine-mesh screen that effectively shields the center electrodes from each other.

volts) is briefly applied to each set of concentric cylinders by the operation of highly insulated relays. Conducting air passing through the cylinders as a result of their motion then discharges the system, including the grid of the electrometer tube. When the potential of the grid with respect to the filament drops to a second predetermined value, a sensitive relay in the plate circuit is activated and the circuit is again recharged. Simultaneously, this relay circuit modulates a standard radiosonde transmitter whose signals also provide pressure data that are received at the ground and automatically recorded by a high-speed Electronik recorder. The operating signals for the positive and negative units are arranged to provide two different characteristic pulses so that the discharging periods for the two instruments may independently be determined.

The above apparatus was carried aloft by means of a single rubber balloon. The instruments were arranged to hang some 70 feet below the balloon, and the radiosonde transmitter is attached 50 feet farther below. Both devices are supported by means of piano wire, which also serves to minimize any effects of external electric fields upon the conductivity measurements. The balloon is inflated to give an

average rate of ascent of 5 meters per second, and after the balloon bursts the apparatus descends by means of a parachute some five or six times as fast as the ascent. The entire apparatus, including the radiosonde, weighs approximately ten pounds.

The electrical capacity of each unit was measured accurately with a Wulf unifilar electrometer and a precision condenser by standard methods. Each condenser (minus the electronic circuitry) has a capacity of approximately 35$\mu\mu$f. The total capacity of the λ_- and λ_+ apparatus averages about 53$\mu\mu$f and 40$\mu\mu$f, respectively.

The schematic diagrams of the conductivity apparatus appear in Figures

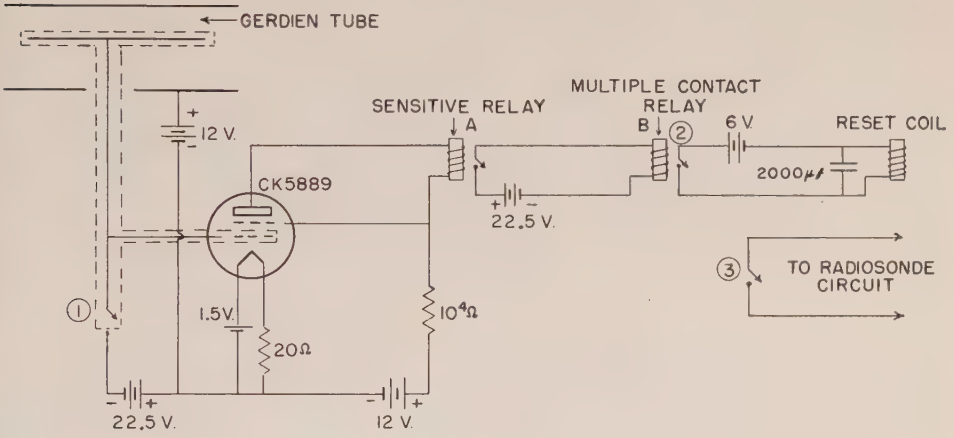

(a) Positive Conductivity

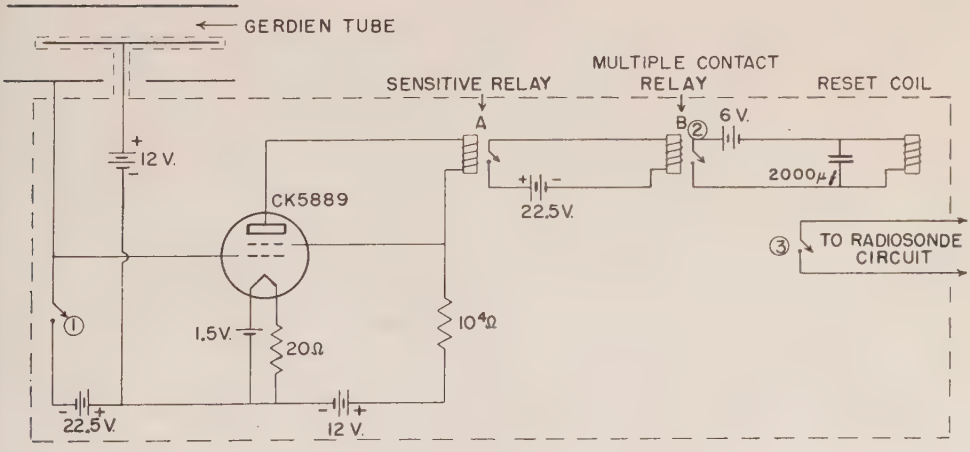

(b) Negative Conductivity

FIG. 2(*a*)—Positive conductivity apparatus circuit diagram. The circuit parts enclosed by the dashed line are highly insulated.

2(*b*)—Negative conductivity apparatus circuit diagram. The circuit parts enclosed by the dashed line are highly insulated.

2(*a*) and 2(*b*). In each diagram, dashed line encloses the components that are highly insulated by Teflon. The plate circuit in each case contains a Sensitrol relay having a 2,000-ohm moving coil which trips at a current of one microampere and is automatically reset by a solenoid built into the base of the relay. This sensitive relay in turn trips a multiple contact relay which *simultaneously* recharges the circuit, modulates the radiosonde signal, and resets the Sensitrol relay. A Raytheon electrometer tube CK 5889 is used in each circuit.

The equation used to calculate the conductivity from the observed time-interval measurements is

$$\lambda = \frac{ln \frac{V_0}{V}}{4\pi(C_V/C_T)t} \qquad (9)$$

where V_0 is the initial voltage across the condenser, V is the voltage to which the condenser is discharged before it trips the relay and is recharged, C_V is the measured ventilated capacity, C_T is the measured total capacity, and t is the time in seconds required for the condenser voltage to drop from V_0 to V. Whenever the discharge time t becomes as short as 25 seconds, a small correction was introduced to allow for the measured delay in response of the first sensitive relay.

4. *Results*

The flights were made between September 1956 and June 1957. Both positive and negative conductivities were continuously measured on four flights, while only positive conductivity was measured on two others. All ascents were begun near noon local time with less than one-tenth cloud cover in a relatively new

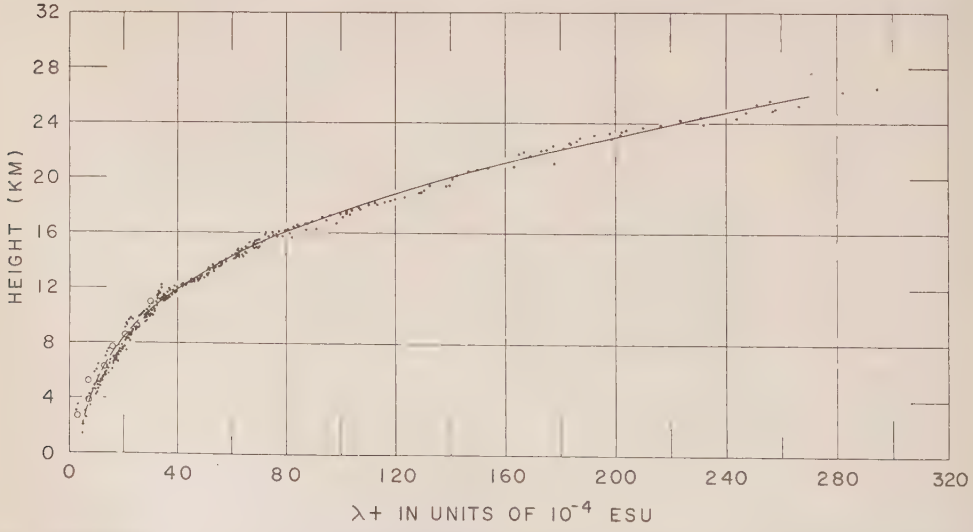

FIG. 3 –Positive conductivity measurements as a function of altitude. The solid line represents a least squares fit, using the data above 10 km. Measurements of λ_+ taken on the descent of the Explorer II flight are plotted as open circles.

high-pressure system. Maximum altitudes ranging from 16 to 26.5 km were reached on the various flights. The data show that, although the conductivities varied considerably from run to run in the lower levels where pollution was probably present, they were remarkably consistent above 10 km.

Ascent data agreed closely with descent data on these flights, showing that ventilation on ascent was more than sufficient to prevent saturation. Since the ascent time intervals could be measured most accurately, the attached curves and analysis represent ascent data only. Each flight provided from 300 to 700 individual and simultaneous measurements of each polar conductivity.

The positive conductivity measurements are plotted against height for all flights in Figure 3. The solid line represents a least squares fit, using the data above 10 km. These data are well represented by Eq. (10). The curve is dashed below 10 km to emphasize the fact that these data were not used to determine the curve. For comparison, values of λ_+ taken on the descent of the Explorer II are plotted as open circles.

Negative conductivity measurements are plotted against height for all flights in Figure 4. Again, it must be noted that the measurements below 10 km were

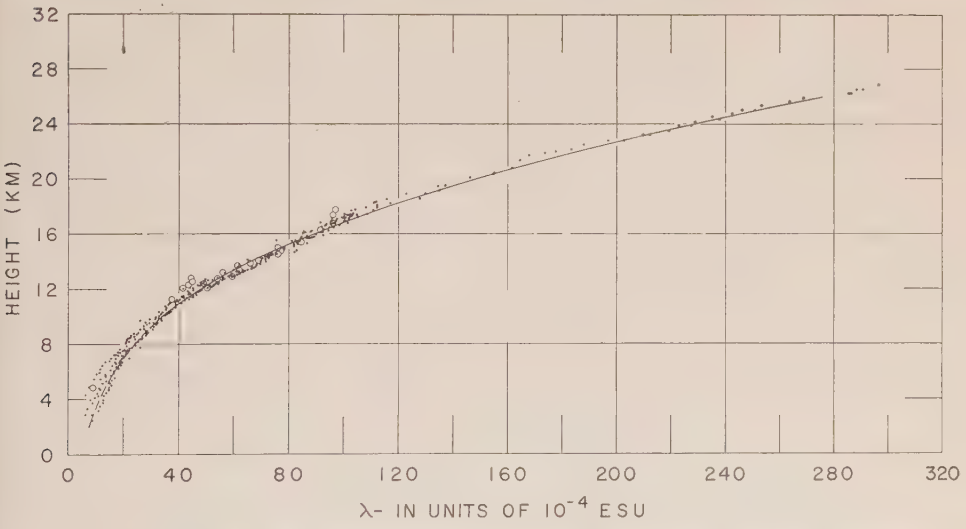

FIG. 4—Negative conductivity measurements as a function of altitude. The solid line represents a least squares fit, using the data above 10 km. Measurements of λ_- taken on the descent of the Explorer II flight are plotted as open circles.

ignored in the least squares fit shown by the solid line. These values of the negative conductivity are well represented by Eq. (11). Values of negative conductivity taken on the descent of the Explorer II are plotted as open circles. Some of the Explorer II measurements showed evidence of saturation phenomena at high levels and these data are not reproduced here.

It is frequently important to express the conductivity in a simple analytical form. Accordingly, a least-square analysis of the data summarized in Figures 3 and 4 has been carried out and expressed in the form of Eq. (8). The analysis

shows that the data may be represented nearly as well by the use of three constants as by the use of four. Accordingly, we have determined the best values for the constants, ignoring the cubic terms in the exponential. The two relations resulting from this analysis are

$$\lambda_+ = 3.00 \times 10^{-4} \exp (0.254 \times 10^{-5}Z - 0.00309 \times 10^{-10}Z^2) \text{ esu} \ldots . (10)$$

and

$$\lambda_- = 4.81 \times 10^{-4} \exp (0.222 \times 10^{-5}Z - 0.00255 \times 10^{-10}Z^2) \text{ esu} \ldots . (11)$$

where Z is in centimeters. From these expressions, the *ratio* of the positive and negative light-ion conductivities is given by

$$\frac{\lambda_+}{\lambda_-} = 0.624 \exp (3.2 \times 10^{-7}Z - 5.4 \times 10^{-14}Z^2) \ldots \ldots \ldots . (12)$$

It may be noted that the conductivity ratio increases steadily towards unity at the highest measured level. It should be pointed out that the above expressions, while useful, are not very reliable *below* five kilometers altitude because of the variability of contamination at these low altitudes.

5. *Discussion*

Although several investigators have measured the light-ion conductivities at various altitudes, the number of measurements have been limited and only one group has attempted to measure *simultaneously* both polar conductivities. Since the electrification of clouds and precipitation in the atmosphere depend critically upon the ratio of the conductivities [1], it seemed important to extend earlier work and pay particular attention to the *ratio* of the positive and negative light-ion conductivities. It is well known that cosmic rays and all ionizers produce ion *pairs*, and, therefore, one might conclude that the ionic population density for the positive and negative ions would always be the same. Further, it is well known that the mobility of the negative ion is some 40 per cent greater than the typical positive ion. Accordingly, it seems clear that when ions can disappear only by recombination with the opposite sign, an equilibrium will be established wherein the ratio of the conductivities is the same as the ratio of the mobilities of the ions. Laboratory measurement shows that this inference is proper, provided the ions are not transferred to cloud droplets or other suspended particulate matter. The role of suspended particles in modifying the conductivity ratio has been well illustrated in our laboratory by the measurements of Phillips, *et al.* [11]. These measurements showed that as the contamination in the atmosphere is removed the ratio of the conductivities progressively changes from unity to the ratio of the ionic mobilities in clean air.

In addition to the role of suspended particles in the atmosphere, the relative conductivities due to the positive and negative ions frequently depend on other electrical effects. For example, the surface of the earth, in clear weather, normally carries a negative charge. This charge imposes a systematic motion of the positive ions towards the earth, and thus establishes a positive space charge in the vicinity of the ground. The role of this space charge in modifying the distribution of charges carried by particulate matter at lower levels is not yet fully understood. It is

known that the population density of the positive ions is greater than one might anticipate, throughout a layer a kilometer or more deep. Electric field measurements under fair-weather conditions do show that there is a marked accumulation of excess charges when abnormal amounts of contamination are present. Recent unpublished simultaneous measurements, made at four stations separated by five miles each, show that space-charge accumulations are frequently limited to relatively small areas within the city. More measurements and analysis will be necessary fully to describe the space-charge characteristics of the lower atmosphere wherein the positive conductivity is normally observed to exceed that of the negative.

All measurements summarized in Figures 3 and 4 were obtained simultaneously and, therefore, the *relative* values at any given altitude are reliable. None of the measurements suggest a decrease in conductivity at high levels of the character reported by Gish and Sherman in their Explorer II flights [4]. Measurements on aircraft made by Callahan, *et al.* [5, 6], have suggested that the positive and negative light-ion conductivities were the same at all altitudes. We find little justification for this conclusion, even at altitudes below 12 km where their measurements were made. The nature of the discrepancy is illustrated in Figure 5, which

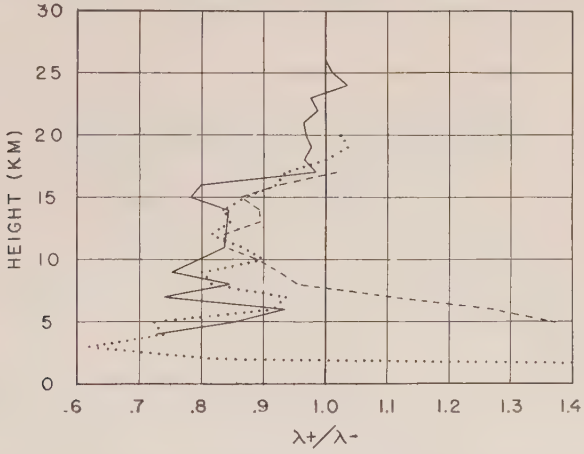

FIG. 5—The ratio λ_+/λ_- is plotted against altitude. The flights of September 18, 1956, November 14, 1956, and May 29, 1957, are represented by a dashed, dotted, and solid line, respectively

summarizes the observed conductivity ratios as a function of altitude. Although these new measurements exhibit considerable scatter in the lowest 5 km, the agreement on various days at altitudes above 10 km is unusually good. This implies, and direct observations show, that the suspended nuclei in the atmosphere decrease sharply above 5 km.

Gish and Wait [3] have given a parabolic expression for the dependence of conductivity on altitude. Our measurements show that this is not a very good approximation outside the limited range of their measurements and we have, accordingly, developed the quasi-empirical form given by Eq. (8). We believe that Eqs. (10) and (11) represent the form as well as the magnitude of the conductivity distribution at Washington, D. C. The magnitude and distribution are doubtless somewhat dependent on the magnetic latitude.

It is of considerable interest to compare the electrical conductivity today with that measured in 1935. The explosion of nuclear bombs within the last ten years has released large quantities of radioactive material in the stratosphere, and it is certain that this material will contribute to the ionization and conductivity. Figures 3 and 4 include open circles that define the conductivity measurements made by Gish and Sherman on the Explorer II. Their measurements were not simultaneous, but it is interesting to observe that they do fall on these new measurements within the limit of experimental error. A comparison of the data implies that the ionization due to radioactive material in the stratosphere is a small fraction of that due to cosmic rays. In any event, the early measurements on the Explorer II and the present series should be useful guides in the future evaluation of radioactive contamination produced in the atmosphere.

The measurements summarized in Figures 3 and 4 above show clearly that the conductivities due to the positive and negative ions are, in general, notably different at most levels in the atmosphere. Thus, electrification of cloud droplets by diffusion or by conductive transport is likely to be important. In the lower 5 or 7 km, the positive conductivity is normally in excess, and above 7 km but below 18 the negative conductivity is in excess.

6. *Conclusions*

In summing up, the preceding data show that (1) the electrical conductivity increases steadily with altitude, (2) considerable variability of both λ_+ and λ_- is present in the lower atmosphere and λ_+ here is usually greater than λ_-, (3) the level of equal conductivities is frequently below 3 km but may be as high as 7 km, (4) above this special level up to approximately 18 km λ_- exceeds λ_+, and (5) between 18 and 26 km λ_- and λ_+ are approximately equal.

7. *Acknowledgments*

The authors wish to acknowledge the helpful advice of Dr. Gilbert D. Kinzer of this Office and the cooperation of the Weather Bureau personnel at Silver Hill, Maryland, in the launching and monitoring of these flights.

References

[1] R. Gunn, Proc. Inst. Radio Eng., **45**, 1331-1359 (1957).
[2] A. Wigand, Terr. Mag., **19**, 93-101 (1914).
[3] O. H. Gish and G. R. Wait, J. Geophys. Res., **55**, 473-484 (1950).
[4] O. H. Gish and K. L. Sherman, Nation. Geog. Soc., Contrib. Tech. Papers, Stratosphere Ser., No. 2, 94-116 (1936).
[5] R. C. Callahan, S. C. Coroniti, A. J. Parziale, and R. Patten, J. Geophys. Res., **56**, 545-551 (1951).
[6] R. C. Sagalyn and G. A. Faucher, J. Atmos. Terr. Phys., **5**, 253-272 (1954).
[7] C. G. Stergis, S. C. Coroniti, *et al.*, J. Atmos. Terr. Phys., **6**, 233-242 (1955).
[8] L. B. Loeb, Fundamental Processes of Electrical Discharge in Gases, John Wiley and Sons, Inc., New York, p. 112 (1947).
[9] M. E. Gardner, Phys. Rev., **53**, 75-83 (1938).
[10] R. A. Millikan, Rev. Modern Phys., **21**, 1-13 (1949).
[11] B. B. Phillips, P. A. Allee, J. C. Pales, and R. H. Woessner, J. Geophys. Res., **60**, 289-296 (1955).

THE INITIAL RADIUS OF METEORIC IONIZATION TRAILS*

By L. A. Manning

Radio Propagation Laboratory, Stanford University, Stanford, California

(Received November 2, 1957)

ABSTRACT

The formation about the path of a meteor of regions of ionized and neutral atoms of meteoric material is investigated from the viewpoint of kinetic theory. It is found that the high initial velocity of the diffusing particles causes the trail to quickly reach an "initial radius" from which normal diffusion then proceeds. It is shown that the reflected signal may for most purposes be computed on the assumption that the trail reaches this initial radius instantaneously. The value of the initial radius is approximately 14 mean-free-paths; it is thus greater for the neutral than for the ionized trail. It is shown that at very high frequencies the initial radius may reduce the amplitude of the returned signal from under-dense trails by as much as 50 db. If heating is neglected, it is shown that the effect of initial radius on over-dense trails is marked at the same heights and frequencies as for under-dense trails.

I. STATEMENT OF THE PROBLEM

When a meteoric particle interacts with the atmosphere, a trail of ionization is left behind in its path. The trail contains a concentration of free electrons that can be measured by radio reflection techniques. From spectral observation of meteor trails, it is found that ionized and excited atoms of meteoric material are present as well [see 1 of "References" at end of paper].

We shall call the region containing meteoric ions the ion-trail. Neutral atoms of meteoric material are also deposited in the atmosphere, and for distinction we shall refer to the region in which they are present as the atom-trail. The two trails thus defined will have a different radial extent. We shall use subscripts i and n to denote quantities characteristic of the ionized and neutral trails; when an equation may be applied to either trail, no subscripts will be used.

To an order of magnitude, the number of electrons produced in the ion-trail is comparable to the total number of atoms in the meteor. As time advances, the ionization produced near the trail diffuses outward to greater radii. On the assumption that the ionized particles are in thermal equilibrium with the surrounding air, the ionization density N a distance r from the trail is

$$N = \frac{Qe^{-r^2/4Dt}}{4\pi Dt} \quad \ldots\ldots\ldots\ldots\ldots\ldots\ldots\ldots\ldots\ldots (1)$$

*Jointly supported by the U. S. Army Signal Corps, the U. S. Air Force, and the U. S. Navy (Office of Naval Research).

where D is the coefficient of diffusion, t is the time, and Q is the initial line density of ionization. The maximum ionization density will occur on the axis, and is $Q/4\pi Dt$. The radial distribution function $\exp[-r^2/4Dt]$ is Gaussian; we may call $R^2 = 4Dt$ the radius of the trail. Thus, on the assumption that the charge is initially confined to a line, the maximum ionization density is at first infinite, and the initial radius R_0 is zero.

When the radio echo strength scattered from the ionization distribution (1) is computed, two cases must be distinguished. First, if the line density Q is less than about 10^{14} electrons per meter, the presence of the ionization does not materially alter the incident field strength. A first-order scattering theory may be used. It is then found that the back-scattered signal strength per unit length of trail varies with time as

$$e^{-16\pi^2 Dt/\lambda^2} = e^{-4\pi^2 R^2/\lambda^2} \quad \ldots\ldots (2)$$

Experimental studies of the rate of signal strength decay yield mean values of D, of 3 or 4 meters^2/second. The value of diffusion coefficient found in this way is consistent with theoretical values for ambipolar diffusion at meteoric heights.

If the line density of the trail is greater than about 10^{14} electrons per meter, the trail is said to be over-dense, since for sufficiently small values of time there will be a central core of negative dielectric constant that will serve to prevent penetration of the incident wave. The trail is then treated approximately as a metallic cylinder whose radius is determined by the dimensions of the negative dielectric core. This radius is

$$r^2 = 4Dt \ln (81Q/4\pi f^2 Dt) \quad \ldots\ldots (3)$$

where f is the frequency in cycles per second. It is zero at $t = 0$, and rises to a maximum value of $r^2 = 81Q/4\pi f^2 e$; the radius of the equivalent cylinder shrinks to zero, and the echo is over after an interval

$$t_H = \frac{\lambda^2 \times 0.885 \times 10^{-14} Q}{4\pi^3 D} \quad \ldots\ldots (4)$$

The echo durations corresponding to the existence of this core have been used to determine the line densities Q of over-dense trails.

The formula (1) for the ionization density variation with time and radius assumes the ionization to have been formed initially on a line. Suppose instead that the ionization was initially distributed in a Gaussian manner, with an initial radius R_0 . Let t_0 be the time required for the initial radius to have been reached by diffusion from zero radius in accordance with (1). Then we can modify (1), (2), and (3) to conform to the assumed initial radius by substituting $(t + t_0)$ for t in each equation. The effect of initial radius on echoes from under-dense trails is to reduce the initial or maximum echo strength by the factor

$$\eta_0 = e^{-16\pi^2 Dt_0/\lambda^2} = e^{-4\pi^2 R_0^2/\lambda^2} \quad \ldots\ldots (5)$$

This factor becomes increasingly important at the shorter wavelengths, and eventually becomes the limiting factor in echo detectability. In the case of over-dense trails, the maximum received signal strength does not occur at the start of

the echo. Thus, if t_0 is less than the value t_H of (4) divided by e, corresponding to maximum echo strength, little reduction in detectability occurs. The initial radius of the trail R_0 may be related to the "initial duration" t_0 by the formula $R_0^2 = 4Dt_0$. The exact value of R_0 is clearly of great importance in the theory of meteoric reflection at very high frequencies.

II. FACTORS INFLUENCING THE INITIAL RADIUS OF THE TRAIL

Although it has been tacitly assumed in the past that the initial radius of a meteoric ionization trail is equal to the mean-free-path of the atmosphere, closer inspection will show important deviations from this first approximation. Despite the lack of a thorough understanding of the processes of meteoric ionization, we can deduce certain properties of a working model with confidence. We know the velocity of meteoric flight to lie within the limits of 11 to 72 km/s. We know the mean-free-path, air temperature, and diffusion coefficient for ions at meteoric heights, and we know the main constituent of the atmosphere to be molecular nitrogen. As the meteor interacts with the atmosphere, we may assume that meteoric molecules and ions separate from the main body of the meteor and start to diffuse into the atmosphere with an effective kinetic temperature determined by the meteoric velocity. We need not concern ourselves specifically with the diffusion of the electrons, since no matter when or where they are freed they must fill the same volume as do the positive ions from which they are produced, so that neutrality will be preserved. If molecules of air as well as of the meteor are ionized by collision with meteoric molecules, they will share the energy of the meteoric atoms with which they collide, and so will diffuse with velocities similar to those of the meteoric atoms. Since the mean-free-path for ions is only about one-fifth of that for neutral atoms [2], it is, however, important to know whether much diffusion of neutral atoms takes place before ionization, or whether the locations of the ions are determined entirely by their own slower rate of diffusion.

As meteoric ions or atoms traveling, at say, 50 km/s encounter atmospheric atoms with thermal velocities of the order of half a kilometer per second, they will retain, on the average, only a fraction K of their initial speed. Their velocities will simultaneously be redirected through an angle whose probability distribution is a function of the relative mass of the meteoric and air molecules, the velocity of impact through its influence on the collision cross-section, and the velocity of the meteor atom in relation to the thermal velocity distribution of the air. Upon a single collision, a meteoric atom may be expected to retain, on the average, over two-thirds of its initial velocity, and to retain its initial direction of motion as the most probable direction of rebound. Thus, because of the persistence of velocity, the path taken by the meteoric atom between collisions will not be a three-dimensional random walk. If it were, and if the mean path length between collisions were L, the atomic and ionization density distributions after M collisions would be

$$N = \frac{Q}{\pi M} \exp\left\{-\frac{3r^2}{4ML^2}\right\} \quad \ldots\ldots\ldots\ldots\ldots\ldots\ldots\ldots\ldots\ldots (6)$$

A precise solution for the electron density distribution is involved and difficult. Moreover, some of the necessary constants, such as the molecular mass of the

meteoric molecules, are not known exactly. We shall, therefore, proceed with an approximate solution designed to provide a first estimate of the true initial radius of the trail. The problem will be simplified by assuming first that the air molecules are stationary. The resulting diffusion rate will be in little error until the meteor atoms have reached thermal velocities. The curve of radius *vs* time obtained in this way will then be bridged to a curve of radius *vs* time resulting from diffusion at the equilibrium rate for the atmospheric temperature. With this assumption, the mean-free-path for meteoric atoms becomes $\sqrt{2}l_n$, if l_n is the m.f.p. for air molecules at atmospheric temperature; for the diffusion of ions, the m.f.p. will be $\sqrt{2}l_i \cong \sqrt{2}l_n/5$. There will be in addition some change in the m.f.p. because of the high effective velocity. This factor will approach one as the meteoric atoms slow down; as an approximation, we shall assume it unity throughout. Since the meteoric atoms do not execute random walks between collisions due to the persistence of velocity, we cannot equate $\sqrt{2}l$ to the L of (6). We may suppose, however, that after several collisions, the meteoric atoms will have acquired sufficiently random directions of travel so that the theory of random walks may be applied to the units of several collision paths. Since the number of these independent groups of paths will still be proportional to the total number of collisions M, while the effective path length for each of these units will be proportional to the individual mean-free-paths, we may state that when the persistence of velocity is considered, the value of ML^2 from (6) will take the value $pM(\sqrt{2}l)^2$. The constant p is greater than one. It expresses the squared ratio of the distance traveled taking velocity persistence into account to that for a purely random walk. The most appropriate value of p to use is uncertain, as it depends upon the relative mass of the meteoric and air molecules. We shall assume $p = 5$, a value shown in the Appendix to be appropriate for meteor atoms whose mass is that of the air.

The factor K describing the mean fraction of its velocity retained by a meteoric atom in a collision must lie between 2/3 and 1; its actual value depends on the ratio of masses of the colliding particles. We shall assume it to have the value 2/3, corresponding to meteoric atoms of the same mass as the air. If we call the meteor velocity V, and that of the meteoric atom after M collisions v, $v = V \exp(-\alpha M)$, where $\alpha = \ln(1/K) \cong 0.4$. Then the interval between collisions will be $(\sqrt{2}l/V) \exp(\alpha M)$, and the time t required for M collisions will be

$$t = (\sqrt{2}l/V) \int_0^M \exp(\alpha M)\, dM = (\sqrt{2}l/\alpha V)(e^{\alpha M} - 1)$$

where the summation has been approximated by an integral. We get for M

$$M = (1/\alpha)\ln\left[\frac{\alpha V t}{\sqrt{2}l} + 1\right] \quad \ldots\ldots\ldots\ldots\ldots\ldots\ldots\ldots (7)$$

The trail radius $R = \sqrt{4pM/3}\, L$, and $L = \sqrt{2}l$, so

$$R = R_v = l(8p/3\alpha)^{1/2}\ln^{1/2}\left[\frac{\alpha V t}{\sqrt{2}l} + 1\right] \quad \ldots\ldots\ldots\ldots\ldots\ldots\ldots\ldots (8)$$

The symbol R_v will be used to indicate that this is only the component of radius due to the high initial velocity of the meteoric atoms.

This approximate value of radius, based on neglect of the thermal velocities of the air, eventually increases very slowly with time. It must be bridged to the trail radius $R_a^2 = 4D(t + t_a)$ for large time, where t_a is the effective head-start given to the diffusion by the high initial energy of the diffusing particles.

Since the initial diffusion of Eq. (8) is expressed in terms of the mean-free-path, it is desirable to express R_a^2 in terms of l too. Because a diffusion coefficient D_i of 3 m^2/s is observed for meteoric ionization at a height of about 93 km, where the ionic m.f.p. $l_i \cong (1/5)l_n = 1$ cm [3], we shall write

$$\left.\begin{aligned} R_a^2 &= (4D_i/l_i)l(t + t_a) \\ &\cong 1200l(t + t_a) \end{aligned}\right\} \quad \ldots\ldots\ldots\ldots\ldots\ldots\ldots\ldots (9)$$

for atoms or ions, depending on the choice of l.

In Figure 1, values of R^2 from (8) and (9) are plotted *vs* time for a molecular mean-free-path of 5 cm, and a meteoric velocity of 50 km/s. For these mean conditions, it is seen that the effect of the initial velocity of the meteor atoms

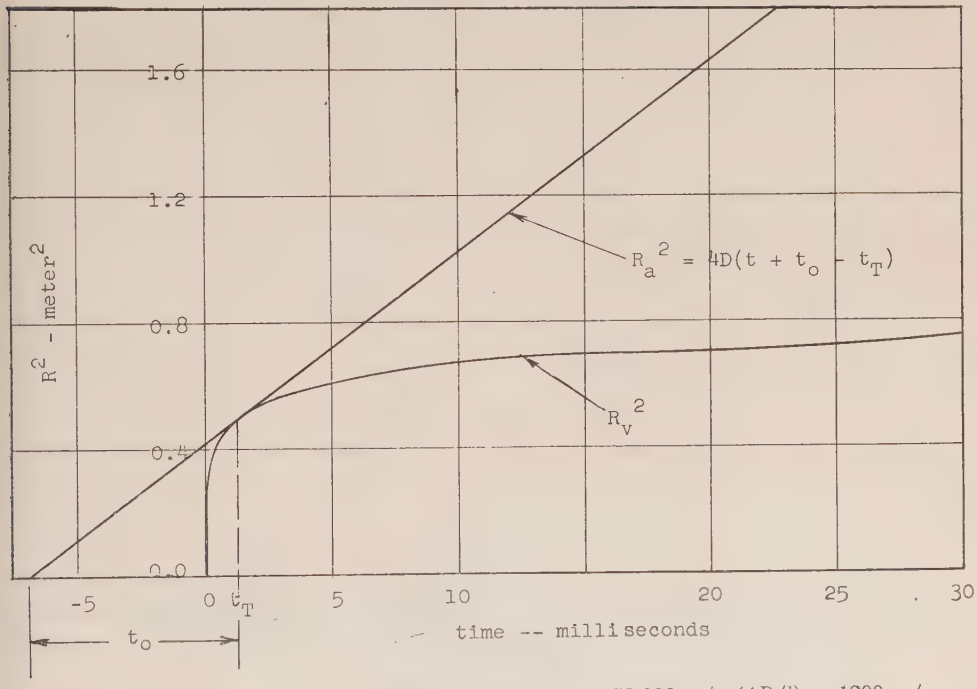

FIG. 1—Squared trail radius *vs* time for $l = 5$ cm, $v = 50{,}000$ m/s, $(4D/l) = 1200$ m/s

is to cause the "atom-trail" to expand to a radius of about 70 cm in a millisecond or so. The ion-trail will be one-fifth as large, if no ionization takes place during diffusion—otherwise of intermediate radius. After the trail reaches this size, diffusion would be increasingly sluggish were it not for the thermal velocities of the air. It is appropriate that the radius R_v achieved almost immediately be treated as an initial radius as far as subsequent diffusion to a radius R_a is concerned.

The value of initial radius R_0 at which the steady diffusion commences can be estimated sufficiently closely by so adjusting t_a that the curves for R_a^2 and R_v^2 are tangent. The value of R at their tangency is then treated as an instantaneously formed trail radius from which normal diffusion starts. This procedure neglects the rather slight further increase in radius of the trail that is to be expected due to the above-thermal energy possessed by the meteor atoms for t greater than at the point of tangency. However, it also neglects the compensating decrease of L from $\sqrt{2}l$ to l in the same region, and the decreased persistence p when thermal velocities are approached.

If we seek the time t_T at which the rates of increase of R_a and R_v are equal, we find

$$t_T = \frac{\sqrt{2}l}{\alpha V}\left[\frac{8pV}{3\sqrt{2}(4D/l)} - 1\right] \cong \frac{8pl}{3\alpha(4D/l)} \cong (1/36)l \quad \ldots\ldots\ldots (10)$$

Substituting this time of tangency into (8), we get for the radius at the tangency

$$R_0 = (8p/3\alpha)^{1/2}\, l\, \ln^{1/2}\{8pV/[3\sqrt{2}(4D/l)]\} \quad \ldots\ldots\ldots\ldots (11)$$

where V is in meters per second. We interpret R_0 to be the initial radius of the trail, from which diffusion proceeds at the rate $R = [(4D/l)lt + R_0^2]^{1/2}$. In view of the many assumptions of the analysis, we may simply conclude that for all velocities

TABLE 1—*R_0/l vs V, assuming $p = 5$, $\alpha = 0.4$, $4D_i/l_i = 1200$ m/s*

V km/s	R_0/l
11	12.3
20	12.9
30	13.5
40	13.8
50	14.1
60	14.3
72	14.5

$$R_0 = 14l \quad \ldots\ldots\ldots\ldots\ldots\ldots\ldots\ldots (12)$$

for either the atom-trail or the ion-trail, taking l as the m.f.p. for either neutral atoms or ions. The initial duration t_0 then is

$$t_0 = \frac{R_0^2}{4D} \cong \frac{0.166l^2}{l_i} \quad \ldots\ldots\ldots\ldots\ldots\ldots\ldots (13)$$

with l in meters. For ions, this becomes $t_{0i} = 0.166l_i = 0.0277\ l_n$. For atoms, $t_{0a} = 0.83\ l_n$. Thus, a meteor trail appears as large after the fraction of a second given by (10) as if it had been diffusing from a straight line at the usual rate for t_0 seconds. Velocity exerts a very slight direct influence on the initial radius or duration, but is an important factor in determining the heights of meteors, and so the mean-free-paths l.

III. INFLUENCE OF INITIAL RADIUS ON METEOR ECHO-STRENGTH FROM UNDER-DENSE TRAILS

As we have defined the initial radius R_0 of a meteoric ionization trail, it is the radius to which the trail expands under the influence of the meteoric velocity. On reaching this radius, diffusion proceeds at a steady pace. Because the radius R_0 is reached so quickly, only that part of the trail immediately behind the meteoric body is of a smaller radius. If the meteoric velocity is 50 km/s, and if the transient period t_T during which R_0 is reached is $l_i/36 = 3 \times 10^{-4}$ second, the length of trail that will not yet have diffused to the initial radius will be only 15 meters long. This length is small compared with both the width $\sqrt{2\lambda d}$ of the first Fresnel zone where d is the range, and with the product of the meteoric velocity and the normal diffusion exponential-decay time constant. Therefore, the signal returned from that part of the trail which is subject to the transient expansion can under most circumstances be neglected in comparison with that from more slowly diffusing parts of the trail. Eq. (5) then correctly gives the reduction in received signal strength η resulting from the rapid initial expansion. For very short wavelengths, however, the reduction in signal strength reaches a limit not shown by (5). We must, therefore, make a more complete analysis of the effect of initial expansion on received signal strength.

Since the time of formation of the initial radius is small compared with the time taken for a meteor to pass through the principal Fresnel zone, we shall discuss the case in which the scattering from all lengths of the trail are in-phase at the receiver. Then the received signal will be the integral over the length of the scattering from elements of age x/V, where x is a trail-length coordinate measured from the head of the trail. Changing variables to the age t of each elemental length of trail, we write an integral I proportional to the total received echo amplitude.

$$I = \int_0^\infty \exp\left\{-\frac{4\pi^2 R^2(t)}{\lambda^2}\right\} dt \qquad (14)$$

Two cases are of interest. First, if diffusion had occurred with fixed diffusion coefficient D from a zero initial radius, the signal would have been proportional to

$$I_A = \int_0^\infty \exp\left\{\frac{-16\pi^2 Dt}{\lambda^2}\right\} dt = t_D \qquad (15)$$

where $t_D = \lambda^2/(16\pi^2 D)$ is the exponential signal-strength decay time-constant. Second, if diffusion occurs initially at a rate $R_v(t)$ given by (8), and thereafter at the rate $R_a(t)$ given by (9), the signal strength will be proportional to

$$I_B = \int_0^{t_T} \exp\left\{\frac{-4\pi^2 R_v^2}{\lambda^2}\right\} dt + \int_{t_T}^\infty \exp\left\{\frac{-16\pi^2 D(t + t_0 - t_T)}{\lambda^2}\right\} \qquad (16)$$

where t_T is given by (10). Upon doing the integrations, one finds

$$I_B = \frac{1}{A}\left[\frac{(At_T + 1)^{1-4\pi^2 K/\lambda^2} - 1}{1 - \frac{4\pi^2 K}{\lambda^2}}\right] + t_D \exp\left\{\frac{-4\pi^2 R_0^2}{\lambda^2}\right\} \qquad (17)$$

where $A = \alpha V/\sqrt{2}l$, and $K = (8p/3\alpha)l^2$.

Since we are interested in the reduction in the total reflected signal strength due to the initial expansion effect alone, we shall normalize I_B of (17) using $I_A = t_D$ of (15). Then we may show that the signal strength reduction factor due solely to the initial radius effect is

$$\eta = (I_B/I_A) = \eta_0 + \eta_1 \quad \ldots\ldots(18)$$

where

$$\eta_0 = \exp\left\{\frac{-4\pi^2 R_0^2}{\lambda^2}\right\} \quad \ldots\ldots(19)$$

is identical with (5); η_0 is the signal amplitude that would be obtained if the expansion to R_0 were instantaneous. Defining B as $(At_T + 1) \equiv (8pV)/[3\sqrt{2}(4D/l)]$, $(l/\lambda)^2 C$ as $1/At_D \equiv (l/\lambda)^2\, 4\pi^2\, \sqrt{2}\, (4D/l)/\alpha V$, and $(l/\lambda)^2 E$ as $4\pi^2 K/\lambda^2 = (l/\lambda)^2\, 4\pi^2\, (8p/3\alpha)$, we may write

$$\eta_1 = (l/\lambda)^2 C \frac{B^{1-E(l/\lambda)^2} - 1}{1 - E(l/\lambda)^2} \quad \ldots\ldots(20)$$

This term is the excess contribution to the received signal strength from the part of the trail undergoing transient expansion. We may represent η_0 of (19) similarly as a function of the ratio of mean-free-path to wavelength using (12). Then

$$\eta_0 = e^{-F(l/\lambda)^2} \quad \ldots\ldots(21)$$

where F is defined as $4\pi^2(14)^2 = 7730$.

The constants B, C, and E of (20) are independent of m.f.p. and so of height. Using $p = 5$, $V = 50{,}000$ m/s, $(4D/l) = 1200$ m/s, and $\alpha = 0.4$, we have $B = 393$, $C = 3.35$, and $E = 1317$. Figure 2 is a plot of η_0 and η_1 *vs* (λ/l). It will be seen that the assumption of an instantaneously formed trail radius R_0 yields nearly the correct reflection coefficient as long as η is not less than about 0.01. If the frequency

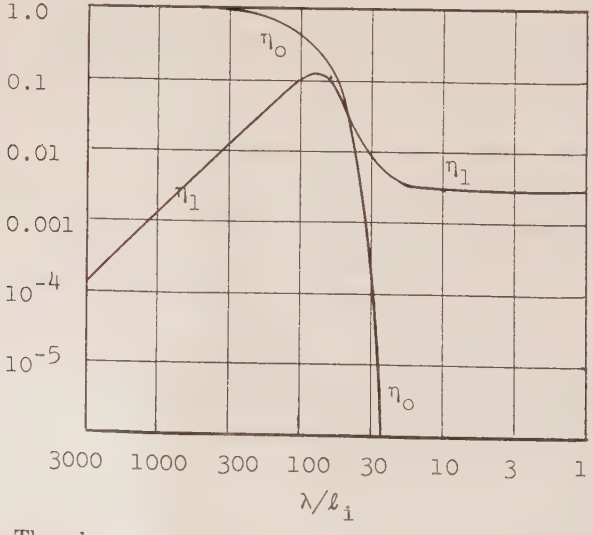

FIG. 2—The echo amplitude-rate reduction factor η for under-dense trails

or height are raised beyond the value where $\eta_0 = 0.01$, the contribution to the received signal from the transient radius becomes dominant and limits the further loss of reflection coefficient. By putting $(\lambda/l) = 0$ in (20), it may be seen that the minimum value of η is $C/E = 3\sqrt{2}\,(4D/l)/8pV$. With the values assumed above, $\eta_{min} = 0.00254$. The corresponding power gain that would be needed to recover this loss is 154,000. Thus, for most purposes, it is legitimate to assume that the radius R_0 is truly an instantaneously formed initial radius of the trail. Eqs. (5) or (21) are then appropriate for use in computing the signal amplitude reduction factor.

In the case of under-dense meteor trails (line density less than 10^{14} electrons per meter), we have seen that Eqs. (5) and (21) give the reduction in signal strength resulting from the finite initial radius of the trail. Provided the total signal strength reduction is not less than η_1, this factor may be multiplied directly into the reflection coefficient deduced at high frequencies for zero initial radius, where the effect of normal diffusion is also important in limiting the effective scattering length of the trail. The loss of reflected energy in decibels due to the initial radius is then $-20 \log_{10} [\exp (-4\pi^2 R_0^2/\lambda^2)]$. Calling this loss Z, and using $R_0 = 14l$ from (6)

$$Z = 68{,}000(l/\lambda)^2 \text{ db} \qquad (22)$$

usable up to $Z = 40$ db. It is immediately apparent that high attenuations may be expected unless the wavelength is very considerably greater than the mean-free-path. In terms of the frequency f, the decibel attenuation is

$$Z = 0.75 l^2 f^2 \qquad (23)$$

where l is in meters, f in megacycles. Since l is determined primarily by the height h, Eq. (23) may be used to find the highest frequency able to return waves from a given height without an energy loss greater than Z decibels. Note that to the extent that the number of echoes received is inversely proportional to the reflected signal strength for under-dense trails, the signal strength reduction factor (5) is also the rate reduction factor. Figure 3 is a plot showing the relation between height and frequency for selected values of this signal strength-rate reduction factor. It will be seen that at any given frequency there is a very sharply defined ceiling on the possible heights of reflection. In Figure 4, the same relation is plotted, using frequency as the parameter. As the frequency is raised, the altitude below which echoes remain detectable drops sharply. For frequencies above a fairly well defined upper limit, nearly the whole meteor altitude range is highly attenuated.

A third useful presentation of the predicted frequency-height-rate relationship is shown in Figure 5. Note that as the frequency is raised, the number of echoes detectable at a given height drops sharply. At the highest frequencies, under-dense trails should not be detected at a high rate except at the lowest altitudes.

In plotting Figures 3 to 5, frequency scales appropriate for the ion-trail were used. If no ions are formed during the initial diffusion, the scale should be correct. However, if ionization is produced during diffusion of the atom-trail by collisions of neutral meteor atoms and air molecules, the resultant ionization distribution will have a larger radius because of the rapid diffusion of meteor atoms before

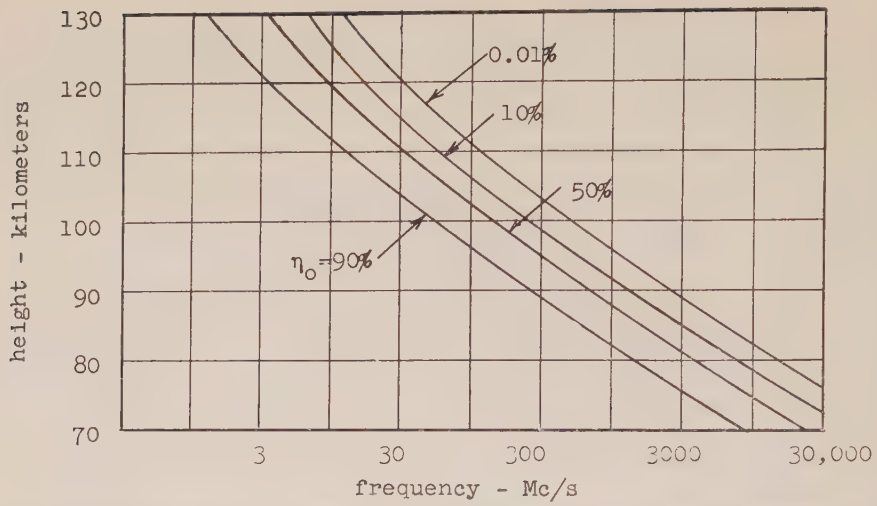

Fig. 3—Under-dense trail echo amplitude-rate reduction factor η_0 *vs* height and frequency, based on the ion-trail radius

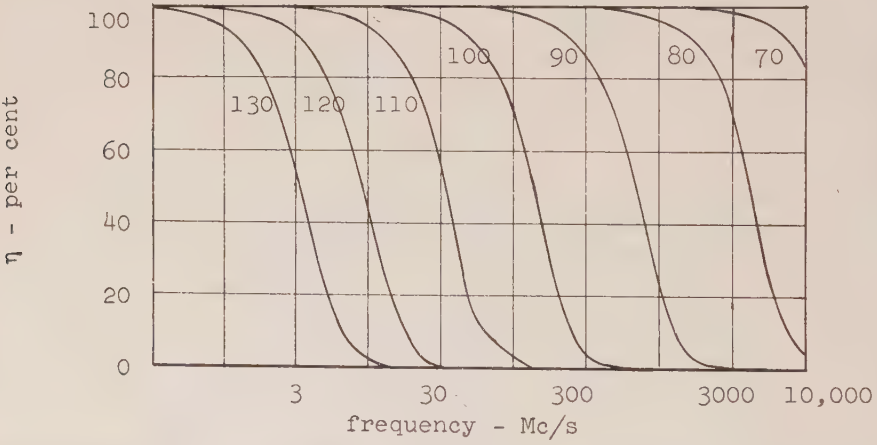

Fig. 4—Under-dense trail echo amplitude-rate reduction factor η *vs* frequency with height as parameter, based on the ion-trail radius

ionization. The atom-trail radius gives an upper limit to the size of the ionization distribution. Actually, the charge distribution is probably little larger than the computed ion-trail, but certainly it cannot exceed the five times larger radius of the atom-trail. In terms of the frequency scales on the Figures, the effect of the production of ionization during diffusion would be the same as lowering the numerical values on the frequency scales by a factor considerably less than five.

Notice also that numerical values of persistence were computed for meteoric and air molecules of the same mass. If the mean mass of the meteoric atoms is taken to be greater than 29, p will be larger, and α will be smaller. Both changes

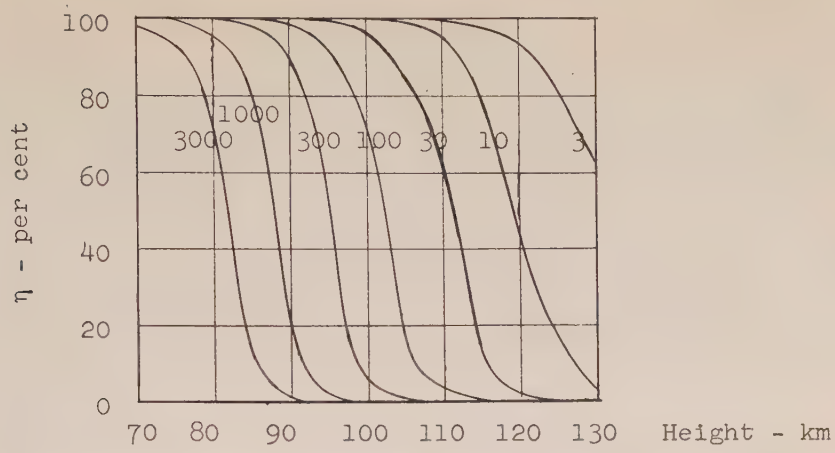

FIG. 5—Under-dense trail echo amplitude-rate reduction factor η *vs* height with frequency as parameter, based on the ion-trail radius

will make R_0 larger, so that the rate reduction will occur at somewhat lower frequencies than plotted.

It is important to emphasize that the equations and curves that have been presented apply to the case of back-scatter. When signals are reflected from under-dense trails at oblique incidence, the effective wavelength is increased by the factor sec ϕ, where ϕ is half the interior forward-scatter angle. Thus, the maximum frequencies usable at oblique incidence with a given attenuation η are sec ϕ times as great as the values given by the curves. For typical paths, sec ϕ may range up to 4 or 5.

IV. THE BEHAVIOR OF OVER-DENSE TRAILS

When a meteoric ionization trail is formed with an electron line density greater than 10^{14} electrons per meter, it is said to be over-dense. Multiple scattering becomes of importance, and the echo strength is most simply analyzed by treating the trail as a reflecting cylinder of radius equal to the zero-refractive-index radius of the cloud. Eq. (4) then gives the echo duration. As a result of the rapid initial expansion of the trail, it reaches the initial radius R_0 in a brief interval t_T given by (10). The trail is then of such size that its age appears to be t_0 as given by (13). If this initial duration t_0 is greater than the echo duration t_H of (4), an echo will not be received from the negative dielectric constant core except during the transient interval t_T .

If an over-dense trail is to produce an echo after the transient interval is over, the necessary condition $t_T < t_H$ becomes

$$R_0^2/4D < \frac{\lambda^2(Q/Q_0)}{4\pi^3 D} \qquad (24)$$

where $Q_0 = 1.13 \times 10^{14}$, roughly the dividing line between under-dense and over-dense trails. Taking $R_0 = 14l$, we find the requirement on Q if the transient expansion is not to dominate the reflection process is

$$\frac{Q}{Q_0} > 6100 \left(\frac{l}{\lambda}\right)^2 \quad \ldots\ldots\ldots\ldots\ldots\ldots\ldots\ldots\ldots\ldots (25)$$

In Figure 6, contours of Q/Q_0 from (25) are plotted *vs* frequency and height. It will be seen that for the higher frequencies and greater heights only ion-trails well above the critical line density Q_0 will produce normal echoes. The remainder will only produce echoes during the transient period t_T . Since the effective length of trail during this period will be considerably less than 15 meters, a relatively small return can be expected when Q is less than the value given by (25). Comparing Figure 6 with Figure 3, it will be seen that the effect of initial radius becomes important at the same heights and frequencies for both under-dense and over-dense trails.

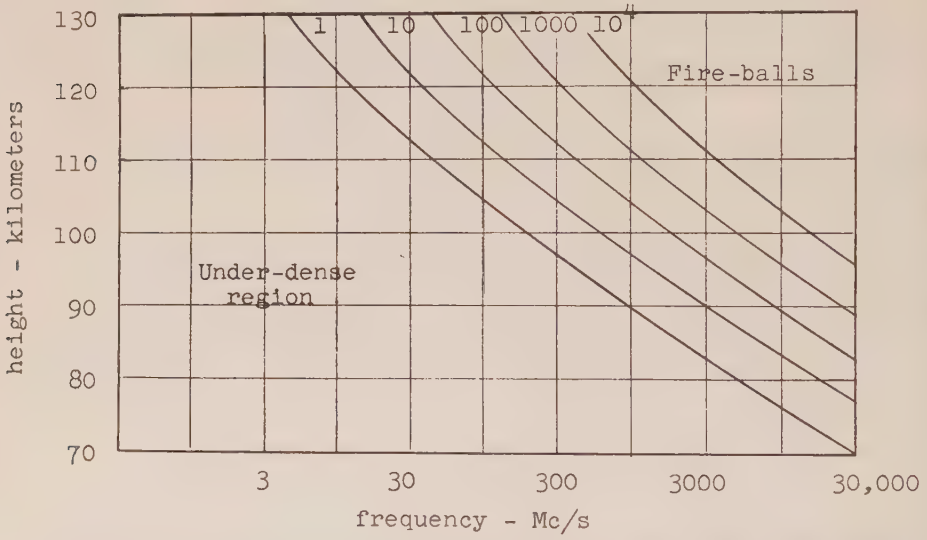

FIG. 6—The relation between height and frequency for over-dense trails plotted *vs* the normalized line density Q/Q_0, if the echo is to endure beyond the period of transient diffusion

Eq. (25) is based on the assumption that heating of the atom-trail does not influence trail expansion. In the next section, it will be shown that heating of over-dense trails cannot always be neglected. Therefore, the rate of expansion may be greater than supposed above.

V. EFFECT OF HEATING ON THE TRAIL

As the high velocity meteoric atoms diffuse into the surrounding air, they supply energy in the form of heat. The exact prediction of the effect of this heating is quite difficult. Here we shall estimate roughly the relative importance of such heating on the trail formation process, in relation to the mass and line density of the meteor.

The kinetic energy of the meteor is $MV^2/2$, with M its mass, V the velocity. The mass M is $n \cdot m/A$, where n is the number of meteoric atoms, m their atomic weight, and A is Avogadro's number. Assuming the number of electrons produced

is related to the number of meteoric atoms by the factor β, the number of meteoric atoms lost from the meteor per unit trail length is $n = Q/\beta$. Thus, $M = Qm/A\beta$. The heat energy H given to the atmosphere is related to the temperature rise by $H = \pi r^2 \rho C T$ if it is assumed that the energy is uniformly distributed in a cylinder of radius r, ρ the air density, and C the specific heat. Equating the kinetic and thermal energies, we get for the temperature rise

$$T = \frac{QV^2m}{2r^2A\beta\rho\pi C} \quad \ldots\ldots\ldots\ldots\ldots\ldots\ldots\ldots\ldots\ldots (26)$$

The value of β and m are rather uncertain, but we shall take $V = 5 \times 10^6$ cm/s, $m = 50$, $A = 6 \times 10^{23}$, $\rho = 5 \times 10^{-9}$, and $C = 2 \times 10^8$ ergs/gm°K. The order of magnitude result for $r = 30$ cm and $Q_0 = 1.13 \times 10^{12}$ electrons/cm is

$$T \cong \frac{1}{\beta}(Q/Q_0)°\mathrm{K} \quad \ldots\ldots\ldots\ldots\ldots\ldots\ldots\ldots\ldots\ldots (27)$$

Assuming $\beta = 0.1$, $T = 10(Q/Q_0)$ [4]. Heating can be expected to play a significant role in determining the rate of diffusion when $Q/Q_0 > 20$ or so. Since the distinction $Q/Q_0 = 1$ corresponds roughly to 5th magnitude meteors (the visual limit), it appears that the diffusion of meteors of magnitude greater than 1 or 2 will not be much influenced by heating. On the other hand, brighter meteors may be appreciably affected.

For over-dense meteors, the effects of temperature can be expected to be twofold. First, because the pressure near the trail will rise with the temperature, a column of the atmosphere near the trail will expand until the pressure is that of the surrounding gas. In the process, the temperature will be reduced, but not to that of the original atmosphere. During the expansion, ionization embedded in the air will be swept outwards, so that the initial radius will be greater than if thermal effects were not present. Because of the higher air temperature, the diffusion of the ionization will be more rapid. As time advances, the high temperature about the trail will be reduced to the ambient by diffusion. The net effect will be to accelerate the expansion of the ionized trail, the more so the larger the meteor.

VI. CONCLUSION

When a meteor is consumed in the atmosphere, two types of trail may be distinguished. The first, the "atom-trail," results from the diffusion from the meteoric path of neutral meteoric particles. The second, the "ion-trail," results from the diffusion of ionized meteor atoms and the corresponding electrons. It is the ionization trail that is effective in reflecting radio signals. Because ions have a smaller mean-free-path than do neutral molecules, the ion-trail will expand only one-fifth as fast as will the atom-trail, provided that ionization does not take place during diffusion of the atom-trail.

The atom-trail is of importance even though it does not contain free electrons, since it describes the distribution of the kinetic energy that the meteor gives to the atmosphere as heat. For meteors larger than perhaps first magnitude, the fact that the ion-trail is imbedded in a large and hot atom-trail is of importance. For

smaller "radar" meteors, heating is probably unimportant, and the atom-trail is of less interest.

Both the ion- and atom-trails diffuse initially at very rapid rates, since the diffusing particles start with meteoric velocity. Approximate analysis indicates that at typical heights the rapid transient diffusion for the ion-trail lasts for about a third of a millisecond. Diffusion then settles down to a slower rate fixed by the air temperature. The trail may be considered to have an initial radius of the value achieved during the rapid transient expansion. For the ion-trail, this mean radius of perhaps 14 cm would have been reached only after about one and a half milliseconds of diffusion at the steady-state rate.

Since at the highest frequencies the received signals from trails larger than the "initial radius" are highly attenuated, the very short transient period during which a smaller column exists highly limits the length of trail contributing echoes of appreciable strength. At somewhat lower frequencies, the radius to which the transient expansion brings the trail may be treated as a true initial radius in computing received signal strengths.

The effect of the initial radius of trail formation on radio echoes is to greatly reduce the reflected signal strength and so rate of detection at frequencies of a few hundred megacycles or higher. Since the mean-free-path is an exponential function of height, near the upper frequency limit of detection low altitude meteors are much preferred to those at higher altitudes. The effect is present for both underdense and over-dense trails.

APPENDIX: CALCULATION OF THE PERSISTENCE OF VELOCITY

When an atom or ion of meteoric material collides with an air molecule, the most probable direction of rebound is its original direction of motion. We shall compare the mean distance traveled by a meteoric atom after n free-paths of unit length with the mean distance $\sqrt{n}$ it would have traveled if the direction of rebound were random. The resultant ratio will be called p.

Assume that the velocity of the meteoric atom is much greater than the thermal velocities of the air molecules. Then the velocity of rebound of the meteoric atom does not influence the succeeding mean-free-path; only the direction of rebound need concern us. If $\cos \alpha_k$, $\cos \beta_k$, and $\cos \gamma_k$ are the direction cosines of the k^{th} mean-free-path, the total distance z traveled in n collisions is given by

$$z^2 = \left(\sum_1^n \cos \alpha_k\right)^2 + \left(\sum_1^n \cos \beta_k\right)^2 + \left(\sum_1^n \cos \gamma_k\right)^2$$

Squaring and expanding,

$$\begin{aligned} z^2 = \sum_1^n (\cos^2 \alpha_k + \cos^2 \beta_k + \cos^2 \gamma_k) \\ + 2 \sum_1^{n-1} (\cos \alpha_k \cos \alpha_{k+1} + \cos \beta_k \cos \beta_{k+1} + \cos \gamma_k \cos \gamma_{k+1}) \\ + 2 \sum_1^{n-2} (\cos \alpha_k \cos \alpha_{k+2} + \cos \beta_k \cos \beta_{k+2} + \cos \beta_k \cos \gamma_{k+2}) \\ + 2 \sum_1^{n-3} (\cos \alpha_k \cos \alpha_{k+3} + \cos \beta_k \cos \beta_{k+3} + \cos \gamma_k \cos \gamma_{k+3}) \\ + \cdots \end{aligned}$$

But

$$(\cos \alpha_k \cos \alpha_{k+j} + \cos \beta_k \cos \beta_{k+j} + \cos \gamma_k \cos \gamma_{k+j})$$

is $\cos \theta_{kj}$, where θ_{kj} is the angle between the k^{th} and the $(k + j)^{\text{th}}$ mean-free-path. Thus,

$$z^2 = n + 2 \sum_{j=1}^{n} \sum_{k=1}^{n-j} \cos \theta_{kj}$$

The mean-square walk is

$$\overline{z^2} = n + 2 \sum_{j=1}^{n} (n - j) \overline{\cos \theta_j}$$

where $\overline{\cos \theta_j}$ is $\cos \theta_{kj}$ averaged over all paths k. In the case of a random walk without persistence, $\overline{\cos \theta_j} = 0$, and $\overline{z^2} = n$. To find $\overline{z^2}$ with persistence, we must find the probability of collision through an angle θ. We shall assume collision between elastic spheres of equal mass. The air molecules are assumed stationary. Then the angular deviation θ of the incident sphere on collision is given by $\cos \theta = u$, where u is the distance of the original path of the incident body from the center of the stationary body, normalized by the mean diameter of the bodies. The average value of $\cos \theta$, taking into account the greater probability of collision with u near one, is $\overline{\cos \theta} = 2/3$. Thus, $\overline{\cos \theta_1} = 2/3$.

To find $\cos \theta_2$, we note that from the law of cosines of spherical trigonometry

$$\cos \theta_{k2} = \cos \theta_{k1} \cos \theta_{(k+1)1} + \sin \theta_{k1} \sin \theta_{(k+1)1} \cos \phi_k$$

where ϕ_k is random and $\overline{\cos \phi} = 0$. Averaging over k,

$$\overline{\cos \theta_2} = \overline{\cos \theta_1}^2$$

It may be shown by replacing $\cos \theta_{k1}$ above by $\cos \theta_{k2}$ that $\overline{\cos \theta_3} = \overline{\cos \theta_1}^3$. The general result is

$$\overline{\cos \theta_j} = \overline{\cos \theta_1}^j = (2/3)^j$$

Hence

$$\overline{z^2} = n + 2 \sum_{j=1}^{n} (n - j)(2/3)^j$$

and as n becomes large, $(n - j)$ may be replaced by n. Then $\overline{z^2}$ approaches

$$z^2 = n + 2n \sum_{j=1}^{n} (2/3)^j$$

$$= n - 2n + 2n \sum_{j=0}^{n} (2/3)^j$$

and finally

$$\overline{z^2} = -n + \frac{2n}{1 - 2/3} = 5n$$

The result we seek is then $p = 5$; because of persistence, the length of the mean-square walk is increased fivefold.

References

[1] P. M. Millman, Meteoric ionization, J. R. Astr. Soc. Can., **44**, 209-220 (1950).
[2] L. B. Loeb, Kinetic Theory of Gases, McGraw-Hill Book Co., New York and London (1934).
[3] R. J. Havens, R. T. Koll, and H. E. LaGow, The pressure, density, and temperature of the earth's atmosphere to 160 kilometers, J. Geophys. Res., **57**, 59-72 (1952).
[4] S. Evans and J. E. Hall, Meteor ionizing and luminous efficiencies, Special supplement (Vol. 2) to the J. Atmos. Terr. Phys., "Meteors" (edited by T. R. Kaiser), pp. 18-22, Pergamon Press, Ltd., London and New York (1955).

IONOSPHERE ELECTRON-DENSITY MEASUREMENTS WITH THE NAVY AEROBEE-HI ROCKET

By John E. Jackson and J. Carl Seddon

U. S. Naval Research Laboratory, Washington 25, D. C.

(Received October 12, 1957)

ABSTRACT

Electron densities in the ionosphere above White Sands, New Mexico, were measured continuously from the E region up to the lower $F2$ region with Aerobee-Hi NRL-50, a rocket instrumented by the U. S. Naval Research Laboratory. The results confirm the general structure of the daytime ionosphere above White Sands as deduced from previous NRL flights, namely, that the ionosphere remains dense between the E and $F2$ regions, with only minor valleys in the electron-density profiles. The electron-density distribution is shown to be consistent with the P'-f records obtained during the rocket flight. The sporadic-E condition, seen on these ionograms, was found to be associated with a sharp spike in the electron-density profile at an altitude of 101 km and approximately 1 km thick. This sporadic condition extended over a horizontal distance of at least 80 km.

INTRODUCTION

At 1209 hours MST, on June 29, 1956, the first successful Aerobee-Hi rocket was fired at White Sands, New Mexico (32.5° north, 106.5° west). This rocket, which reached an altitude of 263.7 km, was instrumented by the U. S. Naval Research Laboratory to measure ionospheric electron densities as a function of altitude. The experiment was a continuation of the ionosphere studies which have been conducted by NRL at White Sands since 1946. A total of 15 rockets (V-2's, Vikings, and Aerobees) have been fired to date in connection with this program [see 1 through 7 of "References" at end of paper]. This work has led to revisions in the earlier theories regarding the structure of the ionosphere. NRL rocket results indicate that the daytime ionosphere is not composed of distinct and well-separated E, $F1$, and $F2$ layers, but rather is much more uniform and regular than was previously believed to be the case. Correlations between the electron density measured directly as a function of altitude and the virtual-height (P'-f) soundings made from the ground have resolved the ambiguities present in the P'-f profiles and thus clarified the interpretation of the ground observations [8].

EXPERIMENTAL METHOD

The method used consists of refractive-index measurements based upon propagation phenomena. Two harmonically related c-w signals, at 7.75 Mc and 46.5

Mc, respectively, are transmitted from the moving rocket to receiving stations on the ground. The rocket motion causes each signal to experience a Doppler shift which is related to the refractive index of the medium immediately around the rocket. The high frequency is used as a reference, since its index is essentially unity. Comparison techniques used on the ground plus a knowledge of the rocket trajectory yield, as a function of altitude, the 7.75-Mc refractive index in the region around the rocket. The method is illustrated in Figure 1.

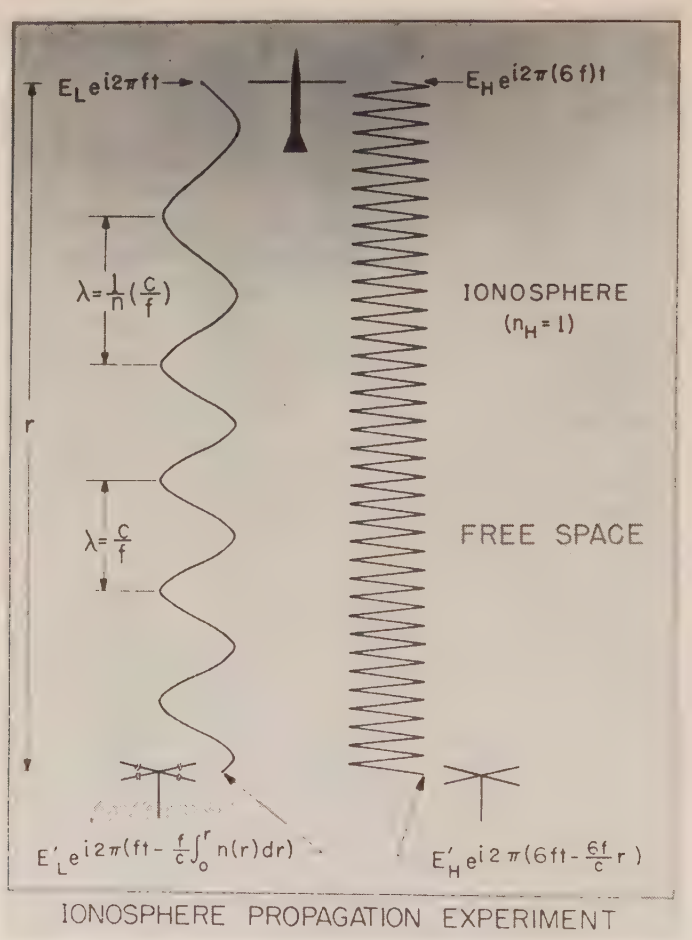

FIG. 1—An illustration of the c-w radio propagation method used by NRL for rocket studies of the ionosphere

At a given instant of time, the rocket is at a position r, transmitting to a ground receiving-station two c-w signals of frequency f and $6f$. The shaded portion represents an electron density gradually increasing with altitude. The high-frequency signal propagates to the ground essentially unaffected by the presence of ionospheric electrons, that is, n_h , the high-frequency refractive index is unity. The effect of the ionospheric electrons on the low frequency, however, is to stretch

the free-space wavelength by a factor $1/n$, where n is the low-frequency refractive index, which is a function of r. Since the rocket velocity is slow compared to propagation velocities, the wave train is essentially under steady-state conditions, and the phase of the signal received on the ground at a given instant is determined by the total electrical path length $\int_0^r n(r)\mathrm{d}r$. The expressions for the phases received at the ground-station antennas are

$$2\pi(6f)\left[t - 1/c \int_0^r n_h(r')\,\mathrm{d}r'\right]$$

for the high-frequency signal, and

$$2\pi f\left[t - 1/c \int_0^r n(r)\,\mathrm{d}r\right]$$

for the low-frequency signal. The distinction between r and r' allows for a possible difference between low- and high-frequency propagation paths. The time derivatives of these phases constitute the received high and low angular frequencies. After frequency multiplication by a factor of 6, the received low-frequency signal is compared with the received high-frequency reference to give a beat note with a frequency

$$\text{F.B.} = (6f/c)\, d/\mathrm{d}t\left[\int_0^r n_h(r')\,\mathrm{d}r' - \int_0^r n(r)\,\mathrm{d}r\right] \quad \ldots\ldots\ldots\ldots (1)$$

The ground-station instrumentation provides a continuous recording of this beat-note signal.

By firing the rockets almost vertically, and by optimizing the locations of the two ground-stations used, a condition of nearly vertical propagation can, in general, be approximated, at one station or the other. These requirements have been fairly well met in the experiments conducted at White Sands, New Mexico, during the period from 1946 to 1954. For this special case of vertical propagation, formula (1) reduces to

$$\text{F.B.} = \frac{6f}{c}(1 - n)\dot{r} \quad \ldots\ldots\ldots\ldots\ldots\ldots\ldots\ldots (2)$$

where it is assumed that $n_h = 1$, and that time variation of the vertical electron-density distribution can be ignored. Thus, the beat-note measurement gives the low-frequency refractive index, $\dot{r}$ the rocket velocity having been determined from a knowledge of the trajectory.

To avoid excessive crowding of Figure 1, only one mode of propagation was shown for the low-frequency signal. The experimental technique used yields separate data for the ordinary and for the extraordinary low-frequency signals. The two modes of propagation are separated on the ground by means of suitable antennas and they are individually compared with the high-frequency reference. Two sets of beat notes, therefore, are obtained, from which both ordinary and extraordinary indices can be computed. The electron densities are independently obtained from these two indices with the aid of the Appleton-Hartree formula. This provides a check of the internal consistency of the measurements.

OBLIQUITY EFFECTS

In the case of Aerobee-Hi NRL-50, the departure from vertical conditions was too large to be ignored. Figure 2 shows the trajectory of this rocket flight

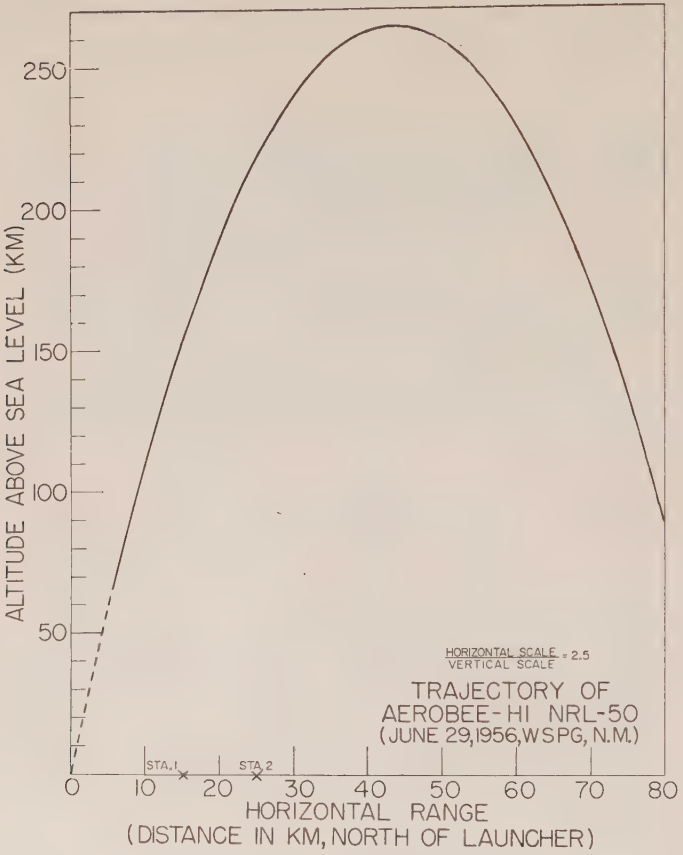

FIG. 2—Geometry of the propagation experiment conducted with Aerobee-Hi NRL-50

with respect to the location of the ground receiving-station 1 and the second receiving-station located 10 km farther up range. It can be seen that during descent the propagation path from rocket to ground station is considerably oblique. Two of the effects of obliquity are illustrated by Figure 3, in which straight-line propagation is assumed.

In Figure 3, the rocket moves in a time Δt along the trajectory P_2P_1 . The resultant change in the geometrical path length is P_2M. Since, however, the electron density is a function of vertical height, it is seen that the electrical length of the path OM is different from the electrical path OP_1 . This effect gives the first correction term to the apparent index of refraction as obtained from the simplified beat-note frequency formula (Eq. 2). A second correction term arises from the fact that the angle with respect to the earth's magnetic-field direction is different for the two propagation paths OP_2 and OP_1 . For the Aerobee-Hi

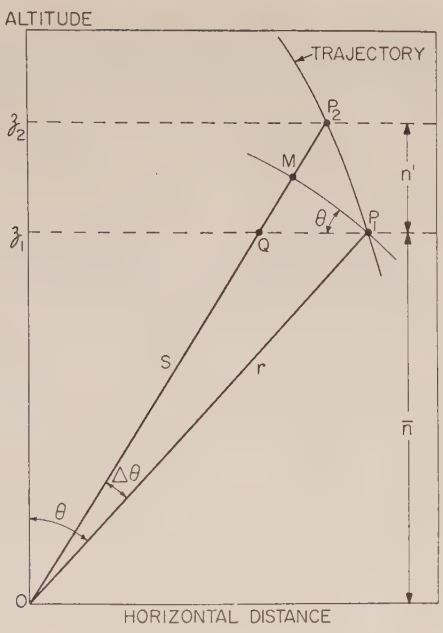

FIG. 3—Oblique-ray paths, assuming straight-line propagation

NRL-50 flight, the first effect introduced a maximum correction of 30 per cent in the computed electron densities at low altitudes during the descent of the rocket. The second correction was of importance only at the higher altitudes, with a maximum value of about 10 per cent during descent at the highest altitude at which data were reduced, that is, three kilometers below peak. Also considered was the effect of ray bending, but this was found to introduce a negligible error of less than one per cent in the computed electron densities. A complete discussion of the effects of obliquity upon the propagation experiment is given in reference [9]. The obliquity analysis consists essentially in the evaluation of Eq. (1), taking into account the geometry of the propagation paths.

DISCUSSION OF THE AEROBEE-HI NRL-50 EXPERIMENT

Experimental conditions

The rocket was fired during a period of moderate ionospheric disturbances, with sporadic-*E* up to 8 Mc, and complete absorption below 3.5 Mc. The zenith-angle of the sun was 9.2° and the sunspot number was 135. The rocket-borne transmitting antennas [7] consisted of two 15-foot whips. These were retracted along the rocket skin during the powered flight and deployed at an altitude of 55 km. The transmission itself was initiated at 58 km. Ionosphere data were continuously received and recorded at the ionosphere ground-stations until 500 seconds after take-off, at which time the rocket whip-antennas were probably torn off due to re-entry into the lower atmosphere.

In view of the excellent radar tracking data obtained for this flight, the rocket trajectory (Fig. 2) was obtained to an accuracy of approximately ± 100 meters,

the peak time was known to an accuracy of about ±0.1 second, and the radial velocities were computed to an accuracy of better than one per cent.

During ascent, and for altitudes less than 245 km, the straight-line paths between the rocket and the ground stations remained within 4° of the vertical. During descent, due to the 90-km horizontal range of the rocket, the propagation was quite oblique, with an inclination reaching 36° in the *E* region. Obliquity corrections were, therefore, included in the reduction of the experimental data. However, during ascent for altitudes below 245 km, these corrections modified the computed electron densities by less than 5 per cent.

Electron-density results

The analysis of the Aerobee-Hi NRL-50 flight indicated that the c-w propagation experiment has provided reliable electron-density measurements up to 260 km.

The measured electron densities are shown in Figure 4. During most of the flight, the frequency of the recorded beat notes changed very slowly as a function

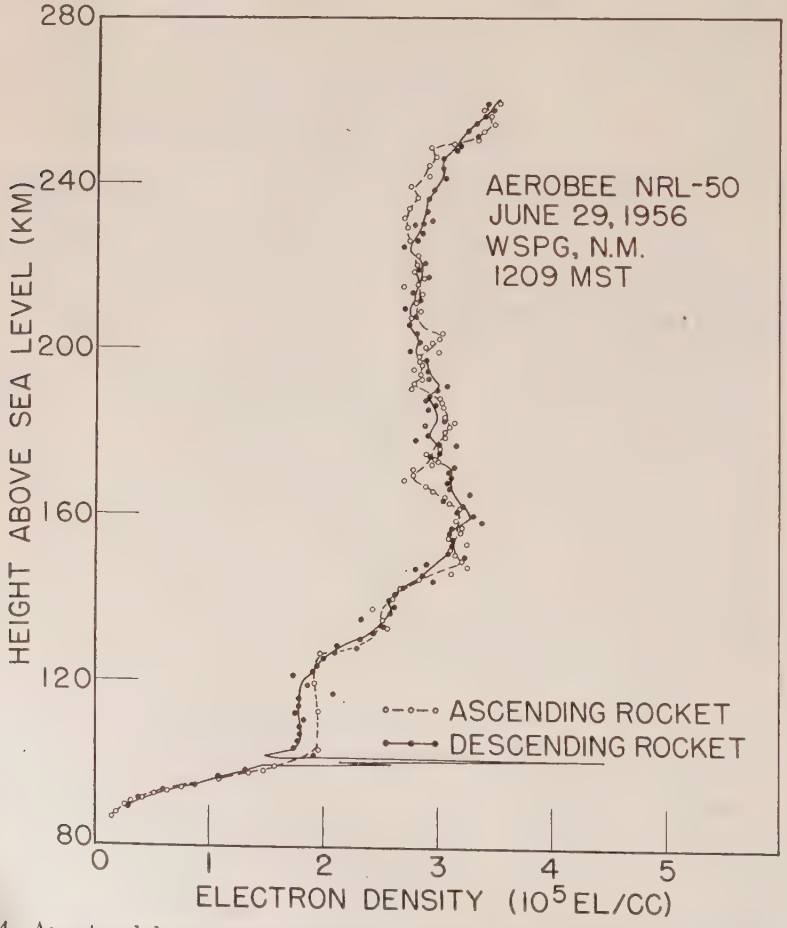

FIG. 4—Ascent and descent measurements of electron densities with Aerobee-Hi NRL-50

of altitude. Consequently, experimental points indicated on the curves correspond to mean values over altitude intervals of approximately one kilometer. Each point represents the average of four separate measurements, since two receiving stations and two polarization modes were used in the density determination. The accuracy of the experimental points shown is estimated to be ±5 per cent, as indicated by a statistical study of the consistency between the four independent measurements.

The ascent and descent are in good agreement in spite of the horizontal separation introduced by the trajectory. The only apparent discrepancy is the absence of the sharp sporadic spike on the ascent data. The rocket data show this sporadic region at the same altitude during ascent. The ascent data, however, could not be read accurately over small height intervals in the corresponding region due to the presence of additional signal components previously reported [2]. These additional signals always appear abruptly during ascent near the maximum of the *E* region. This effect, severe at first, decreases rapidly in magnitude to a point where no serious difficulty occurs in the data analysis. The sporadic condition is discussed later in the text.

Virtual-height recordings were obtained continuously at 30-second intervals during the rocket flight by the White Sands Ionosphere Sounding Station. This station is located approximately 15 km west of the rocket launching tower; the rocket trajectory was due north. Shown in Figure 5 and in Figure 6 are the *P'-f* records taken at 1158, 1203, and 1216 MST, respectively (rocket firing time was 1209 MST). Since the frequency markers did not record properly on the ionograms, the frequency scale had to be reconstructed from the known calibration of the *P'-f* recorder. Due to heavy absorption, the flight ionogram provided insufficient data for a detailed correlation with the rocket measurement. However, a partial check was possible using the *P'-f* record taken at 1203 MST. The superimposed height-marker grid on this record is 7 km too low, as determined by scaling the first and second echoes of the sporadic-*E* reflections. All virtual heights

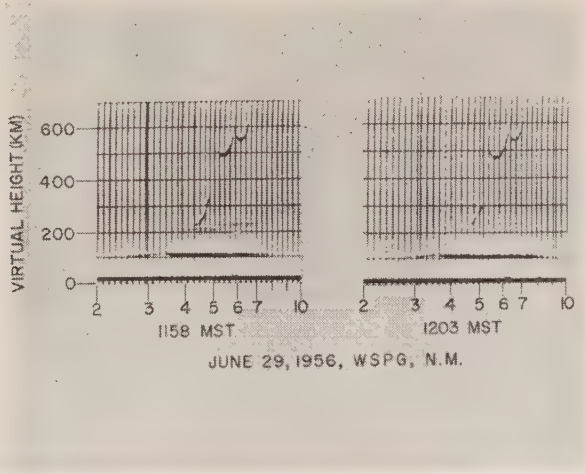

FIG. 5—*P'-f* records taken 11 minutes and 6 minutes prior to the flight of Aerobee-Hi NRL-50

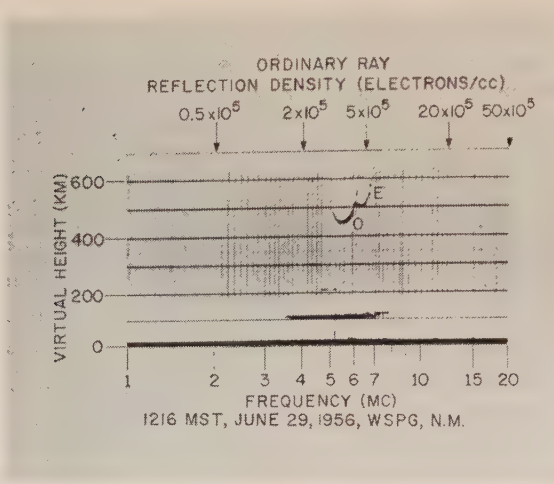

FIG. 6—*P'-f* record taken near the peak time of the Aerobee-Hi NRL-50 flight

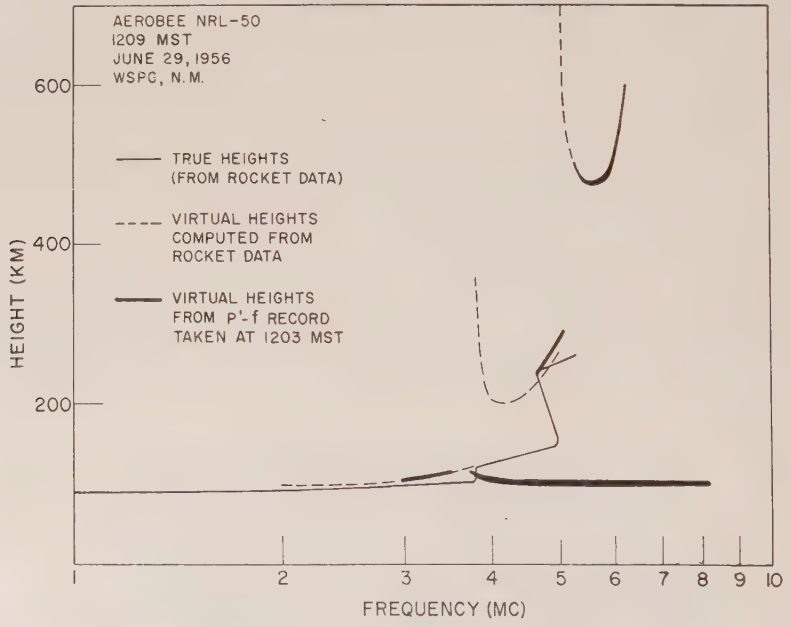

FIG. 7—Correlation between the *P'-f* record and the results of the Aerobee-Hi NRL-50 flight

were corrected accordingly. The results of this comparison, as shown in Figure 7, indicate good agreement at the frequencies where *P'-f* echoes were present. The virtual heights were computed according to previously described techniques [8]. Extrapolation of the rocket data with the aid of the *P'-f* records shows the maximum of the *F*2 region to be in the neighborhood of 300 km.

Discussion of sporadic-E

The 100- to 102-km descent region was the only one where a detailed analysis

was performed, in view of a rapid variation in the beat-note frequency, indicating the presence of a very dense sporadic ionization. The sporadic cloud is shown in more detail by Figure 8, in which the experimental points represent averages over

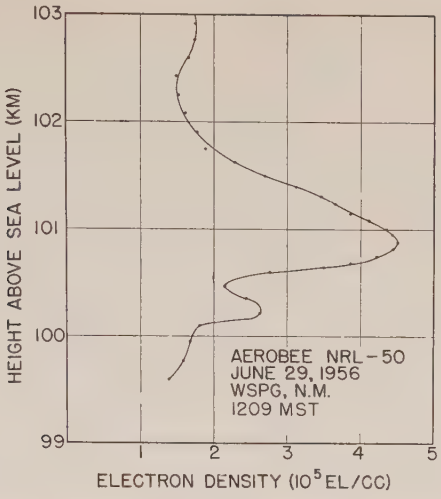

FIG. 8—Vertical cross-section of sporadic ionization detected during the descent flight of Aerobee-Hi NRL-50

height increments of about 100 meters. The results obtained in the 100- to 102-km region provide a good illustration of the resolution possible with rockets exhibiting a minimum of pitch and yaw. This intense, highly-stratified ionization can be seen from an inspection of the raw data shown in Figure 9. For the time interval shown, the rocket velocity can be considered as being essentially constant and the electron density is approximately proportional to frequency. The frequencies of the two beat notes are seen to increase by a factor of two in the neighborhood of $X + 460$ seconds. To provide a somewhat clearer trace, under conditions of poor signal-to-noise ratio, the beat notes are also recorded after going through a low-pass filter with a cut-off at 80 cycles. Thus, the reduced amplitude on the filtered beat notes is another indication of the frequency (and electron density) increase near $X + 460$ seconds. As soon as the rocket is below 100 km, partial reflections occurring from the sporadic region cause the fast interference pattern seen on the AVC trace. This pattern is due to the fact that the reflected rays and the direct rays have Doppler shifts with opposite signs. The reflected-ray amplitude is about 10 per cent of the direct-ray amplitude. The reflected ray remains present on the subsequent descent data. From the geometry of the reflected path, one can assign a horizontal length of 20 km to the locus of the reflection point. This provides a direct indication of the absolute minimum horizontal size of the sporadic region. The reflected ray varies in amplitude, indicating either a horizontal variation in the density of the sporadic region or a variable gradient (ripples in the lower surface of the sporadic cloud). The sporadic condition also existed at the same altitude over the ionosphere recording station, 80 km horizontal distance away. The P'-f records show the continuous presence of this sporadic condition prior to,

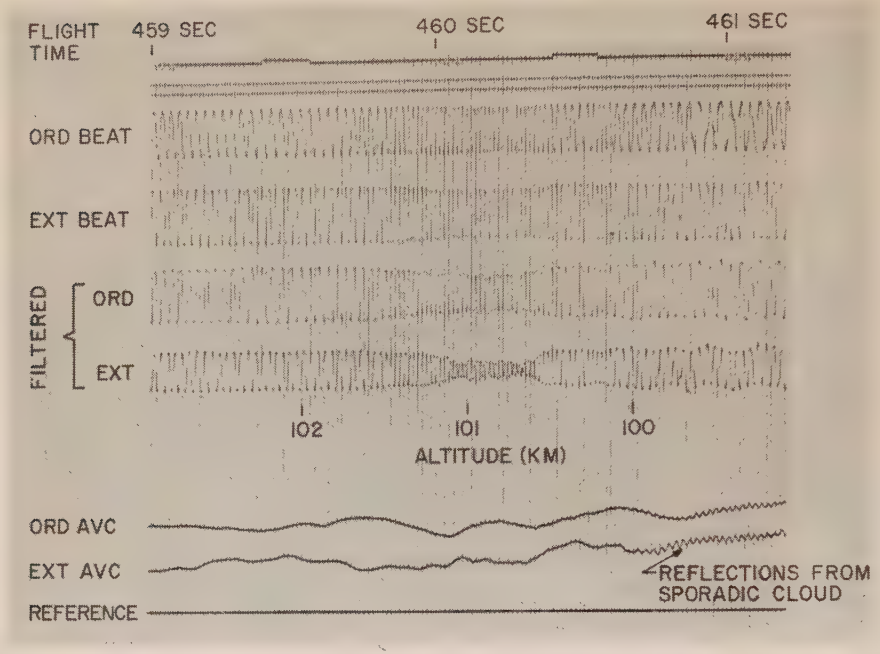

FIG. 9—Section of the Aerobee-Hi NRL-50 flight record (Station 2), showing the sporadic cloud data

during, and after the rocket flight. On the P'-f record for 1216 MST, the penetration frequency was 5 Mc, so that the maximum density would, therefore, be 17 to 30 per cent less than the density at the rocket, if it is assumed that the sporadic region is not composed of many individual clouds, with spacings through which the 5-Mc signal could propagate. The 17 per cent value would apply if the penetrating ray were the Z mode, the 30 per cent value if it were the ordinary ray. Therefore, considering the continuous presence of the sporadic-E on the P'-f records, the rocket measurement of the sporadic density during descent, and the persistence of the subsequent reflected rays, one is led to conclude that the sporadic condition must have extended over a horizontal distance of at least 80 km. Past rocket flights have always shown a high gradient region at the altitudes where the ionosphere virtual-height station indicated sporadic reflections. The horizontal distances from the P'-f station to the rocket have varied from 22 to 80 km, but previous to this flight the increase in density was only about 10 per cent above the smooth profile.

The data above this region were examined for possible evidence of coarse "patchiness" in the sporadic region. During descent, due to differential refraction, the ordinary and extraordinary rays had a horizontal space separation at the bottom of the E region. This spatial difference, which at times exceeded one kilometer, would have caused a substantial difference in the computed electron density around the rocket if this sporadic-E region had consisted of isolated clouds, one km thick, so that at times one ray would penetrate a cloud but the other would not. This is due to the change in the electrical path length $\int n dh$ which would

be introduced by the cloud. There seems to be no definite evidence that this was happening. There could be, however, numerous small clouds close together which would tend to average out the above effects, and thus maintain the agreement between the two density results.

CONCLUDING REMARKS

The gross structure of the ionosphere as revealed by the Aerobee-Hi NRL-50 measurements is in agreement with the results of previous NRL flights. The conclusion regarding the 5 per cent accuracy of the experimental results of the latest flight can also be considered to apply to the three other NRL flights which provided data above the E region. Obliquity corrections were omitted in the analysis of previous NRL ionosphere experiments, since these were conducted under conditions much closer to vertical propagation. The obliquity is indicated in Table 1, in terms of the angle θ, defined as the angle between the vertical and a straight line drawn from a receiving station to the rocket while in the ionosphere.

TABLE 1—*Maximum obliquity for ionosphere experiments conducted at White Sands Proving Ground, New Mexico*

Rocket flight	θ Maximum (degrees)	
	Station 1	Station 2
V-2 No. 49 (Sept. 29, 1949)	2.5	7.5
Viking No. 5 (Nov. 21, 1950)	8.0	14.0
Viking No. 10 (May 7, 1954)	4.5	10.0
Aerobee-Hi NRL-50 (June 29, 1956)	36.0	31.0

The recent investigation of obliquity effects [9] shows that the electron-density data published for the previous experiments do not contain any serious error due to the fact that obliquity corrections were not included in past analyses. The correction formulas now available provide, when necessary, an accurate measure of the effects of obliquity. However, the accuracy and consistency of former measurements could be judged from the agreement in the data provided by the two stations in spite of differences in their respective obliquities. Results could also be checked from comparisons between ascent and descent data. Excellent correlations with P'-f records [8] yielded further verification of these past experimental measurements. These criteria were used in the past to justify the fact that obliquity effects could be ignored in previous experiments.

Since the results thus far have been obtained from daytime measurements at White Sands only, it would be premature to draw general conclusions regarding the

ionosphere at all latitudes. It is likely that the White Sands results can provide a model for the earth's temperate zones. This model, being based on very consistent *in situ* measurements, is the best available at the present time. The investigations which have already started at Fort Churchill, in the auroral zone and, if possible, future studies in the tropics, should eventually reveal the extent to which the present picture can be generalized.

ACKNOWLEDGMENTS

As is the case in most rocket experiments, the results obtained represent the combined efforts of a vast research team. Since a complete list of the supporting personnel would be too extensive, the authors would like to single out a few scientists who should receive special recognition. Mr. G. H. Spaid, of NRL, contributed substantially to the development of the experimental equipment. Mr. A. D. Pickar, formerly of NRL, designed the rocket-borne instrumentation. Dr. J. A. Kane, of NRL, was closely associated with the reduction of the experimental data. The ground stations were set up and operated by Messrs. J. E. Masterson, W. L. Joosten, and E. D. Lee from the New Mexico College of Agriculture and Mechanic Arts.

References

[1] J. E. Jackson, Washington, D. C., Naval Research Laboratory, Rep. No. 3909 (1952).
[2] J. C. Seddon, J. Geophys. Res., **58**, 323 (1953).
[3] J. E. Jackson, J. Geophys. Res., **59**, 377 (1954).
[4] J. C. Seddon, J. Geophys. Res., **59**, 463 (1954).
[5] J. C. Seddon, A. D. Pickar, and J. E. Jackson, J. Geophys. Res., **59**, 513 (1954).
[6] J. C. Seddon, Washington, D. C., Naval Research Laboratory, Rep. No. 4304 (1954).
[7] J. E. Jackson and A. D. Pickar, Washington, D. C., Naval Research Laboratory, Rep. No. 4940 (1957).
[8] J. E. Jackson, J. Geophys. Res., **61**, 107 (1956).
[9] J. E. Jackson, Washington, D. C., Naval Research Laboratory, Rep. No. 4960 (1957).

DIFFERENTIAL ABSORPTION IN THE *D* AND LOWER-*E* REGIONS

BY J. CARL SEDDON

U. S. Naval Research Laboratory, Washington 25, D. C.

(Received October 12, 1957)

ABSTRACT

A method of measuring electron densities in the *D* region making use of the Faraday effect is given. At noon on a day of high absorption, 2,000 el/cc were measured at White Sands Proving Ground, New Mexico, at an altitude of 76 km. The technique also makes possible the determination of the differential absorption, by measuring simultaneously the sum and difference of the amplitudes of the two magneto-ionic components at 7.754 Mc as the rocket rolls. None was found over the range 60 to 88 km. A slow increase then occurred up to 94 km, whereupon it increased very rapidly to a value of 1/2 per km at 96 km. Experimental difficulties prevented higher altitude measurements.

INTRODUCTION

The measurement of the absorption of radio waves in the ionosphere with the aid of rockets has proven to be surprisingly difficult, due to antenna detuning by the thin atmosphere. A method of determining simultaneously the ordinary and extraordinary signal strengths has been evolved which permits the computation of the differential absorption. At the same time, it is possible to compute electron densities down to 1,000 electrons per cc using a frequency of 7-3/4 Mc by making use of the Faraday effect. This work was done by means of a modification of the usual Naval Research Laboratory method of measuring electron densities. One additional high-frequency dipole was required, and a timing circuit with coaxial relays. The procedure used was to modify one of the two ground-stations so that the low electron density and differential absorption measurements could be made, and, then, at a time when the rocket was probably in or through the *E* region, a switch was thrown which placed the station back in normal operation.

The first attempt was made on June 22, 1956, but the rocket motor failed to ignite, and the experiment was a failure. This was very unfortunate, as the frequency used was 4.3 Mc, only about half of the usual operating frequency. This was due to the fact that the predicted maximum altitude was barely through the *E* region. An interim Aerobee-Hi was fired one week later, at 12:09 MST, June 29, 1956. Due to the high predicted altitude, 7.75 Mc was selected for this experiment. This rocket reached an altitude of 263 km, and all equipment worked well. A change in roll rate of the rocket for some unexplained reason caused a loss of data in part of the lower altitude regions. In order to reduce this difficulty should it recur again in the future, two crossed high-frequency dipoles will be used instead of the single dipole. This will greatly improve the ability to determine the rocket's behavior.

THEORY

It has been found on all successful rocket flights, using the NRL continuous-wave method [see 1 of "References" at end of paper] of measuring electron densities, that the ordinary and extraordinary signal strengths could not be used to determine the attenuation of either component. Even though the r-f voltage on the rocket transmitting antennas is only about 250 volts at 7.753 Mc, it is always found that the radiated power is greatly reduced over an appreciable altitude range. This is probably due to an absorption of energy by the low-pressure air about the antenna. It is not known whether the air becomes ionized, or merely excited. It has been suggested [2] that ionization is possible due to some electrons bouncing off molecules at the time of field reversal, so that the energy can be built up in a sort of cyclotron effect. Figure 1 shows an unpublished [3] graph of the r-f voltage on the antenna during flight. A temporary telemetering failure prevented data being obtained between 50 and 80 km during ascent, but descent data were obtained down to about 30 km. The free-space computed value was about 250 volts. It can be seen that over the range from 60 to 110 km, the radiated power must be quite low. The received signals around 90 km are usually very weak, and would probably be unusable were it not for the fact that the receiving system has only 1/2-kc bandwidth with a shape factor of 5. If ionization does actually occur near the antennas, it does not have any observable effect on the measurement of the ambient electron density. Rays leaving the rocket upward, and then reflecting back down from a higher level in the ionosphere, give the same results as those that go straight down through the rocket wake.

Differential absorption is easier to measure. This merely requires that the ratio of the two magneto-ionic components be measured. This is accomplished in this experiment by using two crossed identical dipoles on the low frequency and one dipole on the high frequency which is parallel to one of the low-frequency dipoles. As the Aerobee rocket invariably has shown a history in past flights of appreciable roll, the signals on the antennas should show a variation in amplitude, with one dipole maximizing at the time that the other minimizes. The maximum signal is the sum of the individual ordinary and extraordinary components, and the minimum signal is their difference. Thus, two simultaneous values can be obtained, from which the value of each of the components can be calculated. It might seem that the same result could be obtained by merely measuring the amplitude of each component directly from the record as obtained in the usual NRL method of measuring electron densities. This can be done if there is a large difference between the amplitude of the two components, but usually the difference between the two is small below the E region, so that method of measuring the difference of the two greatly improves the accuracy.

If E denotes the signal amplitude, then the signal amplitudes at an altitude of h_2 can be written in terms of the signal amplitudes at h_1 :

$$E_x^{h_2} = E_x^{h_1} \exp\left\{-\int_{h_1}^{h_2} \tau_x \, dh\right\} \quad (1)$$

$$E_o^{h_2} = E_o^{h_1} \exp\left\{-\int_{h_1}^{h_2} \tau_o \, dh\right\} \quad (2)$$

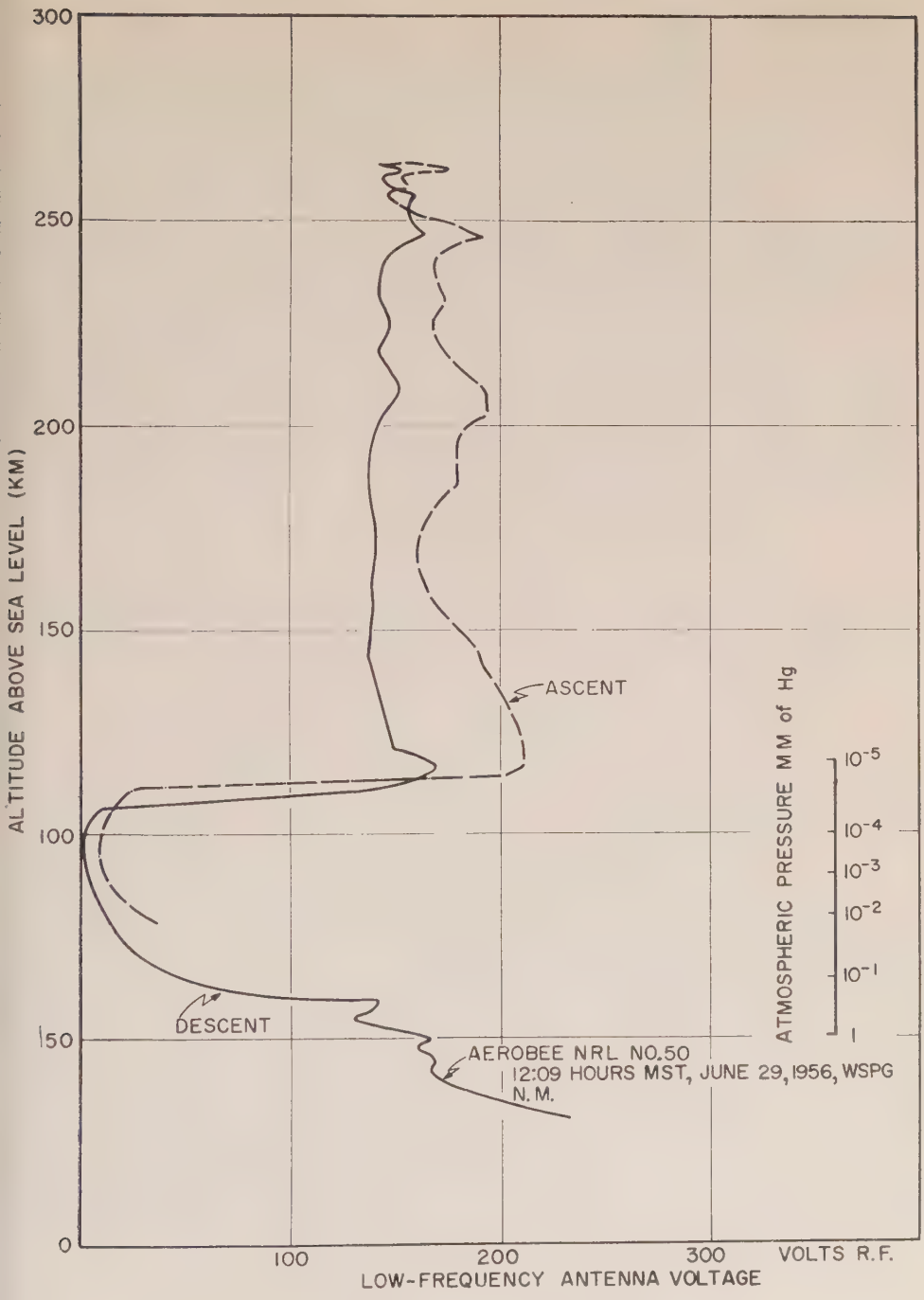

FIG. 1—Variation of 7.754-Mc antenna voltage with altitude

As the radiated power will vary, it is necessary to use the ratio of the amplitudes; therefore, Eq. (1) is divided by Eq. (2):

$$\frac{E_x^{h_2}}{E_0^{h_2}} = R_2 = R_1 \exp\left\{-\int_{h_1}^{h_2} (\tau_x - \tau_o)\, dh\right\} \quad (3)$$

If the difference in the absorption indices is taken as an average over the height interval Δh, Equation (3) can be written approximately

$$R_2 \cong R_1 \exp\{-\overline{(\tau_x - \tau_o)}\, \Delta h\} \quad (4)$$

and the average difference may then be computed. The radial velocity is essentially vertical on the ascent portion of the rocket flight, but on the descent the above formula would have to be corrected to take into account the non-verticality.

The use of the high-frequency dipole permits a measurement of the electron density by means of the Faraday effect. If the rocket rolls at a constant rate, the angle θ_p between the major axis of the low-frequency signal and that of the high-frequency signal may be calculated each time that a null occurs on either low-frequency dipole. In the event that the roll is slow, this may not provide many points, but if the difference in amplitude of the two components is small, θ_p may be calculated approximately from the relation

$$\tan \theta_p \cong \frac{E_{EW}}{E_{NS}}$$

The Faraday effect will alter the rate of rotation of the plane of polarization. If f_r is the roll rate of the rocket, f_x and f_o the frequency of the received magneto-ionic components,

$$\Delta\theta_p = 2\pi f_p\, \Delta t = \frac{2\pi(f_x - f_o)\, \Delta t}{2} = \frac{\pi f v}{c}(n_o - n_x)\, \Delta t \pm 2\pi f_r\, \Delta t \quad (5)$$

where v is the radial velocity of the rocket and c is the velocity of the light in vacuo. Solving for $n_o - n_x$,

$$(n_o - n_x) = \frac{(\Delta\theta_p \pm 2\pi f_r\, \Delta t)c}{\pi f\, \Delta h} \quad (6)$$

where $v\Delta t$ is taken to be the change in altitude Δh. The appropriate sign is used, depending on the direction of the rocket roll.

Above 75 km, the Appleton-Hartree equation may be used at 7.75 Mc without inclusion of the collision-frequency term to compute the electron density, once the value of $n_o - n_x$ has been obtained. Below this altitude, there may be some error introduced by ignoring collisions. In this paper, results were obtained only above 74 km. There are two main advantages in using Eq. (6) rather than the usual method of measuring the beat frequencies. One advantage is that when a null occurs on either low-frequency dipole, θ_p can be determined very accurately, in some cases to less than one degree. Another advantage is that no phase modulation occurs when the rocket antenna points somewhere near the station due to the rocket axis going off from vertical.

RESULTS OBTAINED

The ionosphere-sounding station at the White Sands Proving Ground, 15 km from the launcher, made recordings before, during, and after the firing. At 11:58

MST, 11 minutes before the firing, reflections were recorded down to 2-1/2 Mc, but the absorption increased so that the minimum frequency was about 3 Mc at 12:03 and 3-1/2 Mc at 12:16 during the downward flight of the rocket. The ionograms are shown elsewhere [4].

Figure 2 shows the change in the position of the major axis of the 7.754-Mc signal as compared to that of the 6th harmonic. The nulls at 64 seconds after take-off were essentially simultaneous, indicating no measurable electron density below

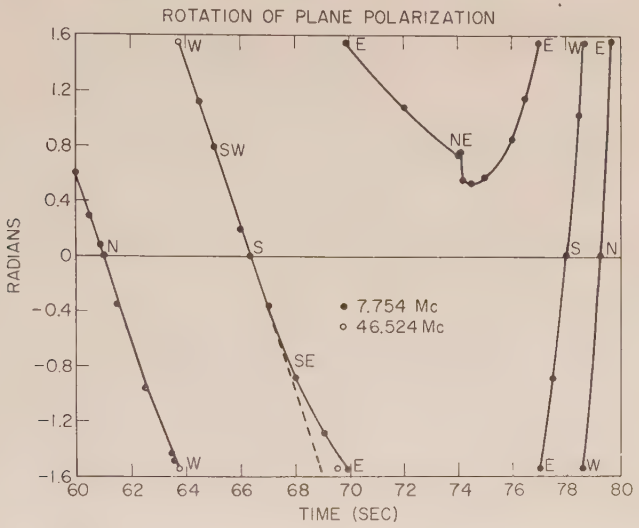

FIG. 2—Rotation of the plane of polarization due to rocket roll and the Faraday effect

this altitude (68 km). The low-frequency null on the E-W antenna at 66-1/2 seconds showed no change in the rocket roll, and therefore no electron density up to this altitude (72-1/2 km). At 67 seconds, however, there was an observable change from a uniform rate. The high-frequency null should have occurred at 69 seconds, but was found to occur at 69-1/2 seconds instead. This indicated that the roll rate was decreasing, even though the rocket was high enough to be beyond any influence of the atmosphere. The reason for this change in rate is unknown. The roll decreased so much that no more nulls were observed on the high-frequency dipole during the observing interval to 90 seconds. The AVC data obtained from the other station on circular polarization showed that the period of the rocket roll changed from its initial period of 12 seconds to a final value of 54 seconds, but the values in the transition period could not be determined. This was unfortunate, as this made the calculation of the electron densities impossible, except at 70 seconds. The average value of the electron density at this time was 2,000 el/cc.

The beat frequencies determined in the usual way from the other station are shown in Figure 3. Up to 86 km, the frequencies observed are almost entirely due to roll. The fact that the ordinary and extraordinary frequencies do not both go to zero indicates that neither the roll nor the electron density is zero. The time that the extraordinary frequency went to zero could be very accurately

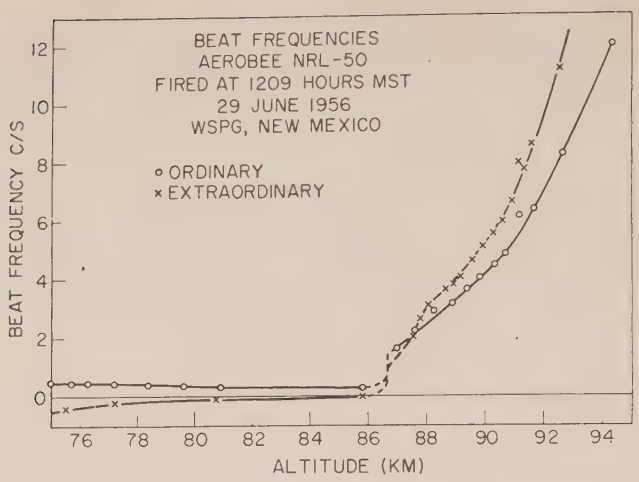

FIG. 3—Beat frequencies obtained by the usual NRL method of measuring electron densities

determined because of the phase reversal on going through zero. The ordinary frequency could not be measured with sufficient accuracy at this same time due to a slight partial null on the high-frequency circularly-polarized antenna. Instead, it was determined by noting the rate of change of the angle of polarization from Figure 2, which provided twice the difference between the ordinary and extraordinary frequencies. The assumption was then made that there were no appreciable effects from ions or electron collisions. The electron density was found to be

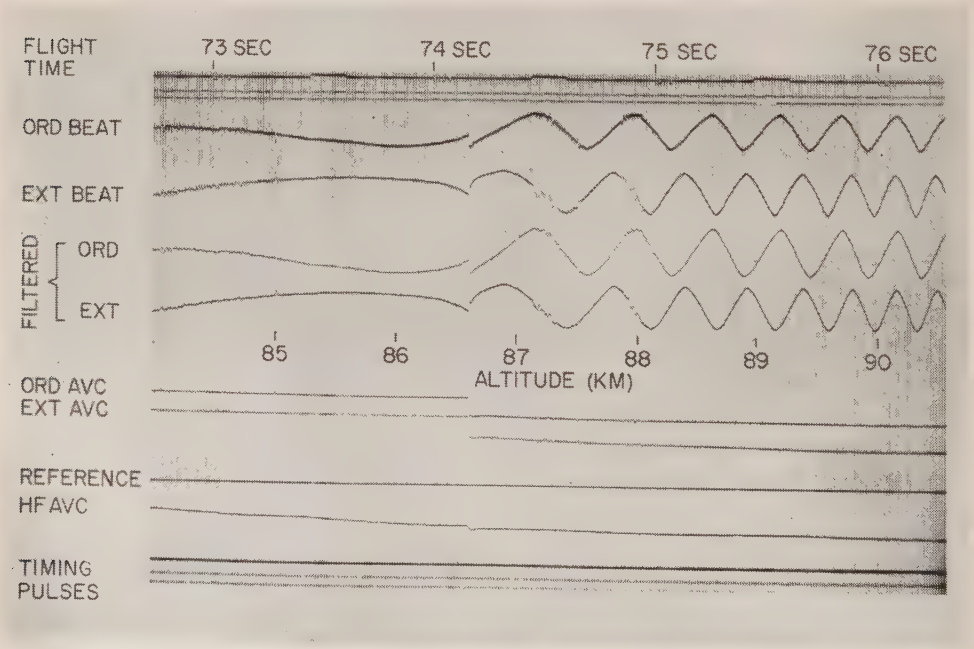

FIG. 4—A section of the data record near 87 km

1,000 el/cc and the roll period 32 seconds. The smooth character of the data between 78 and 86 km indicates that there was nothing very unusual in this region, but it is difficult to obtain accurate results from the beat-frequency data because of the unknown roll rate.

The abrupt change at 86-1/2 km is quite interesting. This is also evident in Figure 2 at 74 seconds. The raw data from the circularly polarized station are also shown in Figure 4. There was an abrupt change in electron density in about 25 meters, followed by a more gradual increase. It is interesting to consider whether this high-gradient region may be the reason for the results reported by Gardner and Pawsey [5], that partial reflections may be obtained on sensitive receiving equipment from an altitude of about 90 km.

In order to obtain a check on the results obtained by the Faraday effect, a comparison was made with the results obtained from the usual beat-frequency method, as shown in Figure 5. The roll period was taken to be 54 seconds for this

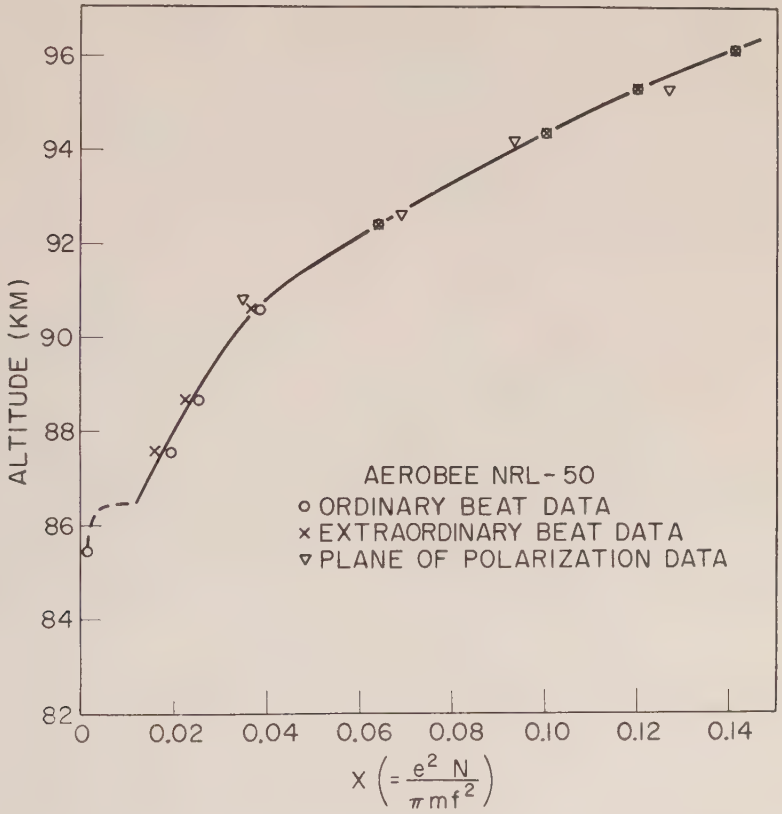

FIG. 5—Comparison of results by the Faraday-effect method with the usual NRL method

Figure, although the period was less than this until about 95 km. Better agreement would be obtained if a shorter period were used, especially in the lower altitudes, where the period was measured to be one-half the period actually used.

The final results are shown in Figure 6. The results indicate an abrupt beginning

of the D region at 74 km, with a decrease in density at the higher altitudes. The lack of differential absorption in the D region at 7.754 Mc, rising abruptly to a value of 1/2 per km at 96 km, indicates that at this frequency the D region has a

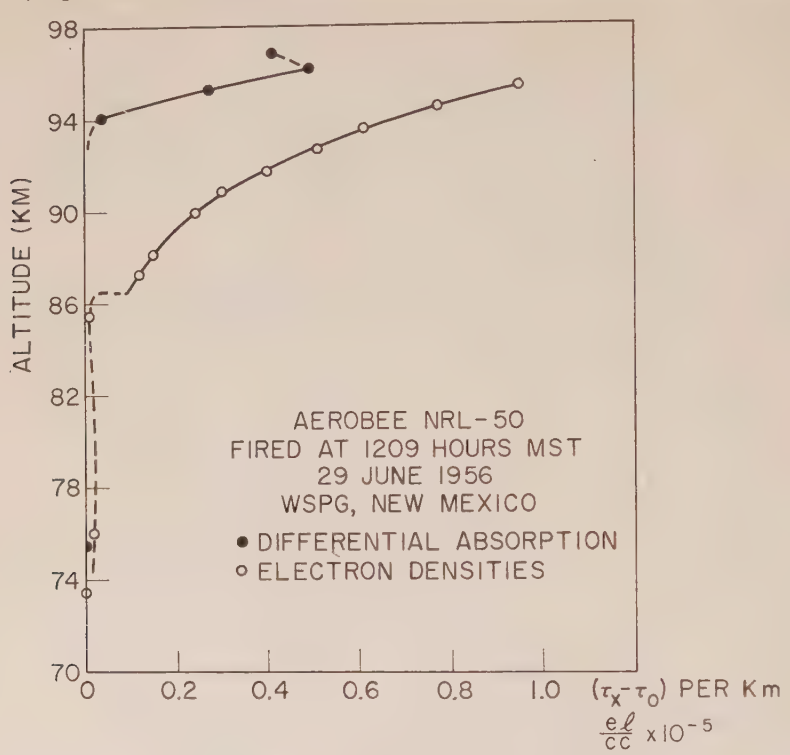

FIG. 6—Results obtained by the new method

relatively small absorption effect compared to the lower portion of the E region, even though the absorption was above normal. The data indicate a maximum value at 96 km, but the highest altitude point shown may have a small amount of error, due to the fact that the additional components that always occur in this region [1] began to make their appearance at this time. Above 97 km, these components were so strong that no further absorption results were obtained.

ACKNOWLEDGMENTS

The author wishes to express his appreciation for the work of Messrs. J. E. Jackson, G. H. Spaid, and W. E. Joosten in incorporating the necessary changes in the ground stations so that these results could be obtained.

References

[1] J. C. Seddon, J. Geophys. Res., 58, 323 (1953).
[2] R. A. Paska, Ballistic Research Laboratory, Rep. No. 944 (August 1955).
[3] J. E. Jackson and A. D. Pickar, Washington, D. C., Naval Research Laboratory, Rep. No. 4940 (May 4, 1957).
[4] J. E. Jackson and J. C. Seddon, J. Geophys. Res., 63, 197 (1958).
[5] F. F. Gardner and J. L. Pawsey, J. Atmos. Terr. Phys., 3, 321 (1953).

THE ROLE OF IONOSPHERIC-LAYER TILTS IN LONG-RANGE HIGH-FREQUENCY RADIO PROPAGATION*

BY SIDNEY STEIN**

Radio Propagation Laboratory,
Stanford University,
Stanford, California

(Received October 26, 1957)

ABSTRACT

An introduction to the role of ionospheric-layer tilts in long-range HF and VHF radio propagation is given. Tilts in the reflecting layers can have a first-order effect on radio propagation as a consequence of the curvilinear geometry of the earth. Low-angle rays reflected from a properly oriented, sufficiently tilted F layer will propagate beyond the bulge of the earth without striking the ground and illuminate the ionosphere again. When sufficient ion density exists at the second illuminated region, the rays will propagate on around the earth. A ray may be reflected several times before striking a properly oriented tilt so that the surface of the earth is illuminated. These modes are called ${}^{n}F$ modes, where n is the number of layer reflections.

Ray trajectories for a simple ionospheric model have been derived as an example of "tilted reflection." Anticipated fading, MUF, and field-strength characteristics of ${}^{n}F$ modes are discussed. The build-up of ${}^{n}F$ backscatter echoes is not linked to the characteristics of thick-layer reflection and is explained in terms of "geometrical" time-delay focusing.

Many different ${}^{n}F$ and combinations of conventional and ${}^{n}F$ modes have been observed on radio frequencies between 12 Mc and 30 Mc. The characteristic ranges on the different frequencies are, to first order, the same. ${}^{n}F$ backscatter echoes are often of high amplitude relative to conventional two-hop F-layer-propagated backscatter. At times, a complete absence of intervening ground backscatter between ground-zero and ${}^{2}F$, ${}^{3}F$, ${}^{4}F$, or ${}^{5}F$ echoes is observed. The times of occurrence of ${}^{n}F$ modes, length of each individual occurrence, direction of occurrence, and combinations of different modes are fundamentally related to the structure of the F layer and the radio frequency of observation.

*The research reported in this paper was supported in part by an Office of Naval Research Contract, jointly supported by the U. S. Army Signal Corps, the U. S. Air Force, and the U. S. Navy. This paper was presented at the Spring URSI Meeting, May 1957, at Washington, D. C.

**Now at the Ionosphere Research Laboratory, The Pennsylvania State University, University Park, Pennsylvania.

In addition, backscatter from the distant E region and reflection from the upper side of the E layer are very noticeably associated with F-layer tilts.

I. INTRODUCTION

This report is intended as an introduction to the effects of tilts in the reflecting layers on long-range HF and VHF radio propagation. The F layer will be of chief concern, since on these frequencies it is the principal reflecting layer. The F layer, as is well known, has complicated local fluctuations, erratic diurnal variation, and is strongly subject to geomagnetic influences [see 1 and 2 of "References" at end of paper]; consequently, great distortions from a simple Chapman region result. No distinction will be made between horizontal variations of ion density with or without accompanying changes in the height of maximum ion density; both cases will be referred to as horizontal gradients or layer tilts.

What are now believed to be the effects of horizontal gradients have been observed for several years. Long-range anomalous transequatorial propagation in the 6-meter amateur band was reported by Ferrell for the previous sunspot maximum [3]. Such propagation occurred at frequencies substantially above the MUF over long-range paths of order 7,000 km. These openings occurred primarily after sunset, mainly during the equinoctial months. Signals during these openings arrived greatly distorted by severe selective fading. The reality of a new propagation mode was convincingly confirmed by scatter-sounder observations made at St. Croix, U. S. Virgin Islands, during the summer of 1956 [4]. Echoes of long delay, corresponding to radar ranges of 6,000 to 8,000 km, were regularly observed on several frequencies between 23 Mc and 46 Mc. On 40 Mc, echoes were consistently received during the day at ranges 8,000 to 11,000 km. The daytime occurrences, the prevalence of these echoes after sunset, and the absence of strong distance-*vs*-frequency dependence are entirely explainable in terms of propagation modes associated with tilts in the F layer.

It was the characteristic violent fading of the anomalous transequatorial propagation that strongly suggested a scattering mechanism, possibly from the diffuse post-sunset F region recorded over the geomagnetic equator at Huancayo [3]. Ferrell reports that in a very large number of cases over the Mexico City-Buenos Aires path the carrier strength fluttered violently at a rate described as two to five times per second. Some distortion was observed on nearly all phone signals. An explanation of this fading will be given in terms of propagation modes associated with tilts in the F layer.

The role of ionospheric-layer tilts in long-range radio propagation was first studied in relation to a subject entirely different from transequatorial propagation. Ever since the inception of continuous backscatter recordings at Stanford, a distinct class of radio echoes from the northern auroral zone was detected [5]. These radio echoes are attributable to reflections from ionization associated with the aurora and have been registered on backscatter recordings on several radio frequencies [5, 6]. The relationship of the auroral region to Stanford (geomagnetic latitude of 43.8°) permits many different ionospheric propagation paths into the heart of the auroral zone, paths by which auroral reflections may be received. In

order to explain the prevalence of auroral reflections detected at the relatively low geomagnetic latitude of Stanford, the previous investigators had assumed the existence of prevalent, strongly reflecting ionized structures at great heights, between 300 km and 1200 km above the surface of the earth [5, 6]. Auroral reflections detected at Stanford were attributed to reflections from such structures. It was proposed that primary auroral particles spiraling in along the magnetic field lines are responsible for these ionization formations.

On the other hand, one of the important ionospheric modes for detection of auroral reflections at Stanford depends upon the existence of tilts in the F layer to the north. These observations of auroral reflections are comprehensively explainable in terms of auroral ionization in the E region over the auroral zone, provided the consequences of reflection from a tilted F layer are considered. What appear to be prevalent, strongly reflecting structures at great heights above the surface of the earth are explainable as the virtual images of auroral structures in the E region mirrored in the tilted reflecting F layer. While it certainly cannot be stated that radio echoes cannot be received from auroral ionization in the outer atmosphere of the earth on low-power broad-beam radars similar to those used in this study, the prevalence of such echoes is drastically less than has hitherto been believed. A full discussion of the altitude distribution of auroral scattering centers responsible for the Stanford observations is presented elsewhere.

The following notation has proved useful for referring to conventional propagation modes and has been adopted throughout this report. Single-hop reflection is labeled $1F$ or $1E$, depending on whether the E or F layer is involved. Successive reflection from the bottom of the F layer and top of the E layer (usually called M reflection) is written as $1F_E$. Double-hop F-layer paths can be written as $1F1F$, but $2F$ is more convenient. Many other paths can be described by combinations of these symbols, such as two successive F-layer reflections followed by reflection from the top of the E layer and another reflection from the F layer. This path has the symbol $2F_EF$.

No attempt has been made to go beyond an introductory presentation of the subject. Many of the areas discussed in this report involve problems of great complexity, deserving detailed consideration in their own right. Ray theory has been exclusively used throughout. The effect of the earth's magnetic field has been neglected.

II. THEORY

Horizontal gradients of ion density in the reflecting layers can have a first-order effect on HF and VHF radio propagation because of the curvilinear geometry of the earth. Low-angle rays reflected from a properly oriented, sufficiently tilted F layer will propagate beyond the bulge of the earth without striking the ground and illuminate the ionosphere again. When sufficient ion density exists at the second illuminated region, the rays will propagate on around the earth. A ray may be reflected several times before striking a properly oriented tilt so that the surface of the earth is illuminated. These modes are called ^nF modes, where n is the number of layer reflections. The symbol ^nF is suggested to be read as super-n-F. After one reflection from a tilted F layer, a ray missing the earth can be intercepted by

ionization in the E region, regardless of whether it is again reflected from the ionosphere. This type of path is called ${}^{1}F$. Various ${}^{n}F$ modes and combinations of ${}^{n}F$ and conventional modes are shown diagrammatically in Figure 1.

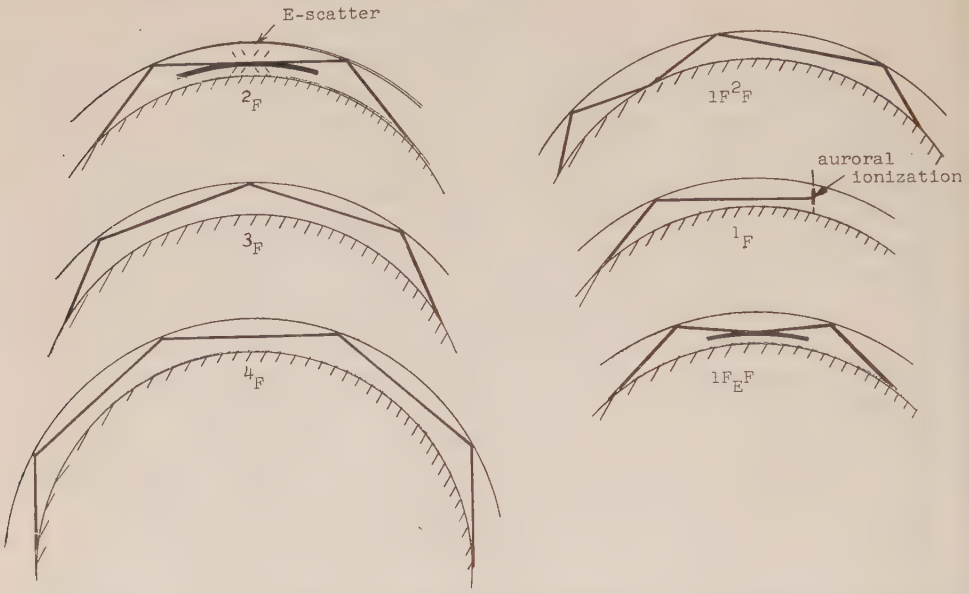

Fig. 1—Schematic of various ${}^{n}F$ and combinations of conventional and ${}^{n}F$ modes. Also shown is the $1F_EF$ mode, which is closely associated with F-layer tilts.

Consider a reflecting layer with strong horizontal gradients of ion density, the ion density decreasing in the direction of propagation. A ray reflected from such a layer will no longer have a symmetrical trajectory. The ray will emerge from the layer less steeply than when it entered, as a consequence of the fall-off of electron density in the horizontal direction in the plane of propagation. If the straight-line portions of the actual path beneath the layer are extended upward, an equivalent geometrical path is obtained with each line segment at a different angle with respect to the vertical at the intersection point. The deviation from symmetrical reflection may be obtained by an assumed tilt in an imaginary reflecting mirror placed at the intersection of the path segments. The angle of tilt is

$$\epsilon = \frac{\theta_r - \theta_i}{2} \qquad (2.1)$$

where θ_i and θ_r are the angles of incidence and reflection with respect to the vertical for the equivalent geometrical path.

A reflecting F layer with horizontal gradients of ion density in the plane of propagation may be characterized by an equivalent layer tilt as a function of take-off angle and radio frequency. The equivalent layer-tilt angle is defined as the tilt angle of assumed mirror reflection for the equivalent geometrical path, Eq. 2.1. If the equivalent tilt is large enough and of proper sign, positive according to our definition, the ${}^{1}F$ mode is excited with the possibility of ${}^{n}F$ propagation.

The general ionospheric conditions generating ^1F paths are more complicated than described in the previous paragraph. Generally, a ray is not launched perpendicular to the tilt axis and lateral deviations off a great-circle path occur. Moreover, the directions of horizontal gradients of ion density at a given time are space varying. Thus, if the straight-line portions of an actual reflected path beneath the layer are extended upwards, there is no assurance that an intersection will occur, that is, the trajectory is not confined to a plane. Yet, lateral deviation off a great-circle path can result in excitation of the ^1F mode as, for example, propagation in either direction along the sunrise line. Such a ray is laterally deviated away from the region of highest ion density off a great-circle course. A reflected ray can emerge less steeply than when it entered, since it travels, after lateral deviation, in a less dense region of the layer. Of course, the structure of the general sunrise gradient is far more complicated than has been implied, involving radical changes of vertical ion distribution, as well as a general horizontal east-west gradient.

The layer-tilt angle ϵ needed for excitation of ^1F rays from a station on the ground is given by

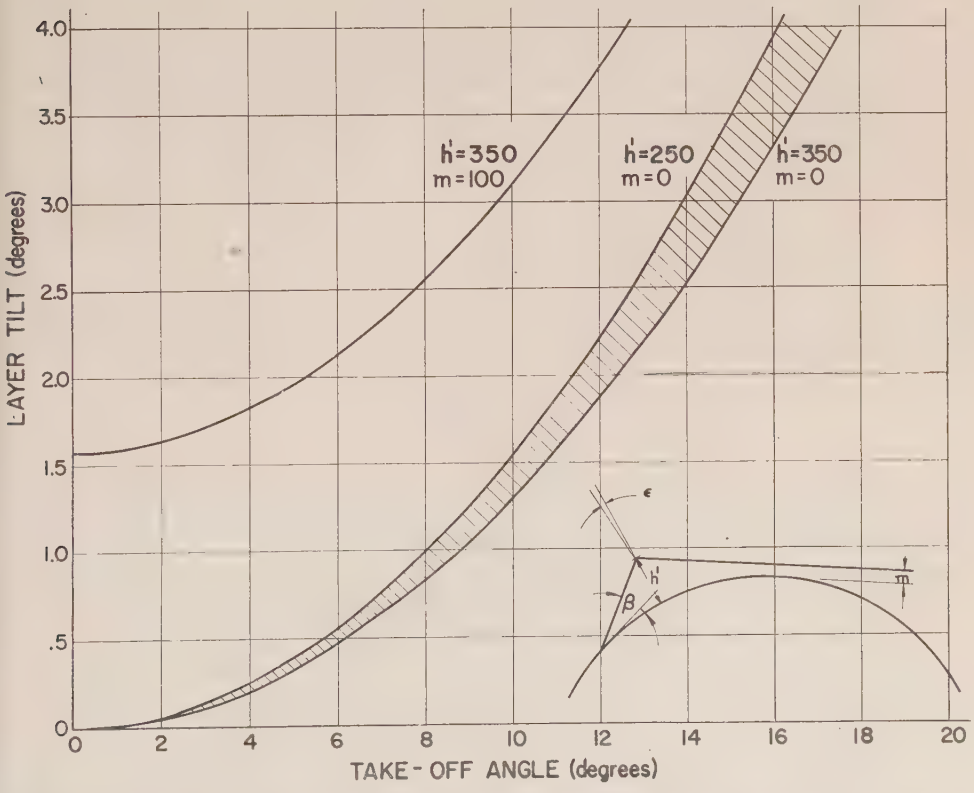

FIG. 2—Geometry of tilted reflection. Each curve has two parameters: the height of equivalent mirror reflection h' and the altitude of tangency m. All points lying above a given curve miss the earth by an amount greater than m, assuming fixed h'.

$$\epsilon = \frac{1}{2}\left[\tan\theta_m - \frac{\sin\theta_0}{\cos\theta_m}\cos\beta\right] \quad (2.2)$$

where $\sin\theta_m = (R + m)/(R + h')$, $\sin\theta_0 = R/(R + h')$, β is the take-off angle, R the radius of the earth, m the altitude of tangency, h' the height of equivalent mirror reflection (see Fig. 2). It is emphasized that Eq. 2.2 is derived from purely geometrical consideration.

The layer tilt needed for tangent reflection to the surface of the earth, the case when $m = 0$, is relatively not sensitive to variations of mirror reflection height between $h' = 250$ km and $h' = 350$ km, values selected as representative of F-layer reflection. This is shown by the shaded region in Figure 2. An equivalent layer tilt of $+2°$ will excite ^1F rays for take-off angles up to about 12°. Thus, a positive tilt of small numerical value will cause low-angle radiation from many practical antenna installations to miss the ground after suffering an F-layer reflection. Values of ϵ for $m = 100$ km are of interest, since rays tangent at this altitude are above the absorbing region in the lower ionosphere. ^nF rays can propagate long distances without the necessity of reentering the absorbing D region, except on the last leg, where the earth's surface is illuminated. It remains to determine the equivalent layer tilts for specific models of the ionosphere.

A simple ionospheric model has been worked out as an example of "tilted reflection." For the case of propagation in the direction of the horizontal gradient, a ray is not deviated laterally; polar coordinates are sufficient to described the trajectory. Fermat's principle in polar coordinates (r, ϕ) yields the differential equation governing a trajectory in an ionospheric model with two degrees of freedom, an arbitrary vertical and horizontal distribution of ion density:

$$r'' = \left[\frac{\mu_r}{\mu}'' - \frac{\mu_\phi}{\mu}\frac{r'}{r^2} + \frac{1}{r}\right][r^2 + (r')^2] + \frac{(r')^2}{r} \quad (2.3)$$

where μ is the index of refraction and μ_r and μ_ϕ are the partial derivatives with respect to r and ϕ. Initial conditions are $r_0 = R$, $r_0' = R\tan\beta$. A parabolic vertical ion distribution is given by

$$N = N_m\left[2\left(\frac{r - r_b}{y}\right) - \left(\frac{r - r_b}{y}\right)^2\right] \quad (2.4)$$

where r_b is the distance from the center of the earth to the bottom edge of the layer and y is the semi-thickness. For linear variation of ion density in the horizontal direction, the index of refraction is given by

$$\mu^2(r, \phi) = 1 - \frac{1}{\rho^2}\left[2\left(\frac{r - r_b}{y}\right) - \left(\frac{r - r_b}{y}\right)^2\right][1 - \lambda(\phi - \phi_0)] \quad (2.5)$$

where λ is the horizontal gradient parameter and ρ is the relative frequency parameter, equal to operating frequency divided by critical frequency at $\phi = \phi_0$.

Figure 3 gives the equivalent mirror height, the equivalent layer tilt, and the altitude of tangency for the special case $\rho = 2.5$ and $\lambda = 0.03$ per degree for the linear varying parabolic model given by Eq. 2.5. The height of maximum ion density is at 300 km, the semi-thickness 100 km. The gradient corresponds to a critical

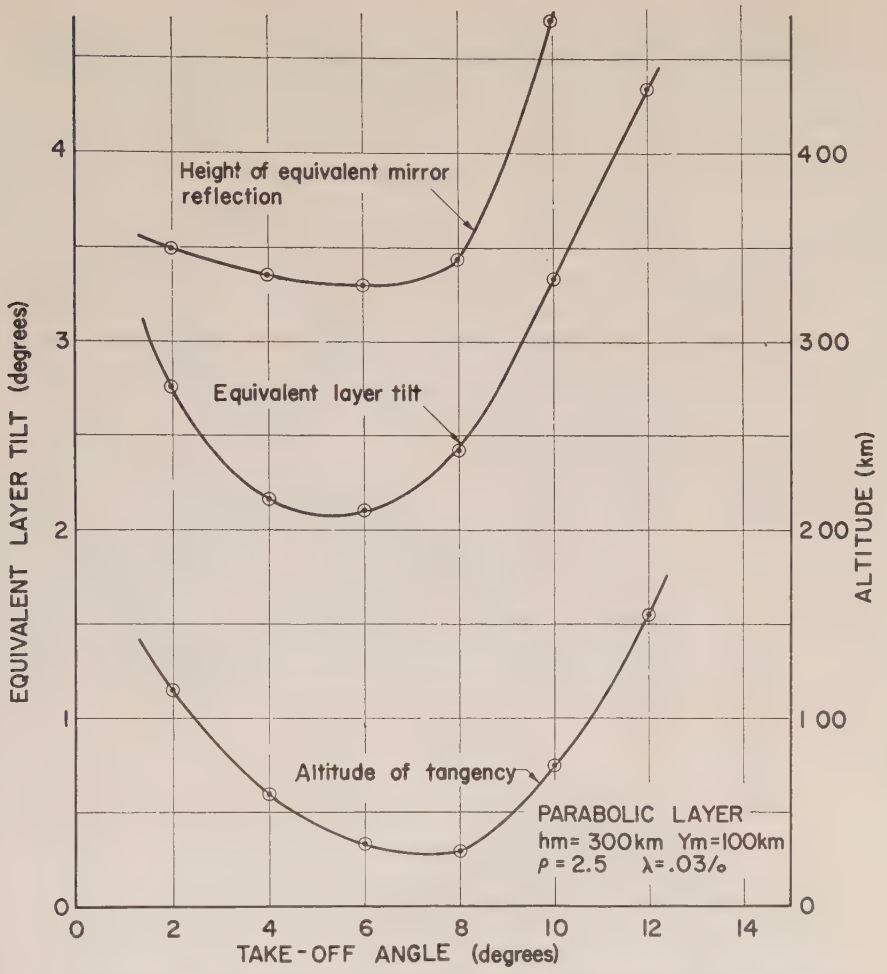

FIG. 3—An *F*-layer model with a parabolic vertical ion distribution and a linear variation of ion density in the horizontal direction

frequency 15 per cent less and 32 per cent less than the critical frequency of the layer over the point of origin, 1,000 km and 2,000 km away, respectively, in the direction of propagation. All the reflected rays miss the earth. The very low-angle rays, which reach the layer at the greatest distance, penetrate the layer.

Reflection at grazing incidence from a concave surface results in convergence of the reflected rays. As is well known, a tangent-ray receiver in the case of a symmetrical layer is on the cusp of a caustic surface, implying intense focusing of low-angle reflected rays. However, the presence of the earth's surface eliminates rays with negative take-off angles. Further, the field intensity of energy radiated and received at low positive take-off angles falls to very low values as the tangent plane is approached, introducing a practical limitation for realization of high field intensities resulting from grazing *F*-layer reflection. As a consequence of layer tilts, nevertheless, grazing reflection from the *F* layer can result in ray focusing

in the region above the surface of the earth. A subsequent reflection from the F layer can illuminate a restricted region of the earth at high field intensity. According to ray theory, these considerations imply that a characteristic of ${}^2F$ and ${}^n F$ propagation is the possibility of high field strengths.

Properties of ${}^n F$ propagation may be discovered using a primitive propagation model. Reflection from the F layer in this model is approximated by mirror reflection at altitude h' with tilt angles ϵ, both h' and ϵ independent of β. The axis of tilt is kept perpendicular to the plane of propagation, that is, propagation is along a great circle. The usefulness of this primitive model stems from the simulation of the curvilinear geometry of the earth. The actual ionosphere, with space-varying horizontal gradients, changing vertical ion distribution, underlying layers, and geomagnetic influences, is enormously complex. These factors are neglected in the primitive model and will not be mentioned unless it is believed they have a controlling influence in ${}^n F$ propagation.

The ground range for ${}^2F$ propagation is normally expected to decrease with increasing angle of take-off. For sufficiently large ϵ, however, part of the ${}^2F$ ray system may be so constructed that a low take-off ray reaches the ground closer to the origin than a ray with greater take-off angle. At still higher take-off angles, the earth is illuminated at grazing incidence; for ground-reflected rays, the ground range decreases with increasing angles of take-off. Thus, the ray system forms a multipath region. A diagram of this situation, based on the primitive propagation model, is shown in Figure 4. For actual ionospheric conditions, the variation of

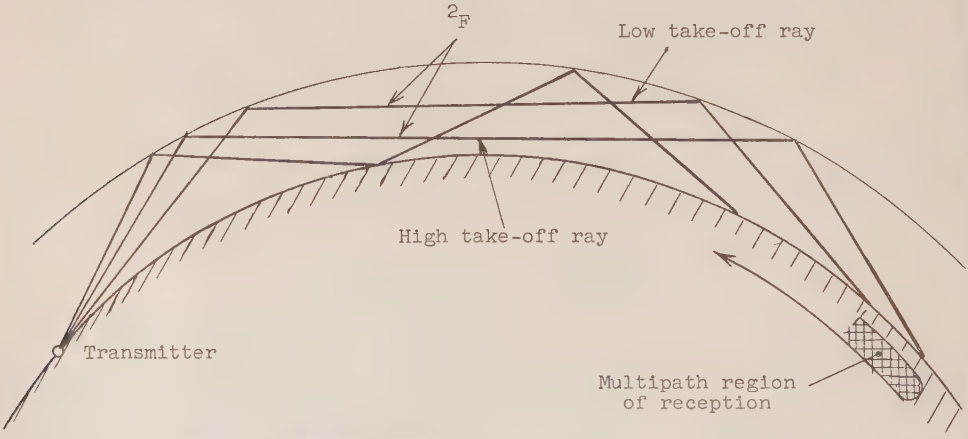

FIG. 4—Primitive model of multipath region for sufficiently large ϵ. A low ${}^2F$ take-off ray reaches the ground closer to the origin than a ray with greater take-off angle. For grazing ground-reflected rays, the ground range decreases with increasing angles of take-off, forming a multipath region.

ground distance with take-off angle is of great complexity, since the equivalent layer tilt and equivalent mirror height, both functions of take-off angle, may deviate substantially from constant values. Even for severe tilts, this particular type of multipath propagation is not always expected, since energy at take-off angles corresponding to the ground-reflected path may penetrate the F layer.

D-region absorption may severely attenuate the grazing ground-reflected signal.

Since severe tilts are associated with post-sunset transequatorial propagation [4], the severe selective fading reported by Ferrell for 6-meter transequatorial propagation is believed to arise from interference between waves reaching the receiver *via* ^2F and ground-reflected paths, as depicted in Figure 4. The fading in this situation is dependent upon the relative phase-path stability between the superposed modes. These modes are supported by the post-sunset *F* layer in the vicinity of the geomagnetic equator, which is known to undergo considerable change at that time. The variation of the *F* layer is believed to be of sufficient magnitude to account for the high fading rates reported. In addition, the difference in path length between the ^2F and ground-reflected rays is in the order of tens of kilometers, representing a great number of wavelengths. Therefore, the selective type of fading is favored. A "hollowness," as well as the flutter, reported for anomalous transequatorial propagation [7], is consistent with this interpretation, where, presumably, the "hollowness" is a result of time-delay differences between the ^2F and $2F$ modes under extreme conditions. This theory predicts that at times of severe selective fading during ^2F transmission the signal is detectable on the surface of the earth near the midpoint of the path.

Under conditions of marked *F*-layer tilts, a vertical sounder at the ground midpoint of a single-hop path would not measure the ionospheric region in which the rays are substantially affected. In this case, the conventional MUF would be lower than the frequency at which communication can be maintained. The skip ray would be shifted in the direction of increasing ion density, assuming the equivalent tilt arises from propagation in the direction of the horizontal gradient. For propagation perpendicular to the horizontal gradient, substantial deviation from a great-circle path can also result in propagation at frequencies higher than the conventional MUF. For the part of the ray system that misses the earth, forming the ^2F mode, the conventional MUF based upon a two-hop path would be substantially below the radio frequency of ^2F propagation. Propagation utilizing ^2F ray corresponds to lower take-off angles and more grazing incidence on the ionosphere than for $2F$ rays. For general ^2F propagation and certainly for ^nF propagation, the prediction of usable frequencies requires a radical modification of conventional methods and practice.

The ground-backscatter technique has proved useful for study of HF propagation [8, 9]. The techique consists of pulsing a high-frequency transmitter, connected to a directive antenna, and listening for echo signals. If the ionization density of an overhead layer is sufficient, the layer will reflect energy radiated at sufficiently low take-off angles back to the ground. Some of the energy is scattered from the ground back in the direction of arrival and may be detected as an echo at the station site. By scanning in azimuth and displaying the received signal on PPI, a characteristic ground-backscatter pattern is obtained, from which the approximate skip distance as a function of azimuth can be deduced. Peterson has shown that the energy arriving first at the receiver arises from a region on the ground beyond the skip distance, corresponding to the "minimum-time-delay" ray. The build-up of the ground backscatter echo is a result of "time-delay focusing," that is, energy corresponding to take-off angles slightly higher and lower

than for the minimum-time-delay ray arrive at the receiver at nearly the same time [10]. The multipath formed by the presence of upper and lower rays also contributes to the build-up of the echo. The ground backscatter echo diminishes rapidly as the distance beyond the skip edge increases. Since ^nF propagation is not intrinsically linked to the characteristics of thick-layer reflection, for example,

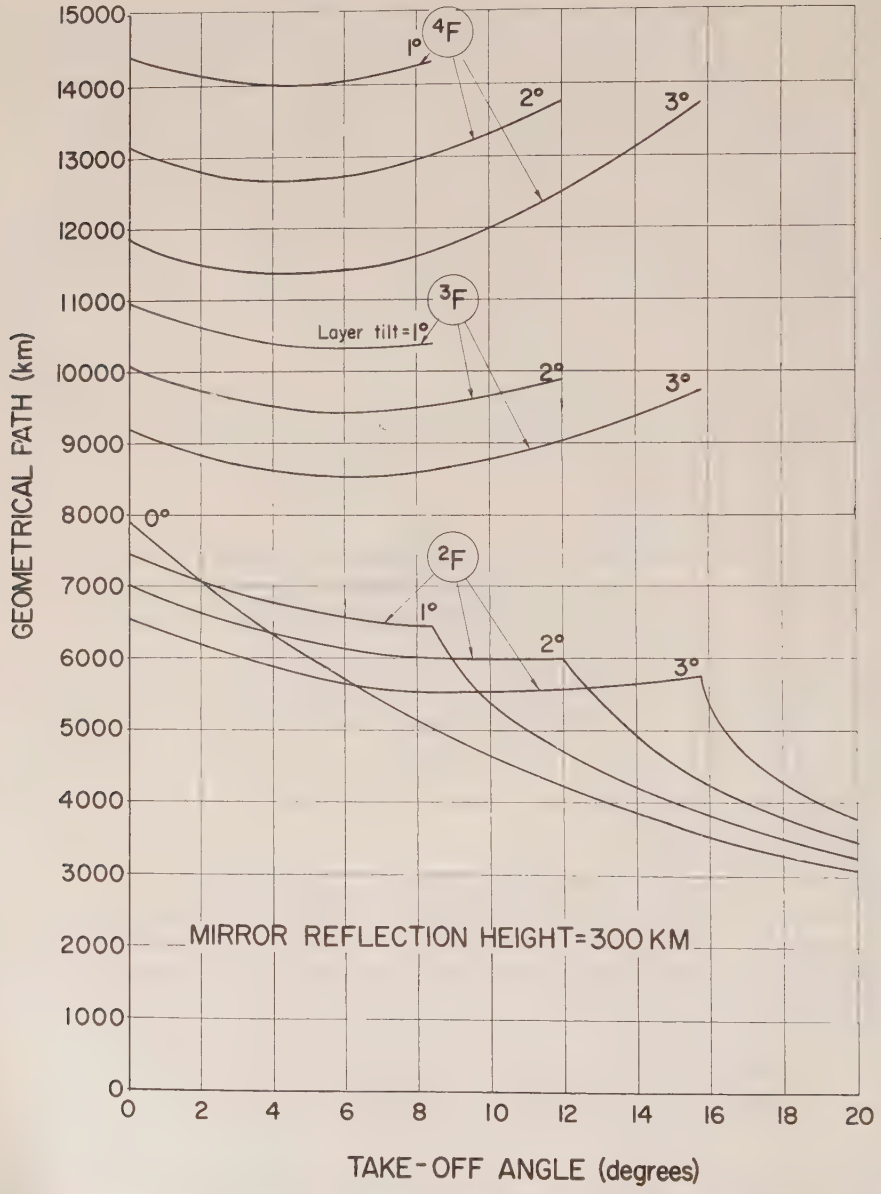

FIG. 5—Geometrical path length as a function of take-off angle for symmetrical ^nF paths of the primitive model

the skip-ray effect, it is not obvious that ^nF-propagated ground backscatter should be generally detectable.

Consider the length p of a symmetrical ^2F path of the primitive model

$$p = 2(R + h')\left[\frac{\cos(\theta + \beta)}{\cos\beta}\right] + 2(R + h')\cos(\theta + 2\epsilon) \quad \ldots\ldots\ldots (2.6)$$

where $\sin\theta = R/(R + h')\cos\beta$. The first term is the length of the path from the ground at take-off to the reflection height, plus the length from the reflection height to the ground at the terminal. The second term is the path length between reflection points. As β increases with fixed ϵ, the first term decreases while the second increases. A broad minimum in $p(\beta)$ results when ϵ is sufficiently large. Figure 5 presents curves for $h' = 300$ km for several values of ϵ. As β increases, the ground is eventually illuminated at grazing incidence. Each $p(\beta)$ curve joins the corresponding curve for a ground-reflected path.

The geometrical path length $p(\beta)$ may be taken as a first-order measure of the time delay (in kilometers) from transmitter to ground. The broad minimum in $p(\beta)$ for sufficiently large ϵ represents a strong time-delay focusing for ground backscatter echoes if effective energy is radiated at the corresponding take-off angles. This effect is called "geometrical" time-delay focusing to distinguish between the build-up of the backscatter echo as a consequence of the geometry of the ^2F path and as a consequence of the skip-distance phenomenon in thick-layer reflection. Geometrical time-delay focusing is another way of regarding the focusing resulting from grazing reflection from the F layer.

Zero tilt at the second reflection point of the primitive model and $-\epsilon$ at the third yields a ^3F path. The consecutive tilts used for ^4F paths are ϵ, 0, 0, $-\epsilon$. The $p(\beta)$ curves for each of these modes are shown in Figure 5; each mode has a characteristic minimum path length. It is concluded that geometrical time-delay focusing of ground backscatter for ^3F and ^4F propagation is operative. Similar to the situation for the ^2F case, the assumed tilts for ^3F and ^4F paths are a gross oversimplification of actual ionosphere conditions; not only is ϵ a function of β, but ϵ may have a different functional dependence at each reflection region.

The shallowness of the $p(\beta)$ curves suggests that the backscatter echoes have a relatively sharply-defined trailing edge, as well as a sharp leading edge. This expected result is borne out experimentally.

^nF rays are laterally deviated by the ionization gradients exciting these modes. The lateral deviation produces a lensing effect for trajectories both along and transverse to the horizontal gradients. A small lensing action at the first layer reflection region would contribute to the build-up of ground backscatter echoes, because more energy off the center of the beam would enter the ^nF mode and any focusing would be operative for the backscattered energy as well as for the outgoing energy. This lateral beam effect is in addition to the high field intensity anticipated on the ground as a consequence of grazing reflections from a concave layer. Quantitative calculations await the solution of suitable models.

Reflection from a tilted layer can illuminate the earth's surface at grazing incidence for rays originating at relatively high take-off angles. After ground reflection, the grazing rays can be easily affected by layer tilts. A great variety of

mixed modes is possible by combining conventional and "F modes. For the primitive model shown in Figure 6, the $p(\beta)$ curve obtained has two characteristic time-delay

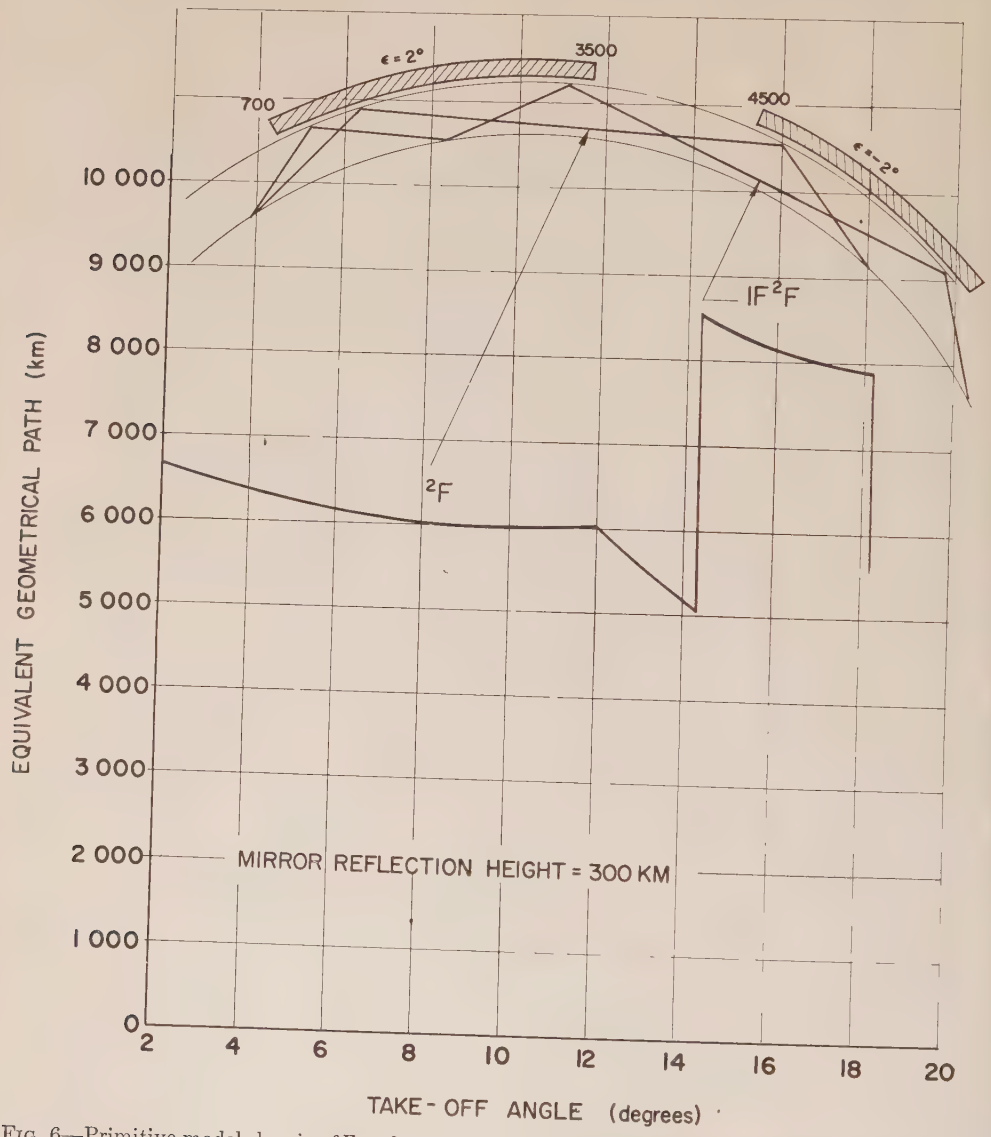

FIG. 6—Primitive model showing ^2F and $1F^2F$ paths, and geometrical path length as a function of take-off angle

focusing distances, near 6,000 km for the ^2F mode and near 8,000 km for the $1F^2F$ mode. The $1F^2F$ mode is excited for take-off angles roughly between 14° and 18°, near the maximum of the main lobe for many practical antenna installations.

The model in Figure 6 shows that ^2F ground backscatter implies the possibility of accompanying $1F^2F$ backscatter. It can be shown by suitable models that ^3F

propagation implies the possibility of detectable $1F^2F$ and ^2F ground backscatter. Many other models can be devised by selecting different tilted regions. These models are useful in elucidating which modes are responsible for backscatter echoes in practical cases.

Reflection from the upper side of the E layer is expected to be prevalent as a consequence of grazing incidence after reflection from a tilted F layer. ^1F rays that would miss the earth by a distance less than the height of the E layer impinge at grazing angles on the E layer. Reflection at grazing angles may occur when the E layer has a very low critical frequency relative to the operating frequency. The earth may easily be blanketed from receiving grazing $1F$ rays. Aside from the large number of mixed modes involving ^nF, nF, and E-layer reflections, the presence of the underlying E layer has prominent effects, associated with F-layer tilts, on backscatter observations.

Reflection from the upper side of the E layer introduces an incomplete geometrical time-delay focusing, so called because a minimum in the $p(\beta)$ curve is not obtained from a primitive model. Reflection from the top of the E layer shortens the geometrical path for low take-off rays, assuming that all reflected rays would reach the ground if the E layer were absent. Detection of $1F_EF$ ground backscatter, in comparison with grazing $2F$ backscatter, is attributed to the avoidance of four oblique passes through the absorbing region of the ionosphere and the incomplete geometrical time-delay focusing.

Grazing rays illuminating the E layer travel long distances in the E region, which can result in enhanced scattering from irregularities of ion density located in that region. For propagation paths in the E region roughly longer than half the pulse length multiplied by the velocity of propagation, the backscattered signal corresponding to the pencil of rays surrounding such a path would be of maximum amplitude at the receiver. For sufficient tilt, ^1F rays corresponding to relatively high take-off angles will intercept the E region "on edge." Consequently, it is to be expected that "E-scatter" and positive F-layer tilts would show a strong correlation on backscatter recordings. This result is borne out experimentally.

III. BACKSCATTER OBSERVATIONS

The prevalence of ^nF backscatter was evident immediately after Stanford's scatter-sounders were modified to detect these echoes. Scatter-sounder records for a typical two-week period in February 1957 and another in April 1957 were selected for detailed study. The equipment operated on 17.70 Mc and 30.64 Mc with nominal 2-kw output, 2-millisecond pulses, and rotating three-element Yagi antennas [11]. For the period in February, the scatter-sounders operated with a 7,500-km sweep. Echoes beyond 8,500 km were often recognizable "around-the-time-base," provided they were not hidden by other signals on the scope. For the later period, the sweep range was extended to 10,000+ km.

Figure 7 shows a typical afternoon sequence of 30-Mc records for the selected period in February. Scans are shown for each hour between 1300 and 1800 on 9 February 1957. On the majority of days during this period, $1F$ backscatter was seen in all directions during the afternoon. At sunset, 30-Mc propagation occurred toward the west into the sunlit portion of the globe. All through the afternoon and

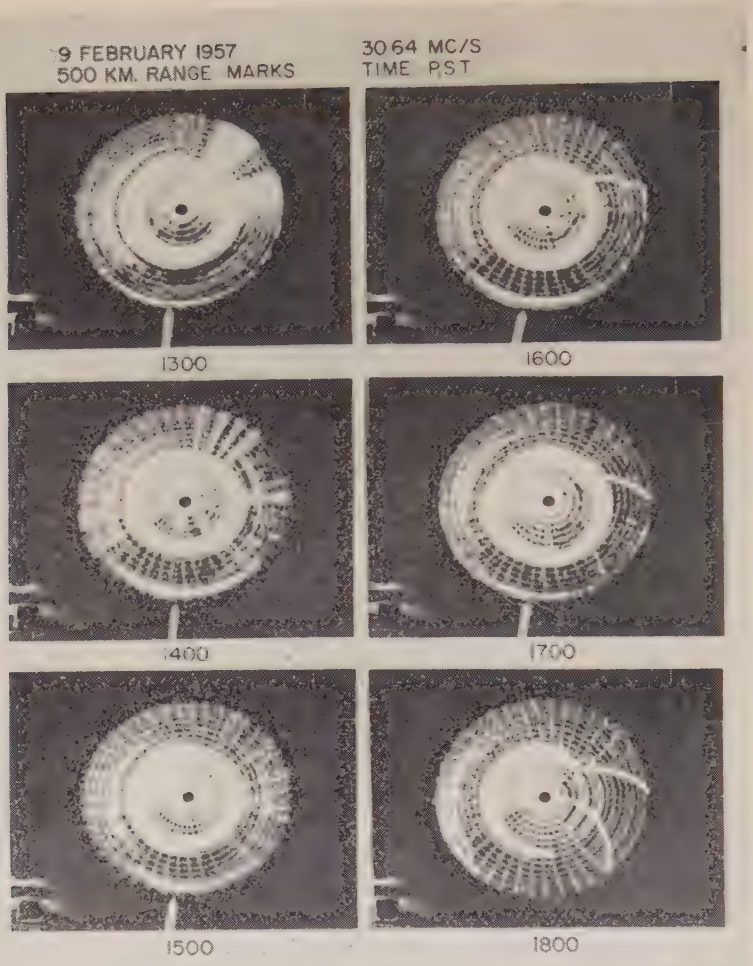

Fig. 7.—Typical afternoon sequence showing ^2F backscatter on 30.64 Mc during two-week period in February, 1957

sunset period, a weaker echo group is visible beyond the $1F$ echo to the west at ranges corresponding to $2F$ propagation. To the east, $2F$ backscatter is visible until 1600 hours. $2F$ backscatter is not expected from the north due to insufficient F-layer ionization. A marked discontinuity occurs between the $2F$-echo groups to the east and west and the strong echo appearing almost due south at a range of roughly 6,500 km. The strong echo at 6,500 km is not interpretable as $2F$, since the two-hop skip distance for propagation to the south is much closer. If this echo were $2F$, merger with the other echoes to the west and east is expected, somewhat similar to the continuous band of $1F$ backscatter. Though amplitude is not readily measurable on a PPI, the echo at 6,500 km is recognizably strong relative to the $2F$-echo groups. This echo is explainable on the basis of a ^2F path and occurs in the direction of known ionospheric gradients appropriate for ^2F

propagation: a region where there is a decrease of critical frequencies along a belt at the geomagnetic equator on the sunlit portion of the globe [2, 12]. Later the same day, an echo appeared at approximately the same direction and range as in the afternoon, though the structure of the ionosphere as it is viewed from Stanford was different. At that time, $1F$ backscatter did not extend all the way in front of the 6,500-km echo, providing strong evidence of a ^2F path. (The horizontal beamwidth, after squaring to account for radar operation, is approximately 60°.)

Figure 8 presents the times of occurrence of ground backscatter echoes in all directions having the distinguishing characteristics of the ^2F echoes just discussed. Only echoes at ranges 7,500 km or less were recorded. All echoes occurred at ranges beyond 6,300 km, while 70 per cent occurred at 7,000 km or greater.

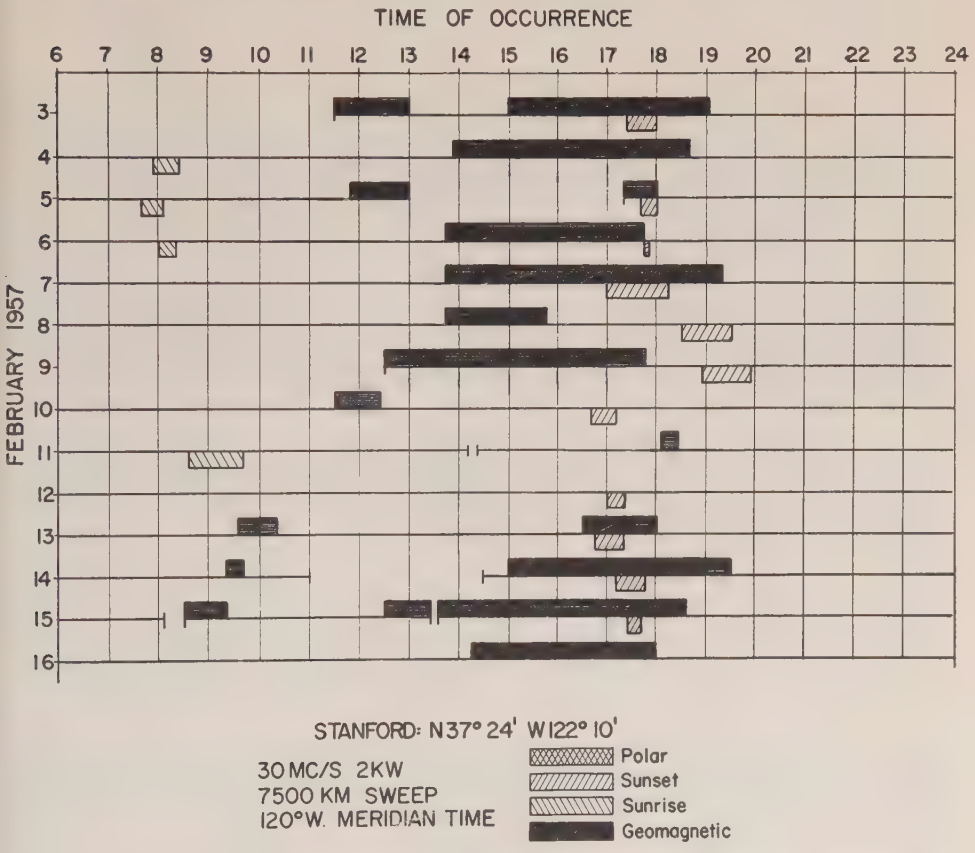

FIG. 8—Occurrence of ^2F backscatter on 30.64 Mc during two-week period in February, 1957. Only echoes at slant ranges 7,500 km or less are recorded.

It is believed useful to relate the ^2F echoes to the major ionospheric gradients that are responsible, since these echoes and the corresponding gradient structures are repetitive, at least over periods measured in weeks. The association is, in many cases, only a guess, since our knowledge of the ionosphere over large areas of the world is incomplete. Reference to the world contour charts contained in CRPL

Series D, "Basic Radio Predictions," gives some idea of the variation of critical frequency within the different longitude zones [12]. Three gradient structures occurring within the daylight zone were found to be sufficient for classification of the ^2F, 30-Mc echoes during the selected period in February. These gradient structures are "sunrise," "sunset," and "geomagnetic" (the belt of decreased ionization along the geomagnetic equator). The correspondence between echoes and gradient structure was made on the basis of the PPI ground-backscatter pattern. Echoes to the south at sunset, linked to the gradients at the geomagnetic equator, were classified with the "sunset" group.

Echoes attributed to the "geomagnetic" gradient occurred in a southerly direction, noticeably centered SSW of San Francisco. This is in agreement with geomagnetic coordinates, as the geomagnetic equator crosses the geographic equator near the 155° meridian (see Fig. 11). All the "sunrise" echoes occurred

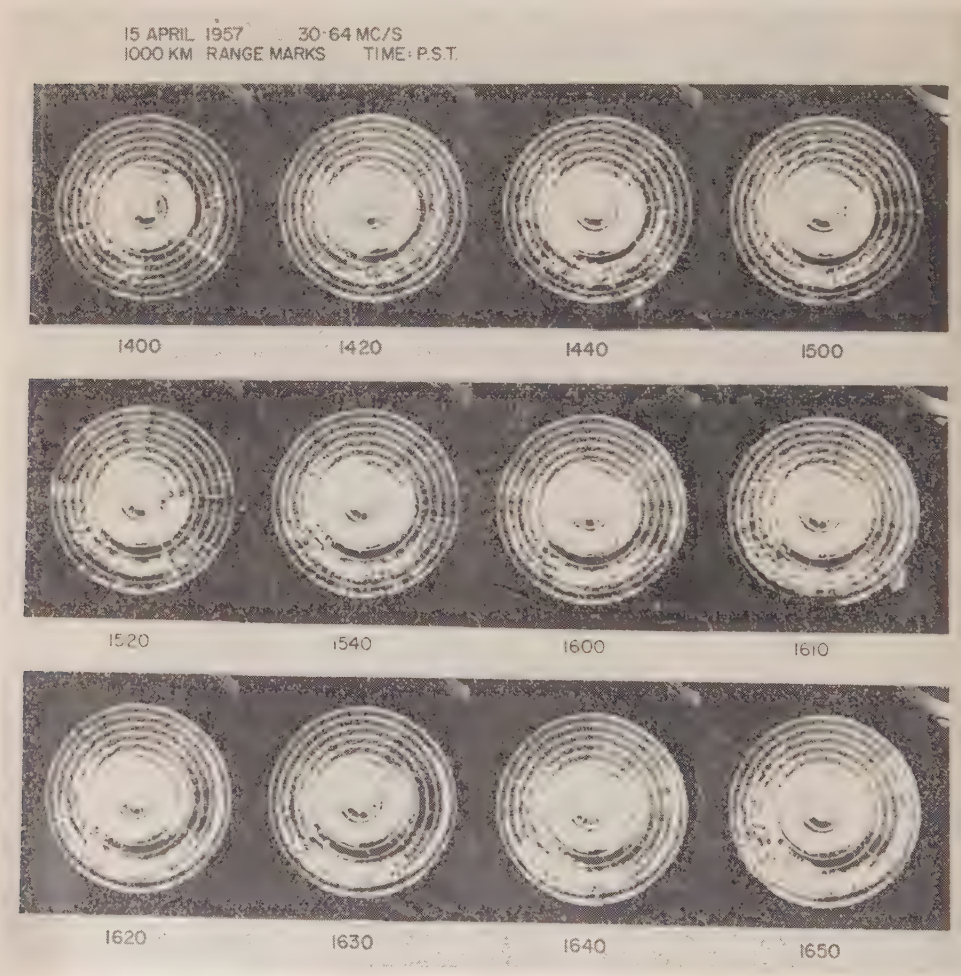

FIG. 9a—Typical sequence of 30.64-Mc backscatter recordings during two-week period in April, 1957. (Considerable fusion of separate echoes occurred during reproduction.)

in a southerly direction, roughly parallel to the severe "sunrise" gradient. "Sunset" echoes were centered ESE of San Francisco. ^2F propagation totaled roughly five hours a day.

Backscatter recordings on 30 Mc for a "typical" day during the selected two-week period in April are shown in Figure 9. A 10,000-km sweep had been arranged for the PPI scans. The following backscatter echoes have the characteristic of ^nF propagation:

Characteristic range *km*	Direction	Times visible on scans *P. S. T.*	Probable mode
6,800	S	1400 to 2040	^2F
7,400	E	1400 to 1420	^2F
9,800	S	1400 to 1840	^3F
8,800	E	1600 to 1800	$1F^2F$
7,200	ESE	1700 to 1910	^2F
8,600	SSE	1750 to 1850	$1F^2F$
9,000	SW	2020 to 2045	$1F^2F$

A list of occurrences cannot describe the over-all complexity of the backscatter patterns; some arbitrariness is involved in scaling. The range during the longest stable period of each echo occurrence is called the "characteristic range." Echoes dependent on layer tilts show considerable range stability even though such echoes often last for hours, which is consistent with the geometrical interpretation of the echo build-up. Typical range behavior of ^2F backscatter echoes would be a decrease as the echo appears, substantially constant range during the major portion of the echo occurrence, and increase during fadeout. The magnitude of the range-shifts is several hundred kilometers compared with characteristic ranges of roughly 7,000 km.

The identification of the probable modes responsible for each occurrence in Figure 9 was made on the basis of range and direction. The obvious consistency that must exist between a proposed mode and the general PPI backscatter pattern is very useful for interpretation of each occurrence.

^nF backscatter echoes (^5F has been observed) have a striking tendency to be narrow compared to conventional backscatter echoes, as can be seen in Figure 9. These echoes are often noticeably stronger than conventional $2F$ backscatter.

Beyond the $1F$ backscatter, due east in Figure 9, an echo is visible at roughly 4,500 km. Since this echo extends to greater range than any portion of $1F$ backscatter, the possibility of minor lobes as a cause is definitely ruled out. This echo is interpretable as backscatter from the E region, resulting from long paths through the E region as a consequence of tilts in the reflecting F layer. This echo is visible adjacent to the open sector of the ring of $1F$ backscatter in a direction, therefore, of known horizontal gradients. Note that as the $1F$-backscatter ring opens in Figure 9*c*, the "E-scatter" shifts first to the southeast and then to the south. Echoes of this type are very prevalent on Stanford recordings and are very noticeably associated with layer tilts. No further observations of this type of backscatter echo will be presented here.

Another type of echo prevalent on Stanford 30-Mc recordings and noticeably

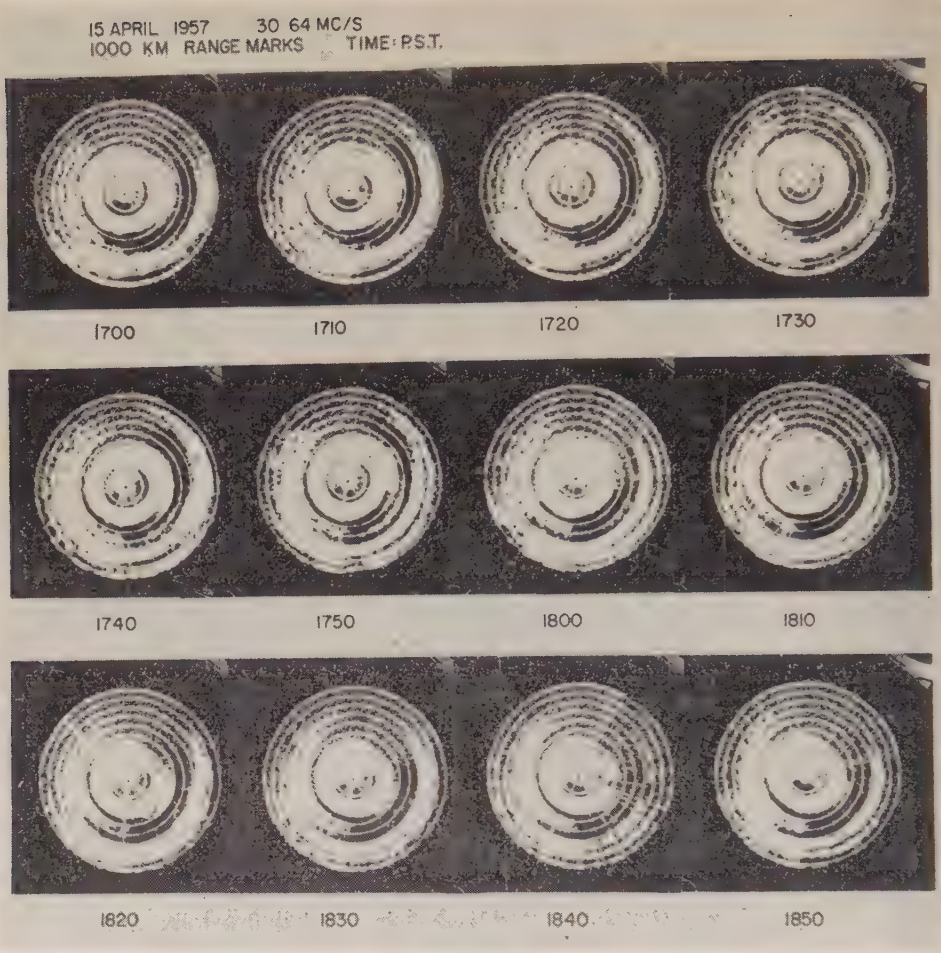

FIG. 9b—Typical sequence of 30.64-Mc backscatter recordings during two-week period in April, 1957

associated with layer tilts is observed at ranges of the order of 6,000 km. This backscatter type is generally weak, often accompanies and sometimes fuses with ^2F backscatter. Some examples appear in Figure 9*a* from 1400 to 1440 hours, southeast, and from 1640 to 1650 hours, south-southwest; in Figure 9*b*, from 1740 to 1800 hours, southeast. This type of echo is interpreted as $1F_EF$ backscatter.

The time of occurrence of 30-Mc backscatter dependent on ^nF propagation during the selected two-week period in April is shown in Figure 10. Only echoes with slant ranges less than 10,000+ km are shown. The most prevalent mode is ^2F in a southerly direction, similar to the results for the period in February. This class of echo occurred on every day, except one, for several hours during daylight. Most of the echoes occurring at ranges 8,400 to 9,200 km are believed to be $1F^2F$; echoes at ranges 9,400 to 10,000+ km are interpretable as ^3F. During this period, ^3F, ^4F, and ^5F backscatter echoes were observed at ranges beyond 10,000 km. A

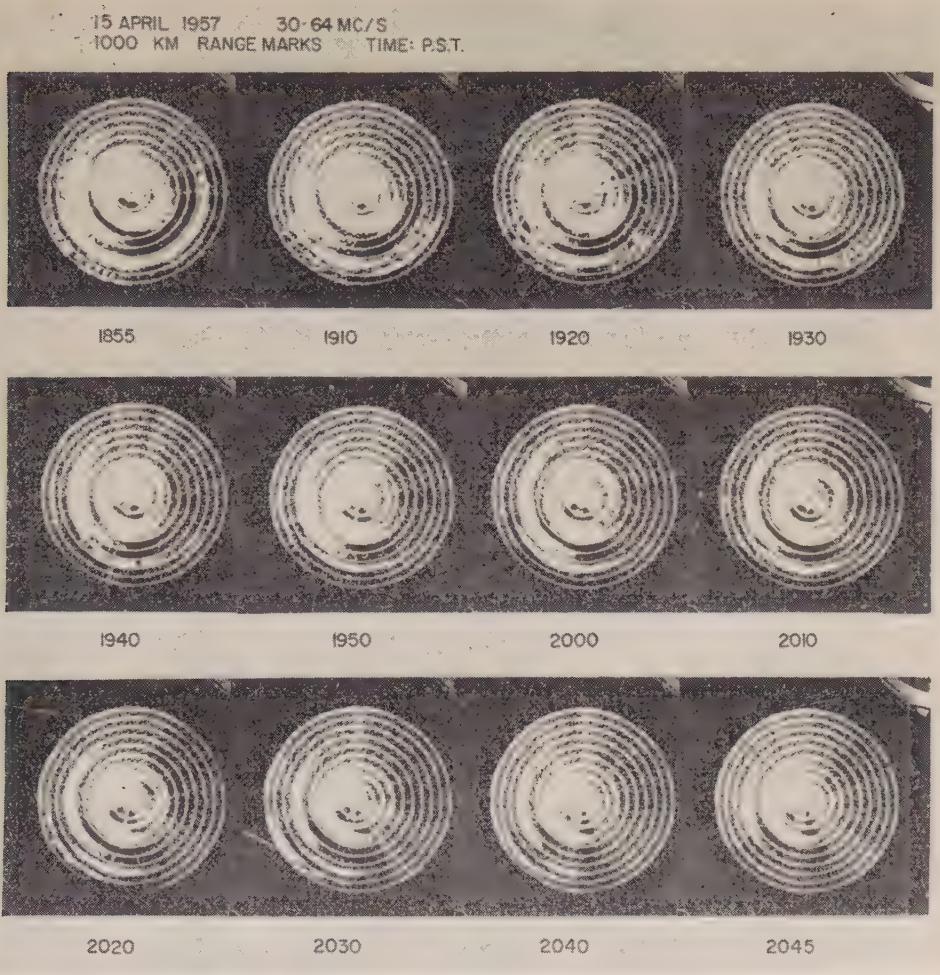

FIG. 9c—Typical sequence of 30.64-Mc backscatter recordings during two-week period in April, 1957

polar plot of echo occurrences registered in Figure 10 superimposed onto an azimuthal equidistant projection centered on San Francisco, California, is shown in Figure 11.

The characteristics of ^{n}F backscatter shown in Figures 10 and 11 are representative *only* of radio frequencies near 30 Mc. The appearance of the F layer is fundamentally related to the radio frequency of observation. It is a simple matter to devise ionospheric models giving a positive equivalent layer tilt to rays of high radio frequency, relative to the critical frequency of the layer, and zero or even negative tilt to rays of low radio frequency, and *vice versa*. A low-frequency ray is deviated near the bottom of the layer, while a high-frequency ray penetrates deeply. If the variation of ion density with height in a model layer coincides near the bottom of the layer at different cross-sections but changes near the height of

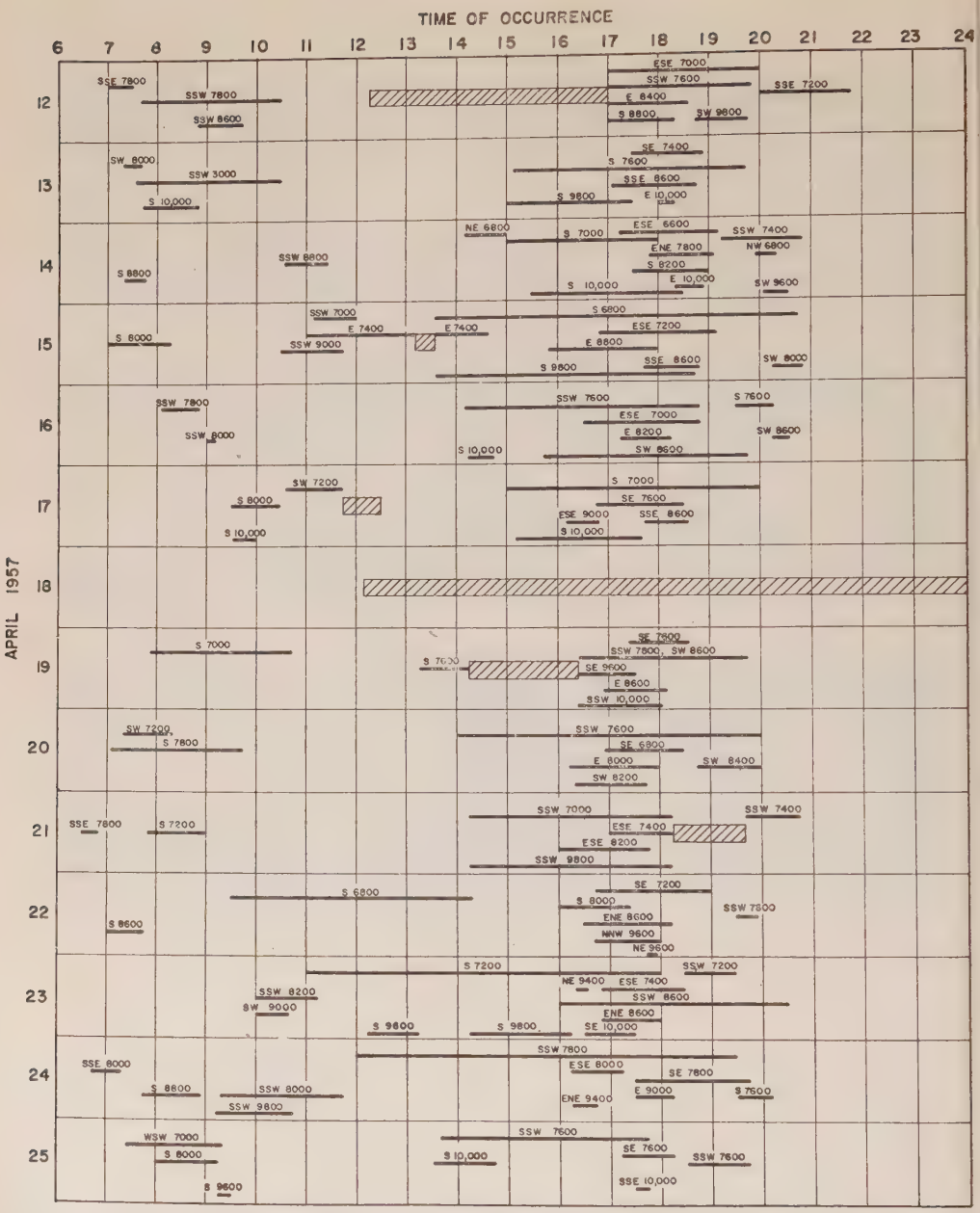

FIG. 10—Occurrence of 30.64-Mc ground backscatter echoes dependent on ^nF and combinations of conventional and ^nF modes during two-week period in April, 1957. Only echoes at slant ranges 10,000+ km or less are recorded. Hatched intervals indicate experimental data are not available.

maximum ion density, a ray must penetrate deeply into the layer to be substantially affected by the horizontal gradient. Conversely, if the variation of ion density with height at different cross-sections coincides near the ion-density maximum

FIG. 11—Polar diagram of backscatter echoes recorded in Figure 10

but changes near the bottom of the layer, a low-frequency ray will be affected, while for a high-frequency ray the bottom of the layer is relatively transparent. In general, both the height of maximum ion density and the lower edge of the layer undergo changes—the equivalent layer tilts as a function of frequency can be very complex.

^{n}F backscatter is observed, to first order, to occur as prevalently on 17 Mc as on 30 Mc, though the temporal characteristics are different on the different frequencies. The characteristic ranges of 17-Mc backscatter are to first order the same as on 30 Mc, which is consistent with the geometrical interpretation of the echo build-up.

During the autumn of 1956, Garriott and Peterson at Stanford, using 12-Mc backscatter equipment feeding a sloping-Vee antenna beamed south, observed long-range echoes at characteristic ranges mainly between 7,000 and 16,000 km. Considerable speculation occurred as to the origin of these echoes. The installation in March 1957, of a newly designed, 12-Mc, rotatable, Yagi-type antenna provided considerable insight into the origin of these echoes, which are explainable, according to these observers, in terms of ^{n}F and various combinations of nF and ^{n}F propagation. The usual hours of occurrence are between sunset and sunrise, daytime occurrences lacking principally as a consequence of high daytime absorption.

These preliminary observations at Stanford may be summarized as follows. On each frequency of observation (30, 17, and 12 Mc) many different ^{n}F and combinations of conventional and ^{n}F modes have been observed. The characteristic ranges of ^{n}F echoes on the different frequencies are to first order the same, in contrast to the range characteristics of conventional modes. ^{n}F backscatter echoes are often of high amplitude relative to $2F$ backscatter. These echoes have a pronounced tendency to be narrower than conventional backscatter echoes. At times, a complete absence of intervening ground backscatter between ground-zero and ^{2}F, ^{3}F, ^{4}F, or ^{5}F echoes is observed. The times of occurrence of ^{n}F modes, length of each individual occurrence, direction of occurrence, and combinations of different modes are fundamentally related to the structure of the F layer and the radio frequency of observation. In addition, "E-scatter" and $1F_{E}F$ backscatter are prevalent on Stanford scatter-sounder recordings and are very noticeably associated with F-layer tilts.

IV. CONCLUSIONS

Distortions from spherical symmetry in the F layer can have a first-order effect on long-range high-frequency radio propagation. Low-angle rays reflected from a tilted F layer may propagate beyond the bulge of the earth, without striking the ground, and illuminate the ionosphere again. A ray may be reflected several times before striking a properly oriented tilt so that the surface of the earth is illuminated. These modes are called ^{n}F modes, where n is the number of layer reflections.

The time and direction of occurrence of ^{n}F propagation depend upon the structure and diurnal variation of the ionosphere visible from the given geographical location. The appearance of the ionosphere is fundamentally related to the radio frequency of operation. After excitation of ^{1}F rays, the eventual type of propagation depends upon the ionosphere in another region of the globe. For locations similar to Stanford, the experimental evidence presented supports the belief that ^{n}F propagation in some direction (unspecified) and on some frequency (unspecified) is possible for over half the time in a 24-hour period.

^{n}F rays may propagate long distances without the necessity of reentering the

absorbing D region, except on the last leg, where the earth's surface is illuminated. Thus, in over-the-pole communication during times of severe polar blackout or in transequatorial propagation during high daytime absorption, ^nF modes may afford a long-range path that can propagate a usable signal.

There is a great need for further study of ray systems for suitable ionospheric models. A general approach is warranted where propagation at all azimuths with respect to the gradient reference direction is considered. Some sought-after goals are further characterization of the ionospheric layers to include the effects of tilts and a control-point approach for predicting usable frequencies for ^nF propagation. The existence of the earth's magnetic field may have some practical consequences.

Remote receiver measurements comprise a relatively inexpensive technique for many useful studies of long-range and, in particular, ^nF propagation. The build-up of ^nF ground backscatter is a consequence of geometrical time-delay focusing. By using spaced receivers in conjunction with a central scatter-sounder, field-strength records can be obtained, while the existence of ^nF and combinations of conventional and ^nF modes can be deduced from the scatter-sounder recordings.

Discrepancies between the predicted MUF and the actual radio frequency usable for transmission over long-range propagation paths have often been reported. In such cases, the usable radio frequency is consistently above the predicted MUF for the path. The conventional two-control-point prediction technique, where control points are selected 2,000 km from each endpoint along the great circle joining the stations, entirely neglects the presence of gradients of ionization density in the F layer, except in so far as the adoption of the two-control-point method is based on empirical evidence. A conclusion of this study is that many discrepancies between observed and predicted MUF's for long-range paths are explainable in terms of the newly discovered, long-range propagation modes dependent on F-layer tilts. Hitherto, conservative results in radio forecasting over long-range paths have almost always been attributed to the presence of sporadic-E along the path with consequent M reflections. While M reflections are believed partly responsible for the discrepancies, even in this case F-layer tilts play an important role. After reflection from a tilted F layer, grazing incidence on the E layer may occur, resulting in reflection from the upper surface at low values of E-layer critical frequency.

The relationship between the radio frequency usable for ^nF propagation and the conventional MUF for such a path can be effectively studied by the sweep-frequency backscatter technique [9]. For example, the range of ^2F backscatter would remain relatively constant, while the range of $1F$ backscatter would show the characteristic increase with frequency. ^2F and ^nF backscatter echoes are expected at radio frequencies higher and lower than the highest radio frequency at which $1F$ ground backscatter is visible.

Effects of tilts on $1F$ paths have been studied, though the consequences of tilts are not as dramatic as on long-range paths [14, 15]. Nevertheless, major alterations of $1F$ paths are expected to occur under conditions of severe layer tilts.

While no systematic study of F-layer-propagated backscatter from the E region has been done, results to date indicate that this class of echo is very prevalent

on HF and VHF fixed-frequency backscatter recordings. The marked correlation between "E-scatter" and positive F-layer tilts is attributed to enhanced scattering resulting from long path lengths through the E region for ^1F rays generated by such tilts. The probability of observing "E-scatter" on scatter-sounder recordings greatly increases if all azimuths are scanned, since detection is generally restricted to the azimuth in which the F layer appears tilted. Therefore, the prevalence of this class of echo is expected to be greater on PPI rather than on fixed-azimuth backscatter records. Silberstein, on the basis of fixed-aximuth sweep-frequency observations, nevertheless, pointed out that scatter from the distant E region may be more important than has generally been thought [9]. Observations of "E-scatter" may provide a useful means for studying the structure of the F layer in the directions in which these echoes occur. It has not been determined whether backscatter from the E region is attributable only to ionization irregularities connected with sporadic-E, whether the scattering centers are at times field-aligned [13], or whether ionization irregularities in the "regular" E region can provide a detectable echo.

In this study, $^n F$ propagation has been intimately associated with F-layer tilts. This results from maintaining the initial and terminal points of the transmission path on the surface of the earth. For communication between elevated points, such as between orbiting vehicles, relay platforms, space craft, etc., which some day may populate the region 100 to 200 km above the earth's surface, the usual mode of long-range communication utilizing reflections from the F layer would be $^n F$. Such propagation can be carried on at higher frequencies than is possible from the ground and would make use of the focusing action of a curved reflector at grazing incidence. For spherically symmetric reflecting regions, the ground need not be illuminated.

Energy introduced into $^n F$ propagation may not encounter a properly oriented layer tilt for illumination of the earth's surface. If this energy does not penetrate the layer at some region of reduced critical frequency and escape into space, many successive reflections within the ionized shell of the ionosphere will occur until the energy is completely absorbed. It has been suggested to the author that long-delay echoes of the type reported by Van der Pol, Störmer, and others, with delays between 3 and 15 seconds, may be associated with $^n F$ propagation inside the ionized shell formed by the F layer. The difficulty with this explanation is that the path length of a long-delay echo is so great that for a signal to be detectable the absorption per kilometer must be extremely low. For propagation within the ionized shell formed by the F layer, this requirement implies that the ionization beneath the F layer is extremely low, perhaps as low as $N/N_{max} = 1{,}000$, where N_{max} is the ion density at the F-layer maximum and N is a representative value of density along the path within the shell.

Attention is directed to the observations of moon echoes by Kerr and Shain [16]. As was suggested by Kerr and Shain, many of their anomalous results are explainable on the basis of tilts in the F layer.

V. ACKNOWLEDGMENTS

The author is indebted to A. M. Peterson and R. D. Egan for permission to

modify the Stanford 17-Mc and 30-Mc scatter-sounders. Sincere thanks are extended to K. H. Renshaw for maintenance of the Stanford equipment and for coping with the long series of equipment failures. W. E. Haney contributed valuable assistance during modification of the equipment. It is a pleasure to acknowledge the many informative and interesting discussions with O. Garriott concerning the 12-Mc backscatter observations.

The support and special encouragement from the staff and fellow students of the Radio Propagation Laboratory of Stanford University are gratefully acknowledged and keenly appreciated.

References

[1] S. K. Mitra, The Upper Atmosphere, Asiatic Society, Calcutta (1952); pp. 296-299.
[2] K. Maeda, Geomagnetic distortion in the *F*2 layer, Report of the Physical Society Conference on the Physics of the Ionosphere held at Cavendish Laboratory, Cambridge, Physical Society (1955); p. 245.
[3] O. P. Ferrell, Very high frequency propagation in the equatorial region, paper presented at URSI meeting, Washington, D. C., May 1951.
[4] O. G. Villard, Jr., S. Stein, and K. C. Yeh, New evidence of anomalous transequatorial ionospheric propagation, paper presented at IRE National Convention, New York, N. Y., March 1957.
[5] A. M. Peterson and R. L. Leadabrand, Long-range radio echoes from auroral ionization, J. Geophys. Res., **59**, 306 (1954).
[6] R. L. Leadabrand, Radio echoes from auroral ionization detected at relatively low geomagnetic latitudes, Radio Propagation Laboratory, Stanford University, Tech. Rep. No. 98 (1955).
[7] G. Jacobs, Propagation, CQ Magazine, p. 90 (April 1957).
[8] O. G. Villard, Jr., and A. M. Peterson, Scatter-sounding: A new technique in ionospheric research, Science, **116**, 221 (1952).
[9] R. Silberstein, Sweep frequency backscatter—some observations and deductions, Trans. Inst. Radio Eng., **AP-2**, 56 (1954).
[10] A. M. Peterson, The mechanism of *F*-layer propagated back-scatter echoes, J. Geophys. Res., **56**, 221 (1951).
[11] A. M. Peterson, A scatter sounder for the study of sporadic ionization in the upper atmosphere, Radio Propagation Laboratory, Stanford University, Tech. Rep. No. 1 (1953).
[12] Basic radio propagation predictions for February 1957, Nation. Bur. Stan., CRPL Series D, No. 147 (November 1956).
[13] P. B. Gallagher, Analysis of a new type of radio scattering from the ionospheric *E*-region, Radio Propagation Laboratory, Stanford University, Tech. Rep. No. 107 (1956).
[14] H. A. Whale, Effective tilts in the ionosphere at places about 1000 apart, Proc. Phys. Soc., B, **68**, 301 (1955).
[15] E. N. Bramley and W. Ross, Measurements of the direction of arrival of short radio waves reflected at the ionosphere, Proc. R. Soc., A, **207**, 251 (1951).
[16] F. J. Kerr and C. A. Shain, Moon echoes and transmission through the ionosphere, Proc. Inst. Radio Eng., **39**, 230 (1951).

INTERNATIONAL DATA ON MAGNETIC DISTURBANCES, THIRD QUARTER, 1957

This report continues the series which has appeared regularly in this JOURNAL since Vol. 54, No. 3, 295 (1949). Please refer to that first report for an explanation of the data given, and to Vol. 59, No. 3, 423 (1954) for the definition of *Ap*.

Preliminary Report on Sudden Commencements

S.c.'s given by five or more stations are in italics. Times given are mean values, with special weight on data from quick-run records.

Sudden commencements followed by a magnetic storm or a period of storminess (s.s.c.)

1957 July *01d 17h 47m*: seven.—*02d 08h 57m*: forty-two.—*04d 23h 42m*: fourteen.—*05d 00h 42m*: twenty-one.—*16d 07h 14m*: forty-four (s.f.e.: Sw Wa).—19d 05h 17m: Ka Pi.—*19d 13h 44m*: twenty-seven.—*22d 04h 19m*: thirty-four.—*27d 19h 59m*: forty-one (s.f.e.: Si).

1957 August *03d 15h 57m*: fifty-five.—*06d 05h 08m*: forty-two.—*09d 13h 47m*: forty-one (s.f.e.: Si Fr Tu Ta Va).—13d 06h 17m: Vi Ag Tu.—*29d 19h 09m*: six (s.f.e.: Ta).—*29d 19h 20m*: fifty-three.—31d 14h 14m: Vi Te.—*31d 18h 12m*: twenty-eight (s.f.e.: Fr).

1957 September *02d 03h 14m*: forty-eight.—03d 12h 33m: YK Si Te.—*04d 13h 00m*: fifty.—*06d 11h 21m*: twenty-five.—*12d 21h 54m*: ten (s.f.e.: Hu).—*13d 00h 46m*: forty-eight.—*21d 10h 05m*: forty-seven.—*22d 13h 45m*: forty-four.—*23d 02h 35m*: twenty-seven.—*29d 00h 16m*: forty-eight.

Sudden commencements of polar or pulsational disturbances (p.s.c.)

1957 July 01d 06h 37m: Te Pi.—03d 00h 42m: YK Sw.—*03d 01h 50m*: five.—03d 20h 33m: So Sw Hr.—04d 19h 58m: Tr So.—*05d 21h 20m*: six.—06d 22h 36m: Ta El Hr.—08d 20h 16m: Tr Do.—08d 21h 20m: Do Db CF.—*09d 22h 08m*: eight.—11d 02h 23m: Ma CF IK Tl.—12d 07h 42m: YK Hu.—12d 18h 47m: So Ba Bi.—14d 23h 02m: Db Eb Tl.—15d 01h 39m: SM Pi.—*17d 21h 07m*: twenty-three.—*19d 22h 12m*: thirteen.—*20d 22h 07m*: six.—20d 22h 56m: Vl Hb.—*22d 19h 12m*: ten.—22d 19h 43m: Vl Eb Ta.—22d 23h 38m: Tl Hr.—23d 22h 33m: YK IK.—24d 07h 48m: YK Vi Te.—*24d 22h 41m*: five.—28d 19h 51m: So Hb Lg Eb.—*29d 02h 54m*: six.—29d 06h 41m: Hb Te.—29d 14h 38m: Mb Ka.—*30d 22h 12m*: five.—*30d 23h 10m*: twenty.—*31d 21h 23m*: six.—31d 21h 35m: Pr Hb Gi Bi.

1957 August 01d 05h 45m: YK Vi.—02d 00h 50m: Db Fu.—*02d 01h 48m*: twenty-one.—02d 18h 01m: Qu Wa.—*02d 23h 31m*: fifteen.—03d 16h 57m: CF

Table 1—*Geomagnetic planetary three-hour-range indices Kp, preliminary magnetic character-figures C, average amplitudes Ap (unit 2γ), and final selected days, July to September, 1957.*

	July 1957									August 1957								
E	1	2	3	4	5	6	7	8	Sum	1	2	3	4	5	6	7	8	Sum
1	7+	7+	7−	3+	2−	5−	7o	5o	43o	2−	2+	2+	1o	2o	1+	2−	1+	14−
2	2−	1o	3−	5−	8o	6+	6−	2+	32+	3o	2o	2−	2−	2+	1+	2o	3o	17o
3	6−	4+	4−	4+	5+	1+	2+	3o	30o	3−	1o	2+	2o	2o	6+	5+	4o	26−
4	1o	1−	0+	1+	1o	2−	4−	5o	15−	5+	2o	2o	1−	1o	2−	1o	2−	15+
5	5−	7+	6o	6−	3+	2o	3o	6−	38−	2−	1o	1o	1−	1−	3−	3+	4+	15+
6	2+	3−	3+	3−	2+	2+	4−	5−	24o	3o	4+	6−	4−	4o	4−	4+	4+	33o
7	2+	3−	2o	1+	2o	1+	3+	2+	17+	3o	2o	3−	2−	2o	1o	1o	1+	15−
8	3−	2+	3o	1+	2o	2+	2−	2o	17+	1o	2o	2+	2o	2o	1−	3−	2+	15o
9	3−	1o	2−	1o	1+	2−	1+	2−	12+	4o	3+	2+	1+	5−	2o	2o	3+	23o
10	2o	2+	1o	1−	1−	1−	1−	1−	9−	4o	3o	1+	2−	0+	1−	1o	2+	14+
11	1+	1−	0+	1+	3−	0+	1o	1+	9o	2−	1−	0+	1o	1+	1+	1o	2−	9o
12	3o	2+	3−	1+	2+	1+	2+	2o	17+	2+	4−	3+	3o	4o	4o	4o	2+	27−
13	1+	1o	1−	1−	1−	1o	1−	0o	6o	4+	5+	6−	4+	4−	3o	4−	3o	33o
14	0+	1o	1−	2−	2o	1+	2−	3−	11+	1−	1+	1o	2−	3−	2+	3−	2+	15−
15	3−	1o	1−	1+	1o	1−	0+	1o	9−	4−	2o	2−	1+	1o	1o	3−	3o	16+
16	1+	0+	3o	4−	3+	4o	4o	3o	23−	2+	2+	1−	1+	1o	1o	1+	1o	11o
17	3−	1+	1−	2+	2+	1+	2+	3−	16−	1−	0+	0+	1−	2−	2o	0+	1−	7−
18	2−	2o	2+	3o	3o	4−	3o	3−	21+	2o	1+	0+	3−	3−	1+	2−	2+	14+
19	4o	3o	3+	3−	4o	4+	5−	4+	30+	4o	4−	3+	3+	2−	1o	0+	1o	18+
20	3o	3o	2o	1+	2o	2o	2+	4−	19+	1−	1+	1+	2o	3+	3o	3−	3+	18−
21	2o	2−	1−	1+	1+	1+	2−	2+	12+	4o	5+	3+	3−	2+	4−	1+	1−	23+
22	2−	3+	4o	4+	3+	3+	6−	4−	29+	0o	1−	1+	2−	1−	1o	1o	1+	8−
23	4−	5−	1o	1o	1−	1−	1−	3−	15o	1−	0o	0+	1o	1+	0+	0+	0+	4+
24	3−	1+	3−	2+	3o	3o	3−	3−	20+	0o	0+	0+	1−	1o	1−	1−	1o	5−
25	2+	1+	2o	1o	1o	2+	2−	2−	13+	0+	1o	1o	1+	2−	2o	3o	3−	13o
26	1+	1o	1o	1o	1+	1−	0+	1−	7+	2−	1o	1−	1+	2+	3−	3−	2+	15−
27	0+	1o	0o	1−	1o	2−	4o	3o	12−	4−	4o	4−	3+	3−	3−	4−	3o	27−
28	3o	2−	2−	1o	1o	1o	1+	1+	12o	2+	2+	3+	2+	3−	2+	2o	3−	19+
29	2o	3+	3−	4−	3o	2o	1+	2o	20o	2+	1+	1−	1+	2o	1+	7−	6o	22−
30	1o	2o	2o	1+	1o	1−	2−	2o	12−	7−	6−	4+	4+	2o	5−	3o	1o	32−
31	2−	1+	2−	2o	2−	2−	1+	3o	14+	2o	3−	3−	2−	4o	5o	7o	5o	30o

	September 1957									Preliminary *C*, 1957			Average amplitude *Ap*		
E	1	2	3	4	5	6	7	8	Sum	July	Aug.	Sep.	July	Aug.	Sep.
1	6−	6−	4+	4−	3+	1+	2o	2+	28+	1.8	0.3	1.2	83	6	28
2	3−	6o	6+	5+	7o	6o	8−	8−	49−	1.5	0.7	1.8	55	9	102
3	7−	6+	6+	7+	8o	9−	6o	5−	54o	1.2	1.2	1.9	30	27	135
4	4−	5−	2+	3−	8+	9o	8o	8+	47o	0.8	0.9	1.9	12	12	145
5	8+	9−	7−	5o	5−	4o	5+	6o	49−	1.6	0.6	1.9	56	10	112
6	5−	5−	2+	5−	6−	5+	4+	2+	34o	0.9	1.3	1.3	16	31	36
7	3o	4−	2o	3o	2o	2+	2−	2o	20−	0.4	0.4	0.7	9	8	11
8	1+	1−	1+	2o	2+	2+	1o	3−	14−	0.6	0.4	0.3	9	7	7
9	3−	4−	4−	4−	3−	2o	2o	1−	21o	0.2	0.9	0.6	6	16	13
10	1o	1+	3−	2o	1+	3−	2+	2−	15o	0.1	0.5	0.4	4	9	8
11	1+	1o	2+	2o	1+	1+	2−	2−	13−	0.3	0.2	0.2	5	4	6
12	2−	2−	1+	2o	2o	2+	1+	3−	15o	0.5	1.1	0.4	9	19	7
13	8−	8+	9−	9−	7o	6o	4o	4o	54+	0.0	1.2	2.0	3	33	160
14	3o	3+	5+	6+	5+	4−	2+	4+	34−	0.2	0.5	1.3	6	8	38
15	4−	4+	2o	2o	2o	2+	3o	3o	22+	0.1	0.5	0.8	5	9	14
16	5−	4−	1+	2−	1+	1+	3−	2−	18+	0.9	0.2	0.7	16	5	12
17	2−	2o	2−	3−	4−	4−	3o	2−	20o	0.6	0.2	0.8	8	4	12
18	4−	3o	2−	1o	2o	3−	3o	3−	20−	0.8	0.5	0.5	13	7	12
19	1+	1+	1+	2−	2−	1o	0+	0+	9o	1.1	0.5	0.1	25	13	4
20	2−	0+	1+	2−	1o	2+	2+	2o	13−	0.7	0.7	0.3	11	10	6
21	3−	2−	1+	7+	6o	7−	7−	7−	39o	0.2	0.9	1.7	6	19	74
22	5−	6−	6−	5−	8o	8+	5o	7o	49o	1.1	0.2	1.9	26	4	104
23	8o	9−	8−	8−	8−	7−	7−	5o	58o	0.7	0.1	2.0	11	2	164
24	5o	5o	4+	5−	5+	3o	3+	2o	33−	0.7	0.0	1.2	12	3	33
25	4−	3o	5−	4o	4o	2−	1o	1+	23+	0.4	0.3	1.0	6	7	18
26	2−	3−	2o	3−	3−	2+	1+	1−	16o	0.1	0.4	0.4	4	8	8
27	0+	0+	2−	1o	1+	1+	1o	2−	9−	0.6	1.0	0.2	8	19	4
28	1+	4−	3o	1+	1o	1+	3o	1+	16o	0.2	0.6	0.3	6	10	10
29	4o	5+	5o	4+	8o	9−	8+	8o	52−	0.8	1.2	2.0	12	28	139
30	6+	6−	5+	6−	5o	5o	4o	5−	42−	0.2	1.3	1.7	5	38	56
31										0.3	1.3		7	36	

TABLE 1—(Concluded)—*Final selected days, July to September, 1957*

Month	Five quiet days	Ten quiet days	Five disturbed days
July	10 11 13 15 26	9 10 11 13 14 15 21 26 28 30	1 2 3 5 19
August	11 17 22 23 24	1 11 16 17 18 22 23 24 25 26	3 6 13 30 31
September	8 11 19 20 27	7 8 10 11 12 19 20 26 27 28	3 4 13 23 29

Ta.—03d 19h 03m: Cm IK.—03d 19h 50m: CF Pi.—03d 23h 37m: Wn Fu IK Eb.—03d 23h 56m: Wn Pr Eb Tl.—*04d 00h 05m*: eighteen.—04d 04h 44m: Qu Te Bi.—05d 17h 22m: Mb Ka Wa.—*05d 18h 29m*: six.—05d 23h 04m: Fu El Hr.—*05d 23h 26m*: seventeen.—06d 08h 19m: Te Pi.—*06d 19h 29m*: sixteen.—*06d 22h 07m*: five.—07d 08h 14m: Me Vi.—08d 06h 20m: YK Me Vi.—08d 23h 29m: Tr Eb El.—*09d 02h 03m*: six.—*09d 22h 17m*: thirteen.—*10d 01h 53m*: twelve.—12d 05h 42m: Vi Ag Te.—12d 12h 52m: Wn CF Hb.—13d 02h 22m: Vl CF Hr. 13d 10h 57m: Mb Ka To.—13d 11h 10m: Co Am.—13d 17h 30m: Mb IK Ka Wa.—13d 20h 08m: So Wn.—*13d 20h 45m*: twenty.—*15d 01h 53m*: eight.—15d 08h 00m: YK Me.—*15d 21h 41m*: eight.—15d 22h 06m: CF IK.—*18d 01h 40m*: fourteen.—*18d 02h 47m*: five.—19d 02h 02m: YK Ag.—19d 09h 55m: YK To.—20d 20h 53m: Sw Ba.—*20d 21h 52m*: nineteen.—21d 00h 09m: Vl Ta Bi.—*21d 02h 48m*: eight.—21d 03h 04m: Vi Te.—22d 08h 17m: YK Me.—*25d 18h 13m*: eleven.—25d 21h 05m: Ba Tn.—*25d 22h 29m*: five.—*27d 00h 08m*: seven.—27d 12h 31m: CF Ba.—*27d 20h 42m*: sixteen.—*28d 23h 04m*: thirteen.—30d 18h 06m: Vi CF.—*31d 00h 20m*: five.—31d 17h 01m: CF Qu.—*31d 13h 03m*: five (s.f.e.: Cm Hr).

1957 September 01d 04h 49m: Te Pi.—01d 05h 58m: YK Te Pi.—07d 04h 30m: Me Ag.—*08d 22h 33m*: twelve.—*09d 02h 12m*: five.—09d 05h 39m: YK Ag.—*09d 19h 10m*: six.—11d 06h 57m: Me Ag.—11d 22h 34m: Hb Eb.—12d 20h 38m: Tr Hb.—*14d 21h 29m*: six.—*14d 22h 31m*: fourteen.—*15d 17h 50m*: five.—*15d 21h 35m*: fifteen.—*16d 18h 12m*: nineteen.—16d 23h 16m: Wi Vl Cm.—18d 22h 00m: Me Vi.—*21d 00h 06m*: twelve.—*21d 00h 34m*: five.—21d 08h 38m: Si Me Vi.—22d 00h 29m: Cm Hr.—22d 10h 39m: Vi Am.—22d 21h 45m: Le Eb.—22d 23h 29m: Cm IK.—23d 20h 27m: Cm IK.—*24d 12h 37m*: six.—24d 19h 01m: Do Vl Db Pr.—25d 23h 17m: Cm Eb Bi El.—26d 04h 28m: Me Vi Ag Hu.—26d 08h 56m: Co Vi.—*28d 19h 10m*: seven.

Sudden impulses found in the magnetograms (s.i.)

1957 July *01d 18h 04m*: five.—*01d 18h 13m*: fourteen.—01d 21h 03m: Hb Ta.—03d 03h 08m: Hb SF.—03d 10h 12m: Cm Fu SF.—*11d 09h 44m*: eleven (s.f.e.: IK).—*19d 14h 57m*: sixteen.—22d 09h 46m: Ks Ta Pi.—23d 03h 41m: Ka Ta.—*23d 05h 00m*: five.—25d 15h 06m: Hb Qu Pi (s.f.e.: Sw Ta Hu).—*29d 06h 04m*: five.—*29d 10h 36m*: six.

1957 August 06d 07h 14m: Si Vi.—06d 11h 10m: Vi Ap Am.—08d 18h 41m: Cm Te.—*09d 06h 24m*: six.—09d 16h 42m: Hu Pi.—12d 04h 14m: Vl Ka Qu Hr (s.f.e.: To).—12d 10h 15m: Te Ba.—12d 11h 29m: CF El.—13d 07h 38m: Vl CF.—*17d 13h 22m*: twenty.—*17d 15h 07m*: seven (s.f.e.: Sw SJ Te Hu Pi).—*18d 10h 16m*: twenty-eight (s.f.e.: Sw).—18d 11h 05m: CF Ba.—25d 15h 05m: SF

Wa Pi Hr.—30d 10h 54m: CF Hb IK.—*30d 16h 28m*: thirty-five (s.f.e.: Ha Fr Tt Va).—31d 05h 55m: Vl CF Pi.—*31d 23h 30m*: five.

1957 September 02d 11h 45m: Cm Vi Te.—*02d 20h 10m*: five.—03d 02h 19m: Vl Cm Ha Ci.—03d 06h 19m: Mb Ka Te Tn?—03d 10h 48m: Wi Ha Ka Hr.—*03d 19h 12m*: eleven (s.f.e.: Fr Ta).—04d 14h 14m: Co YK Cm.—04d 17h 36m: YK Si.—*04d 21h 52m*: five.—05d 03h 35m: Fr Am.—05d 20h 41m: Hb Fr Ka.—06d 01h 17m: Mb Ka Ta.—06d 05h 00m: YK Me.—*07d 02h 32m*: eight.—07d 11h 04m: Me Cm SF (s.f.e.: Vl Ha?).—10d 17h 21m: Vl Mb Te Pi (s.f.e.: Ta).—14d 07h 06m: Cm Mb Ka.—14d 07h 29m: Co Si Me Vi.—*14d 13h 26m*: six.—17d 17h 30m: Hb Te.—*17d 23h 59m*: ten (s.f.e.: Ta).—*18d 04h 23m*: five.—23d 11h 23m: Wi Cm.—*24d 19h 51m*: five.—29d 13h 19m: Cm Fu.—29d 17h 15m: Cm IK.—29d 22h 36m: Vl Hr.—30d 02h 48m: Vl Pi.—*30d 07h 45m*: eleven.

Preliminary Report on Solar-flare Effects

Effects confirmed by ionospheric or solar observations are in italics.

1957 July 01d 19h 46m: Ta.—03d 14h 19m: Cm.—07d 12h 14m: Ks (s.i.: Hb).—08d 16h 25m–16h 36m: SM Tu Hu Pi.—*09d 19h 05m*: Hu.—10d 19h 28m:19h 48m: Es.—13d 18h 34m: Pi.—*16d 07h 31m–07h 54m*: Le Es (p.s.c.: IK Pi).—17d 11h 39m: Si (s.s.c.: YK).—*21d 06h 55m*: Me Cm Gi Ka.—21d 09h 25m: Ma Db.—*21d 13h 34m–13h 55m*: Es Wi Hr (p.s.c.: Ta).—21d 15h 32m–15h 38m: SM.—*24d 18h 00m*: Hu.—25d 15h 06m: Sw Ta Hu (s.i.: Hb Qu Pi).—26d 13h 53m: IK Pi.

1957 August 01d 12h 13m: IK? Eb? Ks (p.s.c.: Sw; s.i.: Hb).—*02d 14h 01m–14h 10m*: Es Vl Ha Eb Pr.—*02d 14h 35m–14h 50m*: Le Es Vl Ha Pr Eb.—*08d 11h 19m–12h 00m*: Wn Wi Cm Tn Hr (p.s.c.: IK Ta).—09d 13h 47m–14h 00m: Si Fr Tu Ta Hu (s.s.c.: forty-one).—*10d 01h 28m*: Am.—12d 08h 30m–10h 15m: El?—12d 11h 30m–12h 50m: El?—13d 17h 00m: Hu.—16d 20h 20m–21h 24m: SJ.—22d 11h 47m–12h 00m: Tn?—23d 09h 30m–09h 50m: Bi.—*23d 19h 02m*: Hu.—24d 17h 48m: Hu.—*24d 19h 26m*: Hu.—*25d 14h 19m*: Cm.—*25d 15h 06m*: Cm.—*28d 09h 22m–09h 30m*: Es.—*28d 20h 18m–20h 24m*: Fr Tu Hu.—*29d 13h 34m–13h 52m*: Wi.—*30d 13h 49m–13h 57m*: Es.—*30d 16h 47m–17h 00m*: Es.—*31d 13h 03m–14h 10m*: Cm Hr (p.s.c.: five).

1957 September *01d 09h 47m–09h 57m*: Es Wi Cm.—*01d 12h 04m–12h 12m*: Es.—05d 13h 51m: Va (s.s.c.: Le).—*06d 10h 33m–11h 00m*: Le.—*07d 08h 10m–08h 50m*: Le Es Wi Vl Cm Ha Eb Tl SF? Ks Tn Wa Hr (s.i.: IK Ba).—07d 10h 55m: Db Pi.—*08d 09h 35m*: IK Wa.—08d 15h 22m: Pi.—11d 16h 22m: Pi.—*12d 03h 35m–03h 50m*: Tn To.—*12d 07h 07m–07h 20m*: Wi Wa Hr.—*12d 15h 14m–15h 52m*: Le Es Wi Vl Cm Ha Db? Eb Ci Tl Fr Tu SJ Tt Hu Va Pi Hr (s.i.: Lg SF El; p.s.c.: Ag).—*12d 18h 38m*: Hu.—*15d 03h 30m*: Wa.—*15d 20h 41m*: Hu.—16d 08h 48m: IK.—*16d 15h 17m–15h 26m*: Es Wi Ha Fr Va (s.i.: Tl SF Tt Hu Hr; p.s.c.: Pi).—*16d 22h 44m*: Ap Am.—*17d 10h 40m–10h 55m*: Hr.—*17d 13h 31m*: Hu (p.s.c.: Am).—17d 18h 37m: Ta Te Hu.—*18d 06h 30m*: Wa To.—*18d 13h 00m–14h 30m*: Le Cm.—18d 17h 35m: Fr Ho Va Pi (s.i.: Te SJ Hu; p.s.c.: Vi Ag).—*19d 04h 01m*: Mb Ka Wa To.—*19d 08h 05m*: Wa.—20d 09h 03m–09h 25m: IK Tl Ks Tn (s.i.: CM Ba Hr).—*22d 12h 55m–13h 05m*: Es.—27d 08h 00m–08h 26m: El Tn (s.i.: Ba Hr).

Ionospheric or solar disturbances without clear geomagnetic effect

1957 July: None.

1957 August: None

1957 September: None

Minor disturbances reported by one station only are listed in the De Bilt quarterly circular, but omitted here.

TABLE 2—*Monthly mean values of Ci, Cp, and Ap, July to September, 1957*

Index	July 1957	August 1957	September 1957
Mean *Ci*	0.63	0.65	1.05
Mean *Cp*	0.64	0.63	1.08
Mean *Ap*	16	14	49

September 1957, with its high average Zürich relative sunspot-number 244, provided also a record in magnetic activity—six heavy storms with sudden commencements occurred. The monthly average of the daily planetary amplitudes, *Ap*, in the usual unit 2γ, was 49. The next highest monthly averages in the available series (1932, 33, and 1937 to date) were 40 (Sept. 1951) and 37 (March 1940). September had three days with $Cp = 2.0$, and five days with $Cp = 1.9$. September 4 brought one of the rare $Kp = 9_0$ (the five preceding cases of 9_0 occurred 1941 March 1, July 5, and Sept. 19, and 1946 July 27 and Sept. 22). The number of three-hour-intervals with high *Kp*-indices in the six months named were

	Number of intervals with $Kp =$	9_0	9−	8+
1941 March		1	2	...
1941 July		1	3	...
1941 September		1	7	1
1946 July		1	3	...
1946 September		1	1	2
1957 September		1	6	6

COMMITTEE ON RAPID VARIATIONS AND EARTH CURRENTS

A. ROMAÑÁ, *Chairman*, Observatorio del Ebro, Tortosa, Spain

COMMITTEE ON CHARACTERIZATION OF MAGNETIC DISTURBANCES

J. BARTELS, *Chairman*
University
Göttingen, Germany

J. VELDKAMP
Kon. Nederlandsch Meteorologisch Instituut
De Bilt, Holland

PROVISIONAL SUNSPOT-NUMBERS FOR OCTOBER TO DECEMBER, 1957

(Dependent on observations at Zurich Observatory and its stations at Locarno and Arosa)

Day	Oct.	Nov.	Dec.
1	244	265	216
2	240	256	206
3	249	230	218
4	233	210	225
5	230	200	258
6	239	180	220
7	224	175	164
8	250	155	187
9	274	190	137
10	270	230	143
11	220	224	150
12	260	220	153
13	246	185	155
14	258	180	164
15	250	177	170
16	289	180	189
17	268	191	205
18	228	225	227
19	223	183	249
20	235	208	284
21	250	235	298
22	255	275	302
23	260	250	330
24	285	236	345
25	247	200	357
26	310	198	366
27	286	171	269
28	340	235	260
29	350	192	275
30	330	162	274
31	306		255
Means.....	262.9	207.3	233.9
No. days.....	31	30	31

Mean for quarter: 235.0 (92 days)
Mean for year 1957: 190.1 (365 days)

M. Waldmeier
Observer-in-charge

Swiss Federal Observatory
Zurich, Switzerland

FREDERICKSBURG THREE-HOUR-RANGE INDICES K FOR OCTOBER TO DECEMBER, 1957

[$K9 = 500\gamma$; scale-values of variometers in γ/mm: $D = 2.7$; $H = 2.5$; $Z = 2.8$]

Gr. day	October 1957		November 1957		December 1957	
	Values K	Sum	Values K	Sum	Values K	Sum
1	5422 3333	25	1222 2222	15	4443 3233	26
2	4411 2323	20	1122 2123	14	3334 3322	23
3	2212 3433	20	3133 3211	17	2233 3221	18
4	2322 2323	19	1000 0111	4	2133 2211	15
5	3311 2223	17	0101 1122	8	3333 3343	25
6	1010 0011	4	0011 2355	17	2435 4432	27
7	1222 2132	15	5333 2221	21	2253 5223	24
8	2001 0011	5	1234 3323	21	2333 2222	19
9	1221 3232	16	3342 3333	24	2223 3333	21
10	3353 2223	23	4334 3332	25	3334 3334	26
11	3444 4222	25	3433 3224	24	3554 4344	32
12	2234 2113	18	4223 3322	21	4434 3433	28
13	5432 2233	24	3122 2223	17	3425 3432	26
14	5554 4345	35	3233 4433	25	3221 2122	15
15	3211 3221	15	3343 3332	24	3333 4432	25
16	0001 1121	6	3212 3221	16	2223 3233	20
17	1112 3222	14	1111 1013	9	3333 3333	24
18	1221 1131	12	3334 4333	26	3223 2222	18
19	1222 2222	15	1222 2112	13	3334 3333	25
20	2212 2324	18	2212 3221	15	2332 3343	23
21	3221 3446	25	1010 1121	7	2332 2221	17
22	3223 2333	21	1110 2221	10	3110 0010	6
23	5233 1233	22	1111 3223	14	1100 1100	4
24	1122 2231	14	2222 3332	19	0112 2222	12
25	2113 2122	14	3254 3333	26	1332 3233	20
26	3112 2122	14	3443 5655	35	2424 3332	23
27	1212 4323	18	5644 2333	30	2110 2222	12
28	4132 2222	18	3344 3332	25	1110 1112	8
29	3232 4234	23	3322 2322	19	0111 2122	10
30	2332 2221	17	2222 3221	16	3234 3322	22
31	0112 3122	12			3356 4334	31

Robert E. Gebhardt
Observer-in-Charge

Fredericksburg Magnetic Observatory
Corbin, Virginia, U. S. A.

PRINCIPAL MAGNETIC STORMS

(Advance knowledge of the character of the records at some observatories as regards disturbances)

ıservatory Observer- -Charge)	Green-wich date	Storm-time GMT of begin.	Storm-time GMT of ending[1]	Sudden commencement Type[2]	Amplitudes[3] D	H	Z	C-figure, degree of activity[4]	Maximal activity on K-scale 0 to 9 Gr. day	Gr. 3-hr. period	K-index	Ranges D	H	Z
(1)	(2)	(3)	(4)	(5)	(6)	(7)	(8)	(9)	(10)	(11)	(12)	(13)	(14)	(15)
	1957	*h m*	*d h*		′	γ	γ					′	γ	γ
ege	Oct. 14	04 00	15 01	.....	.....	.....	.....	ms	14	2	7	180	1040	810
J. Beers)	Nov. 6	18 22	7 21	s.c.*	−29	+255	−27	m	6	7,8	5	115	740	390
									7	4,5,6	5			
	Nov. 8	07 00	12 20	.....	.....	.....	.....	ms	8	4,5	6	190	1000	620
									9	5	6			
	Nov. 24	16 00	28 21	.....	.....	.....	.....	ms	26	6	7	300	1980	1090
	Dec. 1	02 30	2 21	.....	.....	.....	.....	ms	2	4	6	170	1020	510
	Dec. 5	07 00	6 23	.....	.....	.....	.....	ms	6	6	7	300	1180	750
	Dec. 11	03 00	13 22	.....	.....	.....	.....	ms	11	6	6	230	1330	680
									12	4,6	6			
									13	4,6	6			
	Dec. 15	08 00	15 21	.....	.....	.....	.....	ms	15	6	7	130	1000	630
	Dec. 31	03 00	2 22	.....	.....	.....	.....	s	31	3	8	280	1900	1090
a	Oct. 10	03 ..	10 19	.....	.....	.....	.....	m	10	2,4,5	5	48	233	314
L. Bottum)	Oct. 11	05 ..	11 17	.....	.....	.....	.....	ms	11	4	7	64	677	354
	Oct. 14	01 ..	15 01	.....	.....	.....	.....	ms	14	4	7	89	873	474
	Nov. 3	06 22	3 22	s.c.*	+1	−9	0	m	3	4,5	5	37	262	288
	Nov. 6	18 21	7 20	s.c.*	+33	+50	−41	ms	7	1	6	66	373	298
	Nov. 8	05 ..	12 00	.....	.....	.....	.....	ms	8	4,5	6	46	334	450
									9	5	6			
	Nov. 12	08 ..	12 19	.....	.....	.....	.....	m	12	4,5	5	54	241	261
	Nov. 18	02 ..	18 20	.....	.....	.....	.....	ms	18	4,5,6	6	68	520	468
	Nov. 25	05 ..	28 21	.....	.....	.....	.....	ms	26	6	7	107	845	680
									27	3,4	7			
	Dec. 1	02 33	1 23	s.c.*	−3	+14	0	m	1	3	5	33	325	251
	Dec. 2	06 ..	2 21	.....	.....	.....	.....	m	2	4,5,6	5	39	272	255
	Dec. 5	04 ..	6 21	.....	.....	.....	.....	ms	6	4	6	47	477	326
	Dec. 7	07 ..	8 00	.....	.....	.....	.....	ms	7	5	7	54	554	411
	Dec. 10	08 ..	10 20	.....	.....	.....	.....	ms	10	6	6	46	260	340
	Dec. 11	03 ..	13 02	.....	.....	.....	.....	ms	11	3	6	46	473	447
									12	4	6			
	Dec. 13	09 ..	13 22	.....	.....	.....	.....	ms	13	4,6	6	38	255	264
	Dec. 15	08 ..	15 20	.....	.....	.....	.....	ms	15	5,6	6	45	281	365
	Dec. 30	04 10	30 21	s.c.	−2	+6	+2	ms	30	4,5	7	71	647	366
	Dec. 31	01 17	2 21	s.c.	+2	−9	−8	s	31	3,4,5	8	157	1309	861
teveen	Oct. 13	20 00	15 01	.....	.....	.....	.....	ms	14	2	6	35	145	105
van Sabben)	Oct. 21	20 00	22 11	.....	.....	.....	.....	ms	21	8	7	20	215	40
	Nov. 6	18 22	7 12	s.c.	−5	+90	−3	ms	7	1	7	30	290	140
	Nov. 26	14 00	27 24	.....	.....	.....	.....	ms	26	6,7	7	60	300	155
	Dec. 10	15 00	12 24	.....	.....	.....	.....	ms	11	8	6	30	160	80
	Dec. 31	01 00	1 10	.....	.....	.....	.....	ms	31	6,7,8	6	40	210	120
									1	1	6			
dericksburg	Oct. 14	01 ..	15 02	.....	.....	.....	.....	m	14	1,2,3,8	5	30	115	128
E.Gebhardt)	Oct. 21	22 41	23 02	s.c.*	+9	+116	−14	ms	21	8	6	20	119	95
	Nov. 6	18 21	7 12	s.c.*	+4	+68	+22	m	6	7,8	5	26	182	87
									7	1	5			
	Nov. 26	14 ..	27 12	.....	.....	.....	.....	ms	26	6	6	36	178	94
									27	2	6			
	Dec. 11	03 ..	13 22	.....	.....	.....	.....	m	11	2,3	5	31	127	59
									13	4	5			
	Dec. 31	02 ..	2 13	.....	.....	.....	.....	ms	1	1	6	26	134	127

[1]Approximate time of ending of storm construed as the time of cessation of reasonably marked disturbance movements in the ces; more specifically, when the *K*-index measure diminished to 2 or less for a reasonable period.

[2]s.c. = sudden commencement; s.c.* = small initial impulse followed by main impulse (the amplitude in this case is that of the *in impulse only*, neglecting the initial brief pulse; . . . = gradual commencement.

[3]Signs of amplitudes of *D* and *Z* taken algebraically; *D* reckoned positive if towards the east and *Z* reckoned positive if verti- y downwards.

[4]Storm described by three degrees of activity: *m* for moderate (when *K*-index as great as 5); *ms* moderately severe (when = 6 or 7); *s* for severe (when *K* = 8 or 9).

PRINCIPAL MAGNETIC STORMS—Continued

Observatory (Observer-in-Charge)	Greenwich date	Storm-time GMT of begin.	Storm-time GMT of ending[1]	Sudden commencement Type[2]	Amplitudes[3] D	H	Z	C-figure, degree of activity[4]	Maximal activity on K-scale 0 to 9 Gr. day	Gr. 3-hr. period	K-index	Ranges D	H
(1)	(2)	(3)	(4)	(5)	(6)	(7)	(8)	(9)	(10)	(11)	(12)	(13)	(14)
	1957	h m	d h		′	γ	γ					′	γ
Tucson	Oct. 13	15 30	15 03	.....	.....	.....	.....	m	14	2,3,5,6	5	15	120
(R. F. White)	Oct. 21	14 59	24 00	.....	.....	.....	.....						
		22 41	.. ..	s.i.	−5	+79	+3	ms	21	8	6	16	105
	Nov. 6	18 21	7 15	s.c.	−2	+30	+2	m	6	7,8	5	11	203
									7	1	5		
	Nov. 24	14 ..	29 06	.....	.....	.....	.....	ms	26	6,8	6	20	159
	Nov. 26	14 54	.. ..	s.i.	+3	−36	....	...	..	...	...	.....	.....
	Dec. 7	07 00	8 00	.....	.....	.....	.....	m	7	3,5	5	13	79
	Dec. 10	21 ..	13 03	.....	.....	.....	.....	m	11	2,3	5	14	121
	Dec. 31	01 15	2 15	.....	.....	.....	.....	ms	31	3	6	15	140
San Juan	Oct.	None											
(M. Vazquez)	Nov. 6	18 22	7 10	s.c.	+1	+30	−11	ms	6	7	7	7	215
	Nov. 24	12 30	27 22	.....	.....	.....	.....	m	26	6	6	12	177
	Dec.	None											
Honolulu	Oct.	None											
(M. L. Cleven)	Nov. 6	18 21	7 14	s.c.*	−	+	+	ms	6	8	6	7	190
	Dec.	None											
Vassouras	July	None											
(Lelio I.	Aug. 29	19 22	30 06	s.c.	+4	52	+13	m	29	7	5	11	236
Gama)	Sep. 2	03 15	4 06	s.c.	+1	12	+9	ms	3	5	6	24	345
	Sep. 4	13 00	6 04	s.c.*	+2	75	+22	ms	4	6	6	38	562
	Sep. 13	00 46	14 16	s.c.	+4	83	+24	ms	13	4	6	26	454
	Sep. 22	13 44	24 17	s.c.	+3	52	+14	ms	22	5,6	6	22	364
	Sep. 29	00 15	1 05	s.c.	+1	20	+8	ms	29	6	6	24	474
Elisabethville/ Karavia (A. Alexandre)	Oct.	Pas d'orage important											
	Nov.	Pas d'orage important											
	Dec.	Pas d'orage important											
Apia	Sep. 29	00 16	3 24	s.c.	−0	+20	−8	ms	29	5,6,7	6	8	305
(J. G. Keys)	Oct. 14	04 40	15 01	s.c.	+0	+6	−3	m	14	3	5	7	124
	Oct. 20	20 ..	23 24	.....	.....	.....	.....	ms	21	8	6	10	160
	Oct. 27	06 ..	30 18	.....	.....	.....	.....	m	28	1	5	10	134
									29	1	5		
	Nov. 5	18 21	7 14	s.c.	+0	+31	+4	ms	6	8	6	14	152
	Nov. 13	20 ..	16 21	.....	.....	.....	.....	m	14	1	5	7	108
	Nov. 17	22 ..	20 14	.....	.....	.....	.....	m	18	5	5	8	106
	Nov. 26	01 54	30 03	.....	.....	.....	.....	m	26	3,8	5	11	169
									27	2,3,5	5		
	Dec. 1	03 26	3 20	.....	.....	.....	.....	m	1	2,3	5	8	107
	Dec. 28	22 29	2 13	s.c.	0	+8	−3	m	30	3	5	11	244
									31	3,4	5		
Hermanus	Oct. 1	18 ..	1 23	Bay	....	.....	.....	m	1	7	5	.....	.....
(A. M.	Oct. 14	04 40	15 01	s.c.?	0	+7	+2	m	14	2,4,5,8	5	25	98
van Wijk)	Oct. 21	22 41	23 11	s.c.	+5	+94	+66	ms	21	8	6	25	114
	Nov. 6	18 21	7 15	s.c.	+5	+46	+35	ms	6	7	7	30	151
	Nov. 25	01 ..	29 08	.....	.....	.....	.....	ms	26	6,7	6	32	192
	Dec. 1	01 ..	1 12	.....	.....	.....	.....	m	1	2	5	20	135
	Dec. 5	00 ..	6 20	.....	.....	.....	.....	m	5	8	5	23	116
									6	2	5		
	Dec. 7	02 ..	7 15	.....	.....	.....	.....	m	7	5	5	31	90
	Dec. 10	08 ..	13 19	.....	.....	.....	.....	m	10	5	5	37	129
									11	2-5,7,8	5		
	Dec. 15	05 ..	15 20	.....	.....	.....	.....		13	4	5		
	Dec. 19	09 37	21 10	s.c.	+1	+20	+16	m	15	5	5	21	79
	Dec. 25	02 ..	26 20	.....	.....	.....	.....	m	19	7	5	25	76
	Dec. 30	05 ..	30 14	.....	.....	.....	.....	m	26	4,5	5	26	126
	Dec. 31	01 ..	2 14	.....	.....	.....	.....	m	30	4	6	27	117
								m	31	2,3,4	5	37	183

PRINCIPAL MAGNETIC STORMS—Continued

Observatory (Observer-in-Charge)	Greenwich date	Storm-time GMT of begin.	Storm-time GMT of ending[1]	Sudden commencement Type[2]	Sudden commencement Amplitudes[3] D	H	Z	C-figure, degree of activity[4]	Maximal activity on K-scale 0 to 9 Gr. day	Gr. 3-hr. period	K-index	Ranges D	H	Z
(1)	(2)	(3)	(4)	(5)	(6)	(7)	(8)	(9)	(10)	(11)	(12)	(13)	(14)	(15)
	1957	*h m*	*d h*		′	γ	γ					′	γ	γ
ıza	July 2	09 00	2 20	s.c.	−12	+47	−4	m	2	4	...	4	192	32
. Leroy and Dodson)	Aug. 3	15 58	3 24	s.c.	−2	+42	−4	m	3	6,7	...	3	141	8
	Aug. 29	19 21	29 24	s.c.	−1	+71	−1	m	29	7,8	...	5	187	13
	Sep. 2	03 19	3 24	s.c.	−1	+26	−2	ms	2	8,1	...	8	264	18
	Sep. 4	13 05	5 24	s.c.	−1	+26	−3	m	4	6,7	...	8	528	26
	Sep. 6	11 25	6 24	s.c.	−1	+22	−2	m	6	5	...	9	64	29
	Sep. 13	00 48	13 20	s.c.	−1	+94	−4	m	13	3,4	...	10	511	32
	Sep. 21	10 09	21 24	s.c.	−3	+101	−9	ms	21	5,6	...	6	494	39
	Sep. 22	13 48	23 24	s.c.	−1	+22	−3	m	22	6	...	13	251	21
	Sep. 29	00 17	30 24	s.c.	−	+18	−2	ms	29	5	...	9	558	26
	Oct. 14	04 43	14 24	s.c.	+2	+10	+4	m	14	5,6	...	5	176	15
	Oct. 21	22 42	22 24	s.c.	+2	+10	−4	m	22	8,1	...	10	167	33
	Nov. 6	18 24	7 12	s.c.	+2	+64	−5	ms	7	7,8	...	9	246	34
	Nov. 24	09 04	25 24	s.c.	+	+25	−2	m	25	5	...	8	233	62
	Nov. 26	01 59	27 24	s.c.	+	+50	−1	ms	26	6,7	...	9	198	49
	Dec. 1	03 39	1 12	s.c.	+	+25	−1	m	1	2,3	...	10	129	42
	Dec. 19	09 50	19 24	s.c.	+1	+34	−2	m	19	4	...	4	198	29
olangi B. Everingham)	Sep. 29	00 17	1 09	s.c.*	−4	+23	+6	ms	29	6	7	36	382	159
	Nov. 6	18 21	7 18	s.c.	−4	+54	−4	m	6	7,8	5	24	230	35
									7	1	5			
	Nov. 23	23 16	30 09	.....	.....	.....	.....	ms	25	2	6	36	237	117
									26	2,3,6,8	6			
	Dec. 1	03 36	3 10	s.c.*	+1	+32	0	ms	3	3	6	8	118	32
	Dec. 11	.. ..	14 08	.....	.....	.....	.....	...	..	....	...	.....	.....	....
	(*Note:* Storm in progress at $05^h\ 30^m$; no record for beginning of storm)													
	Dec. 15	00 48	18 12	s.c.	+1	+5	0	m	15	3,5	5	24	132	50
									17	3,7	5			
	Dec. 19	09 36	21 10	s.c.	−1	+41	+4	m	19	4,7	5	28	136	55
									20	2	5			
									21	2,3	5			
	Dec. 29	20 40	30 14	.....	.....	.....	.....	ms	30	3	6	11	159	49
	Dec. 31	01 17	.. ..	s.c.	+1	−3	0	...	..	....	...	.....	.....	....
	(*Note:* Storm in progress at $24^h\ 00^m$)													
nberley L. Cullington)	Oct. 14	04 41	15 02	s.c.	1	25	−8	m	14	3	5	22	126	107
	Nov. 6	18 21	7 15	s.c.*	−8	−49	+29	m	6	7,8	5	28	163	61
	Nov. 17	22 00	19 17	.....	.....	.....	.....	m	18	5	5	16	110	54
	Nov. 23	22 00	28 23	.....	.....	.....	.....	ms	26	2,7	6	33	270	157
	Nov. 29	02 26	30 10	s.c.*	1	39	−4	m	29	2	5	16	123	27
	Dec. 1	01 00	3 21	.....	.....	.....	.....	m	1	2,3	5	20	198	35
	Dec. 5	12 00	14 12	.....	.....	.....	.....	m	7	5	5	29	195	86
									11	2,3,7,8	5			
	Dec. 15	22 00	21 18	.....	.....	.....	.....	m	17	2,3	5	24	194	83
									20	2	5			
	Dec. 24	17 00	27 09	.....	.....	.....	.....	m	25	2,3	5	22	189	63
	Dec. 29	20 00	.. ..	.....	.....	.....	.....	ms	31	4	6	24	300	177
	(*Note:* Storm continuing at end of month)													

PRINCIPAL MAGNETIC STORMS—Concluded

Observatory (Observer-in-Charge)	Greenwich date	Storm-time GMT of begin.	Storm-time GMT of ending[1]	Sudden commencement Type[2]	Amplitudes[3] D	H	Z	C-figure, degree of activity[4]	Maximal activity on K-scale 0 to 9 Gr. day	Gr. 3-hr. period	K-index	Ranges D	H	
(1)	(2)	(3)	(4)	(5)	(6)	(7)	(8)	(9)	(10)	(11)	(12)	(13)	(14)	(
	1957	*h m*	*d h*		′	γ	γ					′	γ	
				Additional reports received later										
Instituto	July 2	08 57	3 15	s.c.	0	+29	+7	ms	3	5	6	7	188	
Geofisico de	July 5	00 43	5 13	s.c.	0	+41	+7	m	5	2	5	(6)	177	(
Huancayo	Aug. 3	15 57	4 02	s.c.	−1	+199	+12	ms	3	6	7	10	471	
(A.A.Giesecke,	Aug. 29	19 21	30 20	s.c.	1	+111	+17	ms	29	7,8	6	3	445	
Jr., and	Aug. 31	13 05	1 20	.....	.....	.....	.....	ms	31	7	6	8	371	
M. Casaverde)	Sep. 2	03 14	4 06	s.c.	0	+36	+5	ms	3	6,7	7	18	830	1
				(*Note: H* range from *H* insensitive trace)										
	Sep. 4	13 00	6 04	s.c.	−1	+115	+7	s	4	6,7	8	20	993	
				(*Note: H* range from *H* insensitive trace)										
	Sep. 6	11 22	7 05	.....	.....	.....	.....	ms	6	6	7	11	275	
	Sep. 13	00 44	14 16	s.c.	0	+106	+17	ms	13	1,3,5	7	21	550	
				(*Note: H* range from *H* insensitive trace)										
	Sep. 21	10 05	. . . .	s.c.	0	66	12	s	22	6	8	13	753	
				(*Note: H* range from *H* insensitive trace)										
	Sep. 23	02 35	24 22	s.c.	+2	+160	+17	ms	23	2	7	9	582	
				(*Note:* Superimposed storm; *H* range from *H* insensitive trace)										
	Sep. 29	00 14	1 21	s.c.	0	+33	+5	s	29	6	9	23	841	
				(*Note: H* range from *H* insensitive trace)										
	Oct. 14	04 38	15 01	.....	.....	.....	.....	s	14	6	8	11	467	
	Oct. 21	22 40	22 22	s.c.	−2	+134	+17	ms	22	6,7	6	9	316	
	Oct. 29	08 10	29 23	.....	.....	.....	.....	m	29	6,7	5	7	351	
	Nov. 6	18 21	7 20	s.c.	−7	+355	+20	ms	6	7	7	10	612	
	Nov. 9	10 40	10 22	.....	.....	.....	.....	ms	9	6	6	9	431	
	Nov. 14	00 08	14 23	.....	.....	.....	.....	ms	14	6	7	9	416	
	Nov. 18	06 15	18 23	.....	.....	.....	.....	ms	18	7	6	10	199	
	Nov. 24	09 00	25 23	.....	.....	.....	.....	ms	25	6,7	6	11	411	
	Nov. 26	01 54	27 22	s.c.	0	+34	+4	s	26	6,7	8	16	609	
	Dec. 1	03 27	1 21	.....	.....	.....	.....	m	1	5	5	7	297	
	Dec. 5	03 30	5 22	s.c.	0	+16	+3	ms	5	6,7	6	9	276	
	Dec. 11	06 50	12 22	.....	.....	.....	.....	ms	11	5	7	9	457	
	Dec. 15	11 35	15 20	.....	.....	.....	.....	ms	15	5,6	7	8	335	
	Dec. 19	09 37	20 23	s.c.	−1	+33	+5	ms	19	6,7	6	12	332	
	Dec. 26	09 35	26 20	.....	.....	.....	.....	ms	26	5,6	6	8	260	
	Dec. 31	02 00	1 21	.....	.....	.....	.....	ms	31	6	6	16	408	
Watheroo	Oct. 14	04 40	15 02	s.c.	0	+15	0	m	14	2,4,6	5	18	90	1
(P. McGregor)	Nov. 6	18 21	7 10	s.c.*	+4	+52	+29	ms	6	8	7	33	153	1
	Nov. 25	02 00	27 22	.....	.....	.....	.....	ms	26	3,6	6	23	189	1
	Dec.	None												

NOTES

(1) *New officers of the I.U.G.G.*—At the Eleventh General Assembly of the International Union of Geodesy and Geophysics, held at Toronto, Canada, September 3-14, 1957, the following officers and members of the Bureau of the Union were elected for the next three years: J. Tuzo Wilson (Canada), President; V. V. Beloussov (U.S.S.R.), Vice-President; W. A. Heiskanan (Finland), Vice-President; Colonel G. Laclavère (France), General Secretary; C. E. R. Deacon (United Kingdom), Member-at-large; J. W. Joyce (United States), Member-at-large; and C. Tsuboi (Japan), Member-at-large.

(2) *Radio propagation transmitting station WWI established near Havana, Illinois*—The National Bureau of Standards has announced that this new station is intended to provide experimental and observatory-type transmissions for radio wave propagation studies and research and development on radio systems. The Illinois location was chosen to be roughly central between Boulder, Colorado, and the U. S. east coast, and to provide an east-west transmission path from Boulder, approximately 800 miles in length. While mainly intended for use in VHF transmission research programs of the Central Radio Propagation Laboratory, with transmission directed toward Boulder, the facilities are available to provide experimental radio transmissions on behalf of other governmental agencies or their contractors, to the extent that suitable operating arrangements can be made. It is hoped that regular transmissions in the HF band can be arranged by July 1, 1958.

(3) *Carnegie Institution of Washington to install radio telescope*—A radio telescope, designed to measure the hydrogen clouds between the stars of our galaxy, will be installed this spring at one of the Carnegie Institution of Washington research stations in Maryland, a few miles northwest of Washington, D. C. It is expected to be in operation this summer.

(4) *Proposed radio telescope at University of Michigan*—An 85-foot radio telescope that will follow the sun across the sky by day and receive signals from outer space at night will be erected in June 1958 by the University of Michigan at Peach Mountain, 16 miles from Ann Arbor, Michigan. It will work at wavelengths five to ten times shorter than the world's largest "dish"—a 250-foot unit at Jodrell Bank, Manchester, England. The proposed solid aluminum surface of the "dish" will give good reflection of signals at all wavelengths.

(5) *Kiruna Geophysical Observatory*—During the past summer of 1957, the Kiruna Geophysical Observatory of the Royal Swedish Academy of Science was dedicated. This new observatory in northern Sweden will enable geophysicists interested in arctic phenomena to carry on research under the most favorable conditions. The location of the observatory is particularly significant with respect to the Geophysical Institute in Fairbanks, Alaska, because the two observatories are approximately 180° apart in longitude. This circumstance will make it possible for the two laboratories to undertake certain important types of transpolar research projects on a cooperative basis. Coordinates for Kiruna are as follows: Geographic coordinates, 67.8° north, 20.4° east; geomagnetic coordinates, 65.3°

north, 115.5° east. A grant from the U. S. National Science Foundation has helped to equip the observatory with good basic instrumentation. All proposals for cooperative activities should be addressed to the Director, Kiruna Geophysical Observatory, Kiruna, Sweden.

(6) *Sun photographs from high altitude*—The first photographs of the sun, from an unmanned balloon at an altitude of 80,000 feet, were recently reported by Dr. Martin Schwarzschild and Dr. John B. Rogerson, Jr., of the Princeton University Observatory, and Dr. J. W. Evans, director of the Sacramento Peak Observatory. The photographs were made through a self-aiming twelve-inch telescope at the 80,000-foot altitude, where the field of view is virtually undisturbed by the earth's atmosphere. On future flights, the astronomers plan to send aloft a television camera with the telescope, so that they will be able to make direct observations. By late 1960 or early 1961, they plan to send a 36-inch telescope to a high altitude for study of the planets as well as the sun.

(7) *Publication of proceedings of Symposium on Radio Astronomy, Sydney*—This symposium, under the auspices of the C.S.I.R.O. Radiophysics Laboratory, was held at Sydney, Australia, in September 1956. The printed 85-page publication contains the Chairman's (Dr. F. W. G. White) address, summaries of radio astronomy research in Australia (Dr. J. L. Pawsey) and in the United States (Prof. Bart J. Bok), and outline of possible future work (Prof. Bart J. Bok). Also included are summaries of the 16 papers delivered at the symposium on (1) The solar system, (2) continuous cosmic radio emission, and (3) structure and shape of galaxies.

(8) *Geomagnetic activities of the United States Coast and Geodetic Survey*—Mr. J. B. Campbell, IGY Operations Officer, inspected the magnetic installations at Little America, Guam, and Koror. He also visited the observatories at Amberley, New Zealand, and Muntinlupa, Philippines.

Messrs. A. J. Bilik and R. J. Puhl are making magnetic surveys of repeat stations in southwestern and southeastern United States, respectively.

Two volumes of the MHV series of publications were issued, giving magnetic hourly values and reproductions of magnetograms for 1952 for College and San Juan.

Messrs. J. Annexstad, J. Gniewek, and S. Borrello arrived in Antarctica to relieve Messrs. R. L. Viets, R. Berkley, and L. Davis, who have been operating the stations at Little America, Byrd, and Wilkes, respectively.

Mr. R. Barela has become Observer-in-Charge at Barrow Observatory, Alaska.

(9) *Spring meeting of URSI*—The spring meeting of the International Scientific Radio Union (URSI) is scheduled this year for the Hotel Willard in Washington, D. C., on April 23-26, 1958. The co-sponsors this year will include the IRE Professional Groups on Antennas and Propagation, on Circuit Theory, on Instrumentation, and on Microwave Theory and Techniques. A combined technical session of interest to all participants is scheduled for April 23, to be followed by sessions in each of the following fields: Commission 1—Radio Measurement Methods and Standards; Commission 2—Tropospheric Radio Propagation; Commission 3—Ionospheric Radio Propagation; Commission 4—Radio Noise of Terrestrial Origin; Commission 5—Radio Astronomy; Commission 6—Radio Waves and Circuits; and Commission 7—Radio Electronics.

(10) *Max Planck-Institut für Aeronomie*—This is the new name adopted for

the combination of the Institut für Stratosphären-Physik (founded by Erich Regener) and the Institut für Ionosphären-Physik, both at Lindau/Harz, via Northeim, Germany.

(11) *Successful launching of a United States satellite*—On Friday night (10:49 p.m.), January 31, 1958, the Army's Jupiter-C rocket was successfully fired at Cape Canaveral, Florida, hurling a satellite some 2,000 miles into outer space and into orbit near the middle of our earth. The satellite has been designated "1958 Alpha" and has been named the "Explorer." Its speed is around 19,000 miles per hour, encircling the globe in approximately 115 minutes, or about 12 times a day. The United States expects to launch additional satellites soon.

(12) *Post-shot yield measurement of AEC underground nuclear test*—The Atomic Energy Commission has reported the resultant yield of the deep underground nuclear test conducted at the AEC Nevada Test Site in September 1957 as 1.7 kilotons. The shot was detonated at 09 hours 59 minutes 59.45 seconds Pacific Daylight Time (16:59:59.45 GCT) on September 19, 1957, at the end of a tunnel about 2,000 feet long, dug horizontally into the side of a mesa at the northern edge of the Yucca Basin. The explosion took place in a layer of volcanic tuff. The coordinates of the detonation point are: latitude 37 degrees 11 minutes and 44.8 seconds, longitude 116 degrees 12 minutes and 11.3 seconds, elevation 6,615 feet above mean sea-level. The vertical distance from the detonation point to the mesa surface is 899 feet, and the slant distance to the side of the mean is approximately 800 feet.

(13) *Personalia*—Dr. *F. J. Kerr*, senior research officer, Division of Radiophysics, Commonwealth Scientific and Industrial Research Organization, Sydney, Australia, arrived in the United States on December 7, 1957. During his stay in this country, he visited the observatories at Harvard University, California Institute of Technology, and in Washington, D. C., studied the present state of hydrogen-line radio astronomy.

Dr. *J. L. Pawsey*, assistant chief of the Radiophysics Division, C.S.I.R.O., Sydney, Australia, also visited various laboratories in the United States, and talked on "Recent developments in radio astronomy in Australia," at an Atmosphere and Astrophysics Seminar at the Naval Research Laboratory, Washington, D, C., on January 15, 1958.

Mr. *McClain B. Smith*, Chief of the Administrative and Operating Section, Department of Terrestrial Magnetism, Carnegie Institution of Washington, retired at the end of 1957. His continuous noteworthy service dated from September 16, 1916.

Dr. *Roy W. Goranson* died on December 25, 1957, at Danville, California, at the age of 57. At the time of his death, he was a member of the staff at the University of California Radiation Laboratory in Livermore, California. From 1926 to 1943, Dr. Goranson was physical geologist with the Geophysical Laboratory, of the Carnegie Institution of Washington, and there in 1937-1940 he devised and built equipment which developed three million pounds of pressure per square inch, probably the highest pressure achieved up to that time. He worked in the Office of Science, Research and Development, the Atomic Energy Commission, and at the AEC's Los Alamos laboratories before joining the University staff.

Dr. *Charles F. Brooks*, professor *emeritus* of meteorology and former director

of the Blue Hill Meteorological Observatory, Harvard University, died on January 10, 1958, at the age of 66. He was a noted authority on many subjects, such as meteorological apparatus, eclipse meteorology, snowfall, clouds, climatology of North America, physiological aspects of climates, and weather forecasting.

The death in the prime of life of Dr. *Howard E. Tatel*, chairman of the Earth Physics Section of the Department of Terrestrial Magnetism, Carnegie Institution of Washington, came as a distinct surprise and shock to his friends and colleagues. He died on November 15, 1957, in Washington, D. C., after a brain tumor operation, following his return from a three-month Carnegie seismic expedition to the high Andes in Peru, Bolivia, and Chile. Dr. Tatel was born in New York City on December 22, 1913. He received both B.S. and M.S. degrees from the Massachusetts Institute of Technology, and his Ph.D. from Stanford University. He then spent two years as a research associate in nuclear physics at the University of Michigan. During World War II, he engaged in research and development work at the Applied Physics Laboratory of Johns Hopkins University. He joined the Department of Terrestrial Magnetism in 1947, where he made important contributions in geophysics and seismology. His field work with his Carnegie colleagues on the thickness of the earth's crust down to the Mohorovičić discontinuity and his laboratory model work on the conversion of P-waves to R- and S-waves and *vice versa* are of particular interest. In recent years, Dr. Tatel devoted much attention to the development of special equipment for radio astronomy and in measuring the hydrogen clouds of our galaxy.

LIST OF RECENT PUBLICATIONS

By W. E. Scott

Department of Terrestrial Magnetism,
Carnegie Institution of Washington,
Washington 15, D. C.

(Received January 4, 1958)

A—*Terrestrial Magnetism*

Anderson, K. A. Occurrence of soft radiation during the magnetic storm of 29 August 1957. J. Geophys. Res., **62**, No. 4, 641-644 (1957). [Letter to Editor.]

Annals of the International Geophysical Year. IGY Instruction Manual—Geomagnetism. Pergamon Press, London-New York-Paris, Vol. 4, Pts. 4, 5, 6, and 7, pp. 207-393 (1957).

Aramaki, S., and S. Akimoto. Temperature estimation of pyroclastic deposits by natural remanent magnetism. Amer. J. Sci., **255**, No. 9, 619-627 (1957).

Barta, Gy. Report on the geomagnetic and telluric researches carried out in Hungary during the period of 1954-57. Budapest, Acta Technica, **18**, Fasc. 1-2, 161-166 (1957).

Bell, B., and H. Glazer. Geomagnetism and the emission-line corona, 1950-1953. Smithsonian Contrib. Astroph., **2**, No. 3, 51-107 (1957).

Bozorth, R. M., D. E. Walsh, and A. J. Williams. Magnetization of ilmenite-hematite system at low temperatures. Phys. Rev., **108**, No. 1, 157-158 (1957). [Letter to Editor.]

Chopra, K. P. Magnetic fields in a conducting fluid sphere with volume currents. J. Geophys. Res., **62**, No. 4, 573-579 (1957).

Cole, G. H. A. The earth and its magnetic field. Sci. Prog., **45**, No. 180, 628-645 (1957).

Djakarta (Batavia-Kuyper) Observatory. Magnetic observations, 1937-1940. Meteorological and Geophysical Service, Ministry of Communications, Vol. 40B, 100 pp. approx. (rec'd Nov. 15, 1957). [Published by order of the Government of Indonesia, by F. H. Schmidt, acting director.]

Dombås Magnetic Station. Description of the new station and observations 1952 (with an appendix giving storminess values for 1949-1951). Bergen, Pub. Norske Inst. Kosmisk Fysikk, No. 39, 38 pp. (1957).

Du Bois, P. M., E. Irving, N. D. Opdyke, S. K. Runcorn, and M. R. Banks. The geomagnetic field in Upper Triassic times in the United States. Nature, **180**, 1186-1187 (Nov. 30, 1957). [Letter to Editor.]

Endo, H. On the seasonal change of geomagnetic *Sq* variation. Mem., Kakioka Magnetic Observatory, **8**, No. 1, 1-11 (1957).

Fougere, P., and J. McClay. Preparation of mutually consistent magnetic charts. Air Force Cambridge Res. Center, Geophys. Res. Papers No. 55, 39 pp., mim. (June 1957). [Astia Document No. AD 117268.]

Frøshaug, J. Two experimental investigations on the reliability of the QHM-magnetometer for measuring the geomagnetic horizontal force. Geophysica, **5**, No. 3, 147-149 (1957).

Gebhardt, R. E. Fredericksburg three-hour-range indices *K* for July to September, 1957. J. Geophys. Res., **62**, No. 4, 633 (1957).

Geographical Survey Institute. The second order magnetic survey of Japan (2). Bull. Geog. Surv. Inst. Japan, **5**, Pts. 1-2, 13-29 (1957).

Grenet, G. Sur l'influence de la self-induction des bobinages à noyau magnétique utilisés pour l'enregistrement des variations rapides du champ magnétique terrestre. Ann. Géophys., **13**, No. 3, 249-251 (1957).

Herrinck, P. Sur les perturbations du champ magnétique terrestre considérées comme variations de relaxation. Ann. Géophys., **13**, No. 3, 211-221 (1957).

Kakioka Magnetic Observatory. Report of the Kakioka Magnetic Observatory, Geomagnetism, 1952, 1953. Kakioka, No. 23, 124 pp. (1957).

Kakioka Magnetic Observatory. Report of the Kakioka Magnetic Observatory, Geomagnetism, 1954, 1955. Kakioka, No. 24, 119 pp. (1957).

Kato, S. Time characteristics of magneto-hydrodynamical dynamos. J. Phys. Earth, 5, No. 1, 15-24 (1957).

London, Meteorological Office. The Observatories' year book 1939, comprising the meteorological and geophysical results obtained from autographic records and eye observations at the Lerwick, Aberdeen, Eskdalemuir, Valentia, and Kew observatories, and the results of soundings of the upper atmosphere by means of registering balloons. London, H.M. Stationery Office, Pub. M.O. 599, 200 pp. (1956).

Obayashi, T., and J. A. Jacobs. Sudden commencements of magnetic storms and atmospheric dynamo action. J. Geophys. Res., 62, No. 4, 589-616 (1957).

Parker, E. N. Sweet's mechanism for merging magnetic fields in conducting fluids. J. Geophys. Res., 62, No. 4, 509-520 (1957).

Pratap, R. The effect of solar flares on the geomagnetic field. J. Geophys. Res., 62, No. 4, 581-588 (1957).

Romañá, A., J. Bartels, and J. Veldkamp. International data on magnetic disturbances, second quarter, 1957. J. Geophys. Res., 62, No. 4, 629-632 (1957).

Sinno, K. Method of magnetic storm forecasting from the activities of flares accompanied by the solar radio noise outbursts. J. Radio Res. Lab. Japan, 4, No. 17, 267-276 (1957).

Tamao, T. Distortion of the outer geomagnetic field. Sci. Rep. Tôhoku Univ., Ser. 5, Geophysics, 9, No. 1, 1-28 (1957).

Teale, R. W., and G. Rowlands. Some magnetothermal relations for ferromagnetics. Proc. Phys. Soc., B, 70, No. 456, 1123-1134 (1957).

United States Coast and Geodetic Survey. Magnetograms and hourly values, College, Alaska, 1952. Washington, D. C., U. S. Coast Geod. Surv., No. MHV-Co52, 187 pp. (1957).

United States Coast and Geodetic Survey. Magnetograms and hourly values, San Juan, P. R., 1952. Washington, D. C., U. S. Coast Geod. Surv., No. MHV-SJ52, 149 pp. (1957).

Volland, H. Zur Feinstruktur des erdmagnetischen Sonnenfinsterniseffektes. (The fine structure of the geomagnetic solar eclipse effect.) J. Atmos. Terr. Phys., 11, No. 1, 1-13 (1957).

Watson, R. A. Magnetic activity following a solar flare. J. Atmos. Terr. Phys., 11, No. 1, 59-61 (1957).

Wohlfarth, E. P., and D. G. Tonge. The remanent magnetization of single domain ferromagnetic particles. Phil. Mag., 2, No. 23, 1333-1344 (1957).

Yamaguchi, Y. The lunar diurnal variation of the magnetic declination at Kakioka. Mem., Kakioka Magnetic Observatory, 8, No. 1, 13-25 (1957).

Yokouchi, Y. Some statistical investigations of geomagnetic disturbances observed at Kakioka. Mem., Kakioka Magnetic Observatory, 8, No. 1, 27-47 (1957).

B—*Terrestrial Electricity*

Clark, J. F. Airborne measurement of atmospheric potential gradient. J. Geophys. Res., 62, No. 4, 617-628 (1957).

Gunn, R. The electrification of precipitation and thunderstorms. Proc. Inst. Radio Eng., 45, No. 10, 1331-1358 (1957).

Hewitt, F. J. Radar echoes from inter-stroke processes in lightning. Proc. Phys. Soc., B, 70, No. 454, 961-979 (1957).

Khastgir, S. R., B. A. P. Tantry, and R. S. Srivastava. Electric field changes during cloud-to-cloud lightning discharges. J. Sci. Industr. Res., B, 16, No. 7, 318-320 (1957). [Letter to Editor.]

Pierce, E. T. Nuclear explosions and a possible secular variation of the potential gradient in the atmosphere. J. Atmos. Terr. Phys., 11, No. 1, 70-72 (1957). [Research note.]

Stergis, C. G., G. C. Rein, and T. Kangas. Electric field measurements in the stratosphere. J. Atmos. Terr. Phys., 11, No. 2, 77-82 (1957).

Stergis, C. G., G. C. Rein, and T. Kangas. Electric field measurements above thunderstorms. J. Atmos. Terr. Phys., 11, No. 2, 83-90 (1957).

C—*Cosmic Rays*

Anderson, K. A. Effects of non-primary cosmic radiation on the number-energy relation and geomagnetic correlations near the top of the atmosphere. Nuovo Cimento, sup., **5**, No. 3, 389-416 (1957).

Clark, G. W. Arrival directions of cosmic-ray air showers from the northern sky. Phys. Rev., **108**, No. 2, 450-457 (1957).

Farley, F. J. M., and J. R. Storey. Time variations of extensive air showers. Proc. Phys. Soc., B, **70**, No. 453, 840-844 (1957).

Jongejans, B., and F. Schurink. Measurements on extensive air showers at mountain altitudes at the geomagnetic equator. Physica, **23**, No. 10, 977-986 (1957).

Laster, H. Factors affecting the galactic diffusion of cosmic rays. Phys. Rev., **107**, No. 4, 1112-1118 (1957).

Lockwood, J. A., and A. R. Calawa. On the barometric pressure coefficient for cosmic-ray neutrons. J. Atmos. Terr. Phys., **11**, No. 1, 23-30 (1957).

McDonald, F. B. Study of geomagnetic cutoff energies and temporal variation of the primary cosmic radiation. Phys. Rev., **107**, No. 5, 1386-1395 (1957).

Parsons, N. R. The solar daily variation of cosmic ray meson intensity at $\lambda = 52°$S. and $\lambda = 73°$S. Aust. J. Phys., **10**, No. 3, 387-396 (1957).

Wilson, R. R. Atmospheric signals caused by cosmic-ray showers. Phys. Rev., **108**, No. 1, 155-156 (1957).

Winckler, J. R., and K. A. Anderson. High-altitude cosmic-ray latitude effect from 51° to 65°N geomagnetic latitude. Phys. Rev., **108**, No. 1, 148-154 (1957).

D—*Upper Air Research*

Abbott, W. N. Quelques intéressantes variations du souffle de fond observées sur les fréquences de 17.6 Mc/s. J. Atmos. Terr. Phys., **11**, No. 1, 72-74 (1957). [Research note.]

Annals of the International Geophysical Year. IGY Instruction Manual—The Ionosphere. Pergamon Press, London-New York-Paris, Vol. 3, Pt. 1, pp. 1-167 (1957).

Annals of the International Geophysical Year. IGY Instruction Manual—The Ionosphere. Pergamon Press, London-New York-Paris, Vol. 3, Pts. 2, 3, and 4, pp. 173-381 (1957).

Annals of the International Geophysical Year. IGY Instruction Manual—Nuclear Radiation, Aurora and Airglow, and Longitudes and Latitudes. Pergamon Press, London-New York-Paris, Vol. 4, Pts. 1, 2, and 3, pp. 7-201 (1957).

Bai, C. L. Application of the generalized magneto-ionic theory to the propagation of radio waves at the magnetic dip-poles of the earth. J. Atmos. Terr. Phys., **11**, No. 1, 31-35 (1957).

Barsis, A. P. Long distance tropospheric propagation measurements between North Africa and Spain. Part II. Results of the measurements. Boulder Laboratories, Nation. Bur. Stan., NBS Rep. No. 5524, 27 pp. + 8 Figs., mim. (Oct. 15, 1957).

Barsis, A. P., and R. S. Kirby. Long distance tropospheric propagation measurements between North Africa and Spain. Part I. Theoretical estimates, path description, and method of operation. Boulder Laboratories, Nation. Bur. Stan., NBS Rep. No. 5067, 16 pp. + 17 Figs., mim. (May 15, 1957).

Bates, D. R., and B. L. Moiseiwitsch. On the remarks of V. I. Krassovsky regarding the O_3 and O_2 hypotheses of the OH airglow. J. Atmos. Terr. Phys., **11**, No. 1, 68-70 (1957). [Research note.]

Bean, B. R., and R. Abbot. Oxygen and water vapor absorption of radio waves in the atmosphere. Geofisica pura e appl., Milano, **37**, 127-144 (1957).

Bean, B. R., and B. A. Cahoon. The use of surface weather observations to predict the total atmospheric bending of radio rays at small elevation angles. Proc. Inst. Radio Eng., **45**, No. 11, 1545-1546 (1957). [Correspondence.]

Beynon, W. J. G., and G. M. Brown. Ionospheric indices of solar activity. J. Atmos. Terr. Phys., **11**, No. 2, 128-131 (1957). [Research note.]

Blagonravov, A. A. Study of the upper strata of the atmosphere by means of high-altitude rockets. Vestnik Akad. Nauk SSSR, No. 6, 25-32 (1957). [Translation by E. R. Hope, Directorate of Scientific Information Service, Defense Research Board of Canada, Pub. No. T 257 R, August 1957.]

Bolgiano, R., Jr. Discussion of the Wheelon paper, "Radio frequency and scattering angle dependence of ionospheric scatter propagation at VHF." J. Geophys. Res., **62**, No. 4, 639-640 (1957). [Letter to Editor.]

Bowden, K. R. R., and J. G. Davies. The time distribution of meteors. J. Atmos. Terr. Phys., **11**, No. 1, 62-66 (1957).

Bowen, E. G. Relation between meteor showers and the rainfall of August, September, and October. Aust. J. Phys., **10**, No. 3, 412-417 (1957).

Bowhill, S. A. Ionospheric irregularities causing random fading of very low frequencies. J. Atmos. Terr. Phys., **11**, No. 2, 91-101 (1957).

Bremmer, H. The mode expansion in the low-frequency range for propagation through a curved stratified atmosphere. Boulder Laboratories, Nation. Bur. Stan., NBS Rep. No. 5518, 21 pp., mim. (Sept. 23, 1957).

Brown, R. R., P. E. Green, Jr., B. Howland, R. M. Lerner, R. Manasse, and G. Pettengill. Radio observations of the Russian earth satellite. Proc. Inst. Radio Eng., **45**, No. 11, 1552-1553 (1957). [Correspondence.]

Burke, M. J., and I. S. Jenkinson. Ionospheric drifts at Brisbane. Aust. J. Phys., **10**, No. 3, 378-386 (1957).

Cailliatte, C. Sur quelques mesures de la luminance du ciel nocturne dans le proche infrarouge. Paris, C.-R. Acad. sci., **245**, No. 20, 1739-1740 (1957).

Chamberlain, J. W. On a possible velocity dispersion of auroral protons. Astroph. J., **126**, No. 2, 245-252 (1957).

Chandrasekhar, S., A. N. Kaufman, and K. M. Watson. Properties of an ionized gas of low density in a magnetic field. III. Annals of Physics, **2**, No. 5, 435-470 (1957).

Chapman, J. H., W. J. Heikkila, and J. E. Hogarth. A new technique for the study of scatter propagation in the troposphere. Can. J. Phys., **35**, 823-830 (1957).

Christchurch Geophysical Observatory. Ionospheric data: Godley Head, 1955; Rarotonga, 1955; and Campbell Island, 1954. Department of Scientific and Industrial Research (Geophysics Division), New Zealand, 266 pp., mim. (1957).

Coulomb, J. Sur une origine aurorale possible de certaines pulsations géomagnétiques. Ann. Géophys., **13**, No. 2, 91-102 (1957).

Dowden, R. L. Short-range echoes observed on ionospheric recorders. J. Atmos. Terr. Phys., **11**, No. 2, 111-117 (1957).

Elgaröy, Ö. Duration of transients in solar radio noise. Nature, **180**, 808-809 (Oct. 19, 1957). [Letter to Editor.]

Ellis, G. R. Measurement of the gyro-frequency in the *F* region. J. Atmos. Terr. Phys., **11**, No. 1, 54-58 (1957).

Evans, J. V. The scattering of radio waves by the moon. Proc. Phys. Soc., B, **70**, No. 456, 1105-1112 (1957).

Forsyth, P. A., E. L. Vogan, D. R. Hansen, and C. O. Hines. The principles of JANET—a meteor-burst communication system. Proc. Inst. Radio Eng., **45**, No. 12, 1642-1657 (1957).

Fricker, S. J., R. P. Ingalls, M. L. Stone, and S. C. Wang. UHF radar observations of aurora. J. Geophys. Res., **62**, No. 4, 527-546 (1957).

Gartlein, C. W., and G. Sprague. Hydrogen in auroras. J. Geophys. Res., **62**, No. 4, 521-526 (1957).

Gladden, S. C. Letter symbols and their application in the scaling of ionospheric vertical soundings. Boulder Laboratories, Nation. Bur. Stan., NBS Rep. No. 5523, 57 pp., mim. (Oct. 11, 1957).

Greenhow, J. S., and E. L. Neufeld. The variation of ionization along a meteor trail. Mon. Not. R. Astr. Soc., **117**, No. 4, 359-369 (1957).

Hibberd, F. H. Self-distortion of radio waves in the ionosphere, near the gyro frequency. J. Atmos. Terr. Phys., **11**, No. 2, 102-110 (1957).

Hines, C. O. Heavy-ion effects in audio-frequency radio propagation. J. Atmos. Terr. Phys., **11**, No. 1, 36-42 (1957).

Hines, C. O., and P. A. Forsyth. The forward-scattering of radio waves from overdense meteor trails. Can. J. Phys., **35**, 1033-1041 (1957).

Houston, Jr., R. E. The effect of certain solar radiations in the lower ionosphere. Pennsylvania State University, Ionosphere Res. Lab., Sci. Rep. No. 95, 73 pp., mim. (July 1, 1957).

Hunten, D. M. Correction for Raleigh-scattered light of sodium observations in twilight. J. Atmos. Terr. Phys., **11**, No. 1, 67-68 (1957). [Research note.]

Inoue, Y. On the ionization mechanism in the ionosphere. Jap. J. Geophys., **1**, No. 3, 21-120 (1957).

Ionospheric Soundings Review and Research Group (R. W. Knecht, Project Leader). Instructions for ionospheric vertical sounding station operation. Boulder Laboratories, Nation. Bur. Stan., NBS Rep. No. 5516, 72 pp., mim. (Oct. 1, 1957).

Jodrell Bank Experimental Station (The Staff), University of Manchester. Radar observations of the first Russian earth satellite and carrier rocket. Nature, **180**, 941-942 (Nov. 9, 1957).

Joshi, G. H. The electromagnetic interaction between two crossing electron streams. Part I. Göteborg Chalmers Tekn. Högsk. Handl., No. 183, 31 pp. (1957). [Res. Lab. Electronics Rep. No. 42.]

Kasuya, I. On the occurrence of the $F1\frac{1}{2}$ layer in Japan. J. Radio Res. Lab. Japan, **4**, No. 17, 291-300 (1957).

Kay, I. On the measurement of virtual height. New York University, Math. Res. Group, Res. Rep. No. MME-5, 11 pp., mim. (July 1957).

Kilpatrick, E. L. Stratification in the ionized D and E regions as recorded at low- and high-sweep frequencies. Boulder Laboratories, Nation. Bur. Stan., NBS Rep. No. 5031, 11 pp. + 7 Figs. (Mar. 5, 1957).

King, I. R., G. C. McVittie, G. W. Swenson, Jr., and S. P. Wyatt, Jr. Further radio observations of the first satellite. Nature, **180**, 943 (Nov. 9, 1957).

Lea, N. Further radio observations of the first satellite. Nature, **180**, 943 (Nov. 9, 1957).

Megaw, E. C. S. (The Late). Fundamental radio scatter propagation theory. Proc. Inst. Elec. Eng., **104**, Pt. C, No. 6, 441-455 (1957).

Millman, P. M. The upper atmosphere and current research. J. R. Astr. Soc. Can., **51**, No. 6, 334-340 (1957). [Highlights of U.R.S.I. meeting at Boulder, Colorado, Aug. 22 to Sept. 5, 1957, and Eleventh General Assembly of the International Union of Geodesy and Geophysics, in Toronto, Canada, Sept. 3-14, 1957.]

Mironov, A. V., and V. S. Prokudina. Identification of the night sky emission around 5300 Å. Astr. J. Sov. Un., **34**, No. 3, 440-441 (1957). [Translation by E. R. Hope, Directorate of Scientific Information Service, Defense Research Board of Canada, Pub. T 259 R, October 1957.]

Montalbetti, R., and A. Vallance Jones. H_α emissions during aurorae over west-central Canada. J. Atmos. Terr. Phys., **11**, No. 1, 43-50 (1957).

Mullard Radio Astronomy Observatory (The Staff). Radio observations of the Russian earth satellite. Nature, **180**, 879-883 (Nov. 2, 1957).

Nicolet, M. A general description of the earth's atmosphere. Pennsylvania State University, Ionosphere Research Laboratory, Sci. Rep. No. 97, 75 pp., mim. (Oct. 1, 1957).

Nikolski, A. P. The world-wide distribution of magneto-ionospheric disturbance and aurora. Doklady Akad. Nauk SSSR, **115**, No. 1, 84-87 (1957). [Translation by E. R. Hope, Directorate of Scientific Information Service, Defense Research Board of Canada, Pub. T 266 R, October 1957.]

Omholt, A. Photometric observations of rayed and pulsating aurorae. Astroph. J., **126**, No. 2, 461-463 (1957). [Note.]

Pavlova, Ye. N. Energy distribution in the spectrum of the night sky luminescence. Doklady Akad. Nauk SSSR, **98**, No. 5, 769-771 (1954). [Translation by E. R. Hope, Directorate of Scientific Information Service, Defense Research Board of Canada, Pub. No. T 255 R, August 1957.]

Peterson, A. M., and Staff. Radio and radar tracking of the Russian earth satellite. Proc. Inst. Radio Eng., **45**, No. 11, 1553-1555 (1957). [Correspondence.]

Raghavendra Rao, C. S. Solar tidal effects in the F_2-region of ionosphere over Delhi. Indian J. Phys., **31**, No. 10, and Proc. Indian Assoc. Cultivation Science, **40**, No. 10, 516-525 (1957).

Robley, R. Variation annuelle de la lumière du ciel nocturne dans le bleu par spectrophotométrie photographique. Ann. Géophys., **13**, No. 3, 222-230 (1957).

Rodionov, S. F., Ye. N. Pavlova, Ye. D. Sholokhova, and L. M. Fishkova. Annual variation of night sky infrared emission. Doklady Akad. Nauk SSSR, **98**, No. 6, 957-960 (1954). [Translation by E. R. Hope, Directorate of Scientific Information Service, Defense Research Board of Canada, Pub. No. T 255 R, August 1957.]

Rogers, G. L. An experimental verification of diffraction microscopy, using radio waves. J. Atmos. Terr. Phys., **11**, No. 1, 51-53 (1957).

Royal Aircraft Establishment, Farnborough (The Staff). Observations on the orbit of the first Russian earth satellite. Nature, **180**, 937-941 (Nov. 9, 1957).

Rumi, G. C. VHF radar echoes associated with atmospheric phenomena. J. Geophys. Res., **62**, No. 4, 547-564 (1957).

Schmerling, E. R. An easily applied method for the reduction of $h'f$ records to N-h profiles including the effects of the earth's magnetic field. Pennsylvania State University, Ionosphere Res. Lab., Sci. Rep. No. 96, 24 pp., mim. (Aug. 1, 1957).

Sen Gupta, P. K. Excitation of the spectrum of the sunlit aurora. Indian J. Phys., **31**, No. 7, and Proc. Indian Assoc. Cultivation Science, **40**, No. 7, 376-383 (1957).

Shimazaki, T. Dynamical structure of the ionospheric $F2$ layer. J. Radio Res. Lab. Japan, **4**, No. 17, 309-332 (1957).

Shuleikin, V. V., and L. A. Korneva. Effect of variable flux of positive solar particles on ionospheric winds. Doklady Akad. Nauk SSSR, **107**, No. 1, 59-62 (1956). [Translation by E. R. Hope, Directorate of Scientific Information Service, Defense Research Board of Canada, Pub. No. T 258 R, 5 pp., mim. (Sept. 1957).]

Silberstein, R. Comments on the Villard-Stein-Yeh paper, "Studies of transequatorial ionospheric propagation by the scatter-sounding method." J. Geophys. Res., **62**, No. 4, 645-646 (1957). [Letter to Editor.]

Simmons, G. J. An appraisal of photon counter measurements of upper atmosphere parameters. J. Geophys. Res., **62**, No. 4, 565-571 (1957).

Skinner, N. J., and R. W. Wright. The effect of the equatorial electrojet on the ionospheric E_s and $F2$ layers. Proc. Phys. Soc., B, **70**, No. 453, 833-839 (1957).

Smith, E. K., Jr., and R. W. Knecht. Some implications of slant Es. Boulder Laboratories, Nation. Bur. Stan., NBS Rep. No. 5503, 8 pp. + 14 Figs., mim. (July 23, 1957).

Storey, L. R. O. A method for interpreting the dispersion curves of whistlers. Can. J. Phys., **35**, 1107-1122 (1957).

Takahasi, K. On the scattering of radio waves in the troposphere, stratosphere and ionosphere. J. Radio Res. Lab. Japan, **4**, No. 17, 333-340 (1957).

Taubenheim, J. Über den Einfluss von Sonneneruptionen auf die ionosphärische E-Schicht. (The influence of solar flares on the ionospheric E layer.) J. Atmos. Terr. Phys., **11**, No. 1, 14-22 (1957).

Union Géodésique et Geophysique Internationale, Association International de Magnétisme et Électricité Terrestres. Problèms de la physique de la haute atmosphère. Communications présentées à la réunion à Rome, Septembre 1954. Paris, International Association of Geomagnetism and Aeronomy, IAGA Bull. No. 15b, 260 pp. (1956; rec'd Dec. 13, 1957).

Unwin, R. S., and M. Gadsden. Determination of auroral height by radar. Nature, **180**, 1469-1470 (Dec. 28, 1957). [Letter to Editor.]

Wait, J. R. A note on the propagation of the transient ground wave. Can. J. Phys., **35**, 1146-1151 (1957).

Wait, J. R. The propagation of V.L.F. pulses to great distances. Boulder Laboratories, Nation. Bur. Stan., NBS Rep. No. 5513, 30 pp., mim. (Sept. 3, 1957).

Wax, N. A note on design considerations for a proposed auroral radar. Göteborg, Chalmers Tekn. Högsk. Handl., No. 182, 16 pp. (1957). [Res. Lab. Electronics Rep. No. 40.]

Weiss, A. A. The incidence of meteor particles upon the earth. Aust. J. Phys., **10**, No. 3, 397-411 (1957).

Wiewall, M., Jr. Determination of ionospheric drifts and turbulence from radio fading records

(final report on study of ionospheric winds). University of Puerto Rico, College of Agric. Mech. Arts, Sci. Rep. No. 4, 167 pp., mim. (Jan. 1957). [Astia Document No. 113603.]

E—*Radio Astronomy*

Akabane, K., and T. Hatanaka. Polarization of solar radio outbursts. Nature, **180**, 1062-1063 (Nov. 16, 1957). [Letter to Editor.]

Carpenter, M. S. Bibliography of extraterrestrial radio noise—List of publications issued during the period 1952-1956 inclusive. Cornell University, School of Electrical Engineering, Res. Rep. EE 332, 93 pp., mim. (June 15, 1957).

Christiansen, W. N., D. S. Mathewson, and J. L. Pawsey. Radio picture of the sun. Nature, **180**, 944-946 (Nov. 9, 1957).

Covington, A. E. VII. Solar radio astronomy. J. R. Astr. Soc. Can., **51**, No. 5, 298-307 (1957).

Dagg, M. Radio-star ridges. J. Atmos. Terr. Phys., **11**, No. 2, 118-127 (1957).

Elgaröy, O. Frequency drift of short-time transients in solar radio noise. Nature, **180**, 862 (Oct. 26, 1957). [Letter to Editor.]

Kerr, F. J., J. V. Hindman, and M. S. Carpenter. The large-scale structure of the galaxy. Nature, **180**, 677-679 (Oct. 5, 1957).

Mayer, C. H., T. P. McCullough, and R. M. Sloanaker. Evidence for polarized radio radiation from the Crab Nebula. Astroph. J., **126**, No. 2, 468-470 (1957). [Note.]

McVittie, G. C. Counts of extragalactic radio sources and uniform model universes. Aust. J. Phys., **10**, No. 3, 331-350 (1957).

Pawsey, J. L. Vistas in radio astronomy. Reprinted from Australian Acad. Sci. Year Book, pp. 65-80 (August 1957). [Reprinted for the Commonwealth Scientific and Industrial Research Organization, Australia.]

Radiophysics Laboratory, C.S.I.R.O., Australia. Symposium on Radio Astronomy (Sydney, September 1956). Commonwealth Scientific and Industrial Research Organization, Melbourne, 85 pp. (1957).

Reid, G. C. The variation with sidereal time of radio star scintillation rates. Can. J. Phys., **35**, 1004-1016 (1957).

Squires, P. The equatorial clouds of Jupiter. Astroph. J., **126**, No. 1, 185-194 (1957).

Westfold, K. C. Magnetohydrodynamic shock waves in the solar corona, with applications to bursts of radio-frequency radiation. Phil. Mag., **2**, No. 23, 1287-1302 (1957).

Whitfield, G. R., and J. Högbom. Radio observations of the Comet Arend-Roland. Nature, **180**, 602 (Sept. 21, 1957). [Letter to Editor.]

F—*Earth's Crust and Interior*

Adams, R. D. Exploration of the deep ocean floor. Nature, **180**, 778-780 (Oct. 19, 1957).

Eckelmann, W. R., and J. L. Kulp. Uranium-lead method of age determination. Part II: North American localities. Bull. Geol. Soc. Amer., **68**, No. 9, 1117-1140 (1957).

Gouin, P. An electronic seismic transducer for visual recording. Ann. Geophys., **13**, No. 3, 234-241 (1957).

Gutenberg, B. The 'boundary' of the earth's inner core. Trans. Amer. Geophys. Union, **38**, No. 5, 750-753 (1957).

Kapustinsky, A. F. A geochemical hypothesis of the earth's structure. Nature, **180**, 1245-1246 (Dec. 7, 1957). [Summary of a paper read at the Symposium on Geochemistry held in Paris in July 1957.]

Knopf, A. Measuring geologic time. Sci. Amer., **85**, No. 5, 225-236 (1957).

Öpik, E. J. The age of the earth and the universe. Discovery, **18**, No. 11, 487 (1957). [Letter to Editor.]

Raitt, R. W. Seismic-refraction studies of Eniwetok Atoll. U. S. Geol. Survey Prof. Paper, No. 260-S, pp. 685-698 (1957).

G—*Miscellaneous*

Bowen, I. S. Instrumentation at the Mount Wilson and Palomar Observatories. Pub. Astr. Soc. Pac., **69**, No. 410, 377-384 (1957).

GARFINKEL, B. On the motion of a satellite of an oblate planet. Ballistic Research Laboratories, Aberdeen Proving Ground, Md., BRL Rep. No. 1018, 33 pp., mim. (July 1957).

GILVARRY, J. J. Nature of the lunar surface. Nature, 180, 911-912 (Nov. 2, 1957). [Letter to Editor.]

GREENWICH OBSERVATORY. Results of measures made at the Royal Greenwich Observatory of photographs of the sun taken at Greenwich, the Cape and Kodaikanal in the year 1950. London, H. M. Stationery Office, viii + 137 pp. (1957).

HEISKANEN, W. A. (ED.). Symposium, "Size and shape of the earth" held at the Ohio State University, Columbus, Ohio, November 13-15, 1956. Ohio State University, Inst. Geod., Photogram. and Cartogr., Pub. No. 7, 107 pp. (1957).

HULTQVIST, B. The Kiruna Geophysical Observatory, Sweden. Nature, 180, 828-830 (Oct. 26, 1957).

NORTHCOTT, R. J. (ED.). The observer's handbook, 1958. Royal Astronomical Society of Canada, 84+ pp. (rec'd Nov. 18, 1957).

WALDMEIER, M. Provisional sunspot-numbers for July to September, 1957. J. Geophys. Res., 62, No. 4, 633 (1957).

AN APPARENT IONOSPHERIC RESPONSE TO THE PASSAGE OF HURRICANES

In the course of an investigation designed to explore different aspects of a possible connection between tropospheric and ionospheric changes as indicated by a previous study,[1] an interesting effect was noted.

During 1954 and 1955, four hurricanes—Hazel (1954), and Connie, Diane, and Ione (1955)—came close to Washington, D. C., for which meteorological and geophysical data were analyzed. Figure 1 shows the smoothed paths of these hurricanes according to the U. S. Weather Bureau Hurricane Tracking Chart.[2]

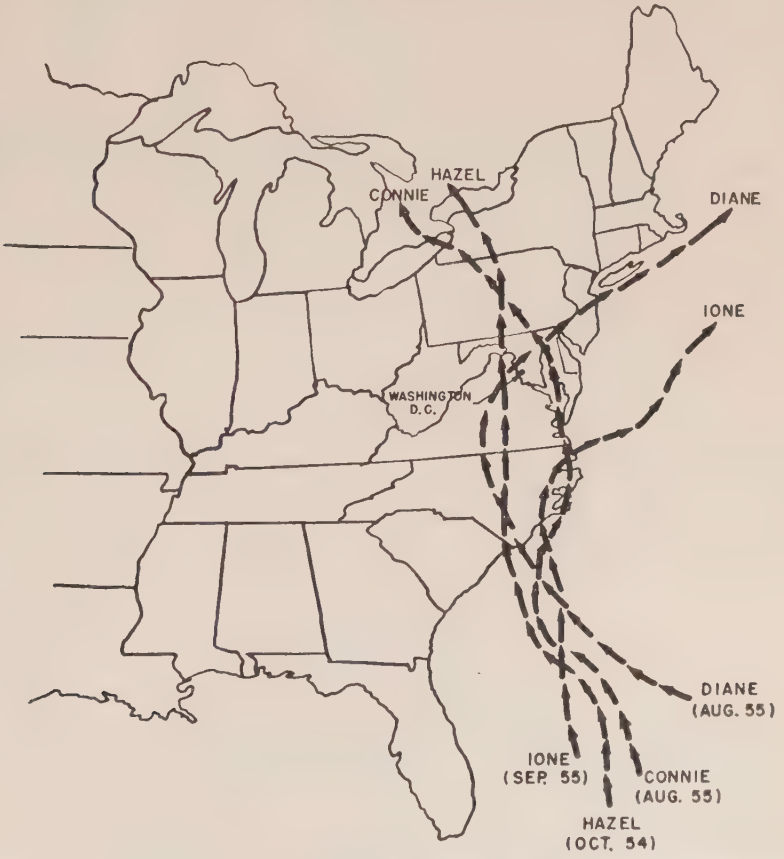

FIG. 1—Paths of hurricanes Hazel, Connie, Diane, and Ione (from *Weatherwise*)

[1]S. J. Bauer, A possible troposphere-ionosphere relationship, J. Geophys. Res., 62, 425-430 (1957).

[2]G. E. Dunn, W. R. Davis, and P. L. Moore, Hurricanes of 1954, Mon. Weath. Rev., 82, 370-373 (1954); Hurricanes of 1955, Mon. Weath. Rev., 83, 315-326 (1955).

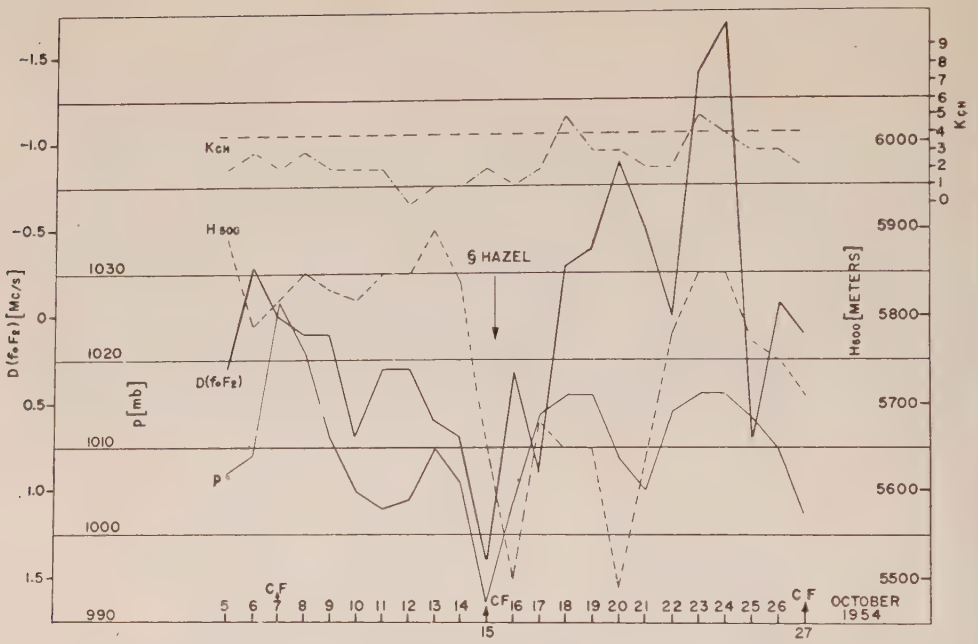

Fig. 2 —Meteorological and geophysical data for Washington, D. C., October 1954 (passage of Hazel)

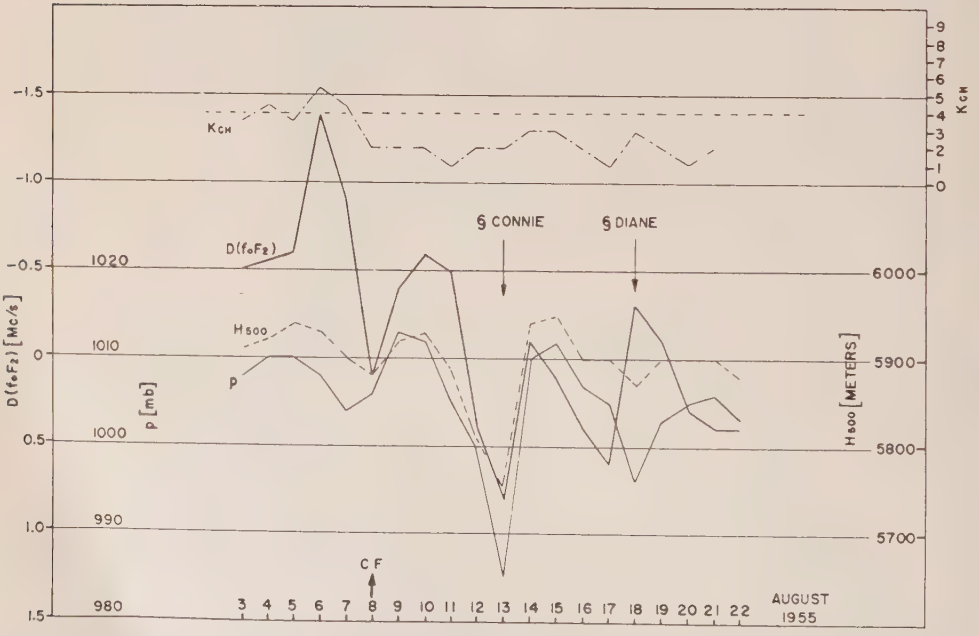

Fig. 3—Meteorological and geophysical data for Washington, D. C., August 1955 (passage of Connie and Diane)

Figure 2 presents the critical frequency of the $F2$ layer in terms of its departure from the monthly mean, $D(f_0F2)$, the geomagnetic index K_{CH} (Cheltenham, Md.), surface pressure p, and the height of the 500-mb pressure surface H_{500} for the period of October 5 to 27, 1954. Figures 3 and 4 show the same quantities for

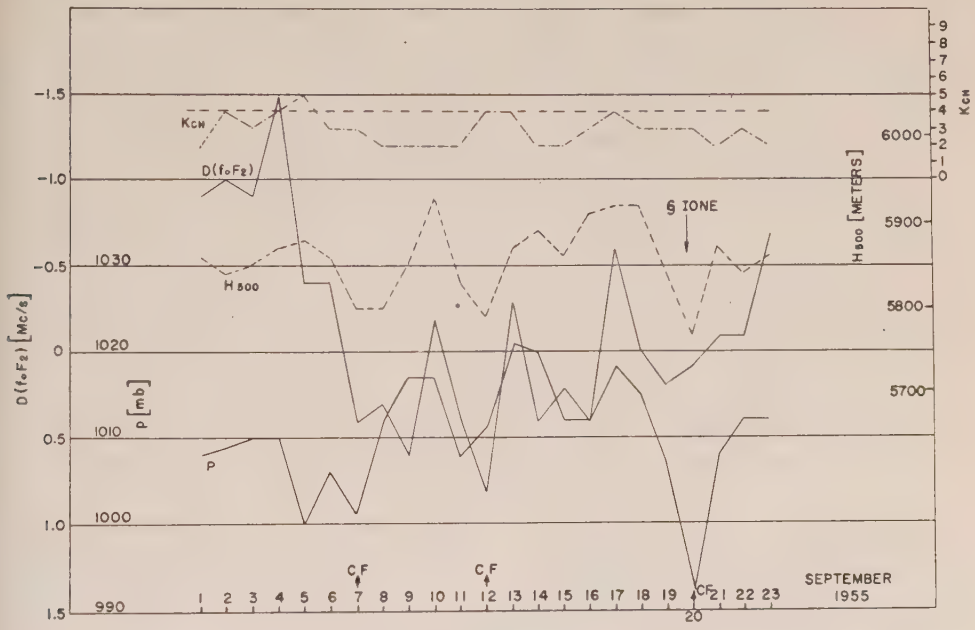

FIG. 4—Meteorological and geophysical data for Washington, D. C., September 1955 (passage of Ione)

August and September 1955, respectively. (Cold front passages are indicated by "CF".) The departures of critical frequencies from their monthly means are represented by the mean values of half-hourly observations from 0800 to 1200 hours EST, the pressure data by the 1000-hour EST observations. Inspection of these curves gives a quite good association between pressure and $D(f_0F2)$, especially for the days close to the passage of hurricanes.

It appears that with an approaching hurricane (falling pressure) the critical frequency begins to rise, reaching its maximum at about the time of minimum pressure (when the hurricane passes closest to the station).* In the case of hurricane Diane, the positive departure $D(f_0F2)$ occurred one day before the pressure minimum, while on the day of hurricane passage, $D(f_0F2)$ became negative. This apparent discrepancy, however, may be explained as a result of the hurricane's path, as will be shown later.

In the case of hurricane Ione, which passed Washington, D. C., at a distance of about 200 miles, the increase in f_0F2 is clearly indicated, although $D(f_0F2)$ did

*The departures of virtual height from the monthly mean, $D(h'F2)$, for the same time periods also showed good correlation with tropospheric pressure, a decrease of $D(h'F2)$ corresponding to falling pressure, and *vice versa*.

not reach an absolute maximum. This might possibly be the result of the decreasing trend of f_0F2 that occurred parallel to the decline in solar activity at that time.

The apparent association between the passage of a hurricane and the change in $D(f_0F2)$ could possibly be explained in the following fashion: Generally speaking, a hurricane, as well as an extratropical cyclone into which a hurricane is finally transformed, represents a low-pressure system and is, as such, associated with an area of low-level convergence extending over a major portion of the area covered by the system, while to the rear there is a zone of divergence. Low-level convergence is associated with divergence aloft, as shown by the upper outflow in tropical cyclones. The idea of a compensation in the divergence field, so that zones of convergence (divergence) are superimposed upon zones of divergence (convergence), has been introduced by Dines.[3] According to this model, we could describe the effect of tropospheric changes on the ionosphere as the result of the compensation in the divergence field. Since low-level convergence is associated with divergence in the upper troposphere and lower stratosphere, one could speculate (assuming a three-layer divergence model and dynamic coupling) that this divergence below the ionosphere may give rise to convergence and associated subsidence in the ionosphere, which would lead to an increase in electron density. Martyn[4] has pointed out that in the equation of continuity for the ionosphere,

$$\frac{\partial N}{\partial t} = I(z, t) - \alpha(z, t)N^2 - \text{div}\,(N\vec{v})$$

the divergence term (where N = electron density and $\vec{v}$ = vector velocity) assumes major importance in the $F2$ layer, but is less important in the lower layers, since there the ion production I and the recombination coefficient α, which are functions of height z and time t, are much larger than in the $F2$ layer.**

From the results presented here, it appears that the increase in $D(f_0F2)$ associated with the passage of hurricanes may be induced by the changes in the low-level divergence field. The paths of the hurricanes considered here indicate that for hurricanes Hazel, Connie, and Ione, Washington, D. C., was in the zone of convergence up to the day of passage, while as the result of the course of Diane, Washington came into the influence of the divergence zone on the day of the passage of the center.

The analysis of half-hourly values of $D(f_0F2)$ furthermore revealed that, for all hurricanes, $D(f_0F2)$ reached a maximum value within one to three hours after the hurricane center entered the coast line (Fig. 5). The magnitude of the maximum appears to be dependent on the trajectory of the hurricane relative to the coast line. This effect could also be explained in terms of convergence and its associated vertical motion, since it is known[5] that, with on-land wind, the increased friction

[3]W. H. Dines, Met. Office, London, Geophys. Mem., No. 13 (1919).

[4]D. F. Martyn, Dynamic characteristics of the ionosphere, in Proceedings of the Conference on Ionospheric Physics (July 1950), Pt. B, Geophys. Res. Paper No. 12, edited by L. Katz and N. C. Gerson, pp. 60-62 (April 1952).

**According to current belief (for example, O. Burkard, A new F layer model, Geofisica pura e appl., 37, 135-164, 1957), the electron loss in the $F2$ layer is directly proportional to the electron density, while in the E and $F1$ layer it is proportional to the square of the electron density.

[5]S. Petterssen, Weather Analysis and Forecasting, McGraw-Hill Book Co., Inc., New York, 2nd ed., Vol. 1, 85-88 (1956).

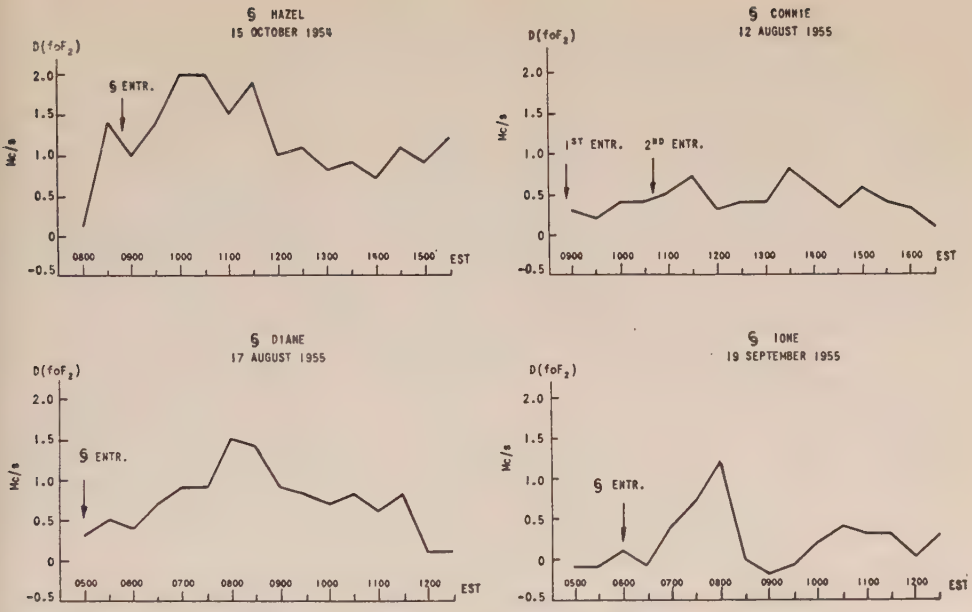

FIG. 5—Half-hourly values of $D(f_0F2)$ for days when a hurricane entered the mainland. (Approximate entrance time of hurricane center is based on radar tracking information, Ref. 2.)

over land will cause a stationary zone of convergence to occur over land, which may add to the convergence field inherent in the structure of the hurricane. During the time of hurricane passage, no ionospheric storm or SID occurred that could have caused the changes in the ionosphere found to be associated with tropospheric changes. Since apparently no extraterrestrial effects can be made responsible for the ionospheric changes during the times of hurricane passage, the explanation is suggestive that certain ionospheric changes may be induced by changes in the divergence field of tropospheric pressure systems.

Acknowledgments—The writer wishes to acknowledge the helpful comments of Dr. D. M. Swingle and the assistance of Mrs. Laura Deininger in the data analysis.

SIEGFRIED J. BAUER

U. S. ARMY SIGNAL ENGINEERING LABORATORIES,
Fort Monmouth, New Jersey, November 5, 1957
(Received November 7, 1957)

NEW ROCKET MEASUREMENT OF IONOSPHERIC CURRENTS NEAR THE GEOMAGNETIC EQUATOR*

Several rocket-borne magnetometers were flown recently near the geomagnetic equator. The record from one of these flights, made at 161° west longitude and 00° latitude, on 18 October 1957, is presented here as new evidence for the existence of electrical currents in the lower ionosphere.[1,2] The total-field magnetometer used in the flights was of the nuclear free-precession type.[3] The scalar magnitude of the earth's magnetic field $|\vec{F}|$ is obtained in terms of the precession frequency (f) of the proton, in this field, and the gyromagnetic ratio of the proton (γ);

$$|\vec{F}| = \frac{2\pi}{\gamma} f$$

The magnetometer, developed in this laboratory for small rocket use, was a lightweight version of a balloon-carried instrument, previously described.[4]

The single coil of the magnetometer was aligned with its axis coincident with the longitudinal axis of the rocket, so that the apparent precession frequency is independent of the rate of rotation of the equipment about that axis.

The magnetometer was mounted on a small, solid-propellant sounding rocket, the Loki II. In order to reach the necessary altitudes for this experiment, the "Rockoon" technique was used.[5] First carried to approximately 75,000 feet by plastic balloon, the rocket is fired by a barometric pressure switch. When launched in this manner, the Loki II is capable of carrying a 9-1/2 pound payload to a summit altitude of 80 miles.

The balloons were released from the helicopter deck of the U.S.S. *Glacier*, in the vicinity of Jarvis Island in the mid-Pacific. Jarvis Island is near the intersection of the geomagnetic and geographic equators, and is the location of one of a group of magnetic observatories in this region.[6] Small variations in $\vec{H}$ such as those that would be produced by horizontal sheets of current in the ionosphere are most readily detected by a total field magnetometer when they are observed near the equator, where $\vec{H}$ and $\vec{F}$ are nearly parallel.

State University of Iowa Rockoon Flight No. 86 left the deck of the U.S.S. *Glacier* at 1243 hours, 165th meridian time (2343 UT). The rocket fired at 71,000 feet at 1355 hours, and the total rocket flight time was 324 seconds. Audio-frequency signals from the magnetometer were transmitted by radio-frequency telemetering

*Assisted by National Science Foundation Project Grant IGY/10.1.

[1]S. F. Singer, E. Maple, and W. A. Bowen, Jr., J. Geophys. Res., **56**, 265 (1951).

[2]S. Chapman, in Rocket Exploration of the Upper Atmosphere, edited by R. L. F. Boyd and M. J. Seaton, Pergamon Press, Ltd., London (1954); pp. 292–305.

[3]M. Packard and R. Varian, Bull. Amer. Phys. Soc., **28**, No. 7 (Dec. 28, 1953); and Phys. Rev., **93**, 941 (1954).

[4]L. J. Cahill, Jr., and J. A. Van Allen, J. Geophys. Res., **61**, 547 (1956).

[5]J. A. Van Allen and M. B. Gottlieb, in Rocket Exploration of the Upper Atmosphere, pp. 53–64, *loc. cit.*

[6]Magnetic observatories on Jarvis, Fanning, and Palmyra Islands are operated by the Scripps Institution of Oceanography during the International Geophysical Year.

to the shipboard receiving station, and recorded on magnetic tape, together with a crystal-controlled reference frequency for later precise measurement. The peak of the trajectory was located in time through assumed symmetry, about the peak, of the magnetic field measurements plotted against flight time. The measurements used to determine the peak were those in the upper half of the trajectory but below the region of expected magnetic disturbance. Several trial trajectories were computed to find one that matched the observed flight time from firing altitude to peak altitude.

The measured values of $|\vec{F}|$ in gammas are shown in Figure 1 as a function of altitude. Lapses in data are due to occasional loss of telemetering signal. Not all available measurements are plotted in the upper 20 km of flight. The inverse-cube-law decrease shown is that computed from the magnetic field value measured

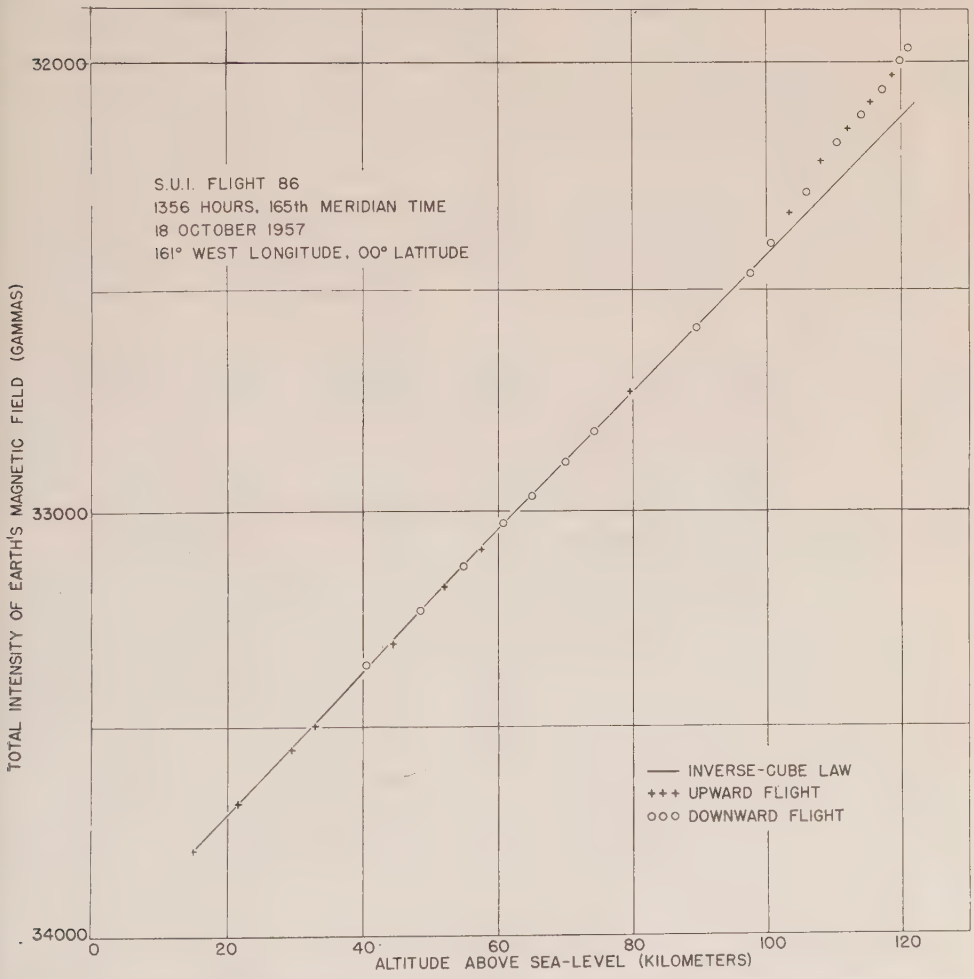

FIG. 1—Total intensity of earth's magnetic field *vs* altitude for State University of Iowa Rockoon Flight No. 86 (note that $|\vec{F}|$ decreases upward on the graph)

at 50,000 feet during the balloon flight. The balloon-flight data from sea-level to 50,000 feet are on another magnetic tape, not presently available for measurement. Agreement between the inverse-cube law and the experimental data is excellent up to 97 km. The increasing slope of the experimental curve above 97 km is attributed to entry of the rocket into an ionospheric current layer. Figure 2 shows the departure of the flight measurements from the inverse-cube law as a function of altitude. The departure at peak altitude is 135 gammas, and the accuracy of

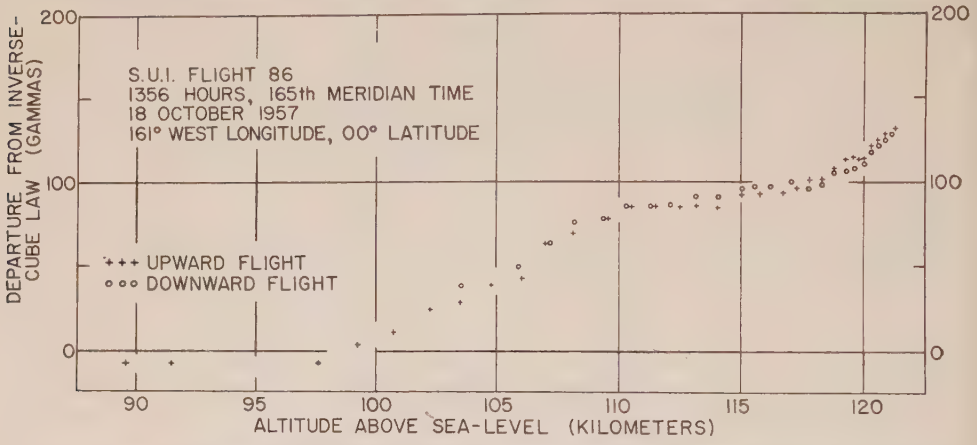

Fig. 2—Negative departures of flight data from inverse-cube law *vs* altitude for upper 30 km of flight

individual measurements is ± 5 gammas. Variometer records from the Jarvis Island observatory are not yet available. Preliminary information, however, indicates that the daily peak variation in $\vec{H}$ at Jarvis Island is between 150 and 200 gammas, and occurs between 1200 and 1400 hours, 165th meridian time.[7] The peaks at Fanning and Palmyra Islands are roughly one-half and one-quarter, respectively, of that at Jarvis Island.

The total change observed in $|\vec{H}|$ upon passing through an infinite horizontal current sheet is twice the variation in $|\vec{H}|$ caused by that current sheet at ground level. Assuming that 75 per cent of the peak ground-level variation is due to external sources, the change in $|\vec{F}|$ (equal to the change in $|\vec{H}|$ in this case) that should be observed in passing completely through all current sheets in the ionosphere above Jarvis Island is between 225 and 300 gammas. The departure of the flight curve from the inverse-cube decrease at peak altitude, 135 gammas, indicates that about one-half of the total current-sheet system has been penetrated between 97 and 121 km. The actual variation in $\vec{H}$ at Jarvis Island for the date and time in question will allow a more exact estimate of the remaining currents above 121 km. Another indication that the current sheet has not been completely penetrated is that the slope of the flight curve has not, at the peak altitude, resumed that of the inverse-cube law.

[7]R. G. Mason, Scripps Institution of Oceanography, private communication.

Further information concerning the structure of the current system is suggested by the shape of the experimental curve between 110 and 117 km. In this segment of the trajectory, the slope of the decrease again approaches that of the inverse-cube law. This is interpreted as passage through a region of little or no current density, with regions of greater current density both above and below it. The lowest current sheet extends from 97 to 110 km; a second is encountered at 118 km, and extends to at least 121 km. An estimate of the current density of these layres may also be obtained from the experimental data.

Analysis of the other magnetometer flights is under way and promises to yield information about the latitudinal extent of the equatorial current system.

Laurence J. Cahill, Jr.
James A. Van Allen

Department of Physics,
State University of Iowa,
Iowa City, Iowa, January 24, 1958
(Received January 27, 1958)

MEDIUM-FREQUENCY OBSERVATIONS OF THE LOWER IONOSPHERE DURING SUDDEN DISTURBANCES

Suggestions have been made by Friedman and Chubb[1] that sudden ionospheric disturbances may be due to an increase in the soft X-ray flux penetrating to the lower ionosphere, rather than to an increase in the intensity of Lyman-α radiation. These workers and their colleagues[2] have shown that during a small solar flare, which did not produce a detectable radio fade-out, an increase in soft X-radiation occurred above 75-km height. In estimating the intensities at various wavelengths necessary to produce extra ionization, Friedman and Chubb have used values of height derived from low-frequency radio observations, mostly of sudden phase anomalies.[3] It is the purpose of this note to present evidence obtained from medium-frequency observations of the condition of the lower ionosphere during disturbances.

The data given below have been gathered during studies of the lower ionosphere by means of a fixed-frequency (1.75 Mc/s) pulse-sounding apparatus of high sensitivity. Typical records and preliminary results of these studies have been presented by the writer.[4] Records taken during undisturbed conditions show partial reflections, from 50 km upwards, which vary in strength, height, duration, and fading rate; and a disturbance is revealed through changes in these reflections. Figure 1 shows a record about noon on February 11, 1956. At the left of the record, above the letter *A*, reflections which are characteristic of summer conditions appear. Partial reflections can be discerned from 67 km up to a sharp reflection boundary at 85 km. Reflections from this boundary merge with those from *E* region, which is judged to be at 95 km by comparison with readings taken 20 minutes earlier. The partial reflection coefficients for the 67-km reflections are estimated to lie between

[1]H. Friedman and T. A. Chubb, Report of the Physical Society Conference on the Physics of the Ionosphere held at the Cavendish Laboratory, Cambridge, September 1954, p. 58 (1955).

[2]T. A. Chubb, H. Friedman, R. W. Kreplin, and J. E. Kupperian, Jr., J. Geophys. Res., **62**, 389 (1957).

[3]R. N. Bracewell and T. W. Straker, Mon. Not. R. Astr. Soc., **109**, 28 (1949).

[4]J. B. Gregory, Aust. J. Phys., **9**, 324 (1956).

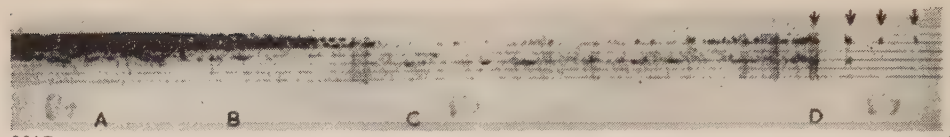

Fig. 1—1.75-Mc/s h'-t record: February 11, 1956, near noon. A disturbance starts at 0020 hours UT (1220 hours New Zealand ST). New reflections appear at 62 km, after higher reflections have disappeared. (Height markers commence at 45 km, and are at 10-km intervals thereafter.)

1.5 and 3.0 $\times$ 10^{-5}; for the 85-km region, between 1.5 and 2 $\times$ 10^{-4}; and for E region, between 3.0 and 4 $\times$ 10^{-4}. The onset of a disturbance is marked by the letter B. The 67-km reflections weaken, and disappear within two and a half minutes of onset. Simultaneously, the E-region reflections at greatest apparent height weaken. (This latter effect is explicable in terms of the polar diagram of the vertically-directed broadside array used in these observations, if it is assumed that greatest apparent height corresponds to a non-vertical path.) Within another minute, E-region reflections disappear, and the 85-km reflections show only intermittently at the maximum of the disturbance (0023 hours UT). At this juncture, there appears at 62 km (above letter C) a new series of partial reflections which are 5 km lower than any reflections noted throughout the preceding half-hour. These persist for some 20 minutes, and at the time of their disappearance (not shown in Fig. 1) the 67-km, 85-km, and E-region reflections resume their original strengths. A partial recovery of these latter reflections occurs prior to the disappearance of the 62-km reflections.

In Figure 1, an automatic registration of reflection amplitudes (gain sweep), which is initiated once per hour, coincides with the disturbance, and occupies the right-hand side of the record (starting above letter D). Receiver gain is reduced in a series of steps, each of about 6 db. (Arrows above the record show the start of each step. The momentary appearance of reflections prior to each arrow is due to an increase of gain while switching between steps.) It will be noted that both the 85-km and the 62-km reflections are reduced in amplitude below recording level by a single 6-db decrease in sensitivity. During the disturbance, the 85-km reflection probably exceeds the 62-km reflection by some 3 db, and, for both, the reflection coefficients lie between 1.0 and 4.0 $\times$ 10^{-5}.

Figure 2 shows another disturbance, occurring at 0344 hours UT on September 5, 1957. Prior to the disturbance, reflections were returned from many heights above 65 km, and up to E region. At 0344 hours, the reflection from E region (above letter F), previously at 95-km height, is rapidly fading, and the "top" of the E-region reflection extends a little in apparent height. This extension is

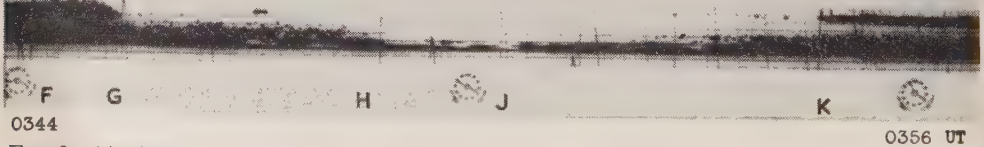

Fig. 2—1.75-Mc/s h'-t record: September 5, 1957. A disturbance starts at 0344 UT (1544 New Zealand ST) and reaches its maximum at 0350. The disappearance of reflections due to increased absorption is clearly visible. (The near-vertical lines are due to interference from a pulse transmitter. Height markers are as in Fig. 1.)

consistent with an increase in scattering from irregularities in E region at slant ranges but probably at constant height. At 0345 (above letter G), reflections from apparent heights of 120 down to 90 km vanish progressively in an interval of some 20 seconds. Lower reflections are only slightly affected, but at 0348 (above letter H) the disturbance enters a new stage and reflections from 90 to about 75 km also vanish. At 0350 (above letter J), the climax is reached. At this instant, reflections above 67–75 km disappear, leaving only reflections at 63–67 km. Comparison with the record prior to the disturbance suggests that the lowest reflection decreased in height from 65 km to 63 km, and that it increased slightly in strength at the peak of the disturbance. After 0350 hours, the disturbance lessens, but does not completely disappear. E region is detectable, at about 105 km, by 0354 hours (at letter K), but subsequent portions of the record show a continuing weakness of reflections from 95 to 105 km, and at 0410 hours, a similar, but much less severe, series of events recur.

Over 40 SID's of widely varying characteristics have been recorded for part or all of their duration throughout a period of 18 months. Visual observations of a monitor oscilloscope support records obtained automatically. In seven instances, no reflections at any height were detectable at the peak of the disturbance. (Minimum detectable signal corresponds to a voltage reflection coefficient, in the absence of absorption, of less than 10^{-5}.) For each of 11 disturbances, only one reflection at a height between 56 and 65 km was recorded. For nine of these latter, new reflections appeared between 56 and 65 km, at a height lower than that noted just prior to the disturbance. When SID's occurred within a few hours of each other, the new reflections appeared at similar heights.

The origin of partial reflections in the lower ionosphere is believed to involve meteorological factors which give rise to discontinuities in electron density. It is thus likely that the position of a partial reflection noted during an SID is due to some factor which is present prior to a disturbance and which serves to reveal newly created ionization. The foregoing results suggest that during some SID's the increase in ionizing radiation is effective at heights as low as 56 km. Further, the disappearance of low height reflections (similar to that shown above "B" in Fig. 1) suggests that in some instances ionization which gives rise to absorption but which does not produce reflection exists below 56 km. Records such as Figure 2 show that the level in the ionosphere at which absorption becomes excessive decreases in a series of steps, and it is tempting to infer that the latter correspond to a decrease in the wavelength of the incident radiation. It has not been possible to determine the actual values of electron concentration at the base of the ionosphere during an SID, but the discontinuities giving rise to partial reflections between 62 and 65 km appear to be due to changes in concentration of up to 20 el/cm^3.

These findings emphasize the argument of Friedman and Chubb that Lyman-α is unlikely to be the agent giving rise to the formation of ionization during solar flares, and are not inconsistent with their suggestion that soft X-rays are responsible for SID's.

J. B. Gregory

Physics Department, University of Canterbury,
Christchurch, New Zealand, January 27, 1958
(Received February 3, 1958)

NOTICE

When available, single unbound volumes can be supplied at $6 each and single numbers at $2 each, postpaid.

Charges for reprints and covers

Reprints can be supplied, but prices have increased considerably and costs depend on the number of articles per issue for which reprints are requested. It is no longer possible to publish a schedule of reprint charges, but if reprints are requested approximate estimates will be given when galley proofs are sent to authors. Reprints without covers are least expensive; standard covers (with title and author) can be supplied at an additional charge. Special printing on covers can also be supplied at further additional charge.

Fifty reprints, without covers, will be given to institutions paying the publication charge of $8 per page.

Alterations

Major alterations made by authors in proof will be charged at cost. Authors are requested, therefore, to make final revisions on their typewritten manuscripts.

Orders for back issues and reprints should be sent to Editorial Office, 5241 Broad Branch Road, N.W., Washington 15, D. C., U.S.A.

Subscriptions are handled by The Editorial Office, 5241 Broad Branch Road, N.W., Washington 15, D. C., U.S.A.

CONTENTS—Concluded